NORTHWESTERN UNIVERSITY

High-density Lipoprotein Mimetic Nanoparticles: Roles in Therapy and Probing Intercellular Communication

A DISSERTATION

SUBMITTED TO THE GRADUATE SCHOOL

IN PARTIAL FULFILLMENT OF THE REQUIREMENTS

for the degree of

DOCTOR OF PHILOSOPHY

Field of Biomedical Engineering

By

Stephen E. Henrich

EVANSTON, ILLINOIS

September 2021

ABSTRACT

Bio-inspired materials have a distinct advantage over other materials by virtue of their mimicry of nature's own products, which have been subjected to the inimitable tests of time and evolutionary pressure. Here we have taken instruction from natural nanostructures that are ubiquitous across the animal kingdom, namely high-density lipoproteins (HDL). These native nanoparticles circulate in the bloodstream and transport lipids between organs and tissues. Primary among the lipids that HDLs and other lipoproteins transport is cholesterol. Cholesterol is an indispensable component of animal cell membranes that regulates a host of biological processes such as ligand-receptor interactions, endocytosis, membrane protein scaffolding, intercellular communication, second messenger signaling and others. There is a vast possibility space for applications of HDL-mimicking nanoparticles (HDL NP), only a fraction of which have been explored to date. In this thesis, we explore three primary applications: 1) anti-atherosclerosis therapy by way of cholesterol transport, 2) probing the cholesterol-dependence of intercellular signaling, particularly via exosomes, and 3) inhibiting viral infection by targeted depletion of cholesterol. In addition to the application of these materials for translational purposes, we also report fundamental strides in HDL NP synthesis. In particular, we describe the fabrication of nanoparticles that mimic mature, spherical HDLs using novel, small molecule-phospholipid conjugates as core scaffolds. These materials are distinctive for several reasons: 1) they represent a successful synthesis of monodisperse lipid nanoparticles in the sub-20 nm size regime, which is extremely challenging without using an inorganic template, 2) most synthetic HDL mimics resemble immature, discoidal HDL, while these particles represent a genuine functional mimic of mature spherical HDL (the most abundant HDL sub-species in humans), 3)

these particles possess a dynamic, hydrophobic core that can accommodate a diverse range of hydrophobic cargo, and 4) these particles reduce atherosclerotic burden in LDL-R$^{-/-}$ mice by approximately 70%. The second major focus of this dissertation is on the cholesterol dependence of exosome communication in the setting of cancer. Others have shown that primary tumors can establish long-range communication with distant organ sites to transform them into fertile soil for circulating tumor cells to implant and proliferate, a process called pre-metastatic niche formation. Tumor-derived exosomes can be potent mediators of pre-metastatic niche formation. Here we explore the role of prostate cancer exosomes as promoters of pre-metastatic niche formation in bone, and we interrogate the cholesterol dependence of this intercellular communication. We show that exosome-mediated communication between prostate cancer cells and bone marrow myeloid cells is highly sensitive to the cholesterol burden of the target myeloid cell population. In particular, reducing cellular cholesterol in myeloid cells in a targeted fashion using HDL NPs reduces the transduction of prostate cancer exosome signaling, ultimately inhibiting both pre-metastatic niche formation and metastasis. HDL NPs enabled us to interrogate the cholesterol dependence of exosome communication *in vivo* with greater precision than other methods due to the intrinsic targeting properties of HDL NPs and their favorable toxicity profile. HDL NPs enabled us not only to identify that cholesterol is a critical parameter for this intercellular communication, but also to demonstrate that cholesterol modulation may be a viable approach to metastasis therapy and prevention. Finally, we demonstrate that HDL NPs can function as anti-viral agents to inhibit infection of a SARS-CoV-2 pseudovirus by targeted depletion of cellular cholesterol.

ACKNOWLEDGEMENTS

I'd first like to thank my advisor, Professor C. Shad Thaxton. Shad was kind enough to welcome me into the lab after I had been working in another lab for one year prior. Upon joining the lab, I was especially grateful that Shad gave me the freedom and flexibility to pursue what I was most interested in. I was fortunate to be able to build upon a wealth of existing knowledge and expertise in the lab with respect to both biomaterials science and basic biology. Shad has been a near limitless source of knowledge, optimism, enthusiasm, and ideas. He has cultivated a lab environment which has been a truly stimulating and inspiring place to earn one's PhD.

My co-workers in the Thaxton Lab have also been outstanding, and I'm grateful to have worked with such intelligent and industrious colleagues. I'd like to thank Mike Plebanek for showing me the ropes with respect to exosome research, and for the strong foundation of results he built which I used as a foundation for the exosome portion of my PhD thesis. I'd like to thank Kaylin McMahon for being the rock of the lab. Without your knowledge, attention to detail, organizational skills, and patience, the rest of us probably would have blown up the lab a long time ago. Thank you especially for teaching me tail vein injections, for expanding my competence with animal work more generally, and for your help on the prostate cancer metastasis mouse model and the atherosclerosis mouse model. And you're welcome for helping you reach the top shelf. Thank you also to Jon Rink. You've been a great colleague to work with on the atherosclerosis project, the PIK-75 studies, and more. Thank you especially for your time and patience when teaching me the cholesterol efflux assay as well as aorta pinning. Please forgive me for the temperature-controlled box debacle, and for all the times you had to remind me to complete my trainings. Thank you to Andrea Calvert—our work on the COVID diagnostic this past year has been very exciting and time-intensive, and I'm glad to have been able to work with you on such an exciting project. Thank you for picking up the slack while I was taking classes, and for taking the initiative to organize and keep a solid record of all our results. I'd also like to thank Tim Feliciano. It's been a pleasure working in the

same group with you after you joined the lab, and I look forward to seeing how your projects unfold over the next year. I can rest assured that much of the soft-core HDL NP work is in good hands with you. I always enjoy our conversations, especially when they stray into the fun topics like physics, math, philosophy, and religion. Finally, I'd like to thank Adam Lin for captaining the PIK-75 project— I'm optimistic regarding the long-term potential of chemo-loaded HDL NPs and look forward to seeing how the *in vivo* studies pan out.

I'd like to thank Prof. Ronit Freeman for her mentorship during the first year of my PhD. Ronit is an outstanding materials scientist, and much of the biomaterials work over the course of my PhD was improved in quality due to the knowledge and expertise she imparted during that first year. I'd also like to thank Jacob Lewis, Nick Tsihlis, and Dounia Dems for their collaboration and guidance during my first year. I would also like to thank the multiple collaborators with whom I've worked with over the course of my PhD, including Prof. Sonbinh Nguyen, Dr. Bong Jin Hong, Dr. Benedito Carneiro, and Prof. Pablo Penaloza-MacMaster. I'd also like to thank my thesis committee members Guillermo Ameer, Evan Scott, and Don Vander Griend for their time, support, and constructive feedback.

It wouldn't be easy to make it through a PhD without great friends; and there are no greater friends in the world than Michelle Lundholm-Kasparie and Alex Kasparie. Thank you to both of you for all of our fun adventures in the Chicagoland area, for being outstanding Escape Room partners, and for many nights spent relaxing and enjoying each others' company after a long day's work. Thank you also to my St. Clement friends. I always looked forward to volleyball, men's group, wine and cheese, and so much more. Thank you also to all of my MD-PhD classmates. It's been a long, fun journey and I wish you all the best as we go our various ways. P.S. sorry for jumping ship.

I'd also like to extend my thanks to my outstanding undergraduate mentors, without whom I wouldn't be where I am today. I'd especially like to thank Heidi Berger and Ron Warnet. Firstly, thank you both for your levity, wit, and humor-- I think those are underappreciated qualities in an academic that can make all the difference for students when engaging with the material and when considering a career in academia. Heidi, thank you for your time mentoring myself and the other students during our summer research program in 2010, and through the academic year. Despite the dirt and maggots, my introduction to intensive academic research couldn’t have been better. Ron, thank you for introducing me to nanoscience and nanotechnology and for being an outstanding organic chemistry professor and life coach. Your mentorship is one of the main reasons I ended up at Northwestern pursuing the path that I did. Finally, thank you to Dr. Krish Kizhatil and Prof. Simon John. Krish was an exceptional mentor during my summer at the Jackson Laboratory in the John Lab who introduced me to all sorts of techniques in biomedical research, and provided an excellent model for me as I moved toward my graduate career. Thank you for your time, guidance, and patience with me during my time at JAX.

Lastly, but most importantly, thank you to my family. My parents, Ed and Laura, and my siblings, Daniel, Rachel, Anna, Elizabeth, Grace, Matthew, and Adam, have been a consistent source of support and encouragement throughout my PhD and I’m fortunate to have them in my life. I’m especially grateful to my parents for their selfless devotion of a great deal of time and energy into their children in order to provide us with the best opportunities for successful and joy-filled lives.

LIST OF ABBREVIATIONS

apoA-1: apolipoprotein A-1

ASCVD: atherosclerotic cardiovascular disease

AuNP: gold nanoparticle

BMDC: bone marrow-derived cell

BMM: bone marrow macrophage

CD: circular dichroism

CE: cholesteryl ester

DLS: dynamic light scattering

DMEM: Dulbecco’s Modified Eagle’s Medium

DMF: dimethylformamide

DNA-PL$_4$: four-armed small molecule-phospholipid conjugate with a DNA linker

EnzR: enzalutamide resistant

ESI MS: electrospray ionization mass spectrometry

FC: free cholesterol

GMP: good manufacturing practice

HDL: high-density lipoprotein

HDL-C: high-density lipoprotein cholesterol

LCAT: lecithin:cholesterol acyltransferase

LC HDL NP: lipid conjugate high-density lipoprotein-like nanoparticle

LDL: low-density lipoprotein

LDL-$R^{-/-}$: low-density lipoprotein receptor knockout

MALDI-ToF: matrix-assisted laser desorption ionization-time of flight

MβCD: methyl-β-cyclodextrin

MDSC: myeloid-derived suppressor cell

miRNA: microRNA

NF-κB: nuclear factor kappa-light-chain-enhancer of activated B cells

NP: nanoparticle

PBS: phosphate buffered saline

PCa: prostate cancer

PL: phospholipid

PL_4: four-armed small molecule-phospholipid conjugate

PLGA: poly(lactic-*co*-glycolic acid)

RANK-L: receptor activator of nuclear factor kappa-light chain enhancer of activated B cells ligand

RCT: reverse cholesterol transport

rHDL: reconstituted HDL

RNAi: RNA interference

RP-HPLC: reverse phase-high performance liquid chromatography

RPMI: Roswell Park Memorial Institute (cell culture medium)

SARS-CoV-2: severe acute respiratory syndrome coronavirus 2

SEC: size exclusion chromatography

SR-B1: scavenger receptor class B type 1

ssDNA: single-stranded DNA

TBS: tris buffered saline

TEM: transmission electron microscopy

TEx: tumor-derived exosomes (also refers to exosomes produced by cancer cell lines)

TG: triglyceride

THBS1: thrombospondin-1 (gene)

Treg: regulatory T cell

TSP1: thrombospondin-1 (protein)

VCAN: versican

WBC: white blood cell

TABLE OF CONTENTS

LIST OF FIGURES and TABLES

Figures

Tables

Chapter 1: Introduction

Four major classes of biomacromolecules comprise the bulk of matter in living things: nucleic acids, proteins, carbohydrates, and lipids. Lipids play many roles in biological systems, but one of the most important is the formation and maintenance of biological barriers such as the cell's plasma membrane.[1] The three dominant classes of structural lipids that comprise the plasma membrane are phospholipids, glycolipids, and sterols.[2] Sterols are a class of lipid with four fused rings and typically an alcohol group which are essential components of eukaryotic cell membranes.[1] Cholesterol is the hallmark sterol of animal cells and plays critical roles in animal cell membranes including 1) regulating membrane fluidity and stability, 2) serving as a precursor for steroid hormones and bile acids, and 3) maintaining the integrity of lipids rafts which, in turn, regulate protein-protein interactions, cell-cell adhesions, intercellular communication, endocytosis, and membrane architecture.[3-4] In *Homo sapiens* and other animals, cholesterol homeostasis is dynamically regulated according to the physiologic demands of particular cells and tissues.[4] Accordingly, cholesterol must be efficiently synthesized and transported between organs and tissues. However, because cholesterol is poorly soluble in aqueous solutions, organisms use carrier particles called lipoproteins to shuttle cholesterol from one place to another in the systemic circulation.[5]

1.1 High-density lipoproteins: overview and roles in atherosclerosis

1.1.1 Native High-Density Lipoproteins: Structure and Composition

Lipoproteins are proteinaceous lipid-containing nanoparticles that vary in size and composition. High-density lipoproteins (HDL) are 7-13 nm in diameter, making them the smallest and most dense of the five classes of lipoproteins (HDL, LDL, IDL, VLDL, and chylomicrons). The surface of HDLs consists of an external phospholipid layer with interdigitated unesterified free cholesterol (FC), while the core of the particle contains mostly hydrophobic lipids, such as cholesteryl esters (CE) and triacylglycerols (TG) (Figure 1.1). The entire particle architecture is stabilized by the HDL-defining protein, apolipoprotein A-I (apoA-I). ApoA-I consists of 11 amphiphilic alpha helical segments. Structural data demonstrate that multiple apoA-I proteins wrap around the surface of growing HDL particles whereupon a portion of the protein is buried in the hydrophobic milieu of the lipids, and the other portion is partially exposed to solvent and responsible for function and targeting of the HDL particle.[6-7] Morphologically, HDLs fall on a spectrum ranging from highly discoidal (nascent) to highly spherical (mature), depending on the stage of maturation.

By weight, HDLs are roughly 30-50% protein with the remainder primarily accounted for by phospholipids, FC, and CE. ApoA-I constitutes about 70% of the protein content of HDLs, while apoA-II is the second most prevalent protein, comprising ~20% of HDL protein.[8] Other HDL proteins include apoA-IV, apoC-1, apoC-II, apoC-III, apoE, and apoM; however, recent data demonstrate a more extensive HDL proteome that impacts HDL structure and functions.[9] The lipid constituents of HDLs are quite diverse, and include glycerophospholipids, triacylglycerols, and sphingolipids. Some of the minority lipid and protein species of HDLs may have targeted, powerful functions in the settings of atherosclerosis and cancer. For instance, the aryldialkylphosphatase paraoxonase, and the sphingolipid sphingosine 1 phosphate (S1P), each have significant association with HDL and seem to have important vascular and immune functions with respect to atherosclerotic cardiovascular disease (ASCVD).[10-12] However, the role of these minor HDL constituents in cancer has been under-investigated. HDLs also frequently harbor RNA cargo, especially miRNA, and function as endogenous RNAi delivery vehicles.[13] However, the functional consequences of miRNA delivery by HDLs in health and disease have not been thoroughly elucidated to-date.

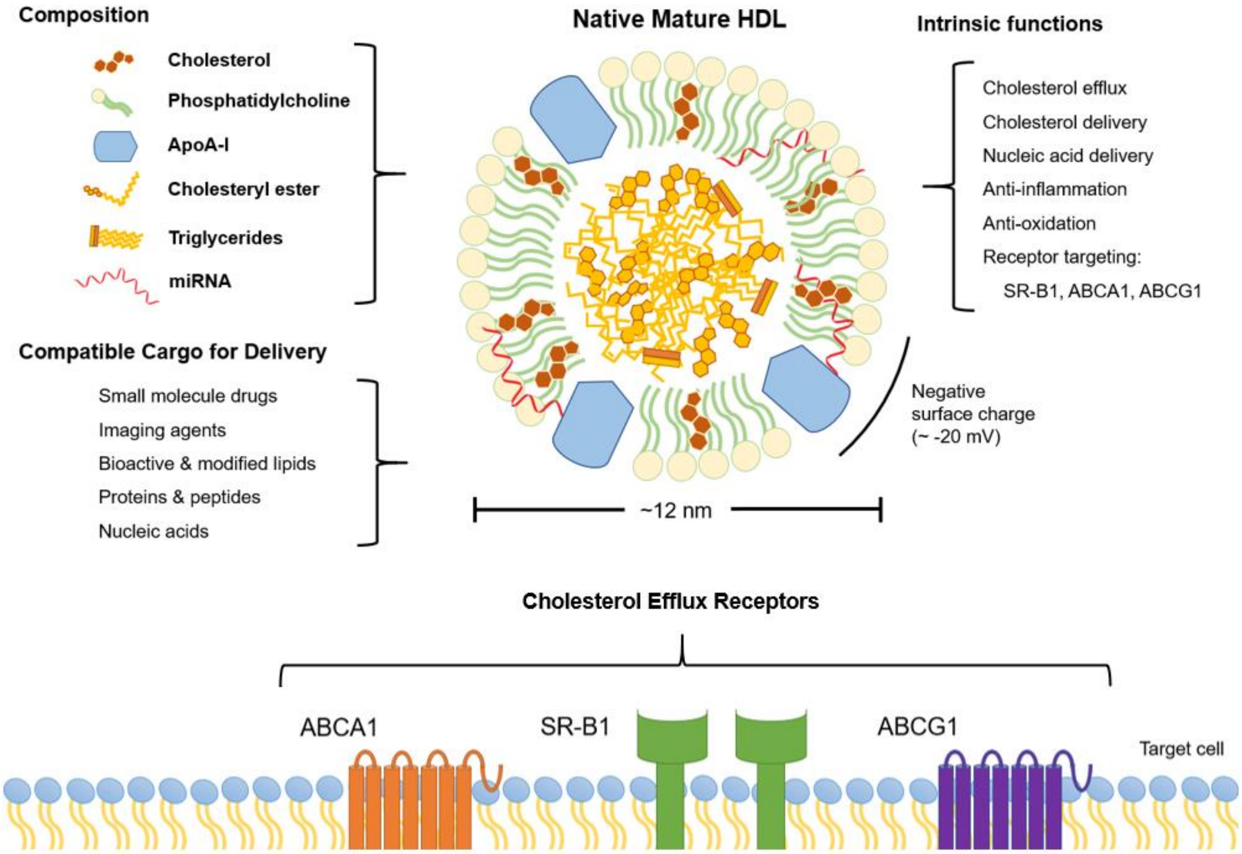

Figure 1.1: Structure and composition of native mature HDL, and properties that make HDLs attractive for therapeutic applications. Adapted from reference.[14]

1.1.2 HDL biogenesis and reverse cholesterol transport

The canonical life cycle of HDL consists of a stepwise maturation process from (a) the free, lipid-poor apoA-I protein, to (b) nascent, immature discoidal HDL, and finally to (c) FC and CE-rich spherical HDL (Figure 1.2).[15] The process begins when apoA-I is synthesized by hepatocytes and enterocytes in the liver and small intestine, respectively.[16] The amphiphilicity of apoA-I then enables the protein to sequester phospholipids and cholesterol, which results in the production of an immature HDL particle that is discoidal in shape as it is released into the circulation. This nascent HDL is also called pre-β HDL, and is cholesterol-poor. Pre-β HDL then continues to mature by accumulating FC and CEs (the latter localizing to the particle core), causing the particle to grow in size.[17] FC is acquired primarily from peripheral cells such as macrophages, where HDL binds to canonical cholesterol efflux receptors on the cell surface and removes cholesterol from the plasma membrane. Some of this FC is then esterified by the enzyme lecithin:cholesterol acyltransferase (LCAT) to generate CEs.[8, 15] HDLs can also exchange their lipid cargo with other circulating lipoproteins. For instance, HDLs can exchange their CEs for TGs from LDL or VLDL via cholesteryl ester transfer protein (CETP).[16] After maturing from discoidal into spherical HDL by scavenging FC and CE, mature HDL eventually returns to the liver to deliver FC and CE for excretion in the bile.[17] Specifically, mature spherical HDLs bind to scavenger receptor class B type I (SR-B1) on hepatocytes which facilitates delivery of FC and CE for excretion (Figure 1.2). This process whereby circulating HDLs scavenge FC and CE from the periphery and deliver it to the liver for excretion is called reverse cholesterol transport (RCT), and is considered to be the primary mechanism by which HDLs exert their atheroprotective effects.[16]

The two major steps in HDL catabolism are lipid hydrolysis and clearance and degradation of the apoA-1 protein. While FC and CE are metabolized in the liver and excreted in the bile as previously mentioned, the phospholipid cargo of HDLs is hydrolyzed by lipases such as endothelial lipase (LIPG).[17] ApoA-1, by contrast, is catabolized by both the liver and the kidney. The precise clearance and degradation mechanism in hepatocytes remains unclear.

However, in the kidney, apoA-1 is filtered by the glomerular apparatus and subsequently uptaken by renal tubular epithelial cells where it is degraded.[17]

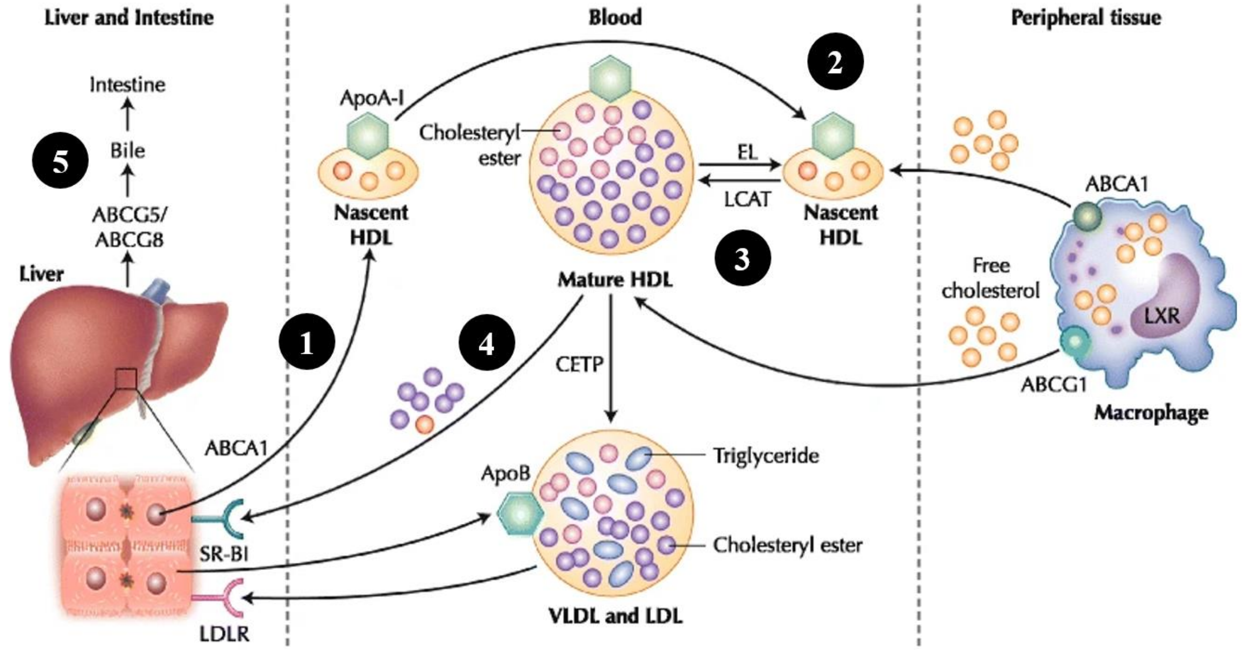

Figure 1.2: Schematic of the canonical HDL life cycle and reverse cholesterol transport

HDL begins its life cycle when lipid-poor apoA-1 is produced by hepatocytes or enterocytes. ApoA-1 then acquires phospholipids and free cholesterol from the plasma membrane via ABCA1 as it is released into the circulation as nascent, discoidal HDL (step 1). Nascent HDL then circulates in the blood until it encounters cells in the periphery that express cholesterol efflux receptors such as macrophages. Nascent HDL then binds to ABCA1 on the surface of peripheral cells to induce cholesterol efflux whereby nascent HDL becomes loaded with free cholesterol (step 2). As nascent HDL becomes loaded with free cholesterol, some of this cholesterol is converted to cholesteryl esters by the enzyme lecithin:cholesterol acyltransferase (LCAT), leading the HDL particle to swell in size due to the successive packing of cholesteryl esters into the core of the particle, resulting in a mature spherical HDL particle (step 3). Mature spherical HDL then returns to the liver where it binds to SR-B1 on the surface of hepatocytes to deliver its cholesterol cargo (step 4). Finally, the delivered cholesterol is transported into the bile by hepatic ABCG5 and ABCG8 for excretion into the intestine (step 5). Adapted from reference.[18]

In addition to the canonical view of the HDL life cycle, there is an alternative view which has recently been detailed by Sacks and others which is consistent with the canonical view in many respects but different in others. The alternative view does not differ in the proposed mechanisms of HDL clearance and catabolism, or of lipid exchange between lipoproteins; however, it does differ in the proposed mechanism of HDL maturation. The alternative view holds that the majority of HDLs are synthesized and secreted into the circulation as already fully-formed particles, with most of these particles being rich in FC and CE, and spherical in shape (Figure 1.3).[19-20] In support of this model, a 2016 article investigating HDL biogenesis in humans by Mendivil et. al. found that pre-β HDL constituted only 8% of total apoA-I secretion.[20] Thus, the authors argue, the bulk of HDL particles in circulation do not follow the canonical maturation process from nascent to spherical particles. According to this view, and contrary to conventional thinking, spherical HDLs would likely be responsible for the majority of HDL function, including atheroprotection and anti-cancer effects. However, the differential functions and clinical benefits of discoidal and spherical HDLs remain the subjects of debate.

HDLs modulate cellular cholesterol levels by interacting with specific receptors on the plasma membrane of target cells. There are three canonical cholesterol efflux receptors: two ATP-binding cassette transporters, ABCA1 and ABCG1, that mediate active cellular cholesterol efflux, and the scavenger receptor SR-B1, which engages in both passive efflux and influx of cholesterol after HDL particle binding.[15] Immature, pre-β HDLs preferentially bind ABCA1, while spherical HDLs typically bind SR-B1 and to a lesser extent ABCG1. Because pre-β HDLs have been presumed to be the predominant species involved in atheroprotection, the ABCA1 efflux receptor has been the subject of much study with respect to HDL therapy. However, if the aforementioned alternative view of HDL biogenesis is correct, then SR-B1 and ABCG1 may play larger roles than previously presumed with respect to atheroprotection.

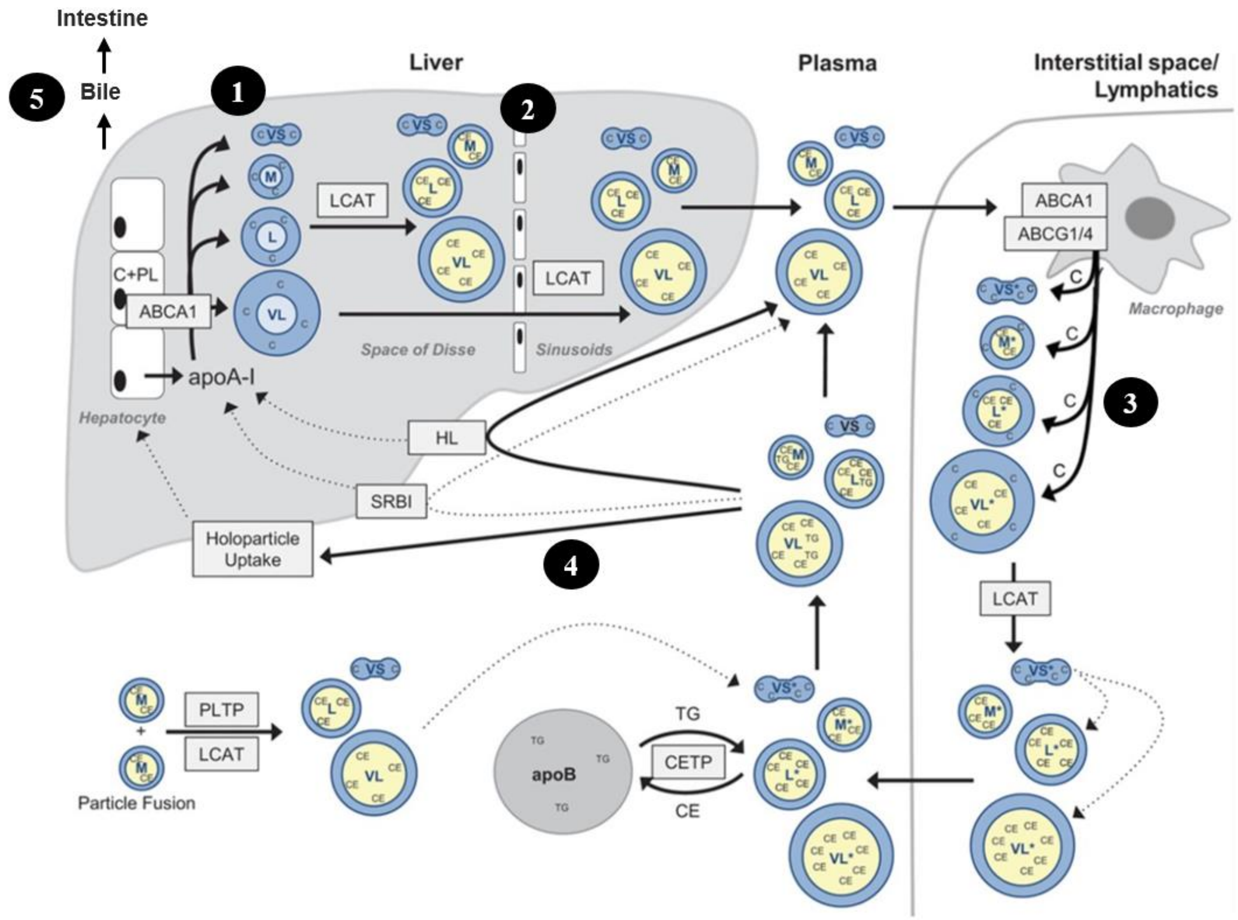

Figure 1.3: Alternative view of the HDL life cycle based on kinetic experiments in humans

According to this model proposed by Mendivil et. al.,[20] after apoA-1 is first produced by hepatocytes and enterocytes it is released into the extracellular space as fully formed HDL particles with the entire size range of HDL particles already represented (step 1). These particles, with a range of cholesterol densities, then undergo LCAT-mediated esterification in several locations before reaching the systemic circulation including the Space of Disse and the hepatic sinusoids (step 2). Upon being released into the circulation, HDL particles may then interact with peripheral cells such as macrophages to induce cholesterol efflux via ABCA1 and other efflux receptors (step 3). After additional interactions with other plasma lipoproteins and LCAT-mediated esterification, the HDL particles are primarily uptaken in the liver via holoparticle uptake (step 4). Finally, the cholesterol delivered by the particles into the liver via holoparticle uptake or via SR-B1-mediated cholesterol influx is then transported into the bile for excretion in the intestinal tract (step 5). Adapted from reference.[20]

1.1.3 Synthesis and Characterization of HDL Mimics

Synthetic HDL platforms fall into two broad categories: 1) mimics of immature, discoidal HDL, and 2) mimics of mature, spherical HDL. The majority of platforms developed to date, and all of the synthetic HDLs used in clinical trials, fall in the former category. Mimics of immature, discoidal HDL are relatively easy to fabricate by using a combination of full-length apoA-I or an apoA-I mimetic peptide, and phospholipids. Scanu was the first to demonstrate that apoA-I and lipids isolated from human serum could, under certain conditions, be recombined to form stable, lipoprotein nanoparticles.[21] Subsequent studies found that the inclusion of the detergent sodium cholate in the recombination process facilitated highly efficient particle self-assembly. This protocol involves co-incubation of phospholipid vesicles and apoA-I or apoA-I mimetic peptides with sodium cholate, followed by dialysis whereby the detergent is slowly removed from the particle solution. This protocol offers several advantages over the direct assembly method, particularly the incorporation of a variety of saturated or unsaturated lipids and precise control over final particle diameter (~ 10 nm).[22] Similar protocols have been used to assemble particles that are closely related to rHDLs for various therapeutic applications.[23-24]

Spherical HDL mimics are generally more difficult to synthesize than discoidal HDL mimics due to the requirement that the particle possess a robust and stable core material. One approach is to start with a discoidal HDL particle such as rHDL, and subsequently “mature” the particle by incubating the particles with cholesterol in the presence of LCAT, leading to incorporation of cholesteryl esters into the particle core. This process, however, can be both costly and time-intensive due to the enzymatic maturation steps necessary to produce these particles. An alternative to this method is the use of inorganic nanoparticles as templates. In these approaches, a robust inorganic nanoparticle is used as a core scaffold, upon which the HDL mimic is then built. One of the first such methods was developed by our group using a 5 nm gold nanoparticle core. First, full-length apoA-I is added to the gold nanoparticle colloid, followed by addition of two phospholipid species: 1) thiol- or disulfide-modified lipids which largely bind "head-down" to the gold nanoparticle surface, forming an inner leaflet, and 2) unmodified phospholipids such as 1,2-dipalmitoyl-sn-glycero-3-phosphocholine to form the outer leaflet of the particle bilayer.[25] The resultant particle strongly resembles native mature HDL in its size (13 nm in diameter), shape, surface chemistry, and cholesterol binding function.[26] Independently, and at nearly the same time, Cormode et. al. also demonstrated the synthesis of spherical HDL mimics via a similar method, using iron oxide nanoparticles, quantum dots, and gold nanoparticles as core scaffolds and then employed the materials for imaging applications.[27]

While synthetic HDLs vary in their composition and physicochemical properties, many of them are quite similar to their native HDL counterparts. Specifically, synthetic HDLs such as rHDLs and gold nanoparticle-templated HDLs (Au HDL NPs) are 10-13 nm in diameter, compared to 7-13 nm diameter for native HDLs. Moreover, native HDLs exhibit surface zeta potentials of approximately -20 mV, while synthetic HDLs generally range from -10 - -50mV. Finally, synthetic HDLs typically harbor full-length apoA-1 or apoA-1 mimetic peptides, along with phosphatidylcholine and/or other phospholipids. For native HDLs, apoA-1 is by far the most abundant and identifying protein (~70% of HDL protein content), while phosphatidylcholine is the predominant lipid species (~110 copies per particle).[28] A common point of distinction between native HDLs and synthetic HDLs is the composition of the particle core. For instance, native HDLs possess a hydrophobic core of cholesteryl esters and triglycerides, while many synthetic HDLs lack cholesterol, cholesteryl esters, and triglycerides entirely. In some cases, this may be desirable to enable synthetic HDLs to better accommodate effluxed cholesterol into the particle upon interaction with the intended target cell. In sum, many synthetic HDLs strongly resemble their native HDL counterparts in composition and physicochemical properties.

. Synthetic HDLs resembling immature, discoidal HDL or spherical HDL have differential binding affinities for the various cholesterol efflux receptors: ABCA1, ABCG1, and SR-B1. Because these receptors are not uniformly expressed across all cell types, this enables synthetic HDLs to specifically target particular cell populations, which provides a significant advantage for therapeutic applications. As an example of this, spherical HDL mimics can exquisitely target SR-B1, which is highly expressed on certain cancer cells and cells of the innate immune system, such as myeloid cells. This targeting capacity reduces off-target effects and imparts synthetic HDLs with a favorable toxicity profile. Moreover, cell-specific targeting, along with the biomimicry of synthetic HDL surface chemistry, gives synthetic HDLs favorable pharmacokinetic and pharmacodynamic profiles.

Incorporation of drug cargo into synthetic HDLs for cancer therapy can be accomplished by several means. First, drugs can be covalently conjugated to lipids and subsequently co-assembled with additional phospholipids and proteins or peptides into the surface lipid layer of the particle. Second, hydrophobic drugs and biomolecules can be loaded into the particles via hydrophobic interactions. This is perhaps the most common approach; and examples of incorporated hydrophobic cargo include retinoids,[29] paclitaxel,[24] curcumin,[30] and amphotericin B.[31] Cholesterol conjugation is also an efficient method that can be used to incorporate drugs or nucleic acids into HDL nanoparticle formulations.[32-33] Finally, several groups have demonstrated that nucleic acids can be successfully incorporated into HDL mimics, typically on the surface of the particle, via charge reconciliation with a cationic lipid.[34-35]

Standard materials characterization of synthetic HDLs typically involves determination of particle size, polydispersity, surface chemistry, and composition. The most common methods used to evaluate particle size and polydispersity are dynamic light scattering, transmission electron microscopy, and size exclusion chromatography.[36] Surface charge is typically determined via zeta potential measurements. Methods used to determine particle composition vary from platform to platform, but may include elemental analysis, UV-Vis spectroscopy, and fluorescent or colorimetric assays to quantify protein, phospholipid, and/or cholesterol content. The secondary structure of apoA-I or apoA-I mimetic peptides in the context of the particle can also be determined via circular dichroism. Finally, functional characterization of synthetic HDLs can be accomplished via many different application-specific assays. As a consequence of the large number of studies examining the function of HDLs in cardiovascular disease, one of the gold standard methods used to characterize HDL function is an *in vitro* radiolabeled cholesterol efflux assay.[37]

The feasibility of scale-up is an important consideration for synthetic HDL platforms aiming for clinical translation. The component of many HDL mimics that presents the greatest challenge for scale-up is the apoA-I protein. To source the apoA-1 protein, apoA-1 can be isolated in large quantities from pooled human serum by serial density ultracentrifugation, or it can be produced recombinantly *in vitro* for instance in Chinese Hamster Ovary (CHO) cells. Human clinical trials have been conducted with apoA-I isolated from human serum and produced from bacteria and mammalian cells.[16] Phospholipids can be synthesized easily at large scales with high purity. The large-scale production of assembled rHDLs under GMP conditions has already been accomplished for use in human clinical trials. Moreover, inorganic core materials used to synthesize spherical HDL mimics, particularly gold nanoparticles, have also already been produced at scale under GMP conditions for human clinical trials. Overall, significant precedents exist that demonstrate the feasibility of scale-up, which should facilitate the translation of HDL-based therapies to the clinic.

1.1.4 Synthetic HDLs for atherosclerosis therapy

ASCVD is the leading cause of morbidity and mortality in the United States, causing about 8 million deaths per year.[38] Low HDL cholesterol (HDL-C) is strongly associated with poor ASCVD outcomes, due in large part to HDL's robust promotion of RCT.[8, 16] As a result, synthetic HDLs have long been attractive as a potential therapy for ASCVD. Synthetic HDLs possess intrinsic atheroprotective and anti-inflammatory properties as well as intrinsic targeting of atherosclerotic plaques.[38] This makes synthetic HDLs particularly attractive for ASCVD therapy over other nanoparticle systems, since they do not need to be functionalized with additional targeting moieties or loaded with anti-atherosclerotic drugs. Synthetic HDLs can be injected into the systemic circulation, bind to their target receptors, ABCA1, ABCG1, and SR-B1, on the surface of foam macrophages in atherosclerotic plaques, induce cholesterol efflux, and then deliver this cholesterol to the liver for excretion.[38]

A wide range of synthetic HDLs have been tested for their therapeutic efficacy in ASCVD. The vast majority of these platforms have been mimics of immature, pre-β HDL.[38-39] The most common synthetic HDL used for this purpose has been reconstituted HDL (rHDL).

These particles are typically synthesized by the cholate dialysis method, and consist of phospholipids and the apoA-1 protein.[21] Another simple HDL mimic which has been tested for ASCVD efficacy is a naturally occurring variant of apoA-1 called apoA-1 Milano.[40] In total, three HDL mimics have been tested in human trials: apoA-1 Milano, CSL-112, and CER-001.[39] A large, multi-center randomized controlled trial was performed to test the efficacy of apoA-1 Milano (MDCO-216) to reduce atherosclerotic burden in post-acute coronary syndrome patients.[40] Five weekly injections were administered and the outcomes measured by intravascular ultrasound (IVUS) were percent atheroma volume, normalized total atheroma volume, and atheroma volume of the most diseased arterial segment. Unfortunately, none of these metrics was found to be significantly different between the treatment group and the controls. Likewise, CER-001 has also been tested for efficacy in reducing ASCVD. CER-001 is an rHDL platform consisting of apoA-1, diphosphatidylglycerol, and sphingomyelin.[39] Early studies showed that CER-001 was able to mobilize significant quantities of cholesterol into the HDL fraction.[41] However, when tested for efficacy in the CHI-SQUARE and CARAT studies, CER-001 failed to produce significant changes in outcomes measured by IVUS and quantitative coronary arteriography (QCA).[39, 41] One observation from these studies was that CER-001 produced a dose-dependent mobilization of cholesterol into the circulation. However, CER-001 also induced a dose-dependent downregulation of ABCA1, which is hypothesized to be the mechanism prohibiting efficacy of this drug and other rHDLs.[42] CSL-112 is an rHDL consisting of apoA-1 and phospholipids which has shown similar mobilization of cholesterol to CER-001. CSL-112 is currently being tested for anti-ASCVD efficacy in the ApoA-1 Event Reducing in Ischemic Syndromes II (AEGIS II) study, which is a phase III, multi-center, double-blind randomized controlled trial expected to conclude in 2022.[43] The results from this trial will provide additional insight into whether dose-dependent reduction in ABCA1 expression is a pervasive obstacle for rHDL-based therapies.

In addition to the synthetic HDL platforms that have been tested in human trials, there are a host of other materials that have been tested *in vitro* and *in vivo*. A study by Muller and colleagues published in 2014 demonstrated that rHDLs could be loaded with statins and used for anti-ASCVD therapy.[44] The authors showed that statin-loaded rHDLs targeted macrophages in atherosclerotic plaques in apo$E^{-/-}$ mice and reduced plaque inflammation. Another group then improved upon this platform by reporting that modifying the statin-loaded rHDL with hyaluronan (HA) increased the targeting and efficacy of the particles by approximately two-fold.[45] HA was used to inhibit the accumulation of rHDLs in the liver and thereby to enhance localization to atherosclerotic plaques. The particles exhibited superior performance in reducing plaque inflammation and plaque lesion size.

Another approach to anti-ASCVD synthetic HDLs was also developed by Muller and colleagues and then expanded upon by other groups. For this tactic, hybrid nanoparticles consisting of a PLGA core surrounded by a corona of phospholipids and apoA-1 were synthesized using a microfluidic device.[46] The resulting particles exhibited cholesterol efflux properties characteristic of synthetic HDLs while also exhibiting the slow release properties of PLGA. In particular, PLGA can be used to encapsulate a wide variety of hydrophobic drugs in the core of the particle, which the group demonstrated using Nile Red as a proof of principle. The group showed that these particles can effectively target atherosclerotic plaques in vivo in apo$E^{-/-}$ mice using fluorescence imaging.[46] However, they did not show therapeutic efficacy for plaque reduction. Liu and colleagues then developed hybrid PLGA-HA-rHDLs which exploited the liver evading properties of HA while simultaneously imparting the slow release properties of PLGA for delivery of statins.[47] Statin-loaded PLGA-HA-rHDLs successfully targeted macrophages in atherosclerotic plaques, promoted cholesterol efflux, reduced the burden of oxidized LDL, and decreased plaque lesion size.

Our group recently reported a novel nitric oxide-modified HDL NP for ASCVD therapy.[48] For this study, we synthesized a spherical HDL mimic using a 5 nm gold nanoparticle as a core scaffold in addition to apoA-1 and two species of phospholipids to form an apoA-1-containing lipid bilayer surrounding the gold nanoparticle core. The key step involved the incorporation of a phospholipid onto the particle surface (DPPNOTE) which was functionalized with an S-nitrosyl (SNO) group to generate SNO HDL NPs. While our group has previously shown that HDL NPs exhibit intrinsic anti-inflammatory properties without the SNO group,[49-50] the addition of DPPNOTE is targeted to specifically ameliorate ASCVD-related inflammation. We found that SNO HDL NPs reduced inflammation, inhibited aortic smooth muscle cell migration, and reduced ischemia/reperfusion injury in a mouse model.[48] Additionally, SNO HDL NP reduced atherosclerotic plaque burden by nearly 50%, which was a greater effect than seen with ordinary HDL NPs.

1.2 High-density lipoproteins: roles in cancer biology

1.2.1 HDL Cholesterol and Cancer: Clinical Correlations and Causal Connection

The relationship between serum HDL cholesterol levels (HDL-C) and cancer has been the subject of much recent study and debate. Most large studies have demonstrated that HDL-C is inversely correlated with cancer risk.[51] However, it remains controversial whether low HDL-C is primarily a biomarker for cancer, or whether it is causative. In 2010, Jafri et. al. published a meta-analysis of 24 randomized controlled trials of lipid-altering interventions, examining the correlation between HDL-C and cancer risk.[52] In total, the trials had 625,477 person-years of follow-up and 8,185 incident cancers. The authors found a significant inverse correlation between HDL-C and cancer risk, such that for every increment of increased HDL-C by 10 mg/dL, there was a corresponding reduction in cancer risk by 36%. In a 2015 study, Yang et. al. used a Mendelian randomization meta-analysis to specifically examine the question of causality. Drawing data from 25 articles and 91,070 participants, the authors demonstrated that low HDL-C may be a causal risk factor for the development of cancer, and not merely a correlative risk factor.[53] Further, several studies have shown that patients with elevated HDL-C respond more favorably to therapy in some populations.[54-55] In addition to pan-cancer correlations, there are many studies that have directly examined the link between HDL-C and particular tumor sub-types. For instance, low HDL-C is associated with increased incidence of lung cancer[56] and non-Hodgkin lymphoma.[57], as well as an increased risk of breast cancer.[58-59] Each of these tumor-specific associations has been demonstrated in large, prospective studies, indicating that there may be a causal connection between low HDL-C and cancer onset. A 2019 study by Penson et. al. corroborated these results by demonstrating that low HDL levels (< 30 mg/dL) was significantly correlated with increased cancer mortality in women, with a hazard ratio of 2.31.[60] In sum, the robustness of the inverse correlation between HDL-C and cancer risk indicates that using synthetic HDLs to augment the ordinary function of HDLs may be an effective therapeutic approach for cancer, in addition to any therapeutic effects afforded by concomitant delivery of chemotherapeutic drugs, photothermal agents, RNAi, etc.

1.2.2. HDL Cholesterol and Cancer: Biology

To deepen our understanding of the clinical correlation between reduced HDL-C and cancer risk with an eye toward therapy, it is important to understand the underlying biology of cholesterol homeostasis in the setting of cancer. Cholesterol is an essential component of the mammalian cell membrane and is required to maintain plasma membrane fluidity, stability, and organization, both in ordinary cells and in cancer cells.[61-62] Consequently, cancer cells require a steady diet of cholesterol to support the generation of new biological membranes during their rapid proliferation. Cholesterol is also a precursor in the synthesis of various hormones and vitamins that are required for cell proliferation and maintenance.[62-64] Prostate cancer, breast cancer, adrenocortical carcinoma and other tumors are highly dependent upon sterol-derived hormones for their growth; and these tumors therefore often have a vociferous appetite for cholesterol.[65] Additionally, cholesterol can be found at high densities in specialized regions of the plasma membrane known as lipid rafts. These membrane microdomains serve as scaffolds for protein assemblies, and thereby regulate a host of ligand-receptor interactions and downstream intracellular signaling processes, many of which are hi-jacked in cancer cells. One instance of this is lipid raft-dependent B cell receptor signaling in B cell lymphomas, which can be inhibited by targeted reduction of cellular cholesterol.[66-68] The fact that synthetic HDLs directly induce cell death in lymphoma cells via this mechanism also provides evidence that HDLs may play a causal role in slowing the progression of malignancy in cancer patients.

Cholesterol homeostasis is maintained at the organismal level *in vivo* by the dynamic regulation of cholesterol synthesis, efflux, and influx. Because cholesterol is minimally soluble in water, it requires transport via amphiphilic carriers. These carriers are the five classes of lipoproteins, which form colloidal suspensions in the blood.[69] LDL is the primary transporter of cholesterol from the liver to peripheral cells. Cholesterol is delivered by LDL to recipient cells via LDL receptor-mediated endocytosis.[70] HDL, by contrast, removes cholesterol from the periphery and delivers it back to the liver for excretion in the bile.[71] However, HDL, unlike LDL, is capable of both delivering and removing cholesterol from cells. HDL removes cholesterol from cells by binding to one of its three receptors, ABCA1, ABCG1, and SR-B1. However, SR-B1 is the only receptor through which HDL can both efflux and influx cholesterol.[72] Because of this, SR-B1 is frequently overexpressed in neoplastic cells and has been the most thoroughly investigated of the cholesterol efflux receptors in the context of cancer.[73-74] A comprehensive treatment of the crossover between HDL biology and cancer, and the respective roles of each of the HDL receptors can be found in a recent review article published by Ganjali et. al..[75]

The ordinary function of the immune system is also highly dependent upon cholesterol homeostasis, which therefore has significant implications for cancer immunotherapy.[76] The immune system can play both tumor-supporting and anti-tumor roles in the setting of malignancy. Anti-tumor adaptive immunity, specifically that mediated by effector T cells, has proven to be especially potent for targeting and eradicating cancer cells.[77] Importantly, innate immune cells play a critical role in facilitating or suppressing anti-tumor adaptive immunity. Myeloid derived suppressor cells (MDSCs) have emerged as important players of the innate immune system which promote focal immunosuppression in cancer.[78] MDSCs are of particular interest for this review given their dependence on cholesterol homeostasis for their function, and their expression of cholesterol efflux receptors such as SR-B1.[79] MDSCs are mobilized from the bone marrow and infiltrate tumors, where they use a variety of signaling processes to enhance the activity of regulatory T cells (Tregs) while suppressing the activity of anti-tumor cytotoxic T cells. This activity can reduce the therapeutic efficacy of immunotherapeutic agents such as checkpoint inhibitors.[78] Highlighting the importance of cholesterol homeostasis in the function of the innate immune system, Yvan-Charvet et. al. found that knocking out ABCA1 and ABCG1 in mice resulted in enhanced proliferation of myeloid cells.[80-81] Furthermore, if HDLs were exogenously administered to these mice, the hyperproliferative effect could be abolished, indicating that HDLs interact with myeloid cells independently of these receptors to regulate their proliferation, likely via SR-B1. Because spherical HDLs are the primary HDL targets for SR-B1, this result is consistent with the hypothesis that spherical HDLs may be highly significant from a therapeutic perspective in cancer. The role of cholesterol homeostasis in innate immunity, and its gate-keeper function for anti-tumor adaptive immunity, may also provide a window into a possible mechanism for the causal connection between low HDL-C and increased cancer risk.

Ordinary HDL biology can also be impaired by pathological processes. To illustrate this, it is interesting to consider the relatively common scenario in which patients with cancer, or patients in a pre-cancerous state, also have concomitant cardiovascular disease. In such cases, pathological processes including inflammation, increased glycation, and oxidative stress can significantly alter HDL properties, potentially resulting in HDLs with impaired function.[82] This raises interesting questions regarding the clinical benefit of elevating HDL-C in these patients. A recent report by Mazidi et. al. found that elevated HDL-C does not always correlate with clinical benefit. Specifically, patients with extremely high HDL (> 100 mg/dL) were found to have higher quantities of inflammatory factors such as C-reactive protein and fibrinogen, and higher mortality rates, consistent with previous studies.[83-84] There are several possible explanations for this observation, including genetic variants in HDL- and RCT-related proteins. From a therapeutic perspective, if the pathological processes of inflammation, glycation, and/or oxidative stress primarily reduce the function of HDLs by negatively impacting particle properties, then exogenously administered synthetic HDLs may benefit these patients. However, this would require that these particles were able to exert their functional effects acutely, prior to undergoing significant pathological modification themselves. However, if the effects of these pathological processes on HDL function occur primarily at the level of the target cell, then exogenously administered synthetic HDLs may have reduced potency. Questions of this sort could be probed by investigating the efficacy of synthetic HDLs as cancer therapy in mice with co-morbid condition(s) and comparing the effects on mice with cancer without co-morbid condition(s).

1.2.3 Synthetic HDLs for Cancer Therapy

Native HDLs are endogenous delivery vehicles for a wide range of biomolecules including lipids, cholesterol, vitamins, hormones, metabolites, and other small molecules.[16] Recently, it was discovered that native HDLs also function as endogenous transporters of miRNA for intercellular regulation of gene expression.[13] This versatile carrying capacity, along with HDL's intrinsic targeting properties, makes synthetic HDLs exceptionally attractive as drug delivery vehicles for cancer therapy.

Optimizing pharmacokinetics and clearance properties is a critical step for any HDL-based drug delivery system hoping to achieve clinical utility. One significant challenge is avoiding rapid clearance of the delivery vehicle and therapeutic cargo by the mononuclear phagocyte system (MPS). The MPS consists primarily of monocytes and macrophages residing in the spleen, liver (Kupffer cells), lymph nodes, and peripheral blood. Nano- and micro- sized particles in the systemic circulation are vulnerable to MPS-mediated clearance largely on the basis of size and charge. Particles less than 100 nm in diameter are considered most favorable to avoid MPS-mediated clearance.[85] Particles with neutral surface charge are considered optimal, compared to positively or negatively charged counterparts. Importantly, the surface charge of circulating nanoparticles also significantly impacts the binding of serum proteins to the surface of the particle, which can increase the hydrodynamic diameter of the particle significantly.[86] Binding of serum proteins can be unfavorable for several reasons, such as preventing efficient renal clearance, and activating MPS clearance mechanisms that reduce therapeutic efficacy. Synthetic HDLs possess a significant advantage in this regard by virtue of their size and surface chemistry. The diameter of synthetic HDLs (~10 nm) is well below the desired threshold for size-dependent MPS-mediated clearance (100 nm). Moreover, the surface of synthetic HDLs usually closely resembles that of native HDLs, providing a “cloaking” mechanism that protects synthetic HDLs from clearance mechanisms which might otherwise be initiated in response to foreign bodies in circulation, such as opsonization and complement activation. Zwitterionic or neutral surfaces are considered optimal for preventing non-specific adsorption of serum proteins. Synthetic HDLs harbor zwitterionic phospholipids on the particle surface, and are usually slightly negatively charged due to the presence of negatively charged apoA-1 and, perhaps, other constituents. It is also important to note that renal clearance is usually an important consideration for nanoparticles that are developed for clinical application. Nanoparticles with hydrodynamic diameters less than 6 nm are cleared by the kidney.[87] The typical route of excretion for HDLs occurs when HDL binds to SR-B1 in hepatocytes, and the particle is subsequently catabolized and the products are largely excreted in the bile. However, the kidneys play an underappreciated role in metabolism of HDLs. Specifically, circulating apoA-1 and small, immature HDLs are able to be filtered by the renal glomerular apparatus, while larger, more mature HDLs are prohibitively large for glomerular filtration.[88] Synthetic HDL nanoparticles often exploit the native HDL recycling process and are typically processed by the liver and excreted in the bile. This clearance route endows synthetic HDLs with favorable pharmacokinetic properties for drug delivery. Reduced excretion by the kidney may make mature, spherical HDL mimics more attractive with regard to pharmacokinetic and pharmacodynamic properties compared to their immature, discoidal counterparts.[88]

Multiple clinical trials have demonstrated that synthetic HDLs exhibit favorable pharmacokinetic and safety profiles.[89-90] One recent randomized clinical trial examined the pharmacokinetics of rHDLs that were formulated using a soybean-derived phospholipid.[91] The study used once or twice weekly systemic infusions of the particles (27 subjects) or placebo (9 subjects). Results of this trial revealed that the half-lives of apoA-1 and phospholipid each had quite wide ranges: 19 - 93 h for apoA-1, and 3 – 82 h for phospholipid. The authors also found that apoA-1 levels remained above baseline for 3 days after infusion. Despite the wide range of half-lives, the mean half lives for both apoA-1 and phospholipid indicate that rHDLs exhibit favorable pharmacokinetic properties for therapy. Other clinical trials have shown that rHDLs can be administered at high doses (up to 8 g of protein per infusion) without adverse effects, demonstrating that synthetic HDLs are safe for therapeutic use.[16] Three different HDL mimics have been tested in humans to date, none of which have produced serious adverse events.[39-41]

Several groups have recently investigated the effects of PEGylation on synthetic HDL pharmacokinetics, pharmacodynamics, and efficacy. A recent article by Li et. al.[92] investigated the impact of PEGylation on the circulation half-life of synthetic HDLs, as well as their cholesterol transport functions. This group found that greater amounts of PEG incorporated onto the surface of synthetic HDLs, as well as longer PEG chains, increased the circulation half life of synthetic HDLs, while preserving the particle's cholesterol efflux and influx efficiency. These results are consistent with a report by Murphy et. al. demonstrating that PEGylation of lipid-poor apoA-1 significantly impaired cholesterol efflux, while PEGylation of holo-HDL particles did not reduce cholesterol efflux function.[93] The group also found that PEGylation appeared to increase RCT *in vivo*, as determined by increased mobilization of plasma FC. An additional testament to the robustness of synthetic HDLs as tumor-targeting agents can be found in data recently published by Tang et. al.[94] Specifically, this group found that PEGylated HDL-like nanoparticles achieved 12-fold and 3-fold more efficient tumor penetration *in vivo* than liposomes and PEGylated liposomes respectively, all prepared using the same lipid components, in a flank tumor murine model of colon carcinoma. While these and other studies illustrate the positive effects of PEGylation on pharmacokinetics, PEGylation also has some potential drawbacks. For instance, PEG modifications can lead to the production of anti-PEG antibodies by the host immune system.[95] Furthermore, PEGylation may also reduce efficacy, for instance by reducing the affinity of ligands on the nanoparticle surface for their target receptor(s).[96]

A recent study showed that SR-B1 expression is an independent prognostic factor for patient outcomes in breast cancer.[97] Of 150 cases examined, 54% of patients were found to have elevated expression of SR-B1. This elevated expression was associated with significantly more advanced pTNB stage, larger tumor volume, and decreased overall survival. As a result, the prospect of using synthetic HDLs for breast cancer therapy has been a topic of great interest, and a significant body of recent work has been devoted to investigating synthetic HDLs as therapy for breast cancer. One recent study investigated the impact of loading reconstituted HDLs (rHDLs) with valrubicin and lapatinib as therapy for triple negative breast cancer.[98] The group found that using rHDLs for drug loading reduced the IC_{50} of valrubicin from 3.5 uM to 2.3 uM, and reduced the IC_{50} of lapatinib from 1.4 uM to 0.8 uM in the breast cancer cell line, MDA-MB-231. Moreover, uptake of the drug from loaded rHDLs into these cells was shown to be inhibited by the SR-B1 inhibitor, BLT-1. A recent paper from Wang et. al. reports the fabrication of a novel rHDL nanoparticle that was formulated for dual loading with paclitaxel and plasmid DNA encoding the p53 gene, for transfection of breast cancer cells.[99] The nanoparticles were assembled by combining lipids, cholesterol and paclitaxel in chloroform followed by evaporation and re-suspension in the presence of a cationic lipid complex containing p53 plasmid DNA. After sonication and several purification steps, apoA-1 was added the mixture to obtain the final dual-loaded rHDL-like nanoparticles. Of note, these particles were larger than typical rHDL particles with a diameter of ~177 nm as determined by dynamic light scattering. The particles were to uptaken by MCF-7 cells *in vitro* in a lysosome-independent mechanism, induced robust p53 expression, and effectively targeted tumors *in vivo*. The nanoparticles also outperformed free drug and all other controls in an *in vivo* study of tumor inhibition using an orthotopic MCF-7 breast cancer model. The dual-loaded nanoparticles achieved 65% inhibition of tumor growth, and an increase in animal subject survival.

Adrenocortical carcinoma (ACC) is a rare endocrine tumor that is particularly well-suited to synthetic HDL therapy, as these cells require cholesterol for steroid hormone production, and achieve this requirement via overexpression of SR-B1. A recent article describes the use of synthetic HDL nanodisks (sHDL) loaded with a natural product compound to treat ACC.[100] The specific natural product these investigators used, withalongolide A 4, 19, 27 triacetate (WGA-TA), is poorly soluble in water, but was able to be efficiently loaded into sHDLs, which were synthesized using the apoA-1 mimetic peptide, 22A. The investigators found that WGA-TA-loaded sHDLs accumulated at the site of ACC xenograft tumors *in vivo*, and significantly inhibited tumor growth.

Synthetic HDLs have also been employed for the delivery of photothermal agents. A recent study was published demonstrating that indocyanine green (ICG) can be efficiently loaded into rHDL for effective photothermal cancer therapy.[101] Encapsulation of ICG by rHDL improved stability, and greatly improved tumor targeting *in vivo*, compared to free ICG and lipid/ICG controls. Formulation with rHDL also enhanced ICG's cytotoxicity in cancer cells; and importantly, the rHDL/ICG showed a near-IR response equivalent to that of free ICG upon exposure to laser radiation.

1.3 Exosomes, cholesterol and pre-metastatic niche formation

The above sections introduce native and synthetic HDLs and their roles in ASCVD and cancer. The following sections will pivot to focus on exosome signaling and pre-metastatic niche formation. The link between these two sets of introductory material lies in our recent discovery that synthetic HDLs can be used to disrupt exosome signaling.[102] As a result, HDL NPs represent targeted agents that could be used to study the role of exosome signaling in various physiologic and pathophysiologic processes both *in vitro* and *in vivo*. Moreover, HDL NPs could potentially be explored as therapeutic inhibitors of exosome signaling in settings where such signaling is pathogenic. Toward these ends, we introduce the following background material regarding exosome signaling and pre-metastatic niche formation to provide adequate context for our work described in Chapter 4 using HDL NPs to probe the cholesterol-dependence of exosome communication in the setting of prostate cancer.

1.3.1. Exosome structure, biogenesis, and signaling

Extracellular vesicles (EV) are particles released by cells into the extracellular space that are delimited by a lipid bilayer and incapable of replication.[103] EVs fall into three main sub-classes: ectosomes, exosomes, and apoptotic bodies.[104] Ectosomes are produced by a direct outward budding of the plasma membrane, while exosomes are of endocytic origin.[105] Microvesicles, or microparticles, are a common sub-class of ectosomes which are typically 0.2-1.0 μm in diameter. Exosomes, by contrast, are typically 30-160 nm in diameter.[105] Apoptotic bodies are a heterogenous group of vesicular structures that are produced as cells undergo programmed cell death, ranging in size from 50-5000 nm in diameter.[104]

Exosome biogenesis occurs in a several step process. First, inward invaginations on late endosomes are separated from the endosomal membrane to produce intraluminal vesicles (ILV) that are contained within the mature late endosome, which upon ILV production is now termed a multivesicular body (MVB). The MVB can then fuse with the plasma membrane to release the ILVs into the extracellular space as exosomes, or alternatively the MVB can fuse with lysosomes whereupon the ILVs are degraded. Because ILVs are produced by inward budding into late endosomes, the inner contents of exosomes are derived from the cytoplasm. [106] As a result, exosomes typically harbor a diverse array of lipids, soluble proteins, membrane-bound proteins, and RNA cargo such as miRNA.[107]

One of the most well-characterized pathways of exosome biogenesis is the endosomal sorting complex transport (ESCRT) pathway. There are four complexes of ESCRT proteins, termed ESCRT-0, ESCRT-I, ESCRT-II, and ESCRT III.[108] In total there are approximately 30 proteins involved in these four complexes.[108] Sorting cargo into membrane domains that are destined for ILV formation frequently requires a ubiquitin signal.[108-109] ESCRT-0, ESCRT-1, and ESCRT-II each have multiple ubiquitin-binding domains that are used to recruit proteins into membrane domains on late endosomes that will eventually become ILVs.[109] ESCRT-0 is primarily responsible for recruiting ILV cargo as well as recruiting the other ESCRT complexes to the endosomal membrane.[108-109] The ESCRT-I and ESCRT-II complexes then facilitate the inward budding of the endosomal membrane followed by ESCRT-III-mediated membrane invagination and vesicle fission. [108-109]

There remains ongoing debate regarding the fundamental reason(s) why cells produce exosomes. One hypothesis is that exosome production primarily serves the purpose of waste removal.[110-111] However, others argue that a fundamental purpose of exosomes is their role as mediators of intercellular communication; and there has been a resurgence of research and interest to this effect over the past decade.[105, 112-113] Despite a lack of consensus on the fundamental purpose of exosomes, it is abundantly clear that exosomes are frequently uptaken by local or distant cells in a manner which alters the recipient cell’s intracellular signaling, gene expression, and cellular phenotypes.[107, 113-115]

There are several mechanisms by which exosomes can interact with a target cell. First, exosomes can bind to the target cell surface via ligand-receptor interactions and stimulate downstream intracellular signaling. Second, exosomes can be endocytosed by clathrin-dependent endocytosis or by macropinocytosis, eventually resulting in either vesicle degradation or successful delivery of exosomal cargo to various intracellular target sites.[116] Finally, exosomes can fuse with the target cell plasma membrane to release their contents into the target cell cytoplasm.[117]

Exosomes can be further classified by several parameters. First, exosome properties sometimes vary according to size.[105] For instance, Lyden and colleagues demonstrated that exosomes of two different size regimes (60-80 nm and 90-120 nm) displayed different characteristic protein, lipid, and miRNA profiles, and also exhibited distinct biodistribution patterns when systemically injected into mice.[118] These results indicate that exosomes of different size regimes may play distinct roles in intercellular communication. Alternatively, exosomes can be classified according to their biomarkers. While there are no proteins that are considered universal exosome markers, there are many proteins that are acknowledged to be enriched in exosomes compared to cell lysates. For instance, CD63, CD9, and CD81 are all considered markers of exosomes. Other exosome-enriched proteins include TSG101, ALIX, Flotillin-1, and others. Classification by protein profiling can sometimes identify distinct exosome sub-populations which may have differential function.[119] Finally, exosomes can also be classified according their function and their cell source.[105]

Exosome characterization typically consists of determining physicochemical properties and molecular profiling. Particle size is often determined by dynamic light scattering (DLS), nanoparticle tracking analysis (NTA), or transmission electron microscopy (TEM).[103] The target size regime is usually between 30 and 150 nm for TEM diameter and between 40 nm and 200 nm for the hydrodynamic diameter. For molecular profiling, western blot for CD63, CD9, and CD81 are most commonly used to identify exosomes.[103] Importantly, the abundance of these proteins should be compared to a paired cell lysate to confirm that there is greater expression in the exosome sample. In addition to CD63, CD9, and CD81, there are often cell type specific markers that are used to confirm the source of the exosome, such as PSMA for prostate-originating exosomes.[120] Specific applications often require further characterization of exosome samples, such as RNA profiling, lipid profiling, or functional assays.[103]

1.3.2. Exosomes in cancer progression and pre-metastatic niche formation

Exosomes are produced by all cells,[105] yet some cell types produce far more exosomes on average than others. In particular, cancer cells notoriously produce an abundance of exosomes compared to their unmutated counterparts,[121-122] and circulating exosomes are elevated in the blood of cancer patients compared to healthy individuals.[122] As a result, exosomes derived from cancer cells have been studied extensively for the roles they play in promoting cancer progression. Tumor-derived exosomes (TEx) are frequently uptaken by a number of different cell types in the tumor microenvironment (TME). Primary among these are stromal cells such as tumor-associated macrophages, neutrophils, fibroblasts, endothelial cells and myeloid-derived suppressor cells (MDSC).[122-123] By interfacing with these various cell types, exosomes have been shown to promote tumor progression locally by a variety of mechanisms. For instance, in renal cell carcinoma and multiple myeloma, TEx can mediate intercellular communication with endothelial cells in the tumor-associated vasculature to promote angiogenesis, ultimately leading to enhanced delivery of nutrients and oxygen to support the growing tumor.[124-125] Moreover, TEx can mediate intercellular communication between cancer cells and tumor-associated macrophages to induce a favorable inflammatory state for tumor progression. For instance, Takano et. al. provided evidence that in colorectal cancer TEx are capable of delivering miRNA cargo to tumor-associated macrophages to induce M2 polarization, ultimately enhancing the metastatic potential of the tumor.[126] A similar phenomenon was reported in hepatocellular carcinoma.[127] In other settings, TEx can act as inhibitors of cancer progression. For instance in breast cancer, TEx have been shown to deliver miRNA to tumor-associated macrophages and inhibit tumor progression by inducing M1 polarization.[128] In addition to exosomes produced by cancer cells themselves, exosomes originating from other cells in the TME such as cancer-associated fibroblasts have also been studied for their roles in cancer progression.[129]

Exosomes have long been investigated for their roles in promoting cancer progression by altering the TME of the primary tumor. However, it wasn’t until a seminal paper was published in 2012 that the field began to recognize that exosomes may also play important roles as promotors of metastasis by communicating with target cells at distant organ sites to prepare the pre-metastatic niche (PMN).[130] The PMN is a microenvironment at a potential site of metastasis that is prepared for the successful implantation and proliferation of circulating tumor cells.[131] A subset of EVs that are produced by primary tumor cells find their way into the systemic vasculature and interact with target cells at pre-metastatic organ sites. These EVs can then facilitate PMN formation by several mechanisms, including promoting inflammation, angiogenesis, or altering extracellular matrix composition to favor the seeding of circulating tumor cells.[115] One important mechanism by which EVs can promote PMN formation at multiple sites of metastasis is by mediating communication with bone marrow-derived cells (BMDC). For instance, Peinado et. al. demonstrated that melanoma-derived exosomes “educate” BMDCs using the hepatocyte growth factor receptor, MET, to promote pro-migratory and pro-vasculogenic phenotypes in these cells.[130] After TEx-mediated education, BMDCs are mobilized from the bone marrow, traverse the systemic vasculature, and then infiltrate the lung to promote PMN formation. In addition, melanoma exosomes can also stimulate PMN formation in the lung directly by inducing vascular leakiness, and enhancing the production of cytokines and chemokines such as TNF-α and S100A proteins to produce a pro-inflammatory microenvironment favorable for the colonization of tumor cells.[115] This pro-inflammatory state can in turn lead to the recruitment of additional BMDCs to the developing PMN.

Exosome-mediated PMN formation has also been demonstrated in other tumor types, including pancreatic cancer and prostate cancer. Costa-Silva et. al. found that exosomes derived from pancreatic ductal carcincoma (PDAC) cells promoted pre-metastatic niche formation in the liver. PDAC exosomes were uptaken by Kupffer cells and stimulated TGF-β secretion, which in turn enhanced fibronectin production by hepatic stellate cells.[132] The resulting fibrotic microenvironment in the liver led to enhanced seeding and growth of PDAC cells in the liver in a metastatic model. Similar to the circumstance in melanoma, PDAC exosomes also promoted mobilization of BMDCs from the bone marrow and enhanced BMDC infiltration at the PMN in the liver. In the setting of prostate cancer (PCa), Dai et. al. found that systemic injections of PCa exosomes led to enhanced seeding of PCa cells in the bone marrow by approximately 115%,[133] ultimately leading to greater metastatic burden. The group found that PCa exosome-mediated enhancement of metastasis was the result of exosomal transfer of pyruvate kinase M2 (PKM2) to bone marrow stromal cells which upregulated CXCL12 production at the bone PMN.[133]

Despite these examples of exosome-mediated promotion of PMN formation, exosomes do not always play a pro-metastatic role. In fact, exosomes from the same tumor type can play different roles at different stages of disease. In melanoma, several groups showed that melanoma cells can switch from a poorly metastatic state to a more aggressive, highly metastatic state that is accompanied by a loss of pigment-derived epithelial factor (PEDF) expression.[134] Plebanek et. al. showed that the TEx produced by poorly metastatic melanoma cells actively inhibit metastasis by stimulating immune surveillance by patrolling monocytes in a PEDF-dependent manner,[135] while TEx produced by highly metastatic melanoma cells promoted metastasis and lacked PEDF.

1.3.3 Cholesterol-dependence of exosome signaling

Exosomes can interact with target cells in multiple ways, including ligand-receptor interactions, endocytosis, or fusion with the host cell plasma membrane.[108] When exosomes encounter the target cell plasma membrane, a subset of the surface proteins that exosome interact with are embedded in cholesterol-rich microdomains called lipid rafts. Lipid rafts are discrete domains on the outer leaflet of the plasma membrane that are more ordered than the surrounding lipid bilayer, but also exhibit a high degree of mobility.[136] Lipid rafts are rich in cholesterol, sphingolipids and sphingomyelin, and serve as scaffolding domains that promote interaction and clustering between membrane proteins.[137] By serving as a solid platform for these interactions, lipid rafts can protect macromolecular membrane complexes from the chaotic forces present in the disorderly liquid phase of the plasma membrane. Disruption of lipid rafts can therefore result in the disruption of key protein-protein interactions that are necessary for downstream signaling pathways or for the uptake of exogenous material.

The cholesterol sequestrant methyl-β-cyclodextrin (MβCD) can be used to extract cholesterol from cells and thereby disrupt the integrity of lipid rafts. Svensson et. al. found that exosome uptake by target cells depends heavily upon the integrity of lipid rafts.[138] The investigators found that treating recipient HUVEC cells with MβCD led to dose-dependent inhibition of exosome uptake. Given these results, a natural next step is to determine whether this cholesterol dependence in exosome uptake could be investigated *in vivo*. However, MβCD is highly non-specific and interacts with many cell types when administered *in vivo* which makes the acquisition of precise mechanistic data challenging.

To circumvent the limitations of non-specific cholesterol sequestrants, our group has investigated the cholesterol-dependence of exosome uptake using targeted HDL-mimicking nanoparticles (HDL NP) which also disrupt lipid raft integrity, albeit in a targeted fashion. HDL NPs specifically bind to cells expressing SR-B1, which include macrophages, hepatocytes, and steroidogenic cells.[139] Thus, HDL NPs represent a powerful tool for interrogating the cholesterol dependence of exosome uptake in cells that express SR-B1, both *in vitro* and *in vivo*. Plebanek et. al. showed that HDL NPs inhibit uptake of melanoma exosomes in macrophages and endothelial cells.[102] HDL NPs bind to SR-B1 on the surface of target cells where they induce cholesterol efflux and inhibit the influx of cholesteryl esters. This results in the disruption of lipid rafts and reduced mobility of SR-B1 on the cell surface, ultimately inhibiting exosome uptake. This previous work indicates that HDL NPs may be powerful tools for inhibiting exosome uptake for numerous cell types and applications.

Chapter 2: Supramolecular assembly of soft-core high-density lipoprotein mimics using lipid-conjugated core scaffolds

2.1. Objectives and Significance

High-density lipoproteins (HDL) are endogenous nanoparticles that circulate in the blood and transport cholesterol. Synthetic mimics of HDL represent promising therapeutic agents for cardiovascular disease by virtue of their cell-specific targeting properties and their ability to reduce inflammation and atherosclerotic burden. However, synthetic approaches to date have been unable to reproduce the key structural features of mature spherical HDL, the most abundant HDL sub-species in humans. In this chapter, we report the synthesis and characterization of a spherical HDL mimic using lipid-conjugated organic core scaffolds. The core design motif constrains and orients phospholipid geometry to facilitate the self-assembly of soft-core HDL-like nanoparticles. We investigated three core scaffolds varying in size, hydrophobicity, and oligonucleotide linker length. We show that two of these core scaffolds support the assembly of HDL-like nanoparticles. The resulting particles strongly resemble native human HDL in their size, polydispersity, surface charge, composition, and protein secondary structure.

2.2 Background and Motivation

HDL cholesterol levels exhibit an inverse correlation with risk of atherosclerotic cardiovascular disease (ASCVD).[140-141] At the cellular level, HDLs target macrophages and hepatocytes to remove and deliver cholesterol respectively, which leads to reduced inflammation and atherosclerotic burden.[81, 142] Due to the favorable association between HDL-C and reduced risk of ASCVD, the cell-specific targeting properties of HDL, and the intrigue of using HDLs for targeted drug delivery, a great deal of effort has focused on synthesizing HDL-like particles that strongly resemble their natural counterparts.[143]

There are multiple HDL species in the blood that serve as synthetic targets. Immature HDLs are cholesterol-poor and discoidal in shape, consisting mainly of the HDL-defining protein, apolipoprotein A-I (apoA-I), and phospholipids. Mature forms of HDL, which also harbor apoA-I and a surface layer of phospholipids, are rich in cholesterol and cholesteryl esters, and are roughly spherical (Figure 2.1). Spherical HDLs comprise the majority of HDLs in circulation.[144-145] Yet, synthetic forms of HDL used in the clinic have exclusively resembled immature, discoidal HDL, largely because these recombinant HDLs (rHDL) are relatively easy to fabricate by self-assembling phospholipids and apoA-I.[36, 89-90, 146-147] Even outside of the clinic, the vast majority of previously reported synthetic HDLs have resembled immature, discoidal HDL.[14, 38] However, emerging evidence suggests that spherical HDLs, not immature discoidal HDLs, may be responsible for a majority of RCT activity.[19-20] To this end, we sought to develop a synthetic mimic of mature spherical HDL both to address the dearth of such mimics in the literature and to provide a tool for investigating the relative anti-ASCVD functions of discoidal vs. spherical HDLs. We also note in passing that a wide range of HDL-like nanoparticles have previously been reported, including soft-core, discoidal particles using amphiphilic peptides,[23] rationally engineered HDL-like nanodiscs,[148-149] and drug-loaded rHDLs.[24, 44, 150]

Spherical HDLs are challenging to synthesize due to the enzymatic steps required to mature discoidal HDLs into cholesterol- and cholesteryl ester-containing spherical HDLs. Our group, and others, have attempted to circumvent these biological maturation steps by using inorganic nanoparticles as templates.[25, 27, 151] The templates can be functionalized with phospholipids and apoA-I, and successfully restrict the size of HDL mimics to < 15 nm in diameter.[152] These HDL-like nanoparticles have demonstrated exquisite properties for modulating cellular cholesterol,[26, 102] *in vivo* imaging,[153] and drug delivery.[32] However, these materials fail to recapitulate a critical feature of native HDLs, namely a robust, soft material core capable of dynamically loading and off-loading cholesterol and cholesteryl esters.

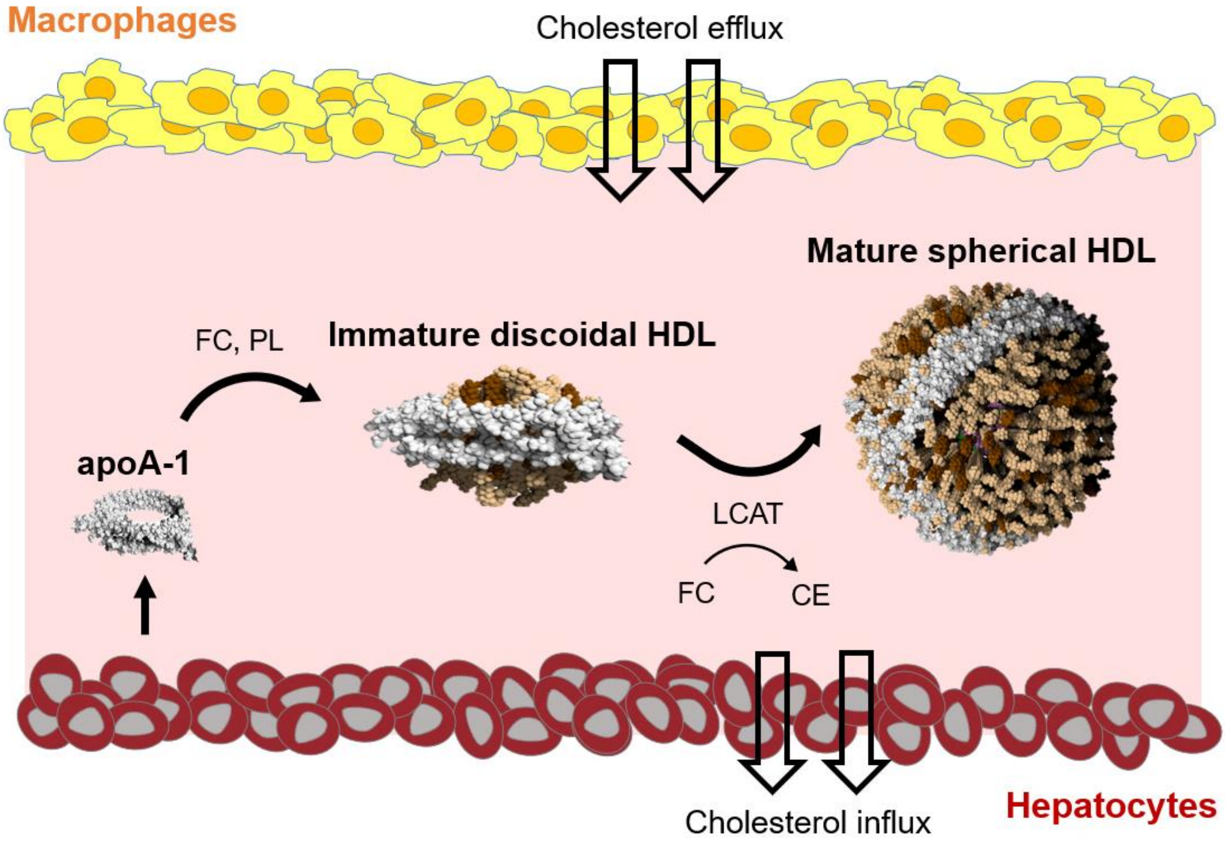

Figure 2.1: The canonical reverse cholesterol transport pathway

Abbreviations: FC = free cholesterol, CE = cholesteryl esters, PL = phospholipids, and LCAT = lecithin:cholesterol acyltransferase.

2.3 Results and Discussion

Herein, we describe the synthesis of soft-core, spherical HDL-like nanoparticles using lipid-conjugated core scaffolds (LC HDL NP). Three organic scaffolds varying in size and composition were investigated. The first scaffold is a highly hydrophobic small molecule-phospholipid conjugate (PL_4) that was synthesized using copper-free click chemistry. Specifically, a headgroup-modified phospholipid harboring a ring-strained alkyne, 1,2-dipalmitoyl-*sn*-glycero-3-phosphoethanolamine-*N*-dibenzocyclooctyl (DBCO PL), was click coupled to *tetrakis*(4-azidophenyl)methane, a small molecule with four terminal azides ($SM-Az_4$) (Figure 2.2 and 2.4a). The molecular weight of PL4 was confirmed by electrospray ionization mass spectrometry (ESI MS). ESI MS results revealed a peak at 4402 m/z which was precisely consistent with theoretical prediction (Figure 2.3).

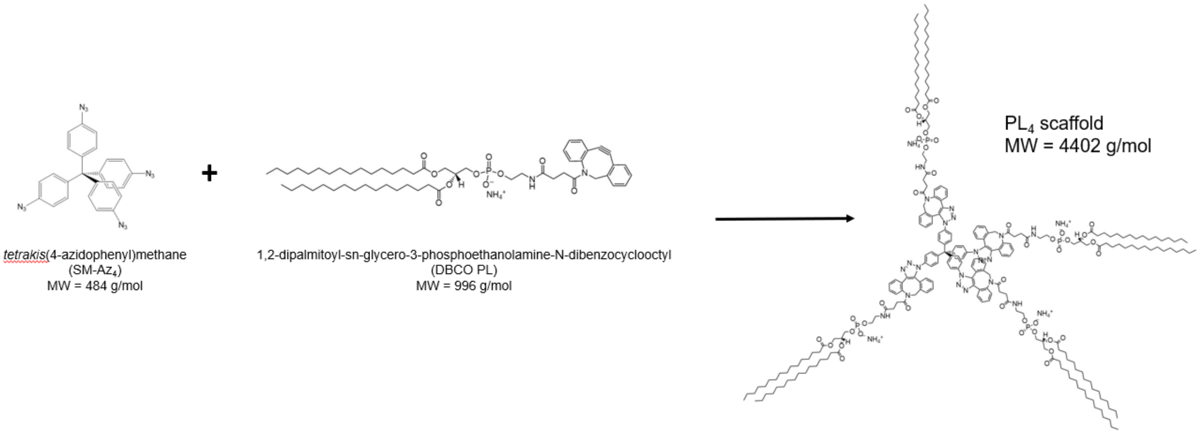

Figure 2.2: PL_4 synthesis scheme

The PL_4 scaffold is synthesized via copper-free click chemistry. A small molecule with four azidophenyl groups ($SM-Az_4$) is conjugated to four equivalents of a DBCO-functionalized phospholipid (DBCO PL) to produce the final PL_4 conjugate.

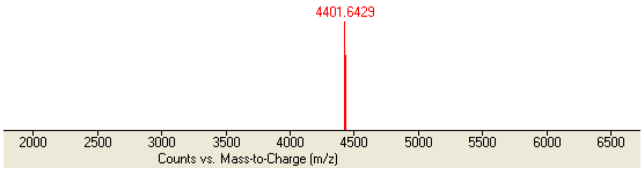

Figure 2.3: Electrospray ionization mass spectrum of PL_4 core

Product m/z = 4401.6 (Theoretical: 4401.7).

The second (9-DNA-PL_4) and third (18-DNA-PL_4) core scaffolds are amphiphilic DNA-linked PL_4 cores, with differing DNA linker length (9- vs. 18-mer dsDNA) (Figure 2.4b) (Table 2.1). While DNA linkers enhance the core's solubility in aqueous solution, externally oriented phospholipid tails enable hydrophobic interaction with apoA-1 and phospholipids. The arm lengths of these core scaffolds can be easily tuned by incorporating DNA linkers of varying length. DNA-PL_4 cores were synthesized in a two-step fashion (Materials and Methods, Section S2a). First, we synthesized DNA-phospholipid conjugates (ssDNA-PL), and tetrahedral small molecule-DNA hybrids ($SMDH_4$). Second, ssDNA-PL and $SMDH_4$ with complementary base-pairing sequences were hybridized to yield the final DNA-PL_4 cores (Figure 2.4b). The ssDNA sequences used for the syntheses of 9-DNA-PL_4 and 18-DNA-PL_4 are shown in Table 2.1.

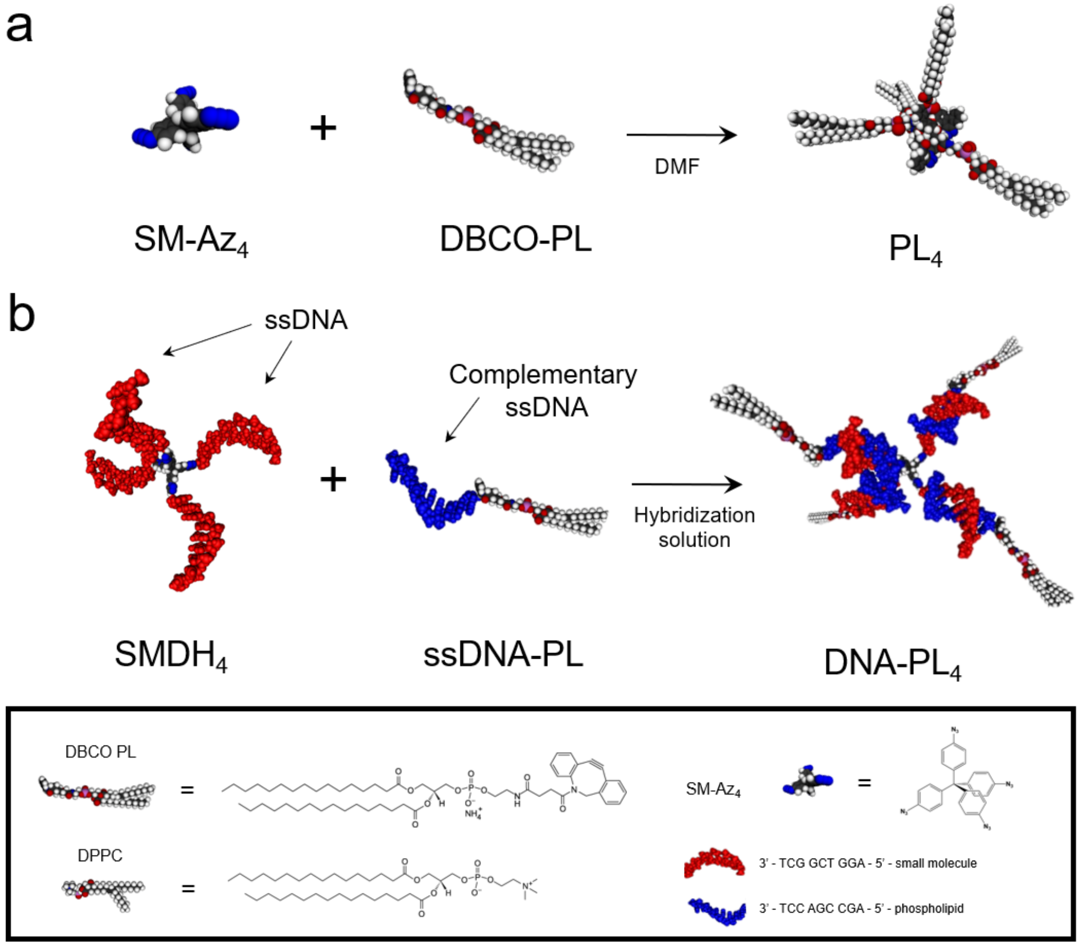

Figure 2.4: Synthesis schemes for PL$_4$ and DNA-PL$_4$ core scaffolds

a) PL$_4$ is synthesized by copper-free click chemistry conjugation of DBCO-functionalized phospholipids (DBCO PL) to a tetrahedral small molecule with four azidophenyl groups (SM-Az$_4$). b) DNA-PL$_4$ scaffolds are synthesized in a stepwise process. First, a tetrahedral small molecule-DNA hybrid with four ssDNA arms (SMDH$_4$) and a ssDNA-phospholipid conjugate (ssDNA-PL) are synthesized and purified separately. Then, the two species are hybridized two produce the final DNA-PL$_4$ scaffold. Chemical structures of DPPC, DBCO PL, and SM-Az$_4$ are shown in the figure legend, along with the DNA sequences used in the synthesis of 9-DNA-PL$_4$.

Table 2.1: List of DNA sequences of $SMDH_4$ DNA arms and DNA-lipid conjugates.

DNA Length	DNA sequences[a]
9-$SMDH_4$	3′-TCG GCT GGA-small molecule
18-$SMDH_4$	3′-TTG CTG AGT ATA ATT GTT-small molecule
9-DNA-PL	3′-TCC AGC CGA-lipid
18-DNA-PL	3′-AAC AAT TAT ACT CAG CAA-lipid

[a] DNA sequences of $SMDH_4$ DNA arms are complementary to those of DNA-lipid conjugates (i.e., 9-$SMDH_4$ to 9-DNA-lipid and 18-$SMDH_4$ to 18-DNA-lipid).

The successful synthesis and purification of 9-$SMDH_4$ and 18-$SMDH_4$ were demonstrated by MALDI-ToF and analytical RP-HPLC while tracking absorbance at 260 nm to monitor DNA content. MALDI-ToF revealed molecular weights of 12,144 m/z and 23,264 m/z for 9-$SMDH_4$ and 18-$SMDH_4$ respectively, which were precisely consistent with theoretical predictions (Figures 2.5 and 2.6, insets). Analytical RP-HPLC revealed a single peak in each case, indicating high purity and consistent with a single species of DNA hybrid with four functionalized arms (Figures 2.5 and 2.6).

Synthesis of DNA-phospholipid conjugates was similarly confirmed by MALDI-ToF. Results revealed molecular weights of 3,340 m/z and 6,115 m/z for 9-DNA-PL and 18-DNA-PL respectively, which were consistent with theoretical predictions (Figures 2.7 and 2.8). Semi-preparative RP-HPLC traces are also shown in Figures 2.7 and 2.8, and the indicated peaks with the longest retention times were collected and used for MALDI-ToF.

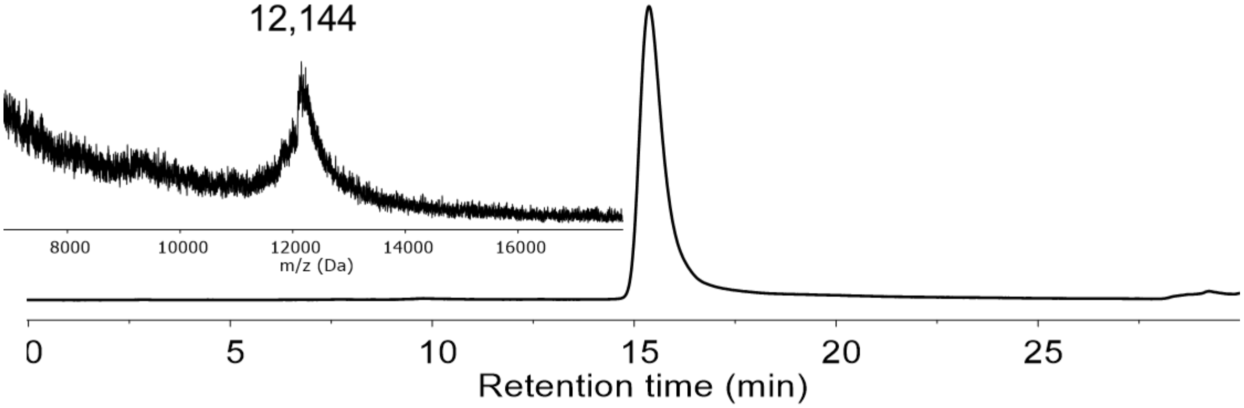

Figure 2.5: Analytical RP-HPLC trace of 9-SMDH$_4$
RP-HPLC trace from the coupling reaction of the *tetrakis*(4-azidophenyl) methane with alkyne-functionalized 9-mer DNAs on the CPGs. The trace is the signal from the diode detector set at 260 nm. Inset shows the MALDI-ToF spectrum of the pure product: m/z =12,144 (12,144.1 theoretical).

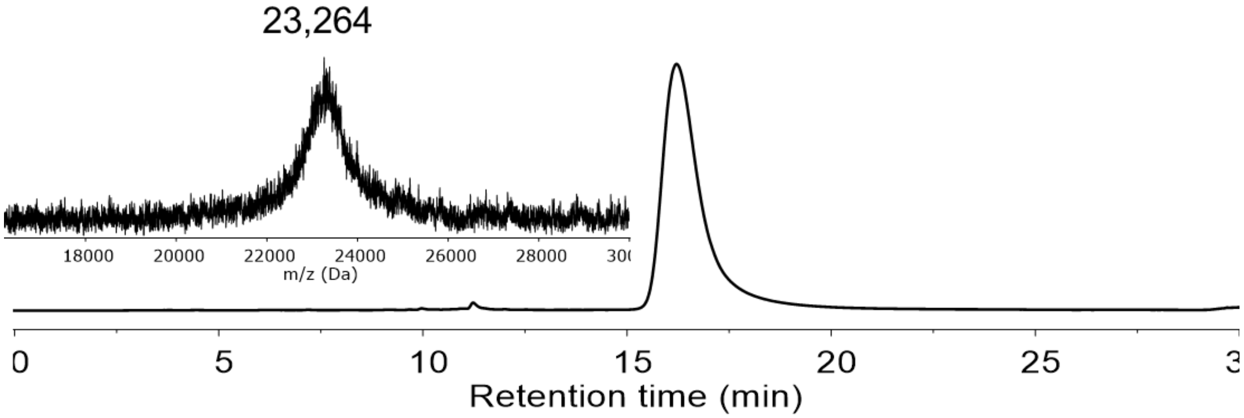

Figure 2.6: **Analytical RP-HPLC trace of 18-SMDH$_4$**

RP-HPLC trace from the coupling reaction of the *tetrakis*(4-azidophenyl) methane with alkyne-functionalized 18-mer DNAs on the CPGs. The trace is the signal from the diode detector set at 260 nm. Inset shows the MALDI-ToF spectrum of the pure product: m/z = 23,264 (23,263.7 theoretical).

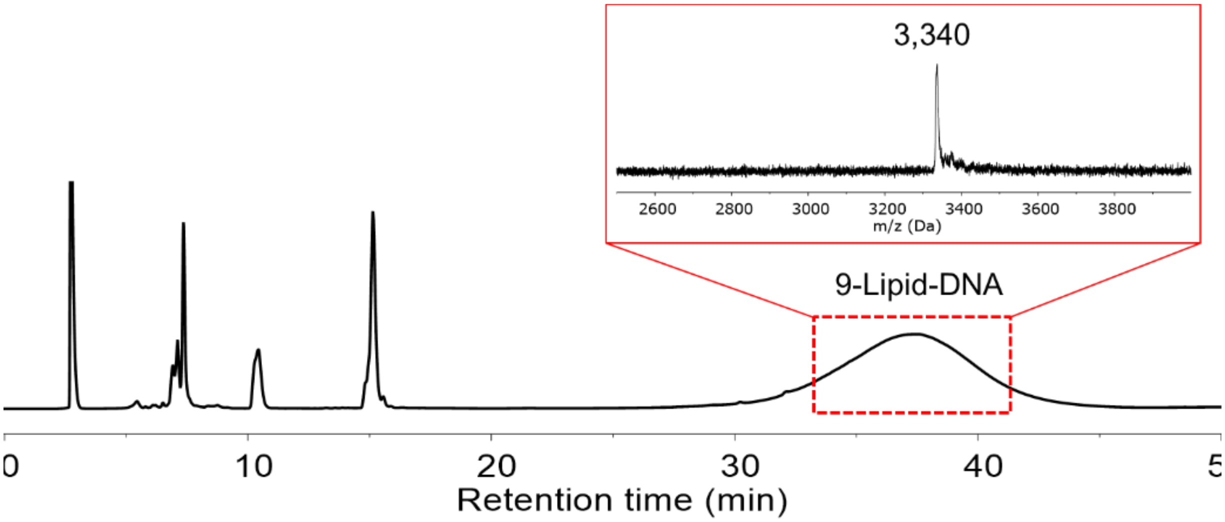

Figure 2.7: Semi-preparative RP-HPLC trace of crude 9-DNA-lipid

The trace is the signal from the diode detector set at 260 nm. The pure 9-DNA-lipid at 33-42 min was isolated and identified by MALDI-ToF (Inset): m/z = 3,340 (3,342.4 theoretical).

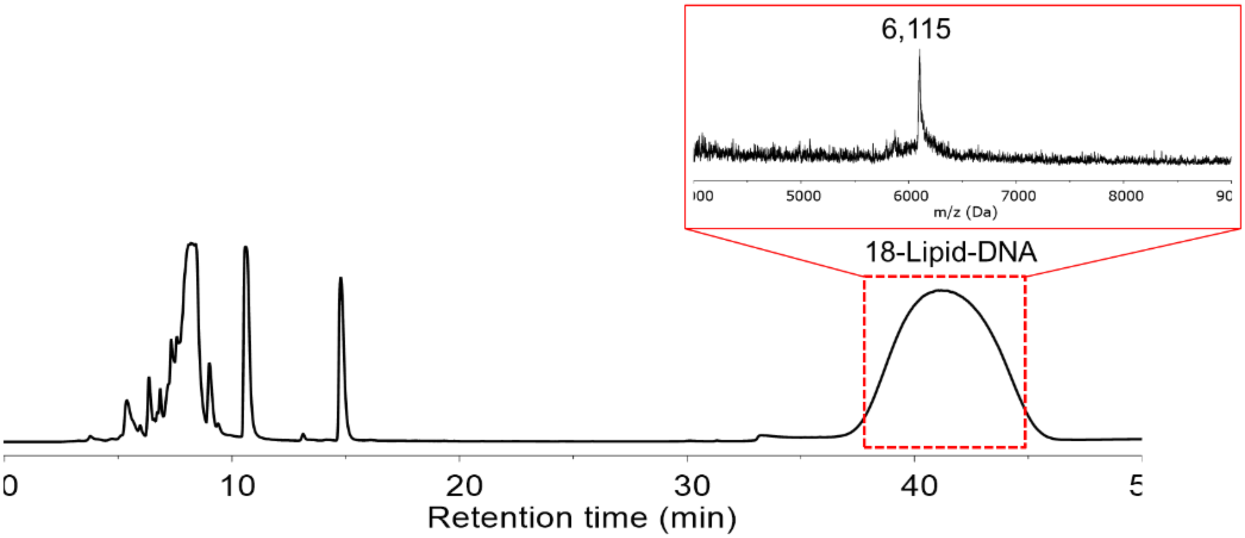

Figure 2.8: Semi-preparative RP-HPLC trace of crude 18-DNA-lipid

The trace is the signal from the diode detector set at 260 nm. The pure 18-DNA-lipid at 38-45 min was isolated and identified by MALDI-ToF (Inset): m/z = 6,115 (6,118.2 theoretical).

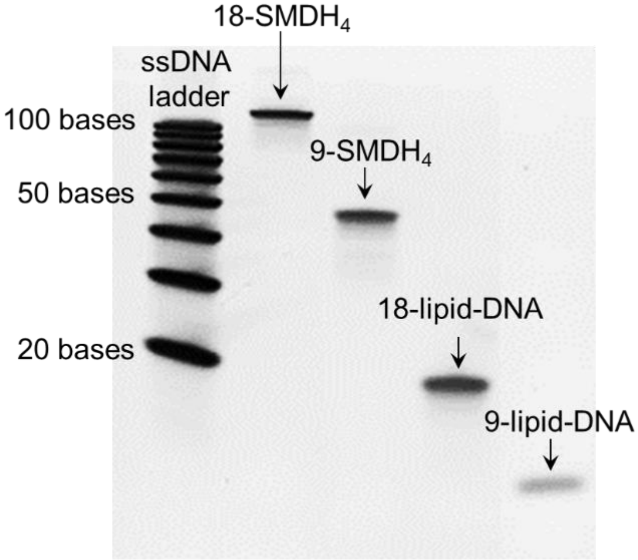

Figure 2.9: **Denaturing PAGE-gel image of 9- and 18-SMDH$_4$'s and 9- and 18-DNA-lipid conjugates.**

The gel experiment was carried out in 1× TBE buffer at 180 V for 1 h and then the gels were stained with SYBR Gold (Thermo Fisher Scientific, Inc., Grand Island, NY) and their pictures were taken using a Typhoon 9400 (GE Healthcare, Pittsburgh, PA).

DNA polyacrylamide gel electrophoresis (PAGE) was used as an additional characterization method for these materials. Results showed that the DNA hybrids migrated on DNA-PAGE in a manner consistent with their varying sizes. In particular, the size of the four hybrids in decreasing order is 18-SMDH$_4$, 9-SMDH$_4$, 18-DNA-PL, and 9-DNA-PL; and the migration distance along the gel inversely correlated with hybrid size (Figure 2.9). 18-DNA-PL and 9-DNA-PL migrated approximately at the expected migration distances of ordinary 18-mer and 9-mer ssDNA. While 18-SMDH$_4$ and 9-SMDH$_4$ possess 72 and 36 nucleotides in total respectively, we hypothesized that the tetrahedral configuration of these hybrids would lead to slower migrations than ordinary 72-mer and 36-mer ssDNA. The results shown in Figure 2.9 are consistent with this hypothesis.

Using the resulting core scaffolds, we then performed and optimized the assembly of LC HDL NPs. We first prepared liposomes from 1,2-dipalmitoyl phosphatidyl choline (DPPC) (Materials and Methods, Section 2c). PL_4 scaffolds were then prepared as thin films, while improved aqueous solubility enabled us to begin with DNA-PL_4 scaffolds already in aqueous buffer. ApoA-1 protein and DPPC liposomes were then added to the core scaffolds and the mixture was subjected to three rounds of sonication, allowed to relax on ice, then filtered and concentrated using a 50 kDa MWCO spin column (Figure 2.10). Illustrations of LC HDL NPs, gold nanoparticle-templated HDL NPs (Au HDL NP), and human HDLs are illustrated in Figure 2.11, highlighting the differences in core composition.

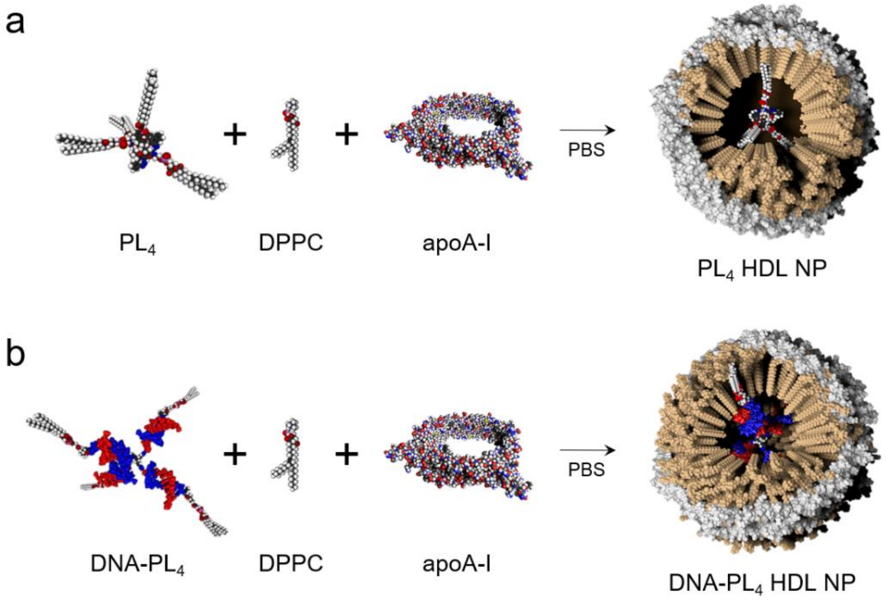

Figure 2.10: Schematics of LC HDL NP assembly

a) PL_4 HDL NPs are assembled by first dissolving PL_4 in an organic solvent and then evaporating the solvent to generate a thin film of the PL_4 core scaffold. DPPC liposomes and the apoA-1 protein are then added to the core scaffold to resuspend the thin film in PBS, which leads to the production of PL_4 HDL NPs after several rounds of sonication and spin filtration. b) DNA-PL_4 HDL NPs are assembled by first preparing an aqueous solution of the hybridized DNA-PL_4 core scaffold. Then, DPPC liposomes and apoA-1 are added to the core scaffold solution to produce DNA-PL_4 HDL NPs after several rounds of sonication and spin filtration.

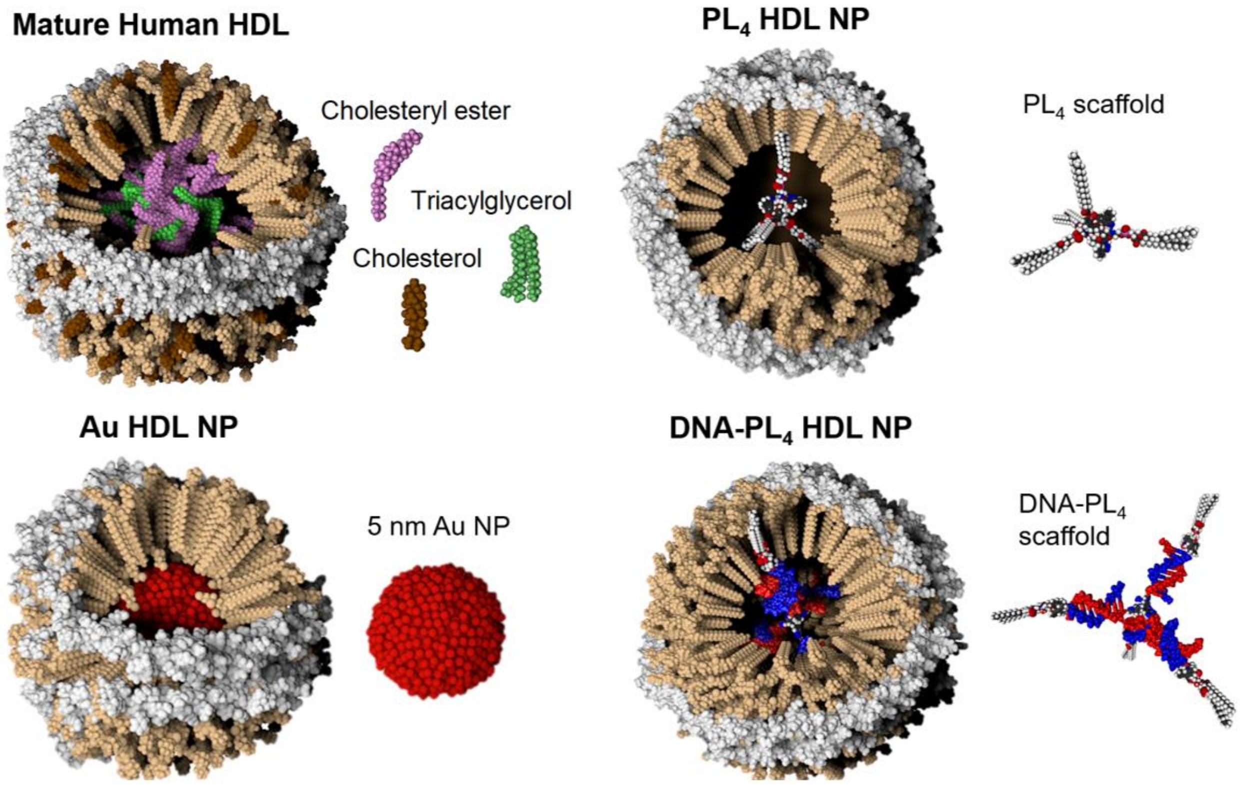

Figure 2.11: Illustrations of native and synthetic HDLs that differ in their core composition

Mature human HDLs possess a hydrophobic core comprised of cholesteryl esters and triglycerides, while free cholesterol is interspersed throughout a surface monolayer of phospholipids. Au HDL NPs possess a gold nanoparticle core that is 5 nm in diameter, surrounded by a phospholipid bilayer consisting of two species of phospholipid.[25] PL_4 and DNA-PL_4 HDL NPs each have a lipid-conjugated core scaffold on the interior of the particle, surrounded by a surface monolayer of phospholipids. Each of these synthetic and native HDL species include the apoA-1 protein that is primarily localized to the surface of the particle.

TEM imaging revealed monodisperse nanoparticles for assemblies using PL_4 and 9-DNA-PL_4 scaffolds (PL_4 HDL NP diameter: 10 ± 2 nm, 9-DNA-PL_4 HDL NP diameter: 9 ± 2 nm) (Figures 2.12 and 2.13). Notably, the morphology of the particles was not characteristic of immature, discoidal HDLs, or rHDLs, both of which exhibit a hallmark rouleaux formation of stacked phospholipid discs.[23, 152, 154] Instead, the particles appeared roughly spherical, with a peripheral hypodense region. Dynamic light scattering demonstrated hydrodynamic diameters of

13.8 nm and 13.3 nm for PL_4 and 9-DNA-PL_4 HDL NPs respectively (Table 2.2), which were found to be similar to the hydrodynamic diameters of native HDL_2 and HDL_3 isolated from human plasma.

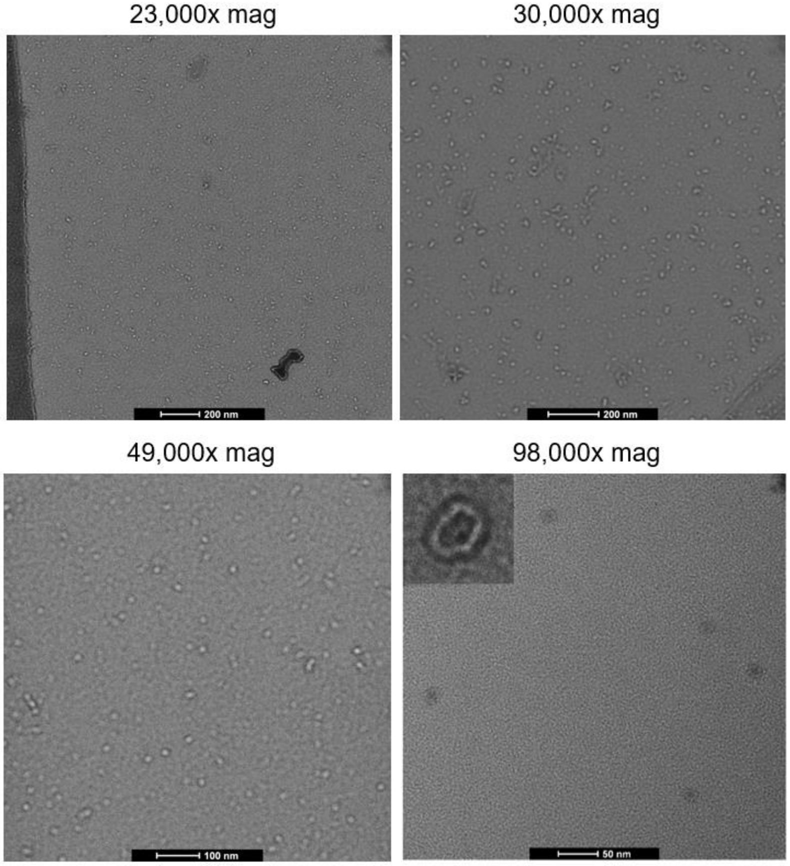

Figure 2.12: Ultrastructural characterization of PL_4 HDL NPs via TEM

Imaging was performed with FEI Tecnai Spirit TEM. Inset (bottom right panel) is under 120,000× magnification. Scale bars labeled on each image, from 50-200 nm.

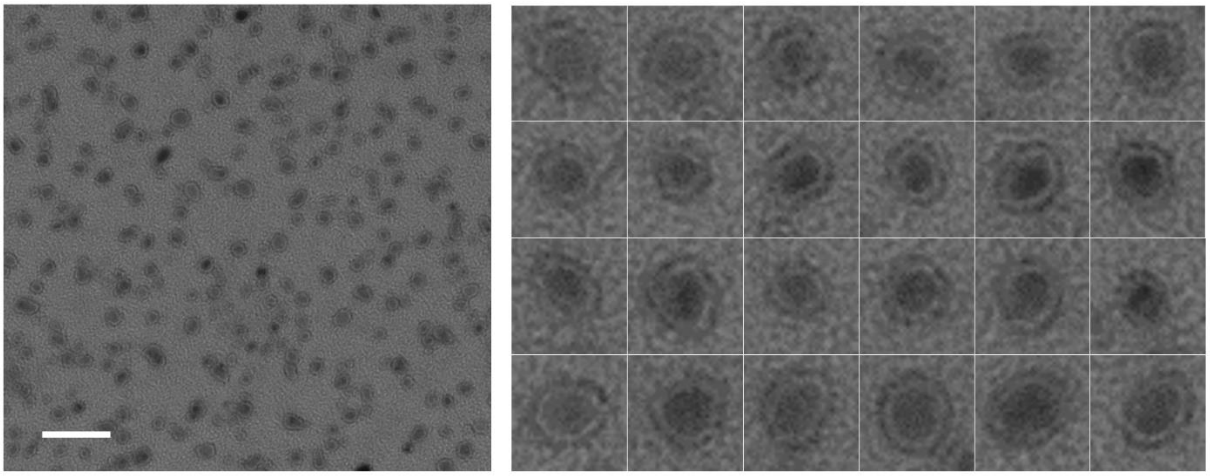

Figure 2.13: Ultrastructural characterization of DNA-PL$_4$ HDL NPs via TEM

Imaging was performed with FEI Tecnai Spirit TEM. Scale bar is 50 nm.

Table 2.2: Hydrodynamic diameters of LC HDL NPs and controls determined by DLS

Sample	Hydrodynamic Diameter (nm)
Free apoA-I	7.6 ± 0.2
Human HDL$_2$	14.1 ± 5.0
Human HDL$_3$	13.6 ± 6.1
PL$_4$ HDL NP	13.8 ± 3.9
DNA-PL$_4$ HDL NP	13.3 ± 4.6

As an additional means of determining particle size and polydispersity, we performed size exclusion chromatography (SEC) on LC HDL NPs and controls. SEC results demonstrated peak retention volumes of 8.22 and 8.88 mL for 9-DNA-PL$_4$ HDL NPs and PL$_4$ HDL NPs respectively (Table 2.3 and Figure 2.14). PL$_4$ HDL NP exhibited two slightly offset peaks, perhaps due to a heterogeneity in apoA-I copies per particle, while DNA-PL_4 HDL NPs exhibited a single peak. SEC also revealed a small amount of free apoA-I protein in LC HDL NP samples, which was also observed for native HDL controls.

Table 2.3: Retention volumes for LC HDL NPs and controls from SEC

Sample	Peak Retention Volume (mL)
Free apoA-I	10.13
Human HDL_2	8.21
Human HDL_3	8.26
PL_4 HDL NP	8.88
DNA-PL_4 HDL NP	8.22
DNA-PL_4 scaffold alone	6.33
apoA-I + DPPC (no scaffold)	6.98

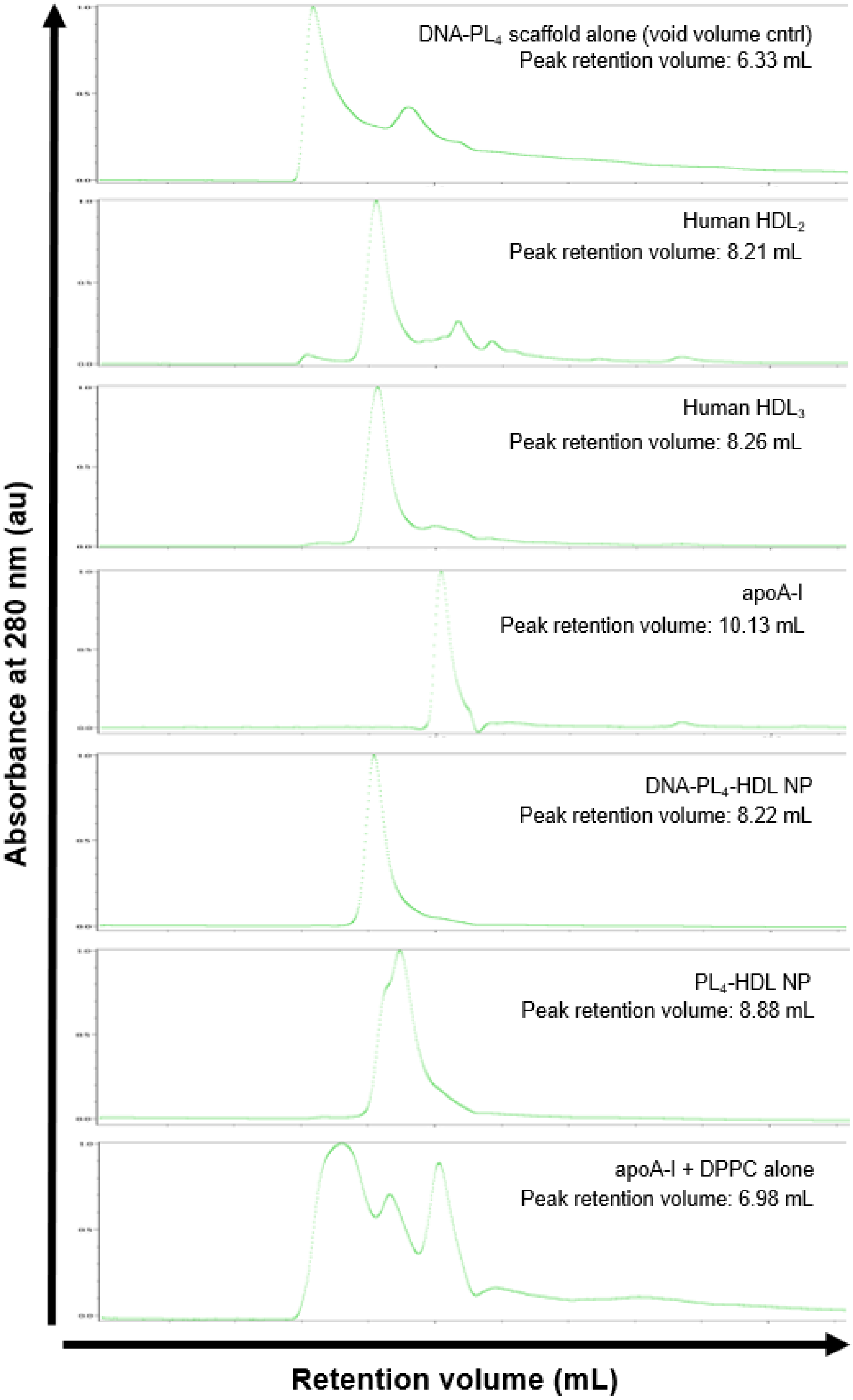

Figure 2.14: Size exclusion chromatography results for LC HDL NPs and controls

UV absorbance at 280 nm (arbitrary units) is plotted against retention volume (mL).

While assemblies using PL_4 and 9-DNA-PL_4 scaffolds successfully generated sub-20 nm particles according to TEM, DLS, and SEC, the assemblies using 18-DNA-PL_4 scaffolds persisted as large vesicular structures after the addition of DPPC and apoA-1 (Figure 2.15). We hypothesize that this is a result of the DNA hybrid's size being prohibitively large for apoA-1 assembly. Interestingly, 9-DNA-PL_4 HDL NPs were not significantly larger than PL_4 HDL NPs. This result, in conjunction with the lack of assembly using 18-DNA-PL_4, suggests that LC HDL NP size may be determined primarily by apoA-1 protein folding, irrespective of core size below a given threshold. All figures and remaining text refer to the particles formed using 9-DNA-PL_4 scaffolds simply as DNA-PL_4 HDL NPs.

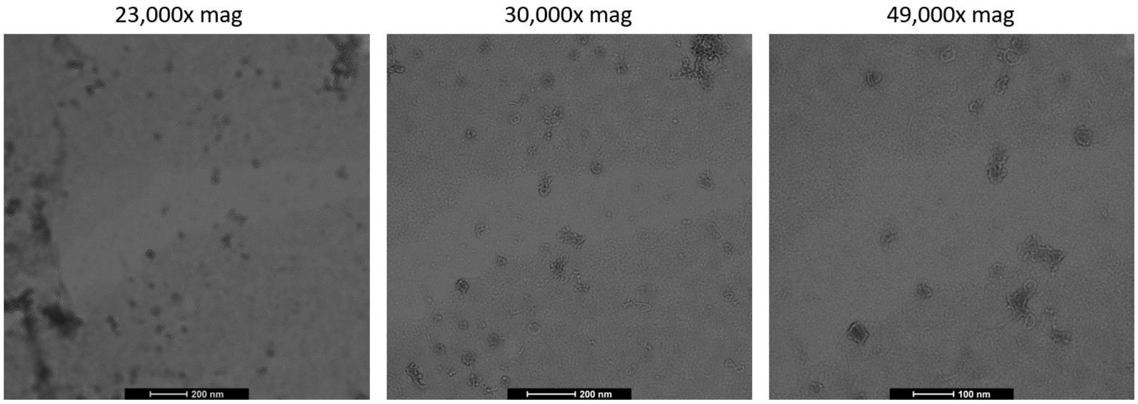

Figure 2.15: **Ultrastructural characterization of the nanoparticle assemblies using 18-mer DNA-PL_4 scaffolds**

Imaging was performed with FEI Tecnai Spirit TEM. Scale bars are 100-200 nm.

To confirm that both apoA-1 and the core scaffolds were required for LC HDL NP assembly, TEM was conducted on control assemblies using 1) each of the core scaffolds with DPPC liposomes without apoA-1 (Figure 2.16), 2) apoA-1 and DPPC without the core scaffolds (Figure 2.17), and 3) the core scaffolds alone (Figure 2.18). In the absence of apoA-1, TEM revealed a heterogenous group of vesicular structures ranging in diameter from approximately

20-100 nm (Figure 2.16), demonstrating that apoA-1 is necessary for the formation of sub-20 nm particles.

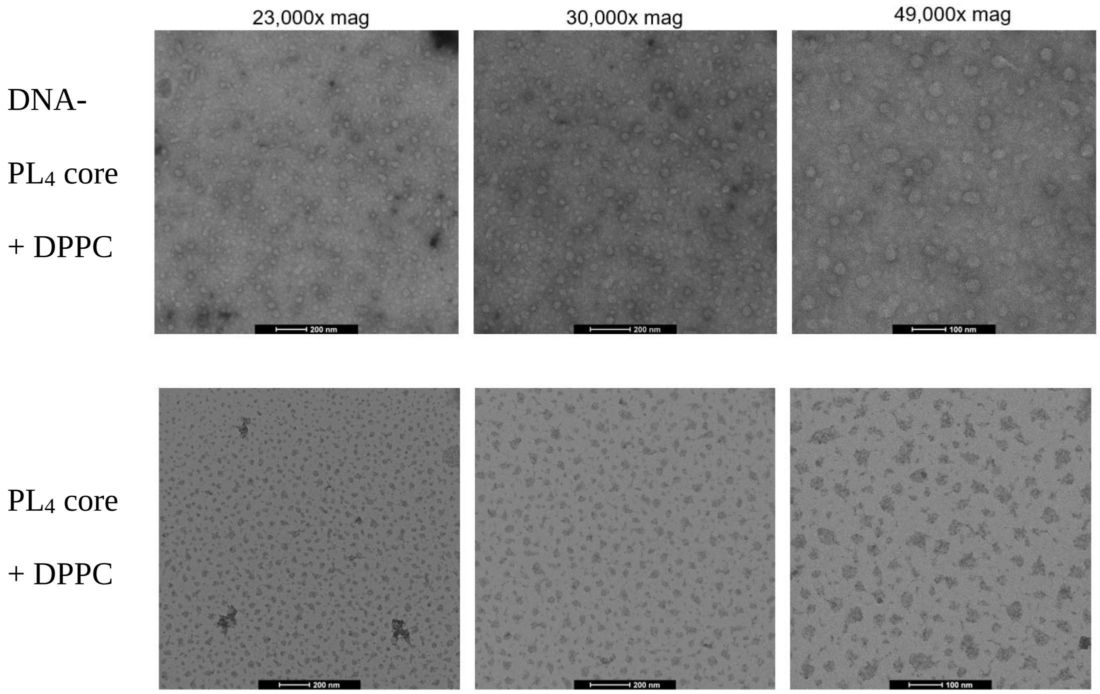

Figure 2.16: **TEM imaging of core scaffolds + DPPC control samples, without apoA-I** Imaging was performed with FEI Tecnai Spirit TEM. We note that DNA-containing samples and non-DNA-containing samples have differential propensities for uptake of uranyl acetate stain. Scale bars are 100-200 nm.

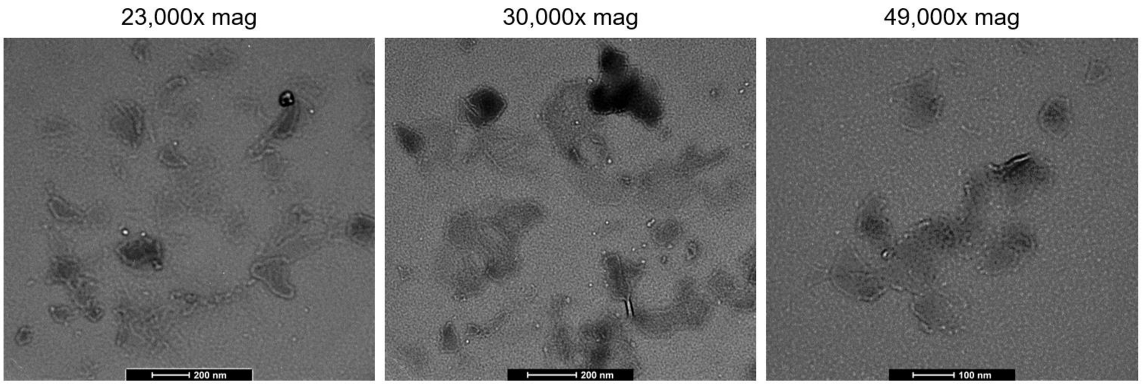

Figure 2.17: **TEM imaging of apoA-I + DPPC control assembly without a core scaffold** Imaging was performed with FEI Tecnai Spirit TEM. Scale bars are 100-200 nm.

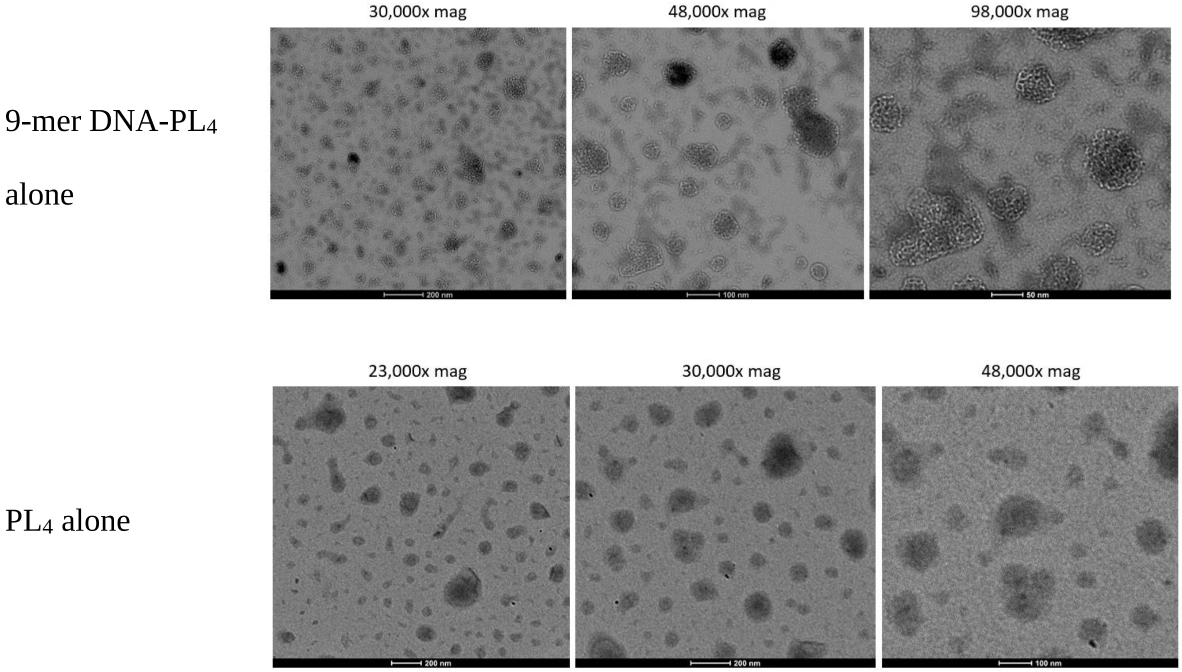

Figure 2.18: **TEM images of core scaffolds alone, without DPPC or apoA-I**
Imaging was performed with FEI Tecnai Spirit TEM. We note that DNA-containing samples and non-DNA-containing samples have differential propensities for uptake of uranyl acetate stain. Scale bars are 50-200 nm.

In the absence of a core scaffold, mixtures of apoA-1 and DPPC under these conditions resulted in the formation of a mixture of large aggregates and vesicles (Figure 2.17), demonstrating that the core scaffolds are required for the formation of sub-20 nm particles. The TEM results for apoA-1 + DPPC without a core scaffold were consistent with the SEC results for the same sample (Figure 2.14). The SEC results showed a heterogenous population of larger particles that eluted off the column at shorter retention times than LC HDL NPs. Finally, solutions of the core scaffolds alone showed the formation of a heterogenous group of vesicle-like structures ranging in diameter from about 20 nm to 300 nm Figure (2.18), which were similar in size and polydispersity to the results shown in Figure 2.16 for the core scaffolds + DPPC without apoA-1.

Table 2.4. Structural analysis of native and synthetic HDLs via circular dichroism

	α-helix (%)	β-sheet (%)	Turn (%)	Unordered (%)
apoA-I	**57 ± 3**	**4 ± 2**	**14 ± 3**	**25 ± 5**
Au HDL NP	**73 ± 1**	**0 ± 0**	**6 ± 1**	**21 ± 2**
Human HDL_2	**50 ± 2**	**7 ± 1**	**18 ± 4**	**24 ± 2**
Human HDL_3	**42 ± 1**	**15 ± 1**	**15 ± 1**	**28 ± 3**
PL_4 HDL NP	**50 ± 1**	**7 ± 1**	**16 ± 5**	**27 ± 1**
DNA-PL_4 HDL NP	**40 ± 1**	**20 ± 2**	**16 ± 2**	**25 ± 7**

We then determined the composition of LC HDL NPs by weight and found that the particles closely mirror the composition of HDL_2 and HDL_3, with the exception that LC HDL NPs do not contain cholesterol or cholesteryl esters (Figure 2.19a). Next, to characterize particle structure in terms of apoA-1 protein conformation, circular dichroism was performed on LC HDL NPs and controls, and was analyzed using three distinct reference protein data bases. PL_4 HDL NPs and DNA-PL_4 HDL NPs were found to closely resemble human HDLs in their protein secondary structure, while Au HDL NPs exhibited excess alpha helicity and less beta sheet and turn content (Table 2.4 and Figure 2.19b). To further characterize LC HDL NP structure, we investigated protein oligomerization state by cross-linking LC HDL NPs with bissulfosuccinimidyl suberate followed by immunoblot.[26] ApoA-1 interaction with LC cores was found to induce stable oligomer formation (Figure 2.20). Moreover, the surface zeta potential of LC HDL NPs was more negative (PL_4: -21 ± 2 mV, DNA-PL_4: -19 ± 1 mV) than apoA-1 alone (-10 ± 3 mV) or apoA-1 and DPPC without the core scaffold (-12 ± 2 mV), but consistent with human HDL_2 (-19 ± 2 mV) and HDL_3 (-21 ± 5 mV).

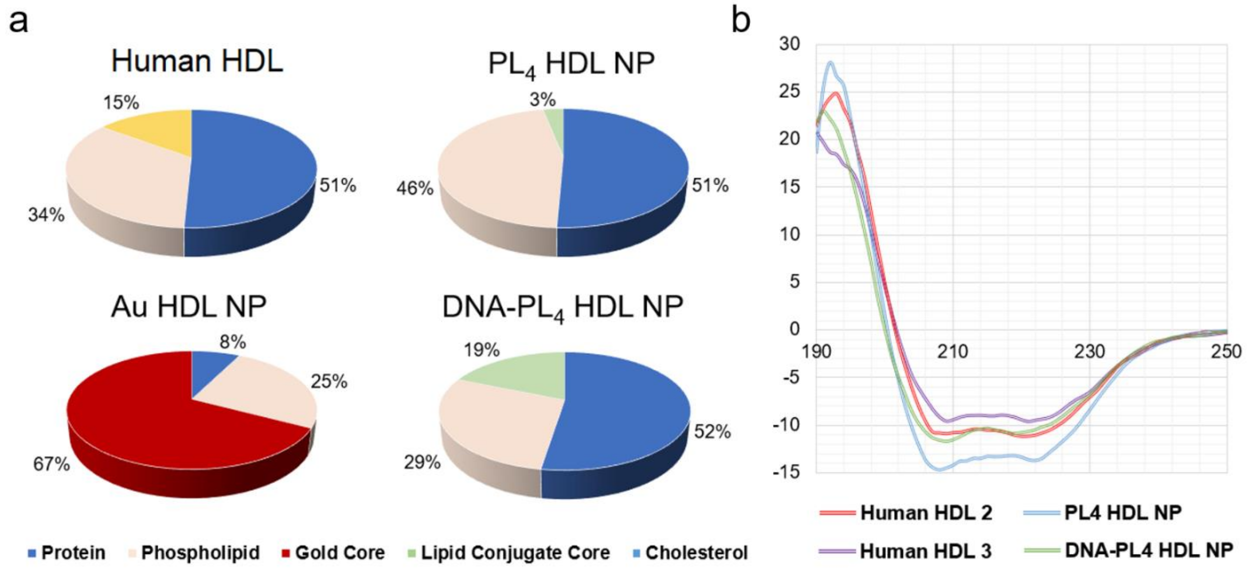

Figure 2.19: LC HDL NP composition and protein secondary structure

a) Composition by weight of human HDL, LC HDL NPs, and Au HDL NPs. b) Circular dichroism spectra of human HDLs and LC HDL NPs.

Table 2.5: Molar composition ratios for PL_4 HDL NPs and DNA-PL_4 HDL NPs.

Sample	apoA-I/core scaffold (mol/mol)	DPPC/core scaffold (mol/mol)	DPPC/apoA-I (mol/mol)
PL_4 HDL NP	--	89*	35
DNA-PL_4 HDL NP	2.56	54	21

*Calculated using the protein/core scaffold ratio experimentally determined for DNA-PL_4 HDL NPs.

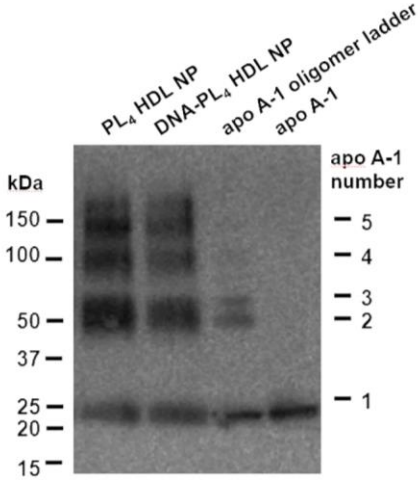

Figure 2.20: **Characterization of apoA-I oligomerization profile of LC HDL NPs**
LC HDL NPs were cross-linked using bissulfosuccinimidyl suberate prior to Western blot for apoA-1.

Having characterized the physicochemical and materials properties of LC HDL NPs using a wide range of techniques, we now offer additional discussion and speculation regarding the structure and organization of LC HDL NPs. On the likelihood of the particles possessing a surface monolayer of phospholipids versus a bilayer, we offer the following calculations. For a spherical particle with a diameter of 10 nm (i.e., as determined by TEM), the surface area of the outer leaflet is $4\pi r^2 = 4\pi(5\text{ nm})^2 = \sim 314\text{ nm}^2$. Given a bilayer thickness of 40 Å,[155] the inner leaflet of a bilayered, 10 nm diameter particle would have a radius of 2 nm and a surface area of ~13 nm^2. Therefore, if we assume that a hydrated phospholipid head group has a surface area of ~0.72 nm^2,[156] the particle would require approximately 454 lipids/particle to form a bilayer, excluding the surface area contribution of apoA-I on the particle. If we allow for apoA-I to assume 50% of the particle surface (a generous estimate), the particles would require approximately ~227 phospholipids to form a bilayer over the remaining surface. If instead we consider a monolayer model, we then predict ~209 phospholipids/particle. The latter estimate is closer to the ratios we observed experimentally. More importantly, the severe curvature required for an inner leaflet of a bilayer to self-assemble at a diameter of 2 nm is extremely unfavorable, and unlikely to occur.

In fact, if we assume that there is only one core scaffold per particle, our determined phospholipid values are below the expected number of phospholipids required for a monolayer. We therefore believe that either apoA-I occupies a greater portion of the particle surface on average than expected (plausible given the oligomerization results), and/or that some fraction of the particles contain more than one core scaffold. If we assume an average of two core scaffolds per particle, we obtain estimates of 106-180 phospholipids per particle, which are more consistent with the estimate calculated above for a monolayer than for a bilayer. Note that these calculations assume the LC HDL NP diameter determined via TEM. The SEC results, for instance in the case of PL_4 HDL NPs, indicate that one could manipulate these assumptions and parameters to account for other populations of particles that may have different numbers of constituents (e.g. apoA-I).

We note that the aforementioned calculations also neglect any perturbations to the outer phospholipid layer, which may be introduced by the externally oriented lipid tails from PL_4 and DNA-PL_4 scaffolds. These perturbations would then increase the effective surface area per phospholipid (i.e., > 0.72 nm^2), which would move the estimated number of phospholipids/particle even lower than the aforementioned estimate for a monolayer, which would trend even more toward our experimentally determined data, and away from a bilayer model. Independently of these calculations, Yetukuri et. al. estimates 109 phospholipids per native human HDL particle.[157] This is directly in the vicinity of our molar composition data, assuming an average of 1-2 cores per particle. While the calculations provided above represent a cursory examination of particle composition as it relates to our proposed model, future studies could be devoted to computational simulations with atomic-level precision in order to determine particle structure more precisely.

Regarding the apoA-I copy number per particle, the cross-linking results presented in Figure 2.20 reveal the highest-intensity bands for particles with 2-3 apoA-I molecules, with significant presence of bands for particles with 4-5 copies. This data is consistent with the best models of human HDL available, for instance in Figures 5 and 6 of a manuscript by Huang et. al.[158] These figures illustrate models in which apoA-I is arranged in HDLs in trimers, tetramers, and pentamers in various conformations.

We offer the following discussion regarding the validity of comparing phospholipid and protein composition between synthetic and native HDLs using our quantification methods, and whether the outputs of the colorimetric assays that we used are reflective of total HDL composition. While native HDLs do certainly harbor a diverse range of phospholipids, non-phosphatidylcholine lipids comprise quite a small minority of total HDL lipid content by mass or mol %. For instance, Yetukuri et al.[157] report the following data for ordinary human HDL:

Table 2.6: **Molar composition of native HDLs**.[157]

	apoA-I	**Sphingomyelins**	**Phosphatidyl Choline**	**Free Cholesterol**	**Cholesteryl Esters**	**Triglycerides**	**Lyso-PC**
Copy #	2	19	109	50	90	19	10

Given this data, we calculate that by quantifying the amounts of PC and lyso-PC (both detected by the choline detection kit), and free cholesterol and cholesteryl esters (detected by Amplex Red assay), we will on average account for 259/297 lipid molecules in a typical native HDL particle. This represents 87% of the total lipid constituents of HDLs. Furthermore, our protein quantification method is unbiased as bicinchoninic acid does not discriminate between the exclusive apoA-I harbored by LC HDL NPs vs the combination of apoA-I (~70%), apoA-II (~20%), and non-apoA proteins in native HDLs. Consequentially, we are confident that our quantification methods are capable of detecting nearly all of the lipids and proteins in native and synthetic HDLs in a largely unbiased fashion.

Here, we provide further discussion regarding our interpretations of the SEC results. First, we used two different control samples with large hydrodynamic diameters to determine the void volume: 1) DNA-PL_4 scaffold alone, which exhibited diameters between 100 and 200 nm via TEM, and 2) Collagen IV, a large extracellular matrix protein (~160 kDa; predicted to be trimerized in aqueous solution). Both DNA-PL_4 scaffold alone (Figure 2.14) and Collagen IV (data not shown) began to elute from the column at ~6.0 mL, defining the void volume. Note that the DNA-PL_4 scaffold alone also exhibited a small peak at 9.28 mL, which likely represents the core scaffold monomers or oligomers, without adopting higher order self-assembled structures such as vesicles. PL_4 HDL NPs and DNA-PL_4 HDL NPs exhibited retention volumes of 8.88 and 8.22 respectively, compared to 8.21, 8.26, and 10.10 for human HDL_2, human HDL_3, and apoA-I respectively. Notably, PL_4 HDL NPs exhibited two slightly offset peaks (8.59 and 8.88 mL), and both LC HDL NPs exhibited small right-sided tails consistent with free apoA-I (~10.10 mL). We also ran apoA-I + DPPC without a core scaffold as a control, and observed a heterogenous mixture of large, intermediate, and small species (Figure 2.14). Importantly, the apoA-I + DPPC control sample assembled primarily into large protein aggregates (consistent with TEM results), as the vast majority of protein was lost upon filtration with a 0.2 µm filter. In sum, SEC results support the other size characterization methods (TEM and DLS) in suggesting that LC HDL NPs are within the size regimes of native HDLs. SEC reveals that LC HDL NPs are generally monodisperse, the PL_4 HDL NP sample has two distinct populations of particles that are of similar size, and that there is a small amount of free apoA-I protein in samples.

Lastly, we provide the following discussion regarding the mechanism of action for LC HDL NP cholesterol transport, taking DNA-PL_4 HDL NPs as a case study. Our working hypothesis for DNA-PL_4 HDL NP particle function is as follows: DNA-PL_4 HDL NP particles diffuse through the aqueous biological medium and bind to HDL-specific cell surface receptors (ABCA1, ABCG1, SR-B1) via the apoA-I protein on the particle surface. Upon binding to the receptor, the particle induces a conformational change in the receptor whereby cholesterol is mobilized from the plasma membrane through a non-aqueous pore in the receptor and onto the particle. The non-esterified, effluxed cholesterol forms constructive enthalpic interactions with the hydrophobic portions of the apoA-I protein and the phospholipid tail groups of the surface monolayer, while the alcohol group may interact with the negatively charged DNA moiety or the phospholipid head groups via hydrogen bonding. Upon sequestering effluxed cholesterol, the particle eventually dissociates from the receptor and diffuses back into the medium. When LCAT is present, apoA-I on the particle serves as a co-factor for the enzymatic esterification of cholesterol in the particle. When this particle-bound cholesterol becomes esterified, the hydrophobic portion of the cholesteryl ester likely reorients preferentially to hydrophobic residues on apoA-I and phospholipid tails. Another possibility is that after esterification, some of the cholesteryl ester is transferred from the DNA-PL_4 particles to other lipoproteins in solution (e.g. via CETP). For delivery function, DNA-PL_4 particles loaded with cholesterol (primarily unesterified cholesterol) engage SR-B1 on the surface of hepatocytes, and transfer cholesterol into hepatocytes via a non-aqueous pore in the receptor. A single cohort of DNA-PL_4 particles may be able to on-load and off-load cholesterol for multiple rounds of efflux and delivery. The mechanism by which PL_4 HDL NPs would be very similar to that of the DNA-PL_4 HDL NPs with the exception that PL_4 HDL NPs can harbor and transport considerably more hydrophobic cargo due to its significantly more hydrophobic core, as evidenced by the enzymatic esterification results.

2.4 Conclusions

We report the synthesis and characterization of soft-core, HDL-like nanoparticles (LC HDL NPs) that strongly resemble native mature, spherical HDLs. We used novel, lipid-conjugated organic core scaffolds to direct the self-assembly of HDL NPs upon addition of apoA-1 and phospholipids (DPPC). LC HDL NPs were found to be 9-13 nm in diameter by TEM, DLS, and SEC, consistent with the standard size regime of native HDLs. LC HDL NPs also closely mimic native mature HDLs in their surface charge, composition, and protein secondary structure.[159]

2.5 Materials and Methods

Unless otherwise stated, all reagents and reagent-grade solvents were purchased from Sigma-Aldrich (Milwaukee, WI) and used as received. All lipids– 1,2-dipalmitoyl-*sn*-glycero-3-phosphoethanolamine-N-dibenzocyclooctyl (DBCO PE) and 1,2-dipalmitoyl-*sn*-glycero-3-phosphocholine (DPPC)– and fluorescent cholesterol (22-(*N*-(7-Nitrobenz-2-Oxa-1,3-Diazol-4-yl)Amino)-23,24-Bisnor-5-Cholen-3β-Ol ((NBD)-cholesterol)),were obtained from Avanti Polar Lipids (Alabaster, AL). Monomeric ApoA-I protein and lecithin:cholesterol acyltransferase (LCAT) protein were obtained from MyBioSource (San Diego, CA). Ultrapure deionized (DI) H_2O (18.2 MΩ·cm resistivity) was obtained from a Millipore system (Milli-Q

Biocel). *Tetrakis*(4-azidophenyl)methane[160] and lipid phosphoramidite[161] were synthesized according to previously published procedures.

The syntheses of hexynyl-functionalized DNA strands and DNA-lipid conjugates were carried out on an Expedite 8909 Nucleic Acid System. DNA products were purified and analyzed on an Agilent 1100 HPLC equipped with reverse-phase (RP) semi-preparative (Dynamax, 250 × 10 mm, Microsorb 300 Å/10 μm/C18, Agilent # R083213C10) and analytical (Dynamax, 100 × 4.6 mm, Microsorb 100 Å/3 μm/C18, Agilent # R0080200E3) columns, respectively. The coupling of hexynyl-functionalized DNA with *tetrakis*(4-azidophenyl)methane was carried out in a Thermomixer R 5355 (Eppendorf AG North America, Hauppauge, NY) instrument.

Absorption spectra of DNA materials were recorded on a Varian Cary 300 Bio UV-vis spectrophotometer (Varian, Inc., Palo Alto, CA) using a masked quartz cell (path length = 10 mm, catalog # 29B-Q-10-MS, Starna cells Inc., Atascadero, CA).

Negative stain transmission electron microscopy (TEM) images were acquired using a FEI Tecnai Spirit TEM operating at 120 kV, using 300-mesh carbon-coated copper grids (Electron Microscopy Services). Dynamic light scattering (DLS) and zeta potential measurements were carried out on a Zetasizer Nano ZS (Malvern Instruments, Malvern, UK) equipped with a He-Ne laser (633 nm). Size exclusion chromatography was carried out with a PSS Suprema column 7.6*250 mm using Agilent 1260 HPLC system equipped with UV detector and connected to Wyatt Heleos II MALS and RI detectors. Confocal imaging was carried out with a Nikon A1R Spectral microscope. Flow cytometry was performed using a BD LSRFortessa cell analyzer. Matrix-assisted laser desorption/ionization time-of-flight (MALDI-ToF) mass spectrometric data were collected as negative ions using the linear mode on a Bruker

AutoFlex III MALDI-ToF mass spectrometer (Bruker Daltonics, Billerica, MA). The instrument was equipped with Smartbeam™ laser technology operated at 30-40% power with a sampling speed of 10 Hz. One thousand scans were averaged for each mass spectrum. Data from Agilent HPLC and Bruker MALDI-ToF instruments were processed using MestreNova software version 8.1.1-11591.

Synthesis and purification of 9- and 18-SMDH$_4$'s

Small molecule-DNA hybrids (SMDHs) with 9 and 18 mer DNA arms (9- and 18-SMDH$_4$'s, respectively) were synthesized and purified according to a previously published procedure[162] and DNA sequences used in this study are listed in the Table S1. To identify the different products that were formed in the SMDH preparation, an aliquot of the collected sample of crude SMDHs was first analyzed using an analytical RP-HPLC column (see Section S1) and a gradient method beginning with 95:5 v/v 0.1 M TEAA (aq):MeCN (TEAA (aq) = triethylammonium acetate, aqueous solution), and increasing to 60:40 v/v 0.1 M TEAA(aq):MeCN over 35 min (at a ramp of +1 vol% MeCN/min), with a flow rate of 1 mL/min. Then, the whole sample was subjected to purification using a semi-preparative RP-HPLC column (see Section S1) and a gradient method beginning with 95:5 v/v 0.1 M TEAA (aq):MeCN and increasing to 60:40 v/v 0.1 M TEAA(aq):MeCN over 70 min (at a ramp of +0.5 vol % MeCN/min, a slower gradient was employed here to ensure adequate separation of the peaks), with a flow rate of 3 mL/min. The identity of the collected SMDH$_4$ product was confirmed by MALDI-ToF MS analysis (insets in Figures S1 and S2) and its purity was reassessed using analytical RP-HPLC (Figures S1 and S2) with the aforementioned analytical RP-HPLC solvent program.

Solid-phase synthesis and purification of DNA-phospholipid conjugates

Syntheses were carried out from the 3′ direction using controlled pore glass (CPG) beads possessing 1 µmol of either adenine (Glen Research, dA-CPG # 20-2001-10, (1000 Å, 28 µmol/g)) or thymine (Glen Research, dT-CPG # 20-2031-10 (1000 Å, 27 µmol/g)) attached to the surface. The CPG beads were placed in a 1 µmol synthesis column and 3′-phosphoramidites (Glen Research, dA-CE phosphoramidite # 10-1000-C5, Ac-dC-CE phosphoramidite # 10-1015-C5, dmf-dG-CE phosphoramidite # 10-1029-C5, dT-CE phosphoramidite # 10-1030-C5) were then added using the standard 1 µmol protocol on an Expedite 8909 synthesizer to make the CPG-3′-ssDNA (see Table S1 for sequences). A lipid phosphoramidite was added to the 5′ end of ssDNA strand and then the beads were dried with a stream of dried nitrogen gas and placed in a vial containing aqueous fresh AMA solution (1 mL of a 1:1 v/v mixture of 30 wt % aqueous ammonium hydroxide solution and 40 wt % aqueous methylamine solution). The vial was then capped and heated at 65 °C for 15 min to cleave DNA-lipid conjugates from the solid supports. The ammonia and methyl amine byproducts were then removed by passing a stream of dry nitrogen gas over the content of the vial until the characteristic ammonia smell disappears. The remaining liquid, which contains the crude DNA-lipid conjugates, was collected by pipette and the remaining beads were further extracted with ultrapure deionized water (200 µL). The extract was combined with the initial solution of crude DNA-lipid conjugates (affording a total volume of 0.4 mL at the end) and filtered through a 0.45 µm nylon syringe filter (Acrodisc® 13 mm syringe filter # PN 4426T). The collected sample of crude product was subjected to purification using analytical RP-HPLC (Figures S3 and S4) and a gradient method beginning with 95:5 v/v 0.1 M TEAA (aq):MeCN (TEAA (aq) = triethylammonium acetate, aqueous solution), and increasing to 100% MeCN over 50 min (at a ramp of +1.9 vol% MeCN/min), with a flow rate of 1 mL/min. The identity of the collected product was confirmed by MALDI-ToF analysis (insets in Figures S3 and S4) and its purity was verified by denaturing polyacrylamide gel electrophoresis (PAGE) (Figure S4).

Hybridization of DNA-phospholipid conjugates and SMDH$_4$

Equimolar mixtures of the as-prepared SMDH$_4$ and its complementary DNA-lipid conjugate in TAMg buffer solution (40 mM Tris, 20 mM acetic acid, and 7.5 mM $MgCl_2$; pH 7.4) were added into 0.5 mL Eppendorf tubes. The resulting solutions were then heated to 90 °C in a heating block (Thermomixer R; Eppendorf, Hauppauge, NY) and kept there for 5 min to remove all initial DNA interactions. The power to the heating block was then turned off to allow the solution to slowly cool to rt over 3 h (for a typical cooling profile of this equipment, please see Fig. S16 in the SI for Yildirim, I.; Eryazici, I.; Nguyen, S. T.; Schatz, G. C. *J. Phys. Chem. B* **2014**, *118*, 2366-2376).

Synthesis of PL$_4$ core scaffold

PL$_4$ core materials were synthesized by copper-free click chemistry conjugation of 1,2-dipalmitoyl-*sn*-glycero-3-phosphoethanolamine-*N*-dibenzocyclooctyl (DBCO PE) with a tetrahedral small molecule core (*tetrakis*(4-azidophenyl)methane) with four terminal azides (Figure S6). In a typical reaction, the DBCO PE and *tetrakis*(4-azidophenyl)methane were each dissolved at 0.1 wt % in *N*,*N*-dimethylformamide (DMF, Sigma Aldrich) and mixed at a 10:1 molar ratio of DBCO PE to *tetrakis*(4-azidophenyl)methane in DMF. The reaction mixture was subjected to three rounds of alternating vortexing and bath sonication, and was then allowed to react at room temperature under vortex for 24 h. HPLC and electrospray ionization mass spectrometry (Figure S7) was then used to characterize the resulting reaction mixture. As Figure S7 only show a single species at the right mass for PL$_4$, we conclude that there is no partially coupled product (PL_3, PL_2, etc.) and use the reaction mixture for the assembly step. As the assembly step (see Section S2c below) involves adding a large excess of DPPC lipids, there is no need to separate the excess DBCO PE molecule from the PL_4 core prior to its use in the assembly.

LC HDL NP assembly

Nanoparticle assembly was carried out by first preparing 1,2-dipalmitoyl-*sn*-glycero-3-phosphocholine (DPPC) liposomes. DPPC was dissolved at 0.1 wt % in chloroform in 5 mL glass vials. A thin film was then generated by evaporating the solvent with N_2 gas. The film was further dried under reduced pressure in a desiccator for > 2 h. Liposomes were then generated by resuspending the thin film in phosphate-buffered saline (PBS, 10 mM phosphate and 137 mM NaCl, pH = 7.4) at a DPPC concentration of 1 mM and then subjecting to alternating bath sonication and vortexing. For PL_4 HDL NPs, the PL_4 core scaffold was prepared by generating a thin film from a 0.1 wt % solution in DMF by evaporating the solvent with N_2 gas. For DNA-PL_4 HDL NPs, the core scaffolds were prepared as a solution in TAMg buffer (40 mM Tris, 20 mM acetic acid, and 7.5 mM $MgCl_2$; pH = 7.4) due to the improved water solubility of the core imparted by the oligonucleotides.

To initiate particle assembly, the non-scaffold nanoparticle components were then added sequentially to the core scaffolds. In a typical assembly, DPPC (20 nmol from a 1 mM suspension in PBS) was combined with the lipid conjugate core scaffold (either PL_4 or DNA-PL_4, 2 nmol from a thin film (PL_4) or a 1 mM suspension in PBS (DNA-PL_4)), followed by the addition of apoA-I (4 nmol from an 1 mg/mL suspension in PBS). This combined suspension was then diluted in PBS to a final core concentration of 10 µM in PBS. Next, the resulting suspension was subjected to three rounds of alternating bath sonication (90 s ON, 30 s OFF) and vortexing, and allowed to relax on ice for 30 min. The particles were then filtered away from the supernatant and concentrated using spin columns (MilliPore; 0.5 mL 50 kDa MWCO). The column was first rinsed in PBS for 10 min at 10,000 *g* at 4°C, prior to three rounds of spin filtration of the particles under the same conditions. An aliquot of PBS (500 µL) was added to the column after each spin. After each round of filtration, the particles were centrifuged by desktop centrifugation to remove aggregates, if any. After the final round of filtration, the small volume of concentrated particles (~ 20 µL) was diluted to 100-200 µL in PBS and the protein concentration was determined by bicinchoninic acid assay (BCA), with spectroscopic measurement of absorbance at 562 nm after incubation with BCA reagents at 37 °C for 30 min. The particles were then either used immediately or placed at 4 °C for short-term storage. For all downstream assays, the concentration of LC HDL NPs was determined by BCA quantification of protein; and protein concentration was held constant across all groups. The core concentration of DNA-PL_4 was determined directly using UV-vis spectroscopy and Beer's Law, upon knowing the molar extinction coefficient of the DNA. After the protein concentration was determined via BCA, a ratio of core to protein could then be determined.

Preparation of controls for TEM

Control samples were prepared to investigate the LC HDL NPs assembly process, and its dependence on the lipid conjugated core scaffold and apoA-I. Core scaffold + lipids without apoA-I controls were prepared by first making DPPC liposomes as described above (Section S2c). DPPC liposomes were then added to core scaffolds at the same concentration and molar ratio as in LC HDL NPs, with PL_4 scaffolds thin filmed and DNA-PL_4 scaffolds in aqueous buffer. The mixtures were then subjected to three rounds of alternating sonication and vortexing, and were filtered and concentrated through 50 kDa MWCO spin columns as above. apoA-I and

DPPC alone controls were assembled in an identical manner, in the absence of core scaffolds. Core scaffold alone controls were subjected to the same sonication and filtering process, without addition of DPPC or apoA-I.

Synthesis of Au HDL NPs.

Au HDL NPs were synthesized and purified as previously reported by the Thaxton group.[26] In the indicated reference, the synthesis and purification protocol can be found in the Materials and Methods section entitled "Synthesis of fmHDL". We note that the Au HDL NPs terminology used in the current work refers to the fmHDLs assembled using ordinary apoA-I, not "apoA-I-SH", which was also being investigated therein.

HDL_2 and HDL_3 isolation from human serum

HDL_2 and HDL_3 were isolated from human universal donor serum. The serum was obtained from the Matthews Center for Cellular Therapy at Northwestern University. A density gradient isolation procedure was used to obtain HDL_2 and HDL_3. First, the serum density was adjusted by adding potassium bromide (KBr) to the density of LDL (1.063 g/mL) using the following formula: g KBr = $((V_i(D_f-D_i))/(1-(\tilde{V} \text{ x } D_f))$, where V_i is the initial volume of the plasma (mL), D_f is the final density (g/mL), $D_i$is the initial density (g/mL), and $\tilde{V}$ is the partial specific volume of KBr (0.298 mg/mL for LDL). Phenylmethylsulfonyl fluoride (PMSF) was added to the serum at a final concentration of 10 µM followed by the addition of KBr. This step was performed on ice. The mixture was constantly stirred to solubilize the KBr. Once KBr was solubilized, 12.5 mL of adjusted-density serum was added to ultracentrifuge tubes with 37.5 mL of KBr (d 1.063 g/mL) layered on top. Tubes were centrifuged in a Beckman Coulter ultracentrifuge (rotor: Ti45) at 4 °C at 41,500 *x g* for 22 hours. After centrifugation the LDL layer (top layer) was removed. Next, we isolated HDL_2 from the LDL-free sample. The density of the LDL-free serum fraction was adjusted to the density of HDL_2(1.125 g/mL) with KBr using the above formula ($\tilde{V}$ = 0.314 mg/mL for HDL_2) and centrifuged as above. The top layer containing HDL_2 was collected. Finally, HDL_3 was isolated from the serum volume remaining after removal of LDL and HDL_2. The density of the HDL_2-free serum fraction was adjusted to the density of HDL_3(1.23 g/mL) with KBr using the above formula ($\tilde{V}$ = 0.318 mg/mL for HDL_3) and centrifuged as above. The top layer containing HDL_3 was collected. Each of the HDL_2 and HDL_3 fractions were dialyzed using 10K cut-off Slide-A-Lyser (TheremoFisher #66830) against 4 L of PBS + 1 mM EDTA at 4 °C overnight. Dialyzed HDL_2 and HDL_3 were then run on a Superdex 200 16/60 size-exclusion chromatography column (GE #28989335). Fractions were collected in 1.7 mL volumes. Fractions that contained either HDL_2 or HDL_3 as determined by SDS-PAGE gel and Coomassie staining were pooled and the concentration determined by BCA assay. The quantified HDLs were frozen in liquid nitrogen and stored at -80 °C.

Transmission electron microscopy (TEM)

For grid preparation, samples were prepared at a concentration of 500nM-2 µM protein in PBS, dropcast on UV-treated carbon-coated copper 300-mesh grids (Electron Microscopy Services) and air dried in a chemical fume hood. The grids were washed twice with PBS, stained twice with 2% uranyl acetate for 20 sec, then washed three times with PBS and air dried prior to imaging. Imaging was conducted using a FEI Tecnai Spirit TEM operating at 80 kV.

Dynamic light scattering (DLS)

DLS and zeta potential measurements were carried out on a Zetasizer Nano ZS (Malvern Instruments, Malvern, UK) equipped with a He-Ne laser (633 nm). Non-invasive backscatter method (detection at 173° scattering angle) was used. Correlation data were fitted, using the method of cumulants, to the logarithm of the correlation function, yielding the diffusion coefficient (D). The hydrodynamic diameters (D_H) of the particles were calculated using D and the Stokes-Einstein equation ($D_H = k_BT/3\pi\eta D$, where k_B is the Boltzmann constant, T is the absolute temperature, and η is the solvent viscosity ($\eta = 0.8872$ cP for water)). The polydispersity index (PDI)—represented as $2c/b^2$, where b and c are first- and second-order coefficients, respectively, in a polynomial of a semi-log correlation function—was calculated by cumulants analysis. Size distribution of particles was obtained by non-negative least squares (NNLS) analysis.[163] Samples were prepared in distilled water or PBS, typically at 10-100 nM particle concentration. For each sample, three measurements were acquired with ten runs per measurement.

Size exclusion chromatography (SEC).

SEC analysis was performed on PSS Suprema column 7.6*250 mm using Agilent 1260 HPLC system equipped with UV detector and connected to Wyatt Heleos II MALS and RI detectors. Flow rate was 1 ml/min with PBS as a mobile phase.

Circular dichroism

Circular dichroism was carried out using a JASCO J-815 CD spectrometer. All samples were diluted to 75 µg/mL protein in distilled water. Spectra were derived from three accumulations of a single sample. Secondary structure data was acquired using CDPro software package running the CONTIN analysis algorithm. Three distinct analyses were performed using different soluble protein reference sets. The values reported in Table 1 reflect the mean ± SEM results of these three analyses.

The CD spectra of the DNA-PL_4 conjugates alone exclusively exhibit circular dichroism peaks at ~ 260 nm, which is typical of nucleic acids, with no signal in the low-UV regions where alpha helicity, beta sheet, or turn content is observed for apoA-I-containing particles.

Composition characterization: protein quantification

To quantify protein content of nanoparticles and native HDL, we used a commercially available bicinchoninic acid (BCA) assay (Thermo Fisher) per the manufacturer's instructions. Briefly, we generated a protein standard curve by diluting bovine serum albumin (BSA) samples from 0.125-2 mg/mL into a final volume of 80 µl per well in 96-well plates using BCA reagent solution. Nanoparticle samples were diluted in the same manner; standards and samples were diluted by a factor of 40. Standards were plated in duplicate and samples were plated in triplicate. Plates were incubated for 30 min at 37°C and then absorbance at 562 nm was measured using a Synergy plate reader.

Composition characterization: phospholipid quantification

Phospholipid content of nanoparticles and native HDL was quantified using a colorimetric Phospholipid Assay Kit (Sigma-Aldrich) per the manufacturer's instructions. Briefly, a phospholipid standard calibration curve was prepared with a 15-200 µM range via serial dilution. Samples were serially diluted in PBS to obtain one or more dilutions within the range of the standard curve.[1] Samples and standards were then incubated with the enzyme reaction mixture for 30 min at rt and then absorbance at 572 nm was determined using a Synergy plate reader.

Composition characterization: cholesterol, cholesteryl ester, and core quantifications

---

[1] As an example calculation, an initial stock solution that contains 20 nmol of DPPC in a volume of 100 µL has a DPPC concentration of 200 µM. After particle synthesis and filtration, dilution and some DPPC loss occurred, reducing the final DPPC concentrations to the 100-200 µM range, which falls nicely in the range detected by the assay kit (range = 3-200 µM).

Cholesterol and cholesteryl ester concentrations were determined using an Amplex Red Cholesterol Assay (ThermoFisher) per the manufacturer's instructions. Briefly, cholesterol standard curves were prepared in kit-provided aqueous buffer (1× Reaction Buffer) from 8 µg/mL to 125 ng/mL. Two sets of samples were prepared in triplicate and diluted into 1× Reaction Buffer. Two reaction mixtures were then prepared containing hydrogen peroxide, resorufin, and the enzymes horseradish peroxidase, cholesterol oxidase, with or without cholesterol esterase to enable quantification of both free cholesterol and cholesteryl esters. One set of samples was then incubated with reaction mixture containing cholesterol esterase, and the other set was incubated with reaction mixture without cholesterol esterase. Microplates were then incubated at 37 °C for 1 h or until fluorescent signal began to decline. The core concentration of DNA-PL_4 HDL NPs was determined by measuring absorbance at 260 nm via UV-Vis spectroscopy. For composition data, the PL_4 core concentration was estimated using the experimentally determined core:protein molar ratio obtained for DNA-PL_4 particles. Composition of Au HDL NPs was reported from previously published work.[26]

Oligomerization assay

The cross-linking agent bis[sulfosuccinidimidyl]suberate (BS3) (Sigma Aldrich) was used to stabilize any higher order oligomerization states of apoA-I in LC HDL NPs upon assembly, prior to detection via immunoblot. The method used here was adapted from a previously reported protocol [26]. LC HDL NPs were prepared as described above and diluted to 50 µg/mL protein in PBS. BS3 cross-linking agent was then added to LC HDL NPs for a final BS3 concentration of 2.5 mM, and the reaction was allowed to proceed for 30 min at room temperature. To produce an apoA-I oligomer ladder, lipid-free pure apoA-I (MyBioSource) was dialyzed in PBS, and then subjected to cross-linking with BS3 (0.25 mM) at elevated protein concentration (500 µg/mL) for 4 h at room temperature. 0.5 M Tris base was used to stop the cross-linking reactions (45 mM final).

BioRad apparatuses were used for gel electrophoresis and protein transfer. Pre-cast 4-20% polyacrylamide gels (MiniProtean TGX, BioRad) were used for separation. Protein transfer to polyvinylidine fluoride (PVDF) membrane was performed using Tris-Glycine buffer with 20 vol % methanol. PVDF membrane was then rinsed in TBS and blocked in 5 wt % nonfat dry milk for 1 h at rt. Primary antibody (rabbit anti-apoAI, Abcam) was added to the membrane at 1:1000 dilution in 5 wt % nonfat dry milk, and incubated at 4 °C overnight. The membrane was then washed in TBS-Tween (0.1%) three times for 10 min each. Secondary antibody (goat anti-rabbit HRP, BioRad) was then added at 1:2000 dilution in 5 wt % nonfat dry milk. The membrane was then washed three times in TBS-Tween for ten minutes each, and then bathed in electrochemiluminescence substrate solution for 1 min, and exposed to autoradiography film for 10-90 sec for optimal exposure duration and developed (Figure S12).

Chapter 3: Soft-core high-density lipoprotein mimics efficiently transport cholesterol and reduce atherosclerotic burden

3.1 Objectives and Significance

HDL mimicking nanoparticles have been tested extensively for their efficacy as anti-atherosclerotic agents (see Section 1.1.4). However, the vast majority of these synthetic HDLs have resembled immature, discoidal HDL, not mature spherical HDL. Having demonstrated that we could synthesize genuine, soft-core mimics of spherical HDL (PL_4 and DNA-PL_4 HDL NPs) that strongly resemble native HDL in their size, composition, surface chemistry, and protein secondary structure, we then sought to determine whether these constructs could function similarly to native HDLs *in vitro* and ultimately whether they could reduce atherosclerotic burden *in vivo*. We first find that LC HDL NPs execute salient HDL functions *in vitro*. Specifically, LC HDL NPs efflux cholesterol from macrophages, deliver cholesterol to hepatocytes, support the enzymatic esterification of cholesterol via lecithin:cholesterol acyltransferase, and suppress inflammation. We then find that systemic injections of LC HDL NPs drastically reduce atherosclerotic burden in LDL-$R^{-/-}$ mice by ~65-75%. These results indicate that LC HDL NPs represent a promising therapeutic agent for atherosclerosis.

3.2 Background and Motivation

Synthetic mimics of HDL have been explored for their efficacy as anti-atherosclerotic agents for the past two decades. The vast majority of synthetic HDLs reported to date, such as rHDLs, have resembled immature, discoidal HDL. This circumstance can largely be attributed to the canonical view that immature, discoidal HDLs are responsible for the majority of RCT activity, and that RCT is the most significant mechanism responsible for ASCVD risk reduction.[164] However, there remains ongoing debate regarding the relative contributions of discoidal and spherical HDLs to anti-atherosclerotic effects, and hence a question about which subspecies are ideal synthetic targets for potential therapies. Clinical trials investigating the anti-ASCVD efficacy of discoidal rHDLs have thus far failed to demonstrate the desired results.[89-90, 147] Moreover, there is also evidence that larger, spherical HDL species are specifically associated with reduced risk of ASCVD.[165-166] This correlative data, in combination with emerging evidence regarding HDL metabolism,[20] has led some investigators to propose an alternative model[19] that suggests spherical HDLs play a primary role in atheroprotection (see section 1.1.2). To this end, we sought to investigate the efficacy of our recently reported class of novel spherical HDL mimics as anti-ASCVD agents.

3.3. Results and Discussion.

Complementary biological assays were performed to investigate whether LC HDL NPs could recapitulate salient HDL functions *in vitro*. A critical property for HDL mimicry is the ability to efflux cholesterol from lipid-laden macrophages. Efflux efficiency of LC HDL NPs was determined using an *in vitro* radiolabeled cholesterol efflux assay.[37] Briefly, J774 macrophages were loaded with tritium-labeled cholesterol ($[^3H]$-chol), cultured with cAMP to upregulate cholesterol-efflux receptors, and then treated with nanoparticles or controls for 4 h. The media supernatant was subjected to liquid scintillation counting to quantify percent effluxed $[^3H]$-chol. Results showed that both PL_4 HDL NPs and DNA-PL_4 HDL NPs facilitated robust cholesterol efflux (PL_4: 6.2 ± 0.7%, DNA-PL_4: 6.5 ± 0.2%; 100 nM protein) in a dose-dependent fashion (Figure 3.1a).

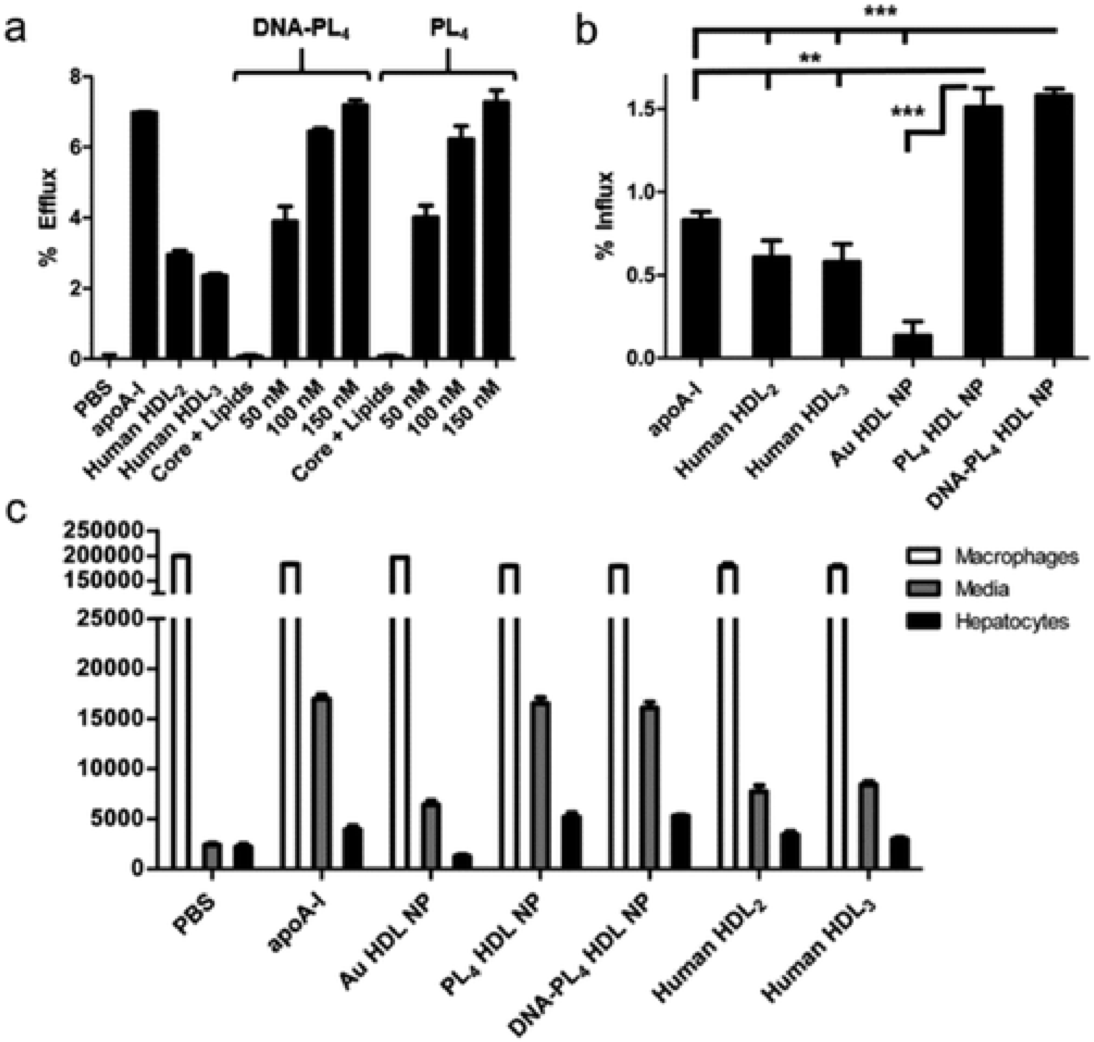

Figure 3.1: LC HDL NPs efflux and deliver radiolabeled cholesterol *in vitro*
(a) LC HDL NPs efflux [^{3}H]-chol from J774 macrophages. (b) % Influx of [^{3}H]-chol to HepG2 hepatocytes in a tandem efflux-influx assay. (c) Quantification of [^{3}H]-chol in all fractions from tandem assay. Two-tailed Student's *t* test: $^{**}p < 0.01$. $^{***}p < 0.001$.

Encouraged by these results, we then designed an experiment to simulate the entire RCT process in a single assay. We accomplished this by carrying out the standard radiolabel efflux assay followed by an influx step where the conditioned efflux media was removed from the original J774 culture wells and introduced to cultured hepatocytes (HepG2). Influx of [^{3}H]-chol was then allowed to proceed for an additional 4 h. Liquid scintillation counting analyses of all three fractions from macrophages, hepatocytes, and media supernatant then revealed that LC

HDL NPs exhibited superior cholesterol transport capacity compared to human HDLs, apoA-1, and Au HDL NP (Figure 3.1b, c). This assay demonstrates not only that LC HDL NPs are capable of robust cholesterol efflux and delivery, but that a single particle cohort can execute these functions sequentially by on- and off-loading cholesterol in a dynamic fashion.

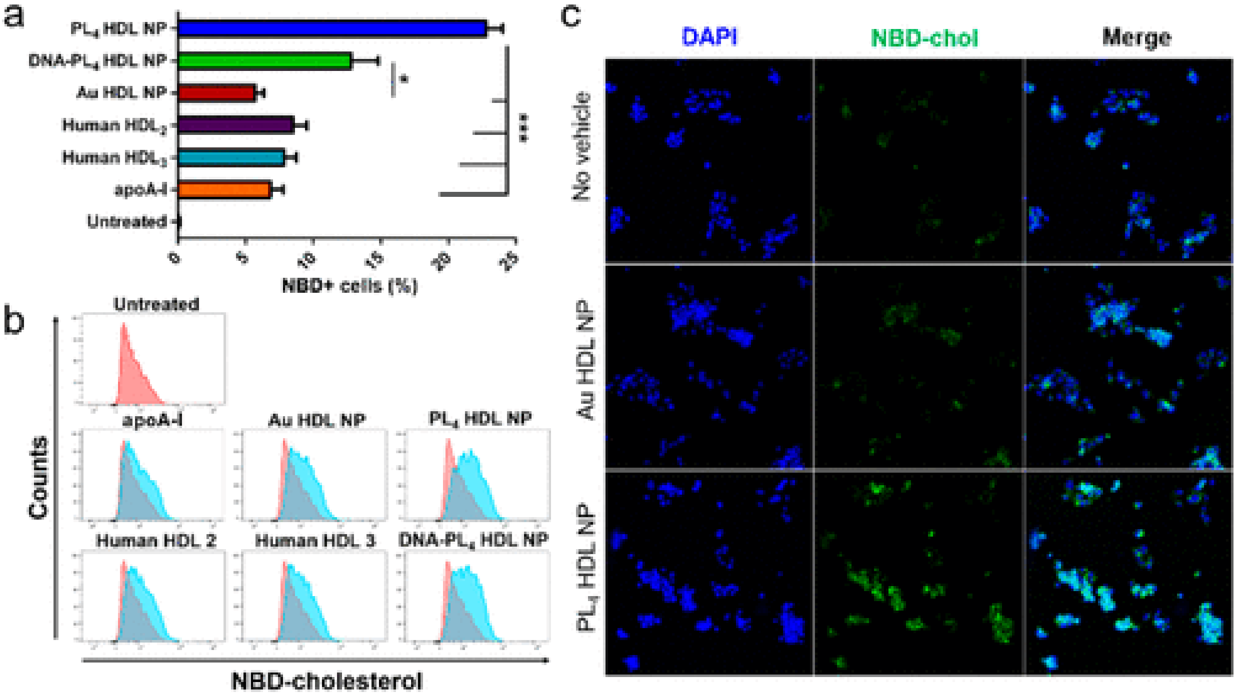

Figure 3.2: LC HDL NPs facilitate delivery of NBD-chol to hepatocytes in 30 min

(a,b) Flow cytometry of HepG2 cells after treatment with NBD-chol and LC HDL NPs, Au HDL NPs, human HDLs, or controls. (c) Confocal microscopy of HepG2 cells of select groups treated with NBD-chol. Two-tailed Student's *t* test: $^{*}p < 0.05$. $^{***}p < 0.001$.

We next investigated the efficacy of LC HDL NPs as cholesterol delivery agents independently of efflux, a function carried out in the native setting by mature HDLs. HepG2 cells were co-treated with fluorescent cholesterol (NBD-chol) and LC HDL NPs or controls, and subsequently processed for flow cytometry or confocal microscopy. Results showed that LC HDL NPs facilitated efficient delivery of NBD-chol in only 30 min (Figure 3.2), with 23% of

PL_4 HDL NP-treated cells being NBD-positive compared to 8.5%, 6.8%, and 5.7% for HDL_2, apoA-1, and Au HDL NP respectively.

Native HDLs also support the enzymatic esterification of free cholesterol, a reaction carried out in the blood by the enzyme lecithin:cholesterol acyltransferase (LCAT). We found that both PL_4 and DNA-PL_4 HDL NPs were able to support LCAT-mediated esterification (Figure 3.3a). However, PL_4 HDL NPs exhibited a substantially greater capacity for esterification over DNA-PL_4 HDL NPs and Au HDL NPs, converting 87% of bound cholesterol to cholesteryl esters. We hypothesize that this can be attributed to the increased hydrophobicity of the PL_4 core over Au and DNA-PL_4 cores, which enables efficient stabilization and sequestration of cholesteryl esters.

Inflammation promoted by macrophage NF-κB activity is a hallmark of ASCVD that drives disease progression and increases morbidity and mortality. We treated human monocyte NF-κB-reporter cells (THP1-Dual) with lipopolysaccharide to stimulate NF-κB activity prior to treatment with LC HDL NPs or controls. While apoA-1 alone exhibited no capacity to reduce NF-κB activity under these low-dosing conditions, both PL_4 HDL NPs and DNA-PL_4 HDL NPs reduced NF-κB activity in a dose dependent manner, by 31% and 16% respectively at concentrations of 150 nM (Figure 3.3b).

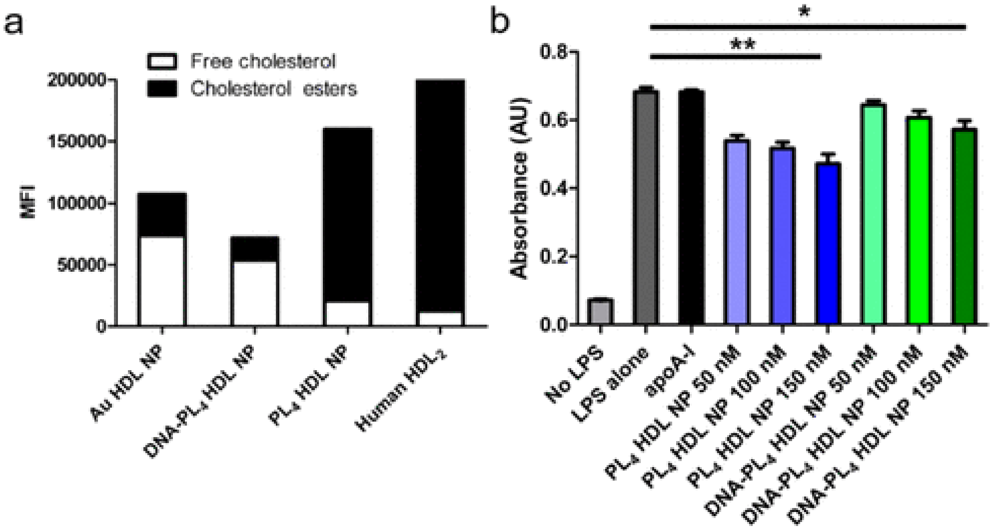

Figure 3.3: LC HDL NPs support enzymatic esterification of cholesterol and suppress inflammation

(a) LC HDL NPs support LCAT-mediated cholesterol esterification. (b) LC HDL NPs suppress pro-inflammatory NF-κB signaling. Two-tailed Student's *t* test: *$p < 0.05$. ** $p < 0.01$.

Having determined that LC HDL NPs efficiently transport cholesterol and reduce inflammation *in vitro*, we then proceeded to investigate whether LC HDL NPs exhibited efficacy as anti-ASCVD agents *in vivo*. For *in vivo* testing, we used LDL-R$^{-/-}$ mice fed on a high fat diet (42% fat), a well-established model of atherosclerosis. LDL-R$^{-/-}$ mice were started on a high-fat diet at 3-6 weeks of age and were fed for 15 weeks before treatment to establish atherosclerotic plaque formation. Mice were then split into four treatment groups: 1) PBS control, 2) reconstituted, discoidal HDL (rHDL) (5 uM), 3) PL_4 HDL NP (5 uM), and 4) DNA-PL_4 HDL NP (5 uM). rHDL was purchased from Genway Biotech and consisted of apoA-1 and 1-palmitoyl-2-oleoyl phosphatidylcholine prepared at a 1 to 100 molar ratio using the cholate dialysis method. PL_4 and DNA-PL_4 HDL NPs were fabricated as previously described. Briefly, the core scaffolds of the particle were synthesized using copper-free click chemistry to generate small molecule-phospholipid conjugates with or without 9-mer DNA linkers. These core scaffolds were then used to facilitate nanoparticle self-assembly upon addition of apoA-1 and free phospholipids.

Mice were treated via tail vein every other day for 4 weeks for a total of 13 injections. Mice were then sacrificed and aortas were harvested for quantification of atherosclerotic plaque burden using Sudan IV staining.

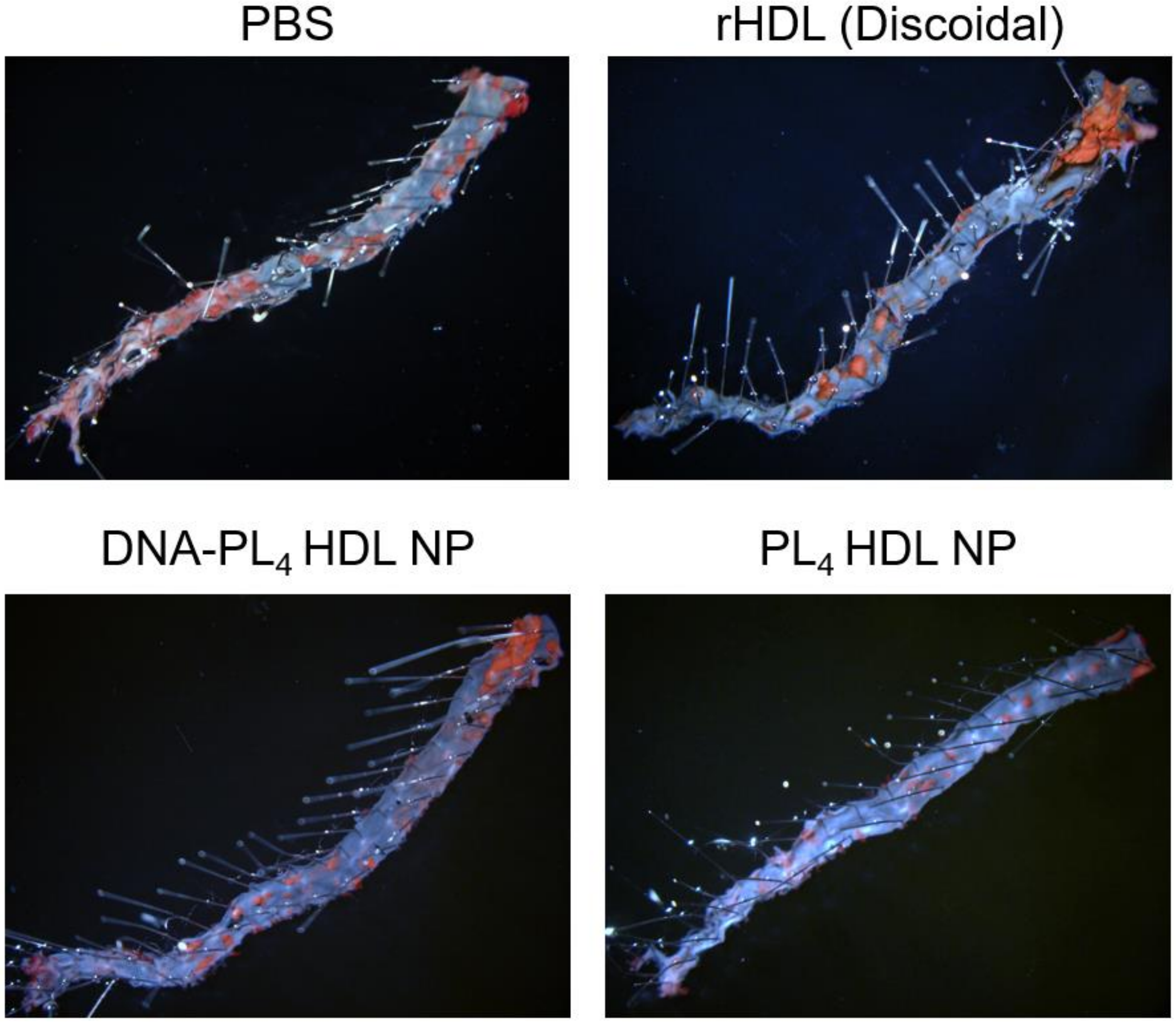

Figure 3.4: LC HDL NPs reverse atherosclerotic plaque formation in LDL-R$^{-/-}$ mice

Mice were injected three times per week for three weeks with saline control (PBS), reconstituted, discoidal HDL (rHDL), or organic core HDL NPs (DNA-PL$_4$ or PL$_4$). Images show mouse aortas stained with Sudan IV. Red regions represent atherosclerotic plaques.

Aortic plaque quantification results revealed that mice treated with PL_4 HDL NPs and DNA-PL_4 HDL NPs exhibited 71.9% and 64.6% less atherosclerotic plaque burden than PBS treated controls, respectively, while mice treated with rHDL exhibited only 29.5% reduced plaque burden (Figures 3.4 and 3.5). PL_4 and DNA-PL_4 HDL NPs also reduced the circulating white blood cell (WBC) counts of treated mice compared to PBS-treated controls (Figure 3.6), consistent with the particles' anti-inflammatory properties that have been previously published.[159]

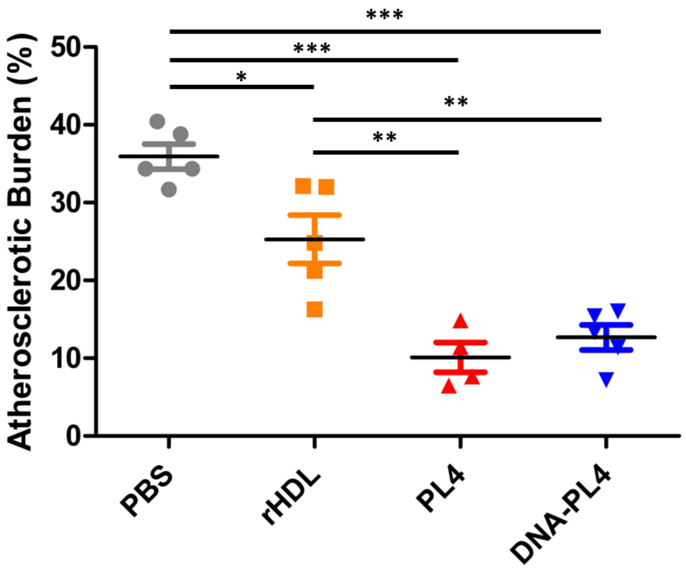

Treatment Group	% Athero
PBS	35.9%
rHDL (discoidal)	25.3%
PL_4 HDL NP	10.1%
DNA-PL_4 HDL NP	12.7%

Figure 3.5: Quantification of atherosclerotic burden in mice fed on a high fat diet treated with PBS control, rHDL, DNA-PL_4 HDL NPs, or PL_4 HDL NPs

Average % of the aorta covered by atherosclerotic plaques as determined by Sudan IV staining.

Serum lipid profiling revealed that mice treated with PL_4 HDL NPs and DNA-PL_4 HDL NPs exhibited elevated levels of circulating LDL cholesterol (Figure 3.7). Interpreting the lipid profiling results in parallel with the aortic plaque results, we hypothesize that the elevated levels of circulating LDL cholesterol are indicative of enhanced mobilization of cholesterol from the periphery. However, it remains unclear why this mobilized cholesterol would partition into the LDL fraction and not the HDL fraction. One possibility is that when LC HDL NPs have effluxed large quantities of cholesterol from the periphery, these particles can dynamically swell as they are loaded with cholesterol and cholesteryl esters, because large enough and hypodense enough to partition into the LDL fraction. An alternative hypothesis is that when LC HDL NPs mobilize cholesterol from the periphery, much of this cholesterol is temporarily transferred to the large number of circulating LDL particles that LDL-R$^{-/-}$ mice possess at baseline, prior to its eventual delivery for biliary excretion. Despite some uncertainty regarding the precise reason why these mice exhibit elevations in LDL cholesterol specifically, a sharp increase in serum cholesterol levels after infusion of synthetic HDLs is consistent with what has been observed clinically in human trials.[39] Overall, these results provide strong evidence that LC HDL NPs are outstanding candidates for anti-atherosclerosis therapy.

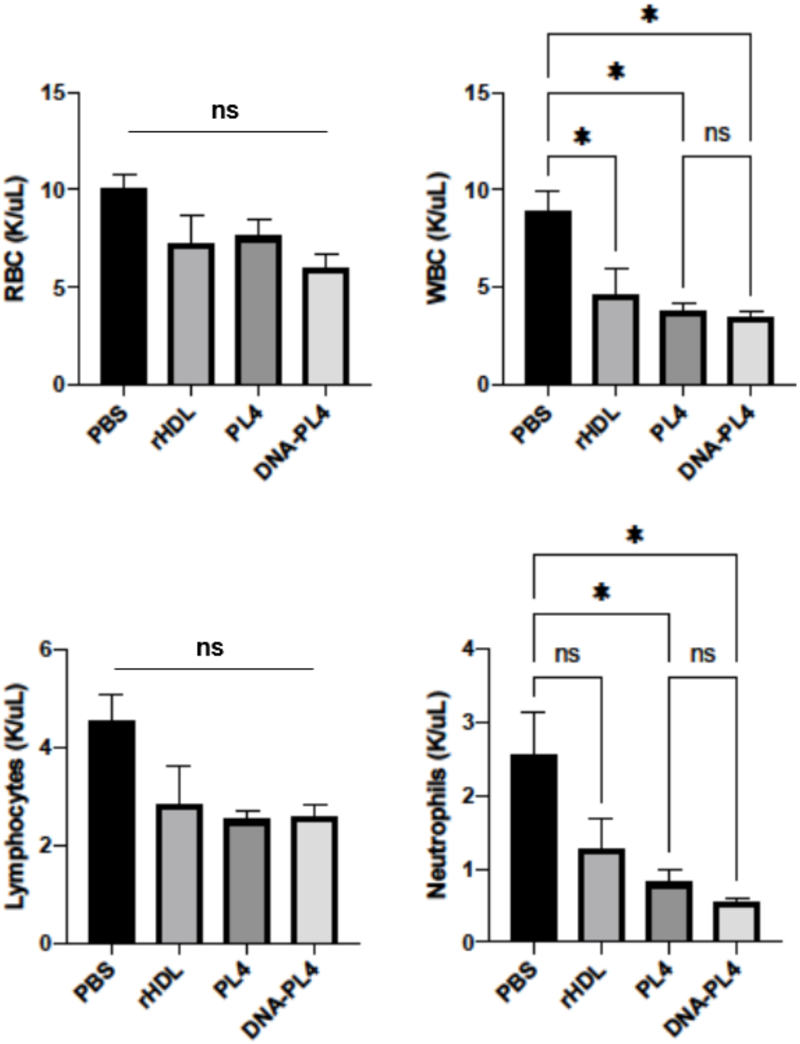

Figure 3.6: Complete blood count (CBC) results for LDL-R$^{-/-}$ mice fed on a high fat diet and treated with HDL NPs or controls.

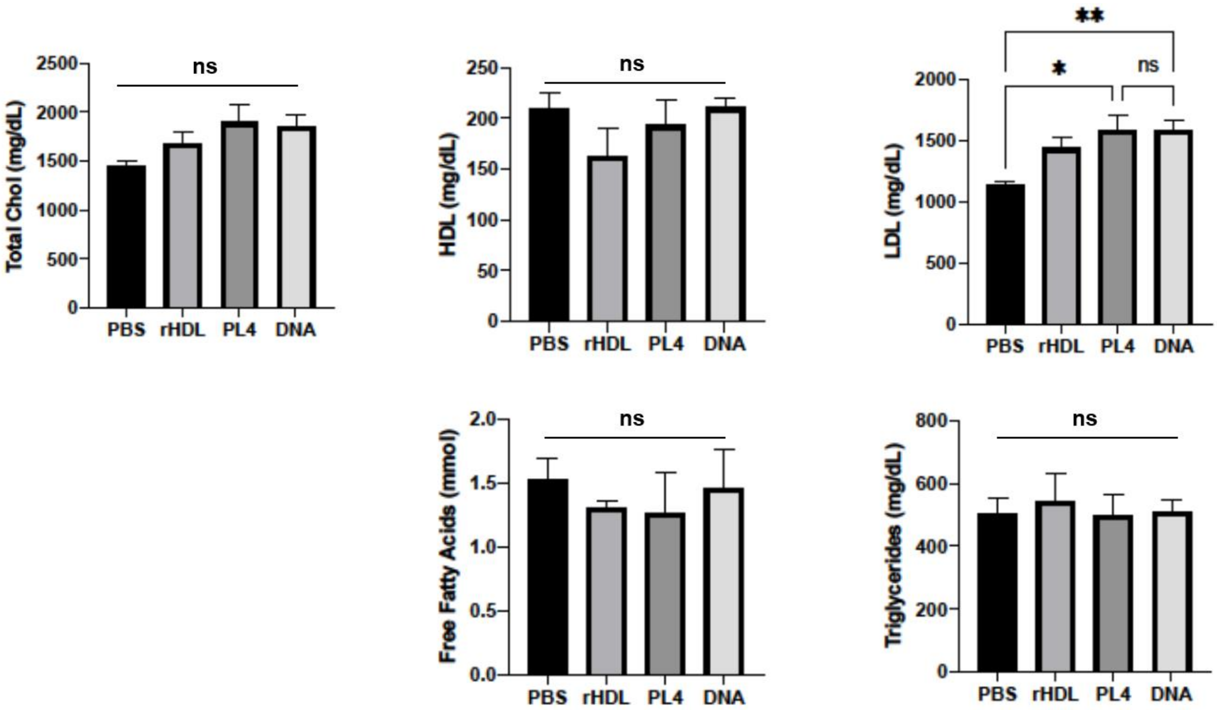

Figure 3.7: Lipid panel results for LDL-R$^{-/-}$ mice fed on a high fat diet and treated with HDL NPs or controls.

3.4 Conclusions

In summary, we determined that LC HDL NPs are efficient transporters of cholesterol *in vitro* and exhibit anti-ASCVD activity *in vivo*. Both PL_4 HDL NPs and DNA-PL_4 HDL NPs interface with macrophages and hepatocytes to remove and deliver cellular cholesterol respectively, closely mimicking the salient cholesterol transport functions of human HDLs. Moreover, LC HDL NPs supported LCAT-mediated esterification of cholesterol and reduced NF-κB-associated inflammation. *In vivo* anti-ASCVD efficacy studies of LC HDL NPs in LDL-R$^{-/-}$ mice demonstrated that LC HDL NPs reduced atherosclerotic plaque burden by 65-75%. Because synthesis of LC HDL NPs is straightforward and does not require time-intensive and costly enzymatic maturation steps, we anticipate these nanoparticles will be strong candidates for the next generation of HDL-based anti-ASCVD therapeutics.

3.5 Materials and Methods

Radiolabel Assays

For efflux experiments, we used the gold-standard assay in the field, efflux of tritium-labeled cholesterol ([^{3}H]-chol) from J774 macrophages. J774 macrophages were cultured for at least two passages prior to seeding at 150,000 cells per well in 24 well plates in RPMI, 10% fetal bovine serum (FBS), 1% penicillin-streptomycin (PenStrep) on Day 1. Ethanol stocks of [^{3}H]-chol were handled under sterile conditions. [^{3}H]-chol stocks were evaporated, redissolved in ethanol (1 mL) and incubated at 37 °C for 60 min. The solution was then evaporated again and redissolved in ethanol (50 µL) and incubated at 37 °C for 30 min. Heat-inactivated FBS (Corning, NY) (1.5 mL) was then added to the [^{3}H]-chol solution and the resulting mixture was incubated at 4 °C overnight.

On Day 2, serum-free RPMI with 1% PenStep and 2 µg/mL Sandoz (Sigma-Aldrich, St. Louis, MO) was added to the [^{3}H]-chol-containing FBS to yield a final labeling media comprising [^{3}H]-chol (2 µCi/mL), 5 vol % FBS in RPMI. Note that Sandoz is an ACAT inhibitor used to prevent esterification of [^{3}H]-chol. Media was aspirated from 24 well plates and 500 µL of [^{3}H]-chol labeling media was added (1 uCi per well). Labeling was allowed to proceed for 24 h.

On Day 3, labeling media was removed, cells were washed twice with MEM, 25 µM HEPES, and upregulation media (RPMI, 1% PenStrep, 300 µM cAMP, 2 µg/mL Sandoz, 1% BSA) was added to upregulate the canonical cholesterol efflux receptor ABCA1. (Note: for cAMP(-) efflux assays (Figure 4d), this media was added without cAMP in order to investigate SR-B1-dependent efflux.) Upregulation was allowed to proceed for 24 h prior to addition of efflux media. Efflux samples containing nanoparticles and controls were prepared in serum-free media (MEM, 25 µM HEPES, 1% PenStrep) to reduce non-specific [^{3}H]-chol efflux by serum cholesterol carriers. Cells were washed twice in MEM, 25 µM HEPES and efflux media was added to each well according to the treatment regimen. Efflux was allowed to proceed for 4 h. Efflux media was then removed, vacuum filtered, and added to 3 mL UltimaGold scintillation fluid for scintillation counting. A separate triplicate cohort of [^{3}H]-chol-loaded macrophages were washed, air dried, and incubated at room temperature in isopropanol to extract [^{3}H]-chol as a measure of total cholesterol at t = 0 at the beginning of efflux.

A PBS treated control cohort was used as a baseline, and the counts obtained for these samples were then subtracted from experimental groups to obtain baseline-corrected counts. Efflux percentages were then calculated as ratios of baseline-corrected counts for efflux media to counts for t = 0 macrophages, indicating the fraction of [^{3}H]-chol which was removed from cells over the course of 4 h treatment not due to diffusion alone. Protein concentration was held constant across all samples at 200 nM for all experiments with the exception of dose-dependence studies.

For tandem efflux-influx experiments, efflux from J774 cells was conducted identically as above (Section 7a). Hepatocytes (HepG2 cells) were plated at 100,000 cells/well in DMEM, 10% FBS, 1% PenStrep in 24 well plates on Day 3. On Day 4, immediately after 4 h of efflux, HepG2 cells were washed twice in serum-free MEM, 25 µM HEPES, and then efflux media from J774 macrophages was removed and added directly to HepG2 cells. Influx was allowed to proceed for 4 h prior to harvesting. Influx media supernatant was then collected and processed identically as efflux media described above. [^{3}H]-chol was then extracted from HepG2 cells and J774 cells by incubating in 500 µL isopropanol for 4 h at rt, sealed in Parafilm. [^{3}H]-chol-containing isopropanol was then collected, evaporated, and redissolved in xylene prior to addition to UltimaGold for scintillation counting.

NBD-cholesterol delivery experiments

For confocal microscopy experiments, HepG2 cells were cultured in Dulbecco's Modified Eagle's Medium (DMEM) containing 10% FBS and 1% PenStrep. One day prior to treatment, cells were plated at 100,000 cells/well in 24 well plates on top of glass coverslips. On the day of treatment, cells were washed three times with PBS and fresh media containing 5 µg/mL NBD-cholesterol was then added to each to each well with or without a delivery agent according to treatment regimen. Uptake was allowed to proceed for 30 min when the cells were fixed and prepared for confocal microscopy. Cells were fixed in 4% PFA for 10 min at rt. Cells were then washed three times in PBS, stained with DAPI (300 nM in PBS) for 5 min, and washed two more times in PBS. Coverslips were then mounted on glass slides, and allowed to seal at rt for at least 24 h prior to imaging. Confocal microscopy was performed using a Nikon A1R Spectral, and image processing was conducted with Nikon Elements and Fiji software.

For flow cytometry experiments, HepG2 cells were plated at 200,000 cells/well in 24-well plates one day prior to treatment. On the day of treatment, cells were washed three times with PBS and fresh media containing 5 µg/mL NBD-cholesterol was then added to each to each well with or without a delivery agent according to treatment regimen. Uptake was allowed to proceed for 30 min prior to harvesting. Cells were then trypsinized, neutralized in serum-containing media, and centrifuged at 300 x *g* for 6 min to pellet the cells. Cells were resuspended in PBS containing 2% bovine serum albumin (BSA) and then subjected to flow cytometry using a BD LSRFortessa cell analyzer (BD Biosciences). Analysis was performed using FlowJo software. Events were gated to exclude cellular debris and aggregates prior to quantification of NBD-chol positivity.

Lecithin cholesterol acyl transferase (LCAT) activity assays

LC HDL NPs and Au HDL NPs (250 nM) suspended in PBS were incubated with LCAT (10 nM) and free cholesterol (100 µg/mL) in PBS at 37 °C for 15 h in a ThermoMixer shaking at 300 rpm. Samples were then centrifuged three times at 10,000 g for 10 min through a 50 kDa spin column to remove excess unbound cholesterol. Samples were then diluted 100 times in 1× Reaction Buffer prior to quantification with Amplex Red Cholesterol Assay (Thermo Fisher). Amplex Red Cholesterol Assay was performed per manufacturer's instructions. Briefly, a cholesterol standard curve was prepared by serially diluting cholesterol in kit-provided aqueous buffer from 8 µg/mL to 125 ng/mL and adding 50 µl to a 96-well black-bottom microplate. 50 µl of sample were also added to each well of the microplate in triplicate. Two sets of Amplex Red reaction mix were prepared, with and without cholesterol esterase. 50 µl of Amplex Red reaction mix were then added to each well. Microplates were incubated at 37 °C for 1 h or until fluorescent signal began to decline.

NF-κB activity assays

For NF-κB activity experiments, THP1-Dual cells were used in conjunction with a QUANTI-Blue secreted embryonic alkaline phosphatase (SEAP) detection kit (Invivogen). THP1-Dual cells were cultured in suspension in RPMI with 10% FBS and passaged at least twice prior to use in experiments. THP1-Dual cells were plated at 100,000 cells per well in 96 well plates. Lipopolysaccharide (LPS) (5 ng/mL) was used to stimulate NF-κB activity. Experimental wells were treated with LPS 1 h prior to addition of nanoparticles or controls. Cells were then incubated with particles or controls for 24 h prior to detection. QUANTI-Blue solution was prepared by dissolving the contents of the packet in endotoxin-free water and incubating at 37 °C for 30 min. QUANTI-Blue solution (180 µL) was added to each well in 96-well plates. THP1-Dual cells supernatant (20 µL) was then added to QUANTI-Blue solution, and the plate was incubated at 37 °C for 2-4 h. SEAP levels were the quantified by detecting absorbance at 650 nm using a Synergy plate reader.

***In vivo* atherosclerosis model:**

LDL-R$^{-/-}$ mice were used as a model of atherosclerosis. LDL-R$^{-/-}$ mice were fed on a high fat diet (42% fat) for four months prior to treatment to establish atherosclerotic plaque formation. Mice were then split into four treatment groups: 1) PBS, 2) rHDL, 3) PL$_4$ HDL NPs, and 4) DNA-PL$_4$ HDL NPs. Mice were then subjected to tail vein injections of the indicated treatment every other day for three weeks for a total of 13 injections. Particle concentration used for all treatments was 5 µM. Injection volume was 100 µl. The day following the last injection, mice were sacrificed, perfused with 10 mL of ice cold PBS, and aortas were harvested and fixed in 10% neutral buffered formalin (NBF). Aortas were then flayed, pinned, and stained with Sudan IV and imaged with a light microscope. ImageJ was used to quantify the percent atherosclerotic plaque.

Chapter 4: Prostate cancer extracellular vesicles mediate intercellular communication with bone marrow cells and promote metastasis in a cholesterol-dependent manner

4.1 Objectives and Significance

Primary tumors can establish long-range communication with distant organs to transform them into fertile soil for circulating tumor cells to implant and proliferate, a process called pre-metastatic niche (PMN) formation. Tumor-derived extracellular vesicles (EV) are potent mediators of PMN formation due to their diverse complement of pro-malignant molecular cargo and their propensity to target specific cell types.[115, 130, 132, 167] While significant progress has been made to understand the mechanisms by which pro-metastatic EVs create tumor-favoring microenvironments at pre-metastatic organ sites, comparatively little attention has been paid to the factors intrinsic to recipient cells that may modify the extent to which pro-metastatic EV signaling is received and transduced. Here, we investigated the role of recipient cell cholesterol homeostasis in prostate cancer (PCa) EV-mediated signaling and metastasis. Using a bone metastatic model of enzalutamide-resistant PCa, we first characterized an axis of EV-mediated communication between PCa cells and bone marrow that is marked by *in vitro* and *in vivo* PCa EV uptake by bone marrow myeloid cells, activation of NF-κB signaling, enhanced osteoclast differentiation, and reduced myeloid thrombospondin-1 expression. We then employed a targeted, biomimetic approach to reduce myeloid cell cholesterol *in vitro* and *in vivo* prior to conditioning with PCa EVs. Reducing myeloid cell cholesterol prevented the uptake of PCa EVs by recipient myeloid cells, abolished NF-κB activity and osteoclast differentiation, stabilized thrombospondin-1 expression, and reduced metastatic burden by 77%. These results demonstrate that cholesterol homeostasis in bone marrow myeloid cells regulates pro-metastatic EV signaling and metastasis by acting as a gatekeeper for EV signal transduction.

4.2 Background and Motivation

Extracellular vesicles (EV) are particles released by cells that are delimited by a lipid bilayer and incapable of replication.[103] Sub-types of EVs include endosome-originating exosomes, plasma membrane-derived ectosomes or microvesicles, large oncosomes, apoptotic bodies, and others. Small EVs (sEV), on the order of 30-200 nm in diameter, are often released in abundance by neoplastic cells and have been shown to promote metastasis by communicating with cells at distant, pre-metastatic organ sites to create tumor-favoring microenvironments, a process called pre-metastatic niche (PMN) formation.[112, 115] This phenomenon has been found to occur in melanoma,[130] pancreatic cancer,[132] prostate cancer[133], and other tumor types. Comparatively little attention has been paid, however, to the factors intrinsic to recipient cells that may influence the ability of tumor-derived EVs to efficiently mediate PMN formation. Here, we investigate the role of recipient cell cholesterol homeostasis in regulating cancer EV-mediated signaling and metastasis in the setting of prostate cancer (PCa).

PMN formation requires long-range intercellular communication to be persistently mediated by soluble or membrane-bound factors that originate from the primary tumor.[115, 131, 168] After traversal of vascular and interstitial spaces, these factors eventually engage with the cholesterol-rich plasma membrane of recipient cells at pre-metastatic organ sites. The synaptic events of intercellular communication, such as ligand-receptor interactions or endocytosis, may then lead to successful transduction of a pro-metastatic signal, for instance by perturbing intracellular signaling and/or gene expression. These events are tightly controlled by the organization of the recipient cell's plasma membrane[169-170] which, in turn, is regulated by cholesterol. Cholesterol comprises approximately 40 mol% of mammalian plasma membrane lipids,[171] and alters membrane organization by influencing protein scaffolding,[172-174] lipid raft stability,[62, 136] and the cohesion and orientation of membrane phospholipids.[175] In addition, cholesterol is required for the structure of clathrin and caveolin-dependent membrane invaginations, and lipid raft-dependent signaling and endocytosis.[136, 176] Hence, cholesterol is well-poised to globally regulate the efficiency of intercellular communication in PMN formation and other settings. Moreover, our group and others have shown that perturbation of cell membrane cholesterol can inhibit uptake of EVs by recipient cells.[102, 138] We therefore hypothesized that cellular cholesterol burden at pre-metastatic sites may critically regulate the efficiency of cancer EV-mediated intercellular communication with target cells at these sites.

The bone marrow compartment is a dynamic repository for triglycerides, fatty acids, and cholesterol, and is particularly sensitive to serum lipid levels.[177-178] Hence, it represents an ideal tissue for probing lipid-dependent intercellular communication. Moreover, bone marrow-derived cells (BMDC) are frequently the targets of pro-metastatic signals originating from the primary tumor, making the bone marrow compartment a hotbed for pro-metastatic signaling and metastasis.[130-132, 179-180] Tumor-derived EVs frequently target BMDCs and have proven to be versatile and potent mediators of PMN formation via horizontal transfer of pro-metastatic biochemical signals.[115, 130, 132-133, 167, 181] Therefore, we investigated tumor-derived EVs as mediators of pro-metastatic signaling and identified bone marrow-resident myeloid cells as a potential target cell population. Finally, we focused on a uniformly lethal metastatic process, namely the development of bone metastases in PCa. Approximately 90% of men who succumb to PCa are found to have bone metastasis at autopsy.[182] Moreover, PCa bone metastases are heavily laden with cholesterol in comparison to healthy bone and metastases of other origins,[183] making PCa bone metastasis particularly attractive for a case study in cholesterol-dependent PMN formation.

4.3 Results and Discussion

We first characterized a previously unreported axis of intercellular communication between PCa cells and bone marrow myeloid cells. We selected enzalutamide resistant (EnzR) CWR-R1 cells as a source of EVs (EnzR EVs) and as a model of bone metastatic PCa. These cells exhibit two important characteristics of late stage PCa in humans: 1) resistance to anti-androgen therapy, and 2) a propensity to seed clinically relevant sites of PCa metastasis (e.g. lung, bone, and liver) when systemically injected into mice.[184] EVs from normal prostate epithelial cells (PNT2 EVs) were used as a control. EnzR and PNT2 EVs were characterized by multiple complementary techniques in accordance with the most recent guidelines for characterization of EVs.[103] The size and morphology of EnzR and PNT2 EVs were evaluated using transmission electron microscopy (TEM) and dynamic light scattering (DLS). TEM revealed vesicles exhibiting a cup-shaped morphology typical of sEVs (Figure 4.1a, b), while DLS demonstrated hydrodynamic diameters in the size regime of sEVs (EnzR: $D_H = 101.0 \pm 23.0$ nm, PNT2: $D_H = 83.56 \pm 31$ nm) (Figure 4.1d, e). Both EnzR and PNT2 EVs expressed EV proteins (CD63, CD9, and Flotillin-1), while they importantly lacked the *cis*-Golgi marker GM130 (Figure. 4.1f), indicating EV isolates of high purity. Moreover, we found that EnzR CWR-R1 cells produced approximately five-fold more EVs (EV protein per cell) than PNT2 cells (Figure 4.1c).

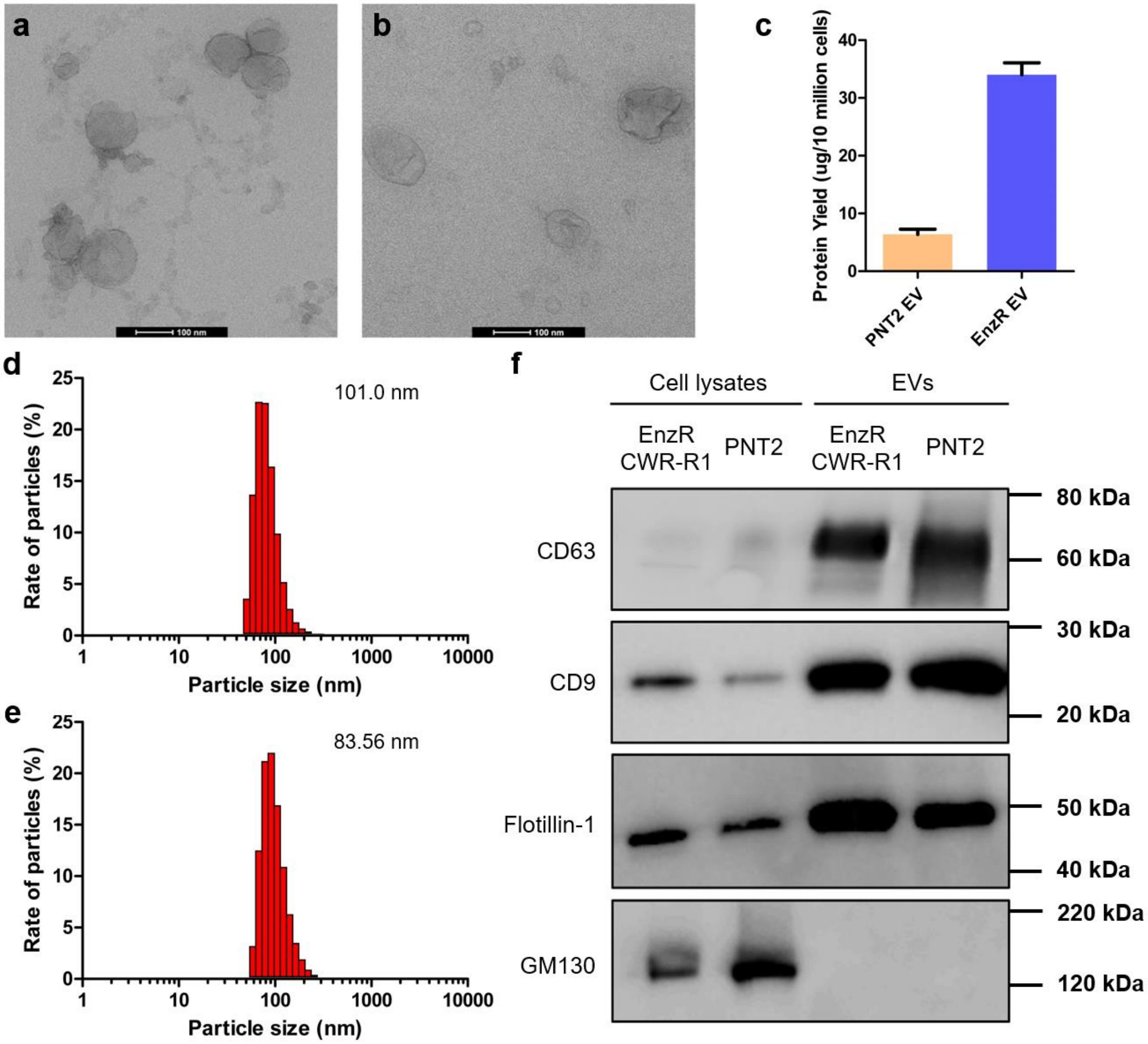

Figure 4.1: Characterization of EnzR and PNT2 EVs

Transmission electron microscopy imaging of a) EnzR EVs and b) PNT2 EVs. c) Quantification of EV production by enzalutamide resistant CWR-R1 cells (EnzR) and normal prostate epithelial cells (PNT2). Size distribution profiles of d) EnzR EVs and e) PNT2 EVs measured by dynamic light scattering. f) Western blots of EnzR and PNT2 EVs and cell lysates for EV-enriched proteins (CD63, CD9, and Flotillin-1) and the non-EV, *cis*-Golgi protein GM130.

The site where circulating tumor cells initially seed the bone, whether in the appendicular or axial skeleton, is the highly vascular bone marrow compartment.[185-187] Therefore, we first investigated whether EnzR EVs were efficiently taken up by bone marrow cells *in vitro* and *in vivo*. We found that fluorescently labeled (DiI) EnzR EVs were robustly uptaken by primary cultures of mouse bone marrow macrophages (BMMs) (Figure 4.3a) and by mouse bone marrow-resident cells *in vivo* (Figure 4.2a, b) as determined by immunocytochemistry and flow cytometry, respectively. Notably, EnzR EVs were taken up by bone marrow cells *in vivo* to a greater extent than PNT2 EVs by approximately five-fold (Figure 4.2b) (mean frequency of EV$^+$ cells: PNT2 = 0.031%, EnzR = 0.14%).

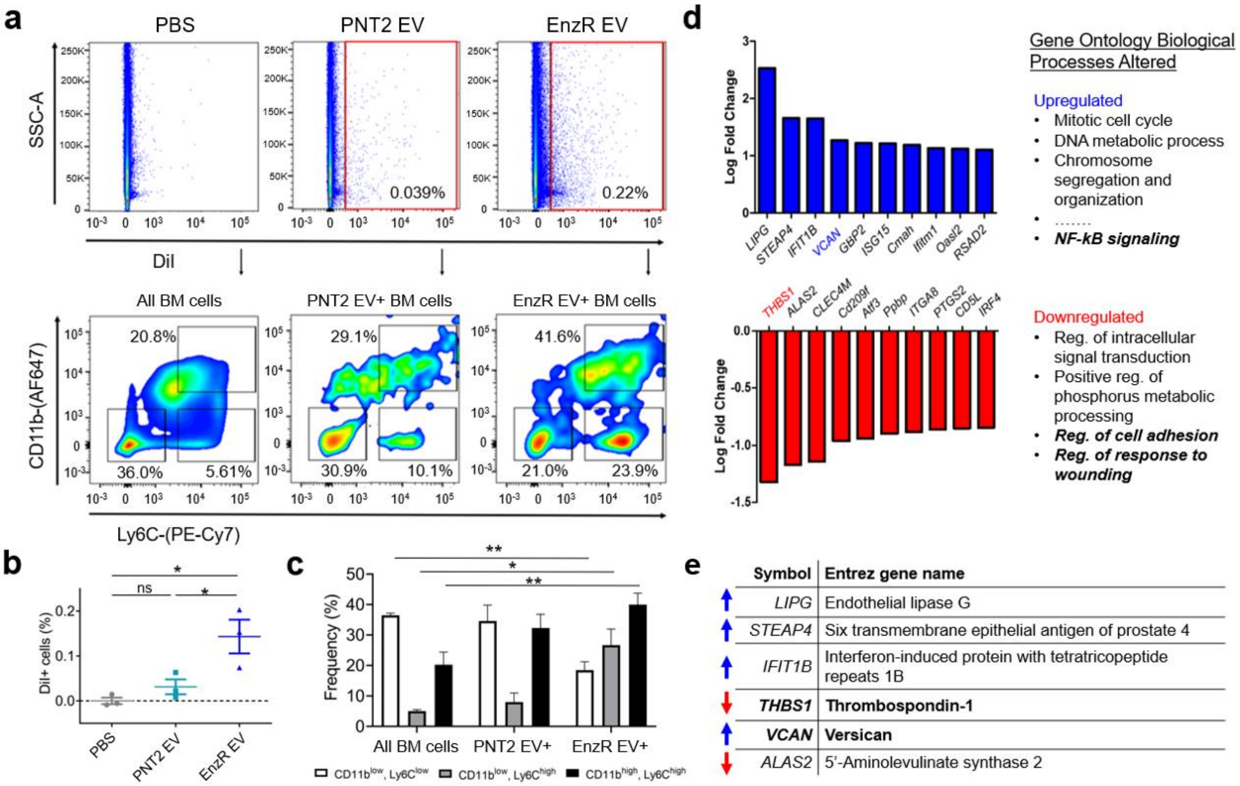

	Symbol	Entrez gene name
↑	*LIPG*	Endothelial lipase G
↑	*STEAP4*	Six transmembrane epithelial antigen of prostate 4
↑	*IFIT1B*	Interferon-induced protein with tetratricopeptide repeats 1B
↓	***THBS1***	**Thrombospondin-1**
↑	***VCAN***	**Versican**
↓	*ALAS2*	5'-Aminolevulinate synthase 2

Figure 4.2: EnzR EVs are uptaken by bone marrow-resident myeloid cells *in vivo* and induce alterations in gene expression

a) *In vivo* uptake of DiI-labeled EnzR and PNT2 EVs in mouse bone marrow (top panel). Bottom panel displays the distribution of CD11b and Ly6C expressing cells. b) Quantification of *in vivo* uptake of EnzR and PNT2 EVs in mouse bone marrow. c) Distribution of CD11b and Ly6C expressing sub-populations in EV-targeted cells vs. PBS-treated control total bone marrow. d) Alterations in gene expression of CD11b$^+$ bone marrow cells harvested from mice conditioned with EnzR EVs, determined by RNA sequencing ($n = 3$ per group), in relation to PBS treated control. e) Entrez gene names for the genes with the greatest log2 fold changes in response to conditioning with EnzR EVs. One-way ANOVA with Tukey's method, two-sided was used to determine significance. *$P < 0.05$, **$P < 0.01$. Data are mean ± s.e.m.

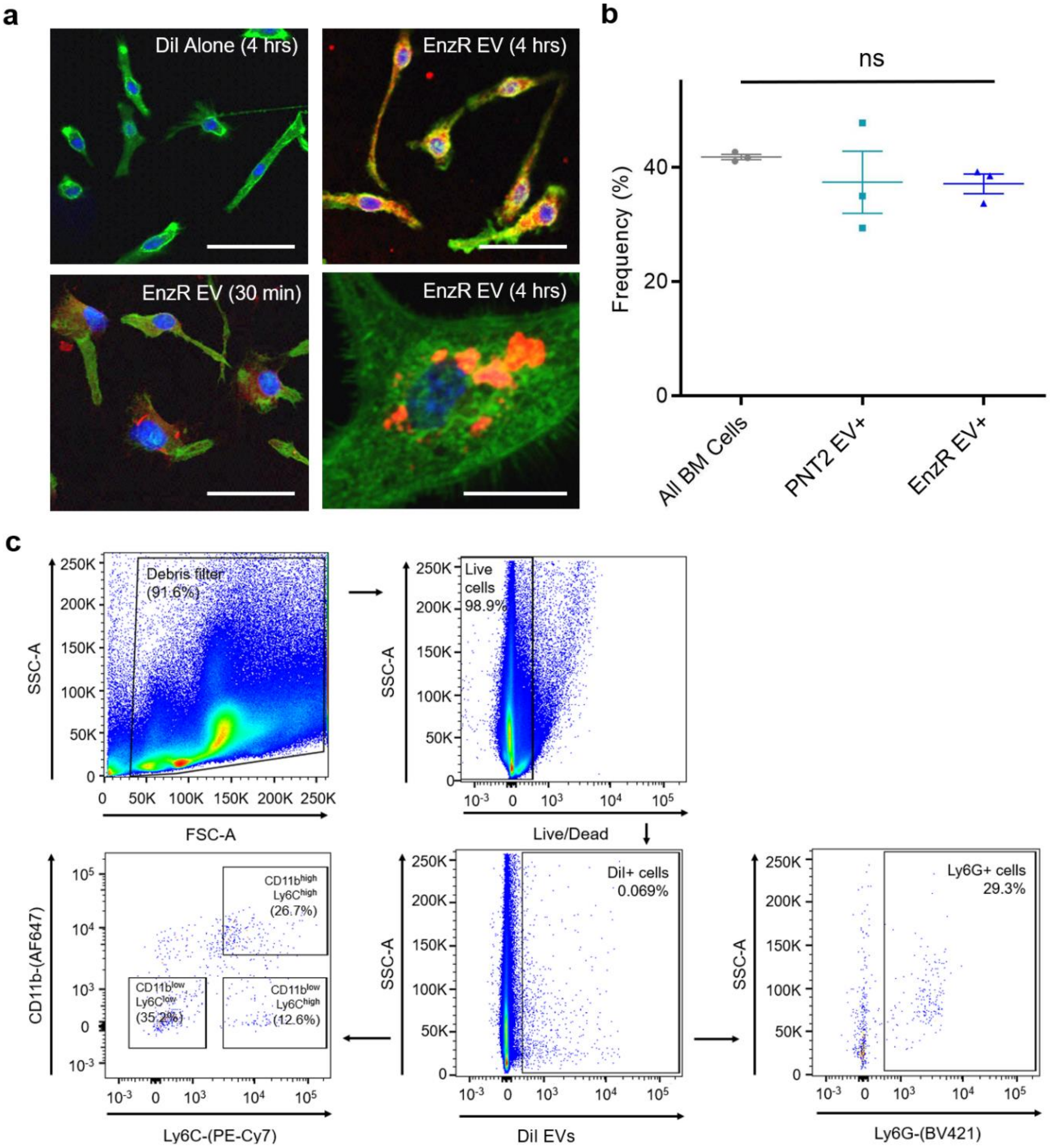

Figure 4.3: EnzR EVs are uptaken by primary cultures of mouse BMMs *in vitro* and do not exhibit preferential targeting of granulocytes in mouse bone marrow *in vivo*

a) Immunocytochemistry of primary mouse BMM cultures treated with DiI-labeled EnzR EVs (red). Far right panel is under high magnification (100X). Green: Phalloidin. Blue: DAPI. Scale bars are 50 µm (top left, top right, and bottom left panels) and 20 µm (bottom right panel). b) Quantification of the frequency of Ly6G$^+$ cells in total bone marrow vs. EnzR and PNT2 EV-targeted cells. c) Sample gating scheme for EV targeting experiments in mouse bone marrow. One-way analysis of variants (ANOVA) with Tukey's method, two-sided was used to determine statistical significance. NS, non-significant. Data are mean ± s.e.m.

Next, we defined the target cell populations of EnzR EVs in the bone marrow compartment with greater specificity. The population of EV-targeted cells was interrogated for myeloid, monocytic, and granulocytic markers (CD11b, Ly6C, Ly6G, respectively). We found that the EnzR EV-positive cell population was enriched in CD11b^{high}, Ly6C^{high} cells (monocytes) (40.0%) compared to the baseline frequency in total bone marrow (20.3%) (Figure 4.2a, c). By contrast, there was no difference in the frequency of Ly6G expressing cells (Figure 4.3b) between EnzR EV-targeted cells and total bone marrow cells, indicating preferential communication of EnzR EVs with monocytic over granulocytic BMDCs. Interestingly, the population of cells targeted by EnzR EVs was enriched in both CD11b^{low}, Ly6C^{high} and CD11b^{high}, Ly6C^{high} cells (Figure 4.2c). Both of these cell types have been recognized as osteoclast precursor populations,[188-189] which led us to further investigate the impact of EnzR EVs on osteoclast differentiation as a feature of PMN formation later in the study.

Next, we performed RNA sequencing of target bone marrow myeloid cells (CD11b^{+}) to identify alterations in gene expression induced by EnzR EVs. To do this, we simulated PMN formation *in vivo* according to precedent literature[130, 132, 135] by subjecting mice to three rounds of systemic injections of EnzR EVs, a process we define as “conditioning”. The most significantly upregulated and downregulated genes by EnzR EV conditioning are displayed in Figure 4.2d. Two of the altered genes were of particular interest with respect to PMN formation: thrombospondin-1 (TSP1; *THBS1*) was the most significantly downregulated gene, while the chondroitin sulfate proteoglycan, versican (VCAN), was significantly upregulated. Interestingly, TSP1 and VCAN have each been reported to play significant roles at the lung PMN; and in both cases, myeloid cells were responsible for aberrant TSP1 or VCAN expression.[190-191] To our knowledge, neither of these alterations has been reported at the bone PMN, or in PCa bone metastases. Using Gene Ontology clustering analysis, we observed that the most upregulated biological processes were related to cell division and proliferation (Figure 4.2d), while NF-κB activity was also upregulated. Activation of NF-κB signaling was later confirmed using an *in vitro* reporter system (Figure 4.4b). Among the most significantly downregulated processes were regulation of cell adhesion and response to wounding, both of which are relevant to PMN formation.

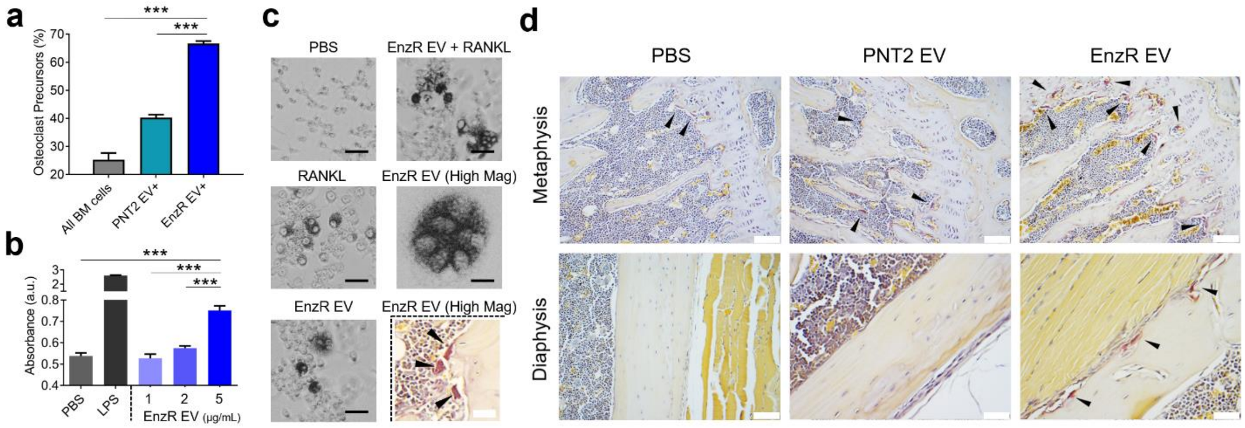

Figure 4.4: EnzR EVs stimulate NF-κB signaling and promote osteoclast differentiation

a) Quantification of the frequency of EV-targeted cells in mouse bone marrow that are potential osteoclast precursors (CD11b^{high}, Ly6C^{high} or CD11b^{low}, Ly6C^{high}) (*n* = 3 per group). Osteoclast precursor % reflects the percent of DiI positive bone marrow cells (EV treated) or total (PBS treated) bone marrow cells that were osteoclast precursors. b) NF-κB activity assay using THP1-Dual monocytes treated with varying concentrations of EnzR EVs (*n* = 4 per group). Absorbance reflects secreted alkaline phosphatase (SEAP) activity which is indicative of NF-κB activation. c) *In vitro* osteoclast differentiation assay using RAW264.7 osteoclast precursor cells. TRAP+ (dark staining), multinucleated cells are osteoclasts. Scale bars are 50 μm. d) TRAP staining of hind limb bones. Arrowheads indicate osteoclasts (TRAP+ multi-nucleated cells, inside or outside lacunae). Scale bars are 200 μm. One-way ANOVA with Tukey's method, two-sided was used to determine significance. ***$P < 0.001$. Data are mean ± s.e.m.

Because EnzR EVs targeted osteoclast precursor populations *in vivo* (Figure 4.2c, Figure 4.4a), we hypothesized that EnzR EVs may promote osteoclast differentiation as a feature of bone PMN formation. In the setting of bone metastasis, increased osteoclast and osteoblast activity is favorable for tumor cells due to the constitutive release of nutrients and growth factors caused by rapid bone formation and resorption.[192-194] Elevated osteoclast activity in particular is associated with increased burden of bone metastases in PCa.[195-198] Moreover, an inhibitor of the osteoclast activating protein, receptor activator of NF- κB ligand (RANKL), delayed the development of bone metastasis among patients with high risk PCa.[199] To test the impact of EnzR EVs on osteoclast activity, we first used a well-established *in vitro* model system (RAW264.7 cells) for osteoclast differentiation.[200] We found that EnzR EVs promoted osteoclast differentiation *in vitro* with and without the addition of RANKL (Figure 4.4c). Confirming these findings *in vivo*, we observed that osteoclasts were more abundant in the hind limbs of mice conditioned with EnzR EVs compared to vehicle (PBS) control, while PNT2 EVs had no impact on osteoclast differentiation (Figure 4.4d) (Figure 4.5a). We also found that EnzR EVs stimulated NF-κB activity (a critical intracellular signaling pathway for osteoclast differentiation) in human monocytes in a dose-dependent manner (Figure 4.4b). We hypothesized that EnzR EVs may express RANK ligand (RANKL) as a means to stimulate osteoclast differentiation, however Western blot revealed no RANKL expression in EnzR EVs, in contrast with positive control PC3 EVs (Figure 4.5b).

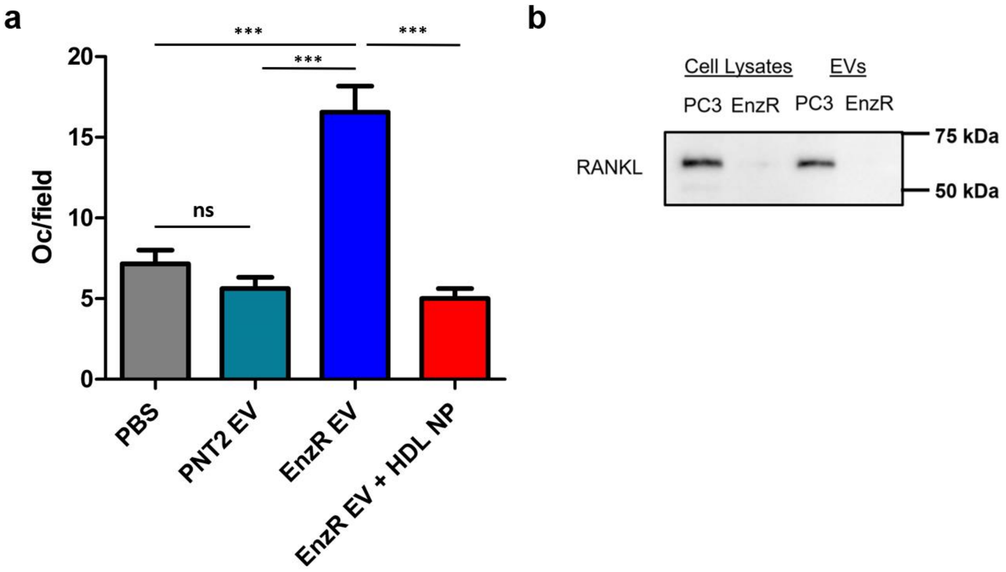

Figure 4.5: EnzR EVs promote osteoclast differentiation *in vivo* in a cholesterol-dependent manner, and do not express RANKL

a) Quantification of *in vivo* osteoclast differentiation assay. Mouse hind limb tissue sections were stained with TRAP to identify and quantify osteoclasts (Oc) (TRAP+, multinucleated cells). b) Immunoblot of EnzR EVs and PC3 EVs (positive control) for RANKL. One-way analysis of variants (ANOVA) with Tukey's method, two-sided was used to determine statistical significance. NS, non-significant. *** $P < 0.001$. Data are mean ± s.e.m.

Recent evidence suggests that EV-mediated intercellular communication may be influenced by cholesterol homeostasis in recipient cells. For instance, treating target cells with the non-specific cholesterol sequestrant, methyl-β-cyclodextrin (MβCD), can reduce EV uptake by disrupting lipid rafts at the cell surface.[138] As a result, we hypothesized that PCa EV-mediated signaling with bone marrow cells may be inhibited or abolished by reducing cholesterol in the target bone marrow cells. To thoroughly investigate this hypothesis *in vivo*, we required an agent that reduces cellular cholesterol in a manner similar to MβCD, while also being compatible with systemic delivery in animal models. In mammals, cholesterol transport is mediated by endogenous lipoproteins that circulate in the bloodstream. The lipoprotein sub-species that is primarily responsible for reducing cellular cholesterol *in vivo* is high-density lipoprotein

(HDL).[15] Therefore, we employed a nanoparticle mimic of native HDL (HDL NP) (Figure 4.6a) which we have previously characterized for *in vitro* inhibition of EV uptake,[102] but which is also compatible with systemic delivery *in vivo*. HDL NPs inhibit EV uptake in a manner similar to MβCD by reducing cellular cholesterol and disrupting lipid raft stability.[102] Importantly, HDL NPs specifically target cells expressing the high-affinity receptor for HDL, scavenger receptor B-1 (SR-B1) (Figure 4.6b), including myeloid-derived cells,[201] and have demonstrated no significant toxicities when used in animal models.[14, 48, 202] Therefore, we investigated the cholesterol dependence of EnzR EV-mediated intercellular communication with myeloid cells using HDL NPs. The HDL NP synthesis scheme is depicted in Figure 4.6a.

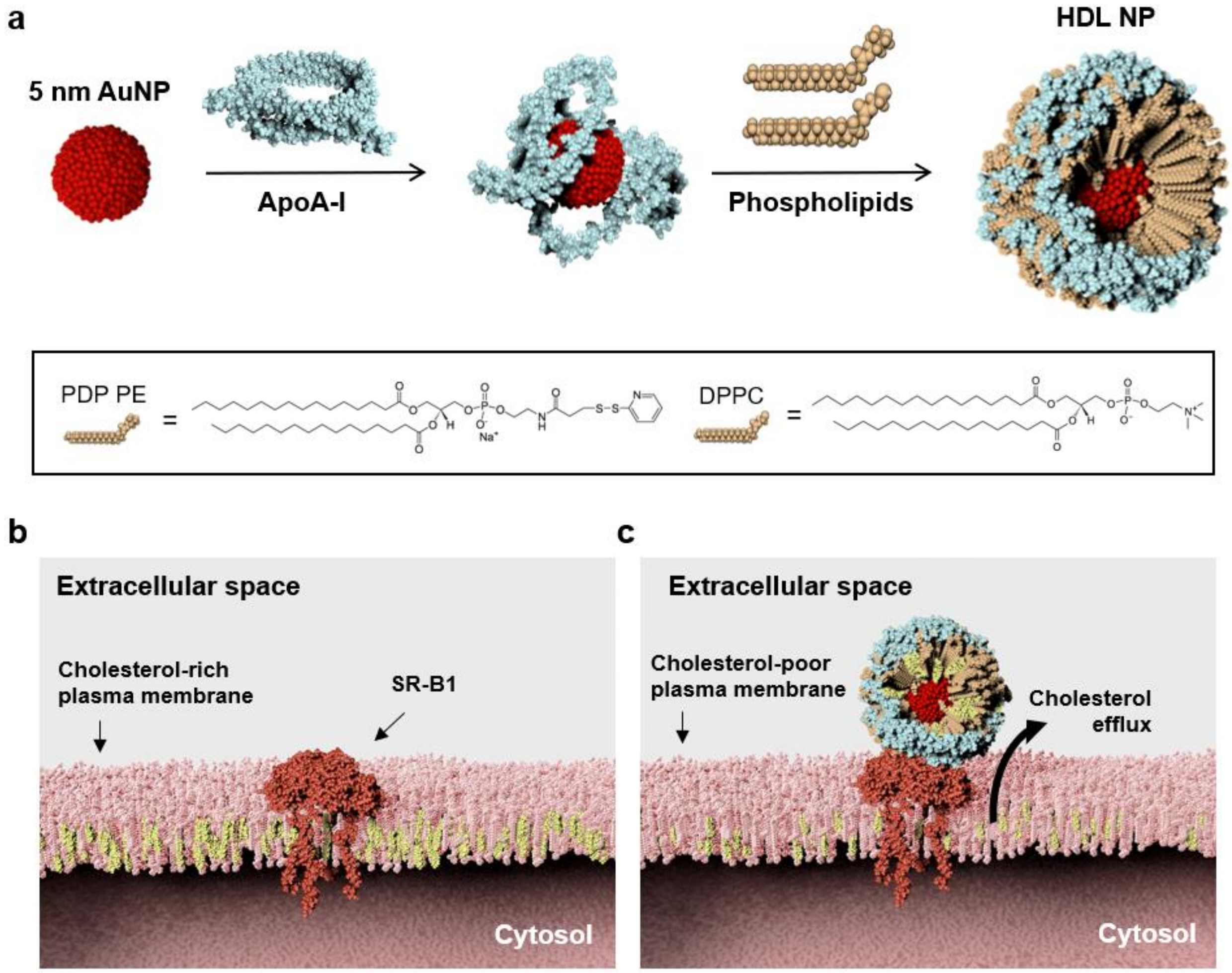

Figure 4.6: HDL NP synthesis scheme and mechanism of cholesterol reduction.

a) Synthesis of HDL NPs is accomplished using a 5 nm diameter gold nanoparticle (AuNP) as a core scaffold. Purified apolipoproteinA-1 (apoA-1) is added to the AuNP core scaffold to confer the cell-specific targeting properties and cholesterol efflux capabilities of native HDL. Finally, two species of phospholipids-- 1,2-dipalmitoyl-*sn*-glycero-3-phosphoethanolamine-*N*-[3-(2-pyridyldithio) propionate] (PDP PE) and 1,2-dipalmitoyl-*sn*-glycero-3-phosphocholine (DPPC) -- are added to stabilize the resulting particle structure and to achieve HDL-mimicking surface chemistry. b) Illustration of the cholesterol-rich plasma membrane of target bone marrow myeloid cells, with the endogenous HDL receptor, SR-B1, displayed at the cell surface. c) Illustration of HDL NPs binding to SR-B1 on the surface of bone marrow myeloid cells and reducing cellular cholesterol via cholesterol efflux. Cholesterol transit from the cell membrane onto the surface of HDL particles occurs via hydrophobic channels embedded in the SR-B1 receptor.[203]

We first confirmed that mouse bone marrow myeloid cells expressed SR-B1 and would therefore be susceptible to HDL NP-mediated reduction of cellular cholesterol (Figure 4.7a). Next, we demonstrated that HDL NP treatment reduced cellular cholesterol in myeloid-derived cells using human monocytes in an *in vitro* radiolabel assay (Figure 4.7b). We then confirmed that HDL NPs reduced myeloid cellular cholesterol *in vivo* by treating mice with HDL NPs prior to harvesting bone marrow cells and quantifying cellular cholesterol. Systemically injected HDL NPs entered the bone marrow compartment and reduced cellular cholesterol in the total bone marrow cell population (Figure 4.7c, d). Importantly, we observed a pronounced reduction of cellular cholesterol in bone marrow monocytes specifically (Figure 4.7e), the dominant target cell population of EnzR EVs.

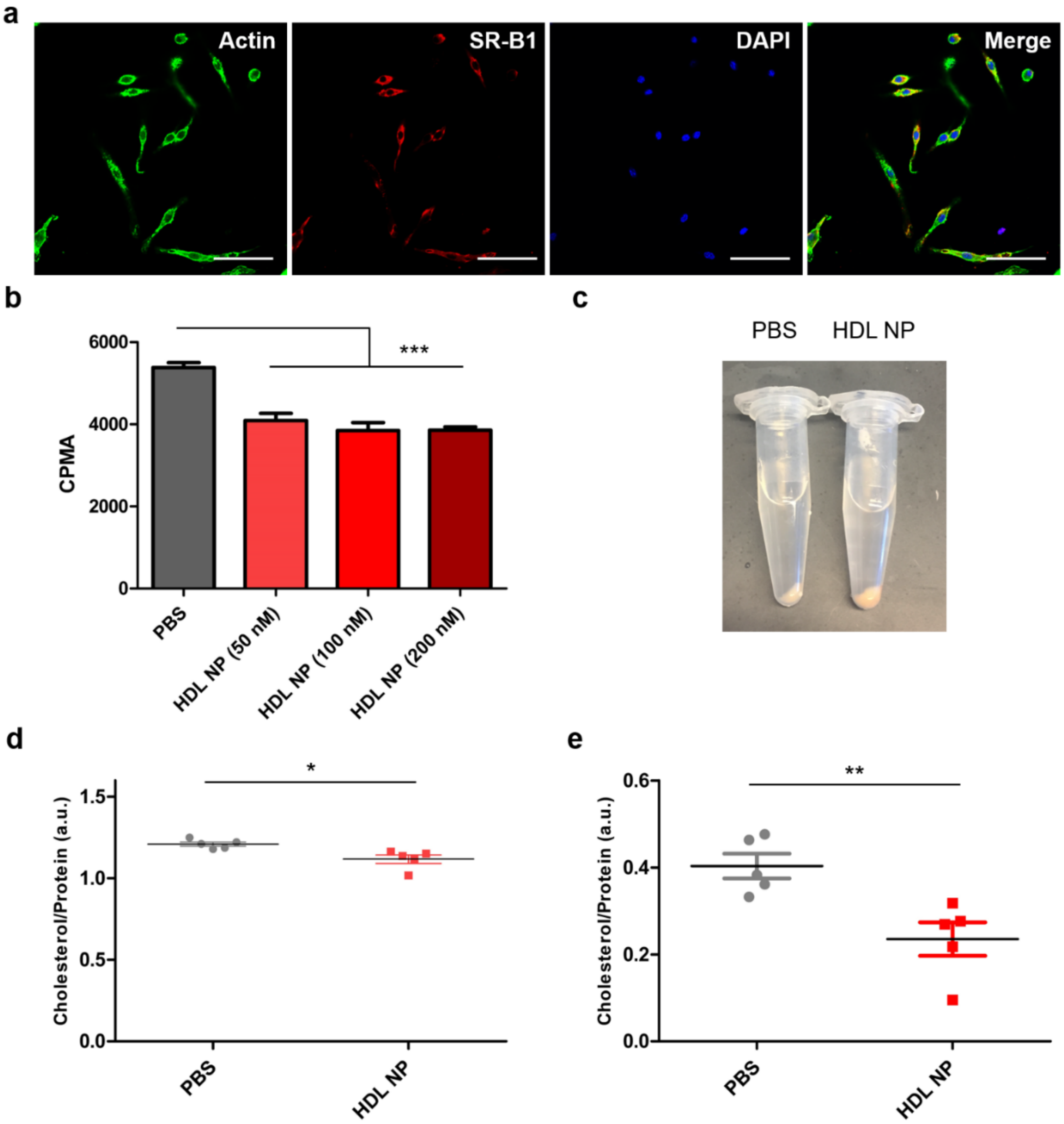

Figure 4.7: Bone marrow myeloid cells express SR-B1 and are susceptible to HDL NP-mediated reduction of cellular cholesterol *in vitro* and *in vivo*

a) Immunocytochemistry of primary mouse BMM cultures to detect expression of the native HDL receptor (and target receptor of HDL NPs), SR-B1. Scale bar = 50 µm. b) Cellular cholesterol measurements of THP1 monocytes after treatment with HDL NPs or PBS in a radiolabel assay. c) Bone marrow cell pellets harvested from mice after systemic injection of HDL NPs (100 µl, 1 µM) or PBS. Yellow/red discoloration is imparted by the gold nanoparticle core. d) Quantification of cellular cholesterol in total bone marrow cells after systemic injection with HDL NPs or PBS. e) Quantification of cellular cholesterol in bone marrow monocytes (EasySep Isolation Kit) after systemic injection with HDL NPs or PBS. One-way ANOVA with Tukey's method, two-sided (b) and two-sided Welch's *t*-test (d,e) were used to determine significance. *$P < 0.05$, **$P < 0.01$, ***$P < 0.001$. Data are mean ± s.e.m.

We then investigated whether HDL NP treatment inhibited EnzR EV-mediated intercellular communication with myeloid cells *in vitro* and *in vivo*. We first found that HDL NPs inhibited EnzR EV uptake by BMMs in a time and dose-dependent fashion (Figure 4.8a-d). Next, we observed that systemic administration of HDL NPs reduced the uptake of EnzR EVs by bone marrow-resident cells *in vivo* via flow cytometry (Figure 4.8e). Importantly, to demonstrate target specificity, we found that HDL NP treatment had no impact on EnzR EV uptake in BMM cultures from SR-B1$^{-/-}$ mice (Figure 4.9), indicating that HDL NP-mediated inhibition requires SR-B1. To determine whether the cholesterol dependence of PCa EV uptake in BMMs was restricted to EVs derived from EnzR CWR-R1 cells, *in vitro* uptake experiments were repeated using PCa EVs derived from DU145, PC3, LNCaP, EnzR LNCaP, and CWR-R1 (non-resistant) cells. HDL NPs were found to significantly inhibit the uptake of each of these PCa EV populations in BMMs (Figure 4.10), strongly suggesting that the cholesterol dependence of PCa EV communication with bone marrow-resident cells is a general phenomenon.

Next, we determined the impact of HDL NPs on EnzR EV function. We found that HDL NPs inhibited EnzR EV-mediated NF-κB signaling (Figure 4.8f) and abolished EnzR EV-induced osteoclast differentiation *in vitro* and *in vivo* (Figure 4.8g) (Figure 4.5). Importantly, we also found that HDL NP pre-treatment prevented EnzR EV-mediated reduction of TSP1 gene expression in bone marrow myeloid cells *in vivo* (Figure 4.11a). Interestingly, HDL NP pre-treatment did not impact the increased expression of VCAN caused by EnzR EVs (Figure 4.11b).

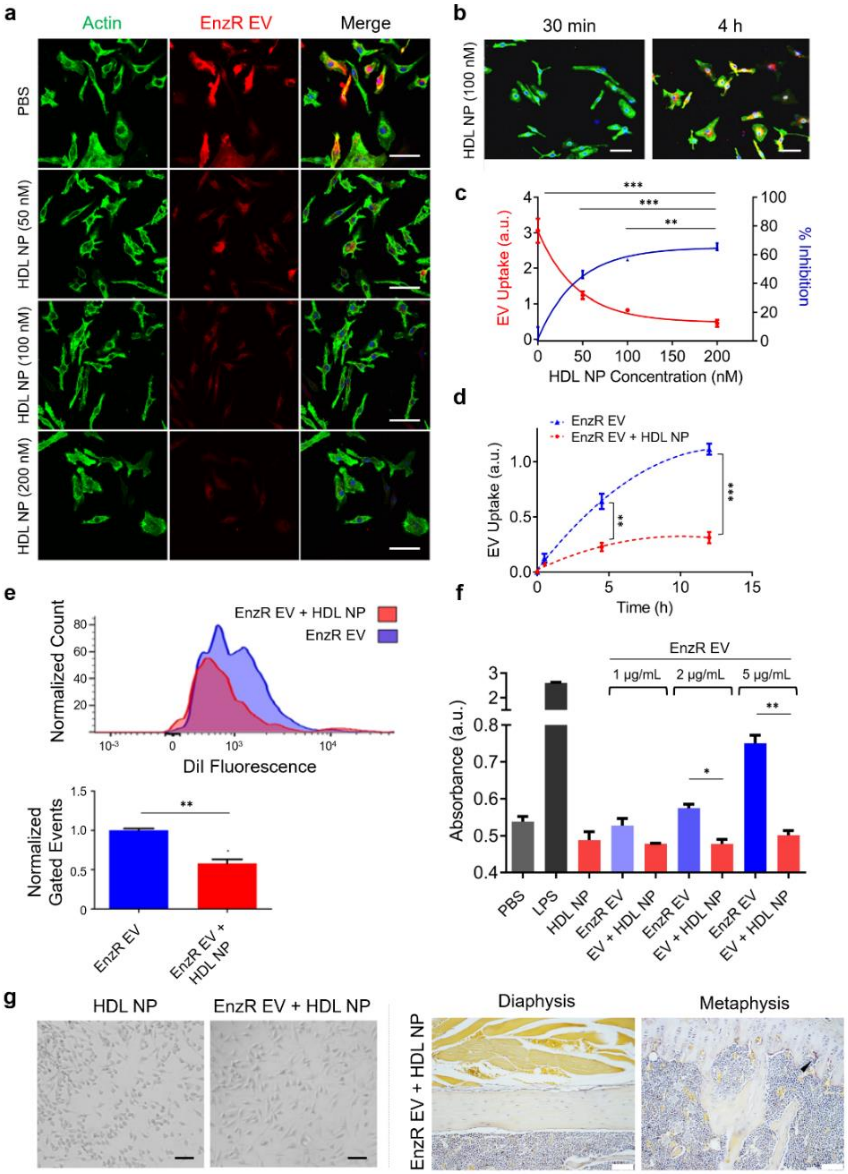

Figure 4.8: EnzR EV-mediated intercellular communication with bone marrow myeloid cells is inhibited by reduction of myeloid cellular cholesterol

In vitro uptake of DiI-labeled EnzR EVs (red) in mouse BMMs pre-treated with HDL NPs at varying a) concentrations and b) time points. Green: actin. Blue: DAPI. Scale bars are 50 μm. c) Dose and d) time dependence of HDL NP-mediated inhibition of EnzR EV uptake. e) *In vivo* uptake of DiI-labeled EnzR EVs in mouse bone marrow with and without HDL NP pre-treatment. f) NF-κB activity in human monocytes treated with EnzR EVs with and without HDL NP pre-treatment. g) TRAP staining of RAW264.1 cells (left panel) or mouse hind limb sections (right panel) after conditioning with EnzR EVs and pre-treatment with HDL NPs. Scale bars are 50 μm (left panel) and 200 μm (right panel). One-way ANOVA with Tukey's method, two-sided (c,d,f) and two-tailed Welch's *t*-test (e) were used to determine significance. $^*P < 0.05$, $^{**}P < 0.01$, $^{***}P < 0.001$. Data are mean ± s.e.m.

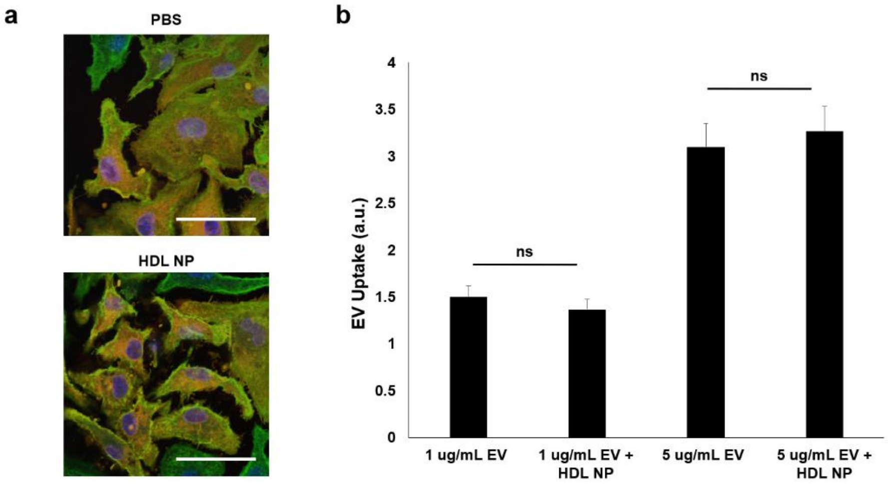

Figure 4.9: HDL NP-mediated inhibition of EnzR EV uptake requires SR-B1

a) Immunocytochemistry of primary mouse BMM cultures harvested from SR-B1$^{-/-}$ mice treated with DiI-labeled EnzR EV (red). Green: Phalloidin. Blue: DAPI. Scale bars are 50 µm. b) Quantification of EnzR EV uptake in BMMs harvested from SR-B1$^{-/-}$ mice, with and without HDL NP treatment. One-way ANOVA with Tukey's method, two-sided was used to determine significance. NS, non-significant. Data are mean ± s.e.m.

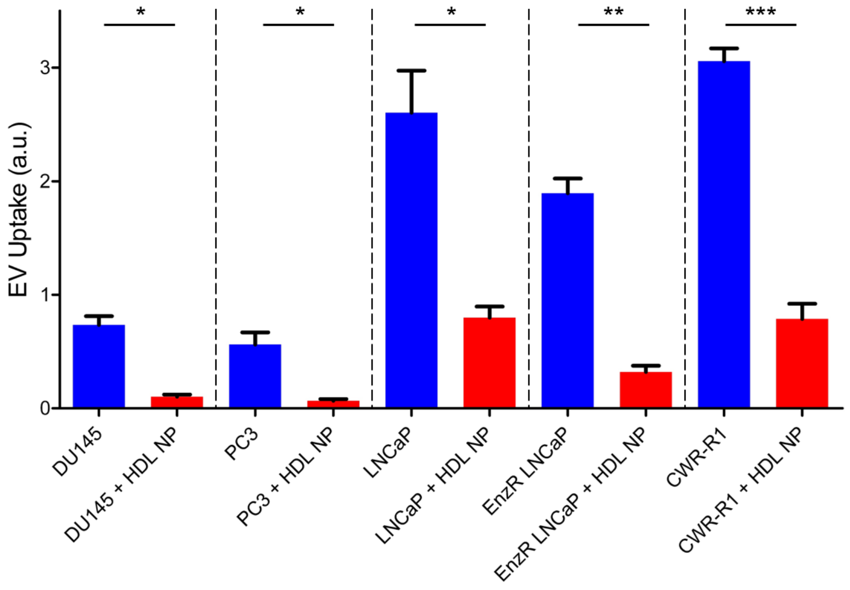

Figure 4.10: HDL NPs inhibit *in vitro* cellular uptake of PCa EVs derived from multiple PCa cell lines

Quantification of EV uptake as determined by confocal fluorescence microscopy of mouse BMM primary cultures treated with DiI-labeled PCa EVs with or without HDL NP pre-treatment (100 nM). Two-tailed Welch's *t*-test was used to determine significance. $*P < 0.05$, $**P < 0.01$, $***P < 0.001$. Data are mean ± s.e.m.

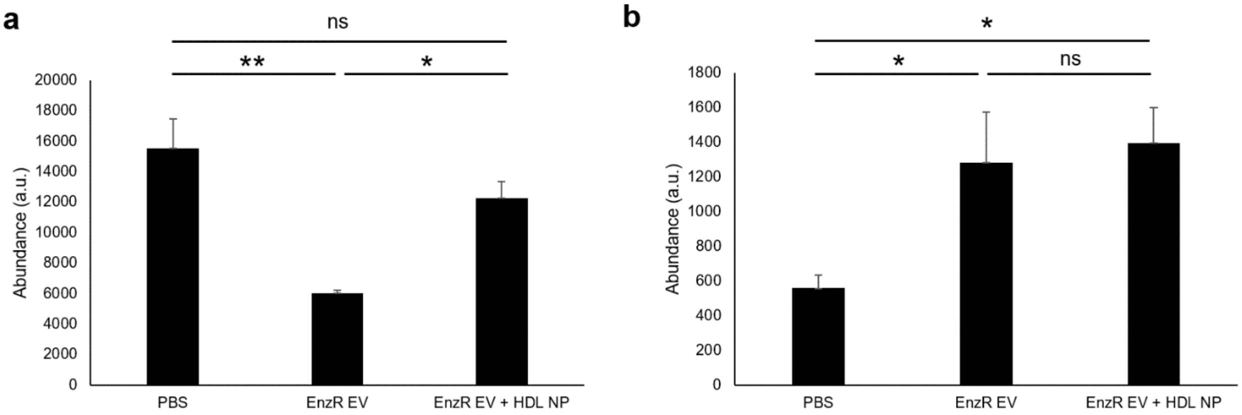

Figure 4.11: Systemic injection of HDL NPs prevents EnzR EV-mediated reduction of marrow TSP1 expression but does not prevent enhancement of VCAN expression

RNA expression of a) TSP1 and b) VCAN in CD11b$^+$ bone marrow myeloid cells harvested from mice conditioned with EnzR EVs with or without HDL NP pre-treatment vs. vehicle (PBS) controls. One-way ANOVA with Tukey's method, two-sided was used to determine significance. NS, non-significant; *$P < 0.05$, **$P < 0.01$. Data are mean ± s.e.m.

Using a metastatic PCa mouse model which has been shown to establish tumors at clinically relevant sites of PCa metastasis, including bone, lungs, and liver,[184] we then tested whether EnzR EV conditioning promoted metastatic tumor burden. A timeline of the model, injection scheme, and monitoring with bioluminescence imaging is shown in Figure 4.12a. To specifically determine whether EnzR EV conditioning altered the initial seeding and growth of tumor cells, we quantified metastatic tumor burden at two weeks after intracardiac injection of tumor cells. We found that EnzR EV conditioning significantly enhanced metastatic tumor burden (Figure 4.12b). Strikingly, mice that were pre-treated with HDL NPs in addition to EnzR EV conditioning exhibited no enhancement of metastatic tumor burden (Figure 4.12b, c).

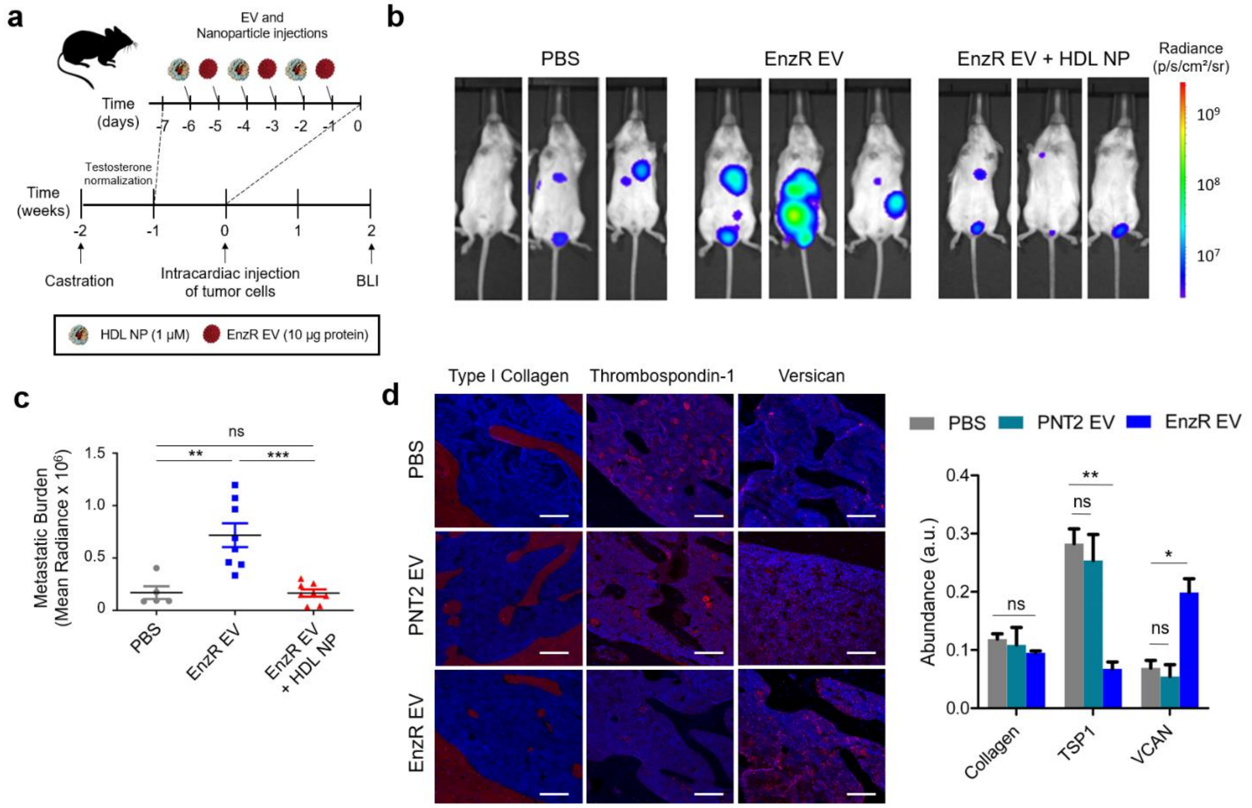

Figure 4.12: EnzR EVs enhance metastasis in a mouse model of metastatic PCa in a cholesterol-dependent manner, and alter the composition of the bone marrow ECM

a) Timeline for the metastatic PCa mouse model, with EnzR EV and HDL NP injection scheme. BLI = bioluminescence imaging. b) Metastatic PCa tumor burden at two weeks post-intracardiac injection of tumor cells via BLI. c) Quantification of metastatic tumor burden at two weeks for mice treated with PBS (*n* = 5), EnzR Exo (*n* = 8), or EnzR Exo + HDL NP (*n* = 8). d) Immunohistochemistry of hind limb bone tissue from mice treated with EnzR EVs or vehicle (PBS) control (left panel), and ECM quantification (right panel). Scale bars are 200 µm. One-way ANOVA with Tukey's method, two-sided was used to determine significance. *$P < 0.05$, **$P < 0.01$, ***$P < 0.001$. Data are mean ± s.e.m.

We then sought to shed additional light on the mechanism by which EnzR EV conditioning led to enhanced metastasis. Motivated by the RNA sequencing results in Figure 2d, we proceeded to determine whether pro-tumorigenic alterations in the mRNA expression of TSP1 and VCAN in CD11b$^+$ cells were reflected in the protein content of the bone marrow niche in general. Immunohistochemistry revealed that EnzR EV-conditioned mice exhibited reduced TSP1 and increased VCAN expression in the bone marrow compartment (Figure 4.12d), consistent with RNA sequencing results. Type I collagen, by contrast, remained stable with EnzR EV conditioning. Moreover, PNT2 EVs did not significantly impact TSP1 or VCAN expression (Figure 4.12d). We hypothesized that EnzR EV-induced alterations in TSP1 and VCAN expression may enhance the ability of tumor cells to seed the metastatic microenvironment by increasing stable cellular adhesion to the ECM. To test this, we conducted an *in vitro* cellular adhesion assay in which the ECM composition of two-dimensionally coated tissue culture wells was varied, using Type I collagen as a filler material. Live cell imaging was used to determine the efficiency with which EnzR CWR-R1 cells adhered and spread to each substrate. Confluence curves exhibited consistent trends across samples, enabling us to identify distinct adhesion and proliferation phases, with the adhesion phase taking place during the first 4 hours (Figure 4.13). Consistent with our hypothesis, we found that greater proportions of TSP1 in ECM coatings led to diminished adhesion of EnzR CWR-R1 cells, while greater proportions of VCAN increased adhesion (Figure 4.14a-e). While there were no statistical differences between groups with 5, 15, and 45% VCAN substrates, there was a significant increase in cellular adhesion between 15 and 45% VCAN compared to collagen only control (Figure 4.14c). The trends observed for TSP1 and VCAN were consistent when each protein was varied in isolation, and when the two proteins were co-varied in the same substrates (Figure 4.14d). Our findings are consistent with previous reports that TSP1 can function as an anti-adhesive matricellular protein in other settings.[204-205]

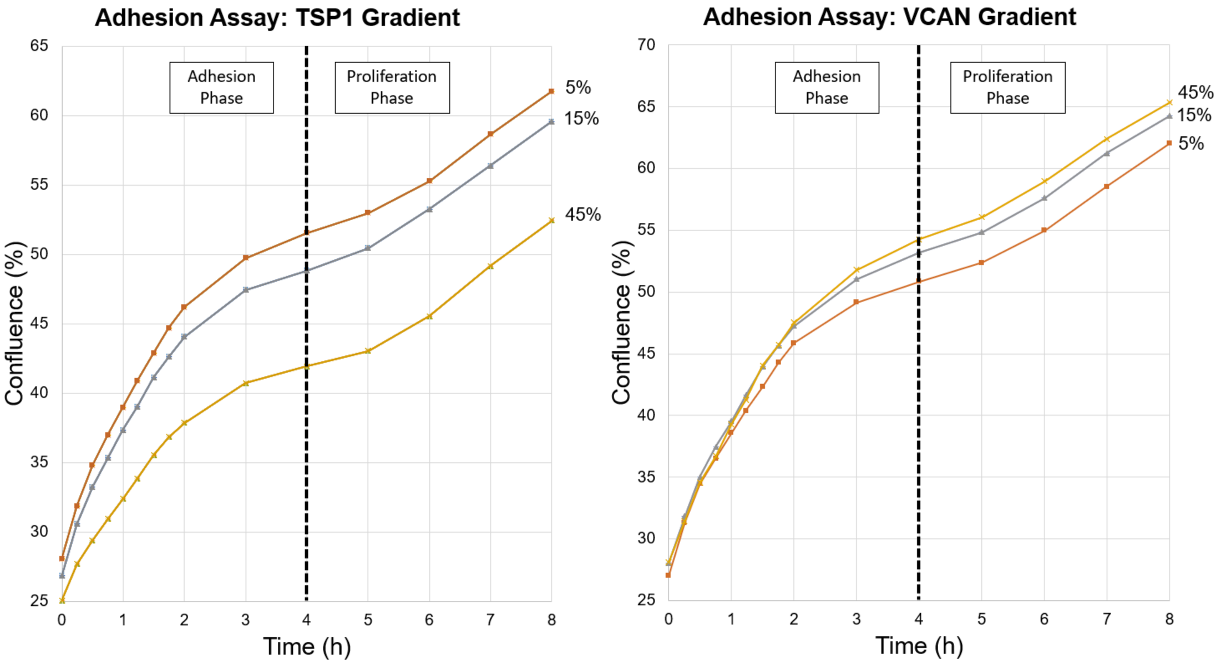

Figure 4.13: Confluence plots for live cell imaging of EnzR CWR-R1 cells introduced into tissue culture wells coated with two-dimensional ECM substrates reveals distinct adhesion and proliferation phases.

Confluence plots for EnzR CWR-R1 cells added to collagenous ECM substrates with varying TSP1 (left panel) and VCAN (right panel) content over 8 h, indicating that adhesion primarily occurs within the first 4 h.

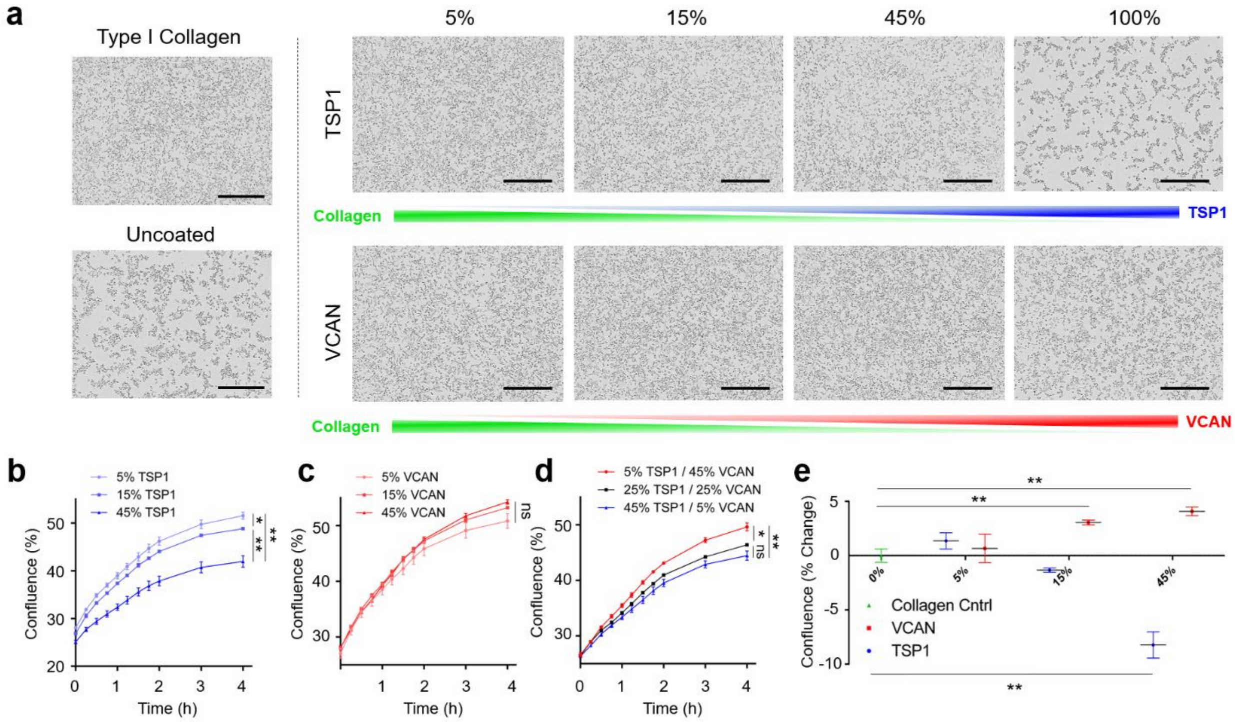

Figure 4.14: Reduced TSP1, elevated VCAN are favorable for PCa cell adhesion to the ECM

a) Live cell imaging of EnzR CWR-R1 cells seeded onto ECM substrates varying in Type I collagen, TSP1, and VCAN. Snapshot images shown were taken 4 h after seeding. Scale bars are 400 µm. b) Quantification of EnzR CWR-R1 cell adhesion to collagenous ECM substrates with variable TSP1 composition, c) varying VCAN composition, and d) co-varying TSP1 and VCAN composition. e) Aggregate analysis at 4 h post-seeding of changes in cellular adhesion of EnzR CWR-R1 cells to substrates with univariate changes in TSP1 and VCAN composition. One-way ANOVA with Tukey’s method, two-sided was used to determine significance. $^{*}P < 0.05$, $^{**}P < 0.01$. Data are mean ± s.e.m.

A graphical abstract summarizing the cholesterol-dependence of PCa EV-mediated signaling in the bone marrow is displayed below in Figure 4.15.

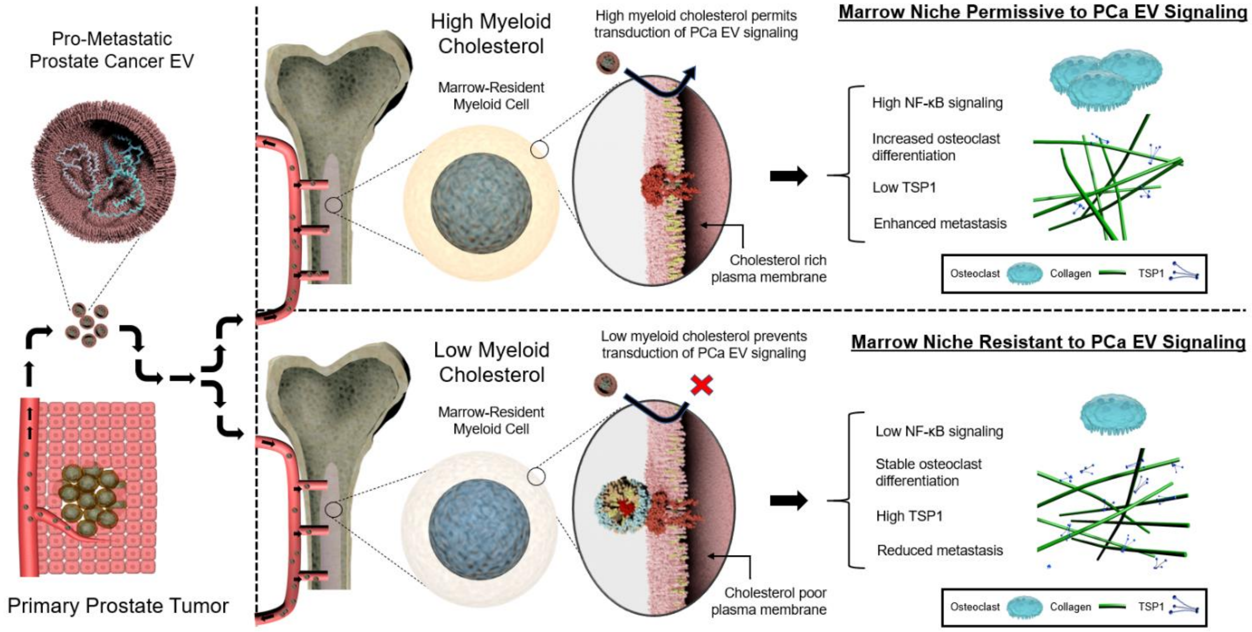

Figure 4.15: Graphical summary illustrating the cholesterol-dependence of PCa EV communication with bone marrow cells and metastasis

Top right panel depicts PCa EV communication with bone marrow myeloid cells with no cholesterol-modifying intervention, in which bone marrow-resident myeloid cells are rich in cholesterol. Bottom right panel depicts PCa EV communication with bone marrow cells after HDL NP treatment, in which the cholesterol content of bone marrow-resident myeloid cells is reduced.

4.4 Conclusions

Over the past two decades, Stephen Paget’s prescient 19th century “seed and soil” hypothesis has now developed into a diverse literature on PMN formation, a significant portion of which attests to the important role that EVs play in promoting metastasis. However, modifiable factors intrinsic to pre-metastatic sites that render them more or less permissive to pro-metastatic EV signaling have not been identified. Our results show that a crucial PMN target tissue, bone marrow, can be rendered resistant to the transduction of PCa EV signaling by reducing myeloid cell cholesterol.[114] Consistent with these findings, metabolomic studies have previously demonstrated that bone metastases are heavily laden with cholesterol compared to healthy bone, and PCa bone tumors in particular bear especially high cholesterol burdens (127.3 vs. 35.85 mg/g tissue).[183] Further, elevated serum total cholesterol and reduced HDL cholesterol are both associated with progression of locally confined PCa to metastatic PCa,[206-209] while statin use is also associated with reduced incidence of advanced disease.[210] Our results provide evidence for a PMN-based mechanism that could partly explain these clinical and epidemiological observations.

Aberrant cholesterol homeostasis can influence cancer progression and metastasis by perturbing neoplastic cells directly.[211-213] However, it perhaps shouldn't be surprising that cholesterol, and likely other metabolic factors, also play critical gate-keeping roles with respect to the reception of pro-metastatic signals by target cells at distant sites, which we demonstrate here. We anticipate that these results will motivate strategic diagnostic and therapeutic interventions aimed at preventing metastasis by modulating global, site-specific, or cellular metabolic factors that regulate PMN formation. More generally, these results contribute to our understanding of how intercellular communication is deciphered by recipient cells according to their cholesterol metabolic state.

4.5 Materials and Methods

Cell cultures: All cells were maintained at 37℃, 5% CO_2, and were handled under sterile conditions in an Esco Class II Type A2 biosafety cabinet. EnzR CWR-R1 cells and EnzR LNCaP cells were gifts from Dr. Donald Vander Griend (University of Illinois at Chicago) and were cultured in Roswell Park Memorial Institute (RPMI) 1640 medium containing 10% FBS, 1% penicillin/streptomycin and 20 µM enzalutamide. PC3, DU145, LNCaP (non-resistant), CWR-R1 (non-resistant), PNT2 and THP1-Dual cells (ATCC, Manassis, VA) were cultured in RPMI containing 10% fetal bovine serum (FBS), and 1% penicillin/streptomycin. RAW264.1 (ATCC) cells were cultured in Dulbecco's Modified Eagle Medium (DMEM) containing 10% FBS and 1% penicillin/streptomycin. Cells were passaged upon reaching approximately 70-80% confluence.

Experimental animals: Mice were housed and maintained in the Northwestern University Center for Comparative Medicine, according to NIH guidelines and in concordance with protocols approved by the Northwestern University Institutional Animal Care and Use Committee (IACUC). Male C57BL/6 mice (3-6 weeks) were obtained from the Jackson Laboratory and male C.B.-17 SCID mice (3-4 weeks) were obtained from Taconic Biosciences.

Bone marrow isolation: Total bone marrow was harvested from healthy male C57BL/6 mice by dissecting hind limbs immediately after euthanasia, soft tissue was removed, and bone marrow cavities of femurs and tibias were flushed with phosphate buffered saline (pH = 7.4) (PBS). Flushed cells and tissue were then passed through 70 µm filters to remove non-cellular tissue components and debris. Cells were then centrifuged at 300 x *g* and resuspended in Red Blood Cell Lysis Buffer (Invitrogen) for 5 minutes to lyse RBCs followed by centrifugation at 300 x *g*.

Primary bone marrow macrophage culture: Bone marrow cells were harvested as described above, cells were resuspended in DMEM containing 10% FBS, 1% penicillin/streptomycin, and 20 ng/mL M-CSF (BioLegend). Cells were then seeded in 6 cm dishes at 1 million cells/dish and macrophage differentiation proceeded for 7 days, with 5 mL of fresh, M-CSF containing medium added at day 4.

EV isolation: Cells were cultured and grown into 15 cm dishes. When cells reached approximately 70-80% confluence, cells were washed with PBS and transferred to fresh media containing EV-free serum for 48 hrs. Media was then collected and subjected to centrifugation at 300 x *g* for 5 min to pellet cells, then 2000 x *g* for 15 min to remove cellular debris. The supernatant was then transferred to ultracentrifuge tubes and ultracentrifuged at 10,000 x *g* for 30 min to pellet and remove large vesicles. The supernatant was then transferred to new ultracentrifuge tubes and ultracentrifuged twice at 100,000 x *g* for 90 min to pellet EVs; the EV pellet was washed with PBS between the two centrifuge steps to remove co-pelleted non-EV components, and then resuspended in PBS. After the final round of centrifugation, EVs were resuspended in PBS and then either stored at 4°C for short-term use (less than 3 days) or stored at -80°C for later use. Protein content of EVs was determined by BCA and treatment dosing was determined by EV protein concentration.

HDL NP synthesis: High-density lipoprotein-like nanoparticles (HDL NPs) were synthesized according to published protocols. Briefly, particle synthesis was initiated by adding purified apolipoproteinA-1 (apoA-1) (MyBioSource) at fivefold molar excess to a solution of 5 nm diameter citrate-stabilized, colloidal gold nanoparticles (Au NPs) (80-100 nM; Ted Pella, Inc). The suspension was vortexed briefly, and placed on shaker at RT for 1 h. Next, two species of phospholipid -- 1,2-dipalmitoyl-*sn*-glycero-3-phosphoethanolamine-*N*-[3-(2-pyridyldithio)propionate] (PDP PE) and 1,2-dipalmitoyl-*sn*-glycero-3-phosphocholine (DPPC) (Avanti Polar Lipids)— were added to the suspension at 250-fold molar excess to Au NPs in a mixture of ethanol and water (1:4) and incubated for 4 h at RT with gentle mixing on a flat-bottom shaker. HDL NPs were then purified and concentrated using tangential flow filtration.

HDL NP concentration was determined using UV-Vis spectroscopy ($\varepsilon_{\text{Au NP}} = 9.696 \times 10^6\ M^{-1}cm^{-1}$, λ_{max} = 520 nm) and size was confirmed using dynamic light scattering.

Transmission electron microscopy and dynamic light scattering: EV samples were fixed by adding an equal volume of 4% paraformaldehyde (PFA) to the EV suspension and incubating at room temperature for 10 min. 5 µl of EV suspension were deposited on 300-mesh carbon-coated copper grids to adsorb for 20 min. Grids were then floated on 100 µl drops of PBS on parafilm for 2 min. Grids were then transferred to 50 µl drops of 1% glutaraldehyde for 5 min. Next, grids were washed on 100 µl drops of PBS for a total of 8 washes and 2 min per wash. Grids were then transferred to 50 µl drops of uranyl oxalate, pH = 7, for 5 min, and finally to 50 µl drops of methyl cellulose-uranyl acetate for 10 min on ice. Excess fluid was then blotted off on filter paper, and grids were dried at room temperature for 20 min prior to imaging or storage. Imaging was performed using a FEI Tecnai Spirit transmission electron microscope (TEM) operating at 80 kV. Hydrodynamic diameter of EVs was determined by dynamic light scattering (DLS), which was performed using a Zetasizer Nano ZS (Malvern). EV samples were diluted to concentrations of 1-10 µg EV protein per mL in PBS. Hydrodynamic diameters reported are the average of three separate measurements of a single sample, with each measurement being the cumulative result of ten runs.

EV fluorescent labeling: EVs were isolated from cultured cells in an identical manner as described above, with the exception that prior to the last round of ultracentrifugation at 100,000 x g, the lipophilic fluorescent dye 1,1'-Dioctadecyl-3,3,3',3'-Tetramethylindocarbocyanine Perchlorate (DiI) was added to the EV sample at a concentration of 2.5 µM in PBS. After the final round of centrifugation, supernatant containing excess DiI was discarded prior to resuspension of the EV pellet.

Flow cytometry: DiI-labeled EVs or vehicle control (PBS) were injected via tail vein into male C57BL/6 mice (10 µg EV protein) 24 h prior to euthanasia. For *in vivo* uptake inhibition experiments, mice were subjected to HDL NP injection via tail vein (100 µM, 100 µl) 24 h prior to injection of DiI-labeled EVs. Bone marrow cells were then isolated as described above, washed in PBS, and resuspended in FACS buffer [PBS containing 1% bovine serum albumin (BSA), 0.1% sodium azide]. Samples were stained in LIVE/DEAD Aqua Dead Cell stain (ThermoFisher) for 20 min at RT, washed in FACS buffer, and then blocked in F_c block (BD Pharmingen) for 20 min at RT. Cells were then incubated in 100 µl of fluorophore-conjugated antibody cocktail (APC anti-mouse/human CD11b, PE-Cy7 anti-mouse Ly6C, Brilliant Violet anti-mouse Ly6G; BioLegend) (1:100 dilutions for all antibodies) for 1 h at 4°C protected from light, and then washed in FACS buffer. Samples were then analyzed using a BD LSR Fortessa Analyzer and data was processed using FlowJo software. A sample of the gating scheme is shown in Figure S1c. Experiments were performed using $n = 3$ mice per group.

***In vitro* EV uptake studies:** Cells were plated at 20,000 cells per well in 24-well plates on top of glass coverslips, in 0.5 mL of culture medium. The following day, cells were washed three times in PBS prior to treatment with DiI-labeled EVs with or without HDL NP pre-treatment (2 h) in serum-free media. For all *in vitro* EV uptake experiments excepting time-dependence studies (Fig. 2a, c, Fig. S1a, Fig. S4), EV uptake was allowed to proceed for 30 min. For time-dependence studies, EV uptake proceeded for 30 min, 2 h, or 12 h. Cells were then washed three times in PBS and fixed in 4% paraformaldehyde for 15 min at RT. Subsequently, cells were washed three times in PBS, and incubated with AlexaFluor488-Phalloidin (1:1000) (Abcam) and DAPI (300 nM) for 1 h at RT. Cells were then washed three times in PBS and mounted on microscopy slides in Fluoromount G mounting medium (Southern Biotech). Three distinct samples from each group were imaged using a Nikon A1R Spectral confocal microscope.

Osteoclast differentiation studies: For *in vitro* osteoclast differentiation assays, RAW264.7 cells were seeded at a density of 25,000 cells per well in 24-well tissue culture plates. After 48 h, cells were incubated with vehicle control (PBS), EnzR EVs (5 μg/mL EV protein) with or without RANKL (20 μg/mL), or RANKL alone for 7 days, with fresh media containing EVs and/or RANKL added at day 4. For *in vitro* HDL NP inhibition studies, HDL NPs (100 nM) were added to the media 2 h prior to addition of EnzR EVs, and osteoclast differentiation was allowed to proceed for 7 days, with fresh media containing HDL NPs and EnzR EVs added at day 4. After 7 days, cells were then fixed in 4% PFA and stained with TRAP using a commercially available kit (Sigma) according to the manufacturer’s protocol. Experiments were performed using three distinct biological replicates per group.

For *in vivo* osteoclast differentiation studies, C57BL/6 mice were subjected to three tail vein injections of EnzR EVs (10 μg EV protein per injection) at 48 h intervals. Mice were euthanized 24 h after the third injection, hind limbs were dissected, soft tissue was removed, and bones were fixed in 10% neutral buffered formalin (NBF) for 3-5 days. Hind limb bones were then rinsed twice in PBS, placed in 70% ethanol for 24 hrs, and decalcified in 20% EDTA for 10 days prior to paraffin embedding, sectioning, and mounting on microscopy slides. TRAP staining was then performed to visualize osteoclasts using a commercially available kit (Sigma) according to the manufacturer’s protocol. Experiments were performed using n = 3 mice per group.

NF-κB reporter assay: THP1-Dual cells were maintained in culture medium containing 10 μg/mL blasticidin and 100 μg/mL Zeocin to maintain selection pressure and passaged every three days. Cells were seeded in 96-well plates at 100,000 cells/well in 180 μl of cell suspension. Then 20 μl of EnzR EVs, vehicle control (PBS), or positive control (LPS) were added to each well to achieve the desired final concentration. Plates were incubated at 37°C for 24 h. QUANTI-Blue solution was then prepared according the manufacturer's instructions, 180 μl of QUANTI-Blue solution were added to each well of a new 96-well plate, and 20 μl of THP1-Dual supernatant were added to each well. Plates were incubated at 37°C for 2 h and SEAP levels were determined by measuring absorbance using a Synergy Plate Reader. For HDL NP inhibition experiments, the experimental conditions were identical with the exception that HDL NPs (100 nM) were added to THP1 cells 2 h prior to addition of EnzR EVs. NF-κB activity was measured from four distinct biological replicates per group.

Radiolabeled cholesterol efflux assay: THP1 monocytes were seeded into 24-well plates at a density of 50,000 cells/well and differentiated into macrophages by incubating with 100 ng/mL phorbol 12-myristate 13-acetate (PMA) for 48 h at 37°C. Cells were then washed three times with PBS and fresh, non-PMA containing media was added to allow cells to recover for 24 h prior to loading with tritium-labeled cholesterol ([^{3}H]-chol). An ethanol stock solution of [^{3}H]-chol was evaporated to generate a thin film, re-dissolved in 1 mL ethanol and incubated at 37°C for 60 min. The solution was then evaporated again, re-dissolved in 50 μl ethanol, and incubated at 37°C for 30 min. FBS was then added to the solution of [^{3}H]-chol at a quantity calculated to enable labeling of cells the following day with 1 μCi [^{3}H]-chol per well in 5% FBS containing culture medium. The resulting mixture was incubated at 4°C overnight. On the following day, serum-free RPMI with 1% penicillin/streptomycin was added to the mixture of [^{3}H]-chol and FBS to yield a labeling medium comprising 2 μCi/mL [^{3}H]-chol, 5% FBS. Cells were washed three times with PBS and 500 µl of labeling medium were added to the cells. After 24 h, cells were washed three times with PBS to remove excess [^{3}H]-chol, and fresh culture medium with HDL NPs or vehicle (PBS) control was added. Cholesterol efflux was allowed to proceed for 4 h when cells were washed three times with PBS, lipids were extracted with isopropanol, and [^{3}H]-chol was quantified using liquid scintillation counting. [^{3}H]-chol was quantified from four distinct biological replicates per group.

***In vivo* bone marrow cellular cholesterol quantification studies:** Male C57BL/6 were injected with HDL NPs (100 µl, 1 µM) or vehicle alone (PBS) via tail vein 2 h prior to euthanasia when hind limbs were dissected and bone marrow cells were isolated as described above. Each bone marrow sample was then divided into two groups: one for quantification of cellular cholesterol in total bone marrow cells and the other for quantification of cellular cholesterol in bone marrow monocytes. For the latter group, a commercially available mouse bone marrow isolation kit (EasySep) was used to isolate monocytes from total bone marrow. Amplex Red Cholesterol Assay (ThermoFisher) was then used to quantify cellular cholesterol in both groups according to the manufacturer’s instructions. Protein content of the samples was determined by BCA, and cholesterol quantification was normalized to the protein content. Experiments were performed using $n = 5$ mice per group.

Immunohistochemistry: Male C57BL/6 mice were subjected to three tail vein injections of EnzR EVs (10 µg EV protein per injection) or vehicle (PBS) control at 48 h intervals. Mice were euthanized 24 h after the third injection, hind limbs were dissected, soft tissue was removed, and bones were fixed in 10% neutral buffered formalin (NBF) for 3-5 days. Hind limb bones were then rinsed twice in PBS, placed in 70% ethanol for 24 hrs, and decalcified in 20% EDTA for 10 days prior to paraffin embedding, sectioning, and mounting on microscopy slides. Tissues were deparaffinized and rehydrated by incubating twice in xylene for 5 minutes, and then undergoing successive 10-minute incubations in 100% ethanol, 95% ethanol, 70% ethanol, distilled water and finally PBS. Tissues were then washed and permeabilized in TBS-Triton (0.025% Triton X-100) twice for five minutes and blocked in TBS with 1% BSA, 10% donkey serum. Primary antibodies (anti-mouse TSP1, Abcam, 1:50 dilution; anti-mouse/human VCAN, Sigma, 1:100 dilution; anti-mouse Type I Collagen, Sigma, 1:100 dilution) were then added using TBS, 1% BSA as a diluent and allowed to incubate for 24 h at 4°C. Tissues were then washed twice in TBS-Triton for 5 minutes each, prior to adding fluorescently tagged secondary antibodies at 1:250 dilutions in TBS, 1% BSA. Tissues were then washed with TBS for 5 minutes, then DAPI (300 nM) in TBS, and once more in TBS for five minutes prior to mounting and cover slipping on microscopy slides in Vectashield mounting media. Slides were imaged using a Nikon A1R spectral confocal microscope. Experiments were performed using $n = 3$ mice per group.

Surgical castration: Male C.B.-17 SCID mice aged 3-4 weeks were surgically castrated two weeks prior to injection of tumor cells. Mice were anesthetized under inhaled isoflurane. The incision area was swabbed with alcohol and betadine prior to surgery. A single 2-4 mm incision was made in the inferior scrotum. One testicle was removed from the scrotum, a knot was tied around the base of the testicle, and the testicle was excised with surgical scissors. The process was repeated for the other testicle. The incision site was then closed with absorbable sutures.

Mice were given intraperitoneal injections of meloxicam (5 mg/kg) once per day for two days following the operation.

Metastasis experiments: Male C.B.-17 SCID mice (Taconic Bioscience) were castrated two weeks prior to intracardiac injection of EnzR CWR-R1 cells. Five days prior to intracardiac injection, mice were subjected to three rounds of tail vein injections with EnzR EVs (10 μg EV protein per injection, 100 μl) or vehicle control (PBS) at 48 h intervals. One group of mice was also subjected to three rounds of HDL NP injections (100 μM, 100 μl) via tail vein on alternating days from EnzR EV injections, beginning 24 h prior to the first EnzR EV injection. On the day of intracardiac injection, mice were anesthetized under inhaled isoflurane, the injection site was swabbed with alcohol and betadine, the syringe needle was then advanced through the skin approximately 1 cm to the left of the inferior sternum and 5 mm inferior to the sternum. The needle was then advanced through the diaphragm and into the left ventricle, and luciferase-expressing EnzR CWR-R1 cells (250,000 cells) were injected into the left ventricle over the course of 15-20 seconds. Mice were monitored for signs of pain following the procedure and meloxicam was administered as needed. Tumor burden was assessed at 2 weeks post-intracardiac injection via bioluminescence imaging. Mice were injected intraperitoneally with luciferin (150 mg/kg) 5 minutes prior to bioluminescence imaging under anesthesia. Experiments were performed using n = 8 mice per group for experimental groups (EnzR EVs; EnzR EVs + HDL NP) and n = 5 mice were used for the PBS control group.

Adhesion assay: Recombinant type I collagen (Sigma), TSP1 (R&D Systems), and VCAN (Ray Biotech) were diluted to 100 μg/mL in PBS. All ECM substrates were then prepared at a final total protein concentration of 5 μg/mL using the appropriate combination of each of the three components. The remainder of the substrate that did not call for TSP1 or VCAN was filled with type I collagen. For instance, a condition that called for 5% TSP1, 45% VCAN would be prepared by adding 5 equivalents of TSP1, 45 equivalents of VCAN, and 50 equivalents of type I collagen. Substrates were then sonicated to achieve greater alignment of ECM fibrils. 100 µl of each substrate were then added in triplicate to wells in 96-well plates and incubated for 2 h at room temperature. Excess substrates were then removed by inverting the 96-well plate over a plastic reservoir and tapping gently. Wells were washed twice with PBS and blocked with DMEM containing 10% FBS for 30 min at 37°C. Wells were washed once with PBS and 50,000 EnzR CWR-R1 cells were added to each well in full serum-containing culture medium and incubated at 37°C in an IncuCyte S3 system to enable live cell imaging of the adhesion process. Cells were imaged at 15 min intervals for the first 2 h and then every hour for the next 6 h. IncuCyte Analysis software was then used to analyze the results. Statistical testing was performed using three distinct biological replicates. Each data point from a single biological replicate represents the mean confluence across five technical replicates (distinct images from five different parts of the same tissue culture well).

RNA isolation for sequencing: For CD11b$^+$ bone marrow cell RNA sequencing studies, male C57BL/6 mice were subjected to three rounds of tail vein injections with EnzR EVs (10 µg EV protein per injection, 100 µl) or vehicle control (PBS) at 48 h intervals. One group of mice was also subjected to three rounds of HDL NP injections (100 µM, 100 µl) via tail vein on alternating days from EnzR EV injections, beginning 24 h prior to the first EnzR EV injection. 24 h after the final injection, mice were euthanized and bone marrow cells were isolated as described above. CD11b$^+$ cells were then isolated from the bone marrow population using a commercially available separation kit (EasySep) according to the manufacturer's instructions. mRNA was then isolated using RNeasy isolation kit (Qiagen). Experiments were performed using $n = 3$ mice per group for CD11b$^+$ RNA isolation and sequencing.

RNA sequencing of CD11b$^+$ mouse bone marrow cells: Stranded total RNA-seq was conducted in the Northwestern University NUSeq Core Facility. Briefly, total RNA examples were checked for quality on Agilent Bioanalyzer 2100 and quantified with Qubit fluorometer. The Illumina TruSeq Stranded Total RNA Library Preparation Kit was used to prepare sequencing libraries from 200 ng of total RNA samples. The Kit procedure was performed without modifications. This procedure includes rRNA depletion, remaining RNA purification and fragmentation, cDNA synthesis, 3' end adenylation, Illumina adapter ligation, library PCR amplification and validation. lllumina NextSeq 500 Sequencer was used to sequence the libraries with the production of single-end, 75 bp reads.

The quality of DNA reads, in FASTQ format, was evaluated using FastQC. Adapters were trimmed, and reads of poor quality or aligning to rRNA sequences were filtered. The cleaned reads were aligned to the *Mus musculus* genome (mm10) using STAR (Dobin et al, 2013). Read counts for each gene were calculated using htseq-count (Anders et al, 2015) in conjunction with a gene annotation file for mm10 obtained from UCSC (University of California Santa Cruz; http://genome.ucsc.edu). Normalization and differential expression were determined using DESeq2 (Love et al, 2014). The cutoff for determining significantly differentially expressed genes was an FDR-adjusted p-value less than 0.05. A pathway analysis was performed on both gene lists using GeneCoDis (Tabas-Madrid et al, 2012; Nogales-Cadenas et al, 2009; Carmona-Saez et al, 2007) to identify pathways enriched with genes that are upregulated and downregulated. Results were obtained from $n = 3$ mice per group. RNA sequencing data has been uploaded to NCBI GEO database (Accession: GSE158012).

Western blot: For Western blotting, 20 µg or 5 µg of total protein were used for cell lysates and EV protein respectively. Samples were diluted in Laemmli buffer and incubated at 98℃ for 5 min. Protein samples were resolved using Tris/Glycine/SDS pre-cast polyacrylamide gels and a BioRad Western blot system running at 200 V for 32 min. Protein was transferred from polyacrylamide gel to polyvinylidene fluoride membranes via wet transfer for 90 min at 70 V. Membranes were then blocked in 5% non-fat milk in TBS-Tween (0.1% Tween 20) for 1 h at RT. Membranes were incubated with primary antibodies at dilutions recommended by the manufacturer (anti-CD9, Cell Signaling Technology, Cat#: D8O1A, 1:500 dilution; anti-CD63, Novus Biologicals, Cat#: NB100-77913, 1:250 dilution; anti-flotillin-1, BD Biosciences, Cat#: 610820, 1:500 dilution; anti-GM130, BD Biosciences, Cat# 610822, 1:500 dilution) in blocking buffer for either 3 h at RT or overnight at 4℃, washed three times in TBS-Tween for 10 minutes, and incubated with HRP-conjugated secondary antibodies in blocking buffer for 1 h at RT. Membranes were then washed three times in TBS-Tween for 10 min and developed in ECL detection reagents (GE Healthcare).

Statistics and Reproducibility: All statistical analyses were performed using GraphPad Prism. Statistical significance was calculated using either unpaired two-tailed Student's *t*-test or one-way ANOVA with Tukey's post-hoc test, two-sided. $^{*}P < 0.05$, $^{**}P < 0.01$, $^{***}P < 0.001$. No statistical methods were used to pre-determine sample sizes, blinding, or randomization methods. The precise n for all experiments is explicitly indicated in each relevant Materials and Methods section, as well as in the main text and figure captions for select experiments. Details regarding the use of technical and biological replicates are described in the Materials and Methods.

Chapter 5: High-density lipoprotein mimics inhibit SARS-CoV-2 infection

5.1 Objectives and Significance

The novel human coronavirus, severe acute respiratory syndrome coronavirus 2 (SARS-CoV-2), emerged in Wuhan, China in late 2019 and has now caused a global pandemic. The disease caused by SARS-CoV-2 is known as COVID-19. To date, few treatments for COVID-19 have proven effective, and the current standard of care is primarily supportive. As a result, novel therapeutic strategies are in high demand. Viral entry into target cells is frequently sensitive to cell membrane lipid composition and membrane organization. Evidence suggests that cell entry of SARS-CoV-2 is most efficient when the target cell plasma membrane is replete with cholesterol; and recent data implicate cholesterol flux through the high-affinity receptor for cholesterol-rich high-density lipoprotein (HDL), called scavenger receptor B1 (SR-B1), as critical for SARS-CoV-2 entry. Here, we demonstrate that a cholesterol-poor synthetic HDL (HDL NP) targets SR-B1 and inhibits cell entry of a SARS-CoV-2 spike protein pseudovirus. Human cells expressing SR-B1 are susceptible to SARS-CoV-2 infection, and viral entry can be inhibited by 50-80% using HDL NPs. These results indicate that HDL NPs may be a powerful therapy to combat COVID-19 and other viral diseases.

5.2 Background and Motivation

COVID-19 disparately impacts the aging population, with the median age of COVID-19-related death being 78 years.[214] Individuals with pre-existing conditions such as coronary artery disease,[215-216] hypertension,[217] and diabetes[218] are also disproportionately susceptible to serious sequalae from severe acute respiratory syndrome coronavirus 2 (SARS-CoV-2) infection. However, the precise reasons why advanced age and pre-existing conditions lead to these disparities remain unclear. Prior evidence indicates that SARS-CoV-1 infectivity is highly sensitive to cholesterol levels in the host cell.[219] Indeed, several recent studies demonstrate that this is also the case for SARS-CoV-2.[220-222] Specifically, cholesterol-rich membrane domains constitute viral entry points for SARS-CoV-2.[220] Moreover, cholesterol helps traffic angiotensin converting enzyme 2 (ACE2) to these domains and increases the binding affinity for SARS-CoV-2 to the cell surface.[220] Conversely, reducing cellular cholesterol reduces viral infectivity. These findings provide valuable mechanistic insight into the existing disparities in COVID-19 outcomes for the elderly and those with pre-existing cardiovascular conditions and suggest that targeted reduction of cellular cholesterol may be a viable therapeutic strategy. Here, we sought to determine whether a targeted, cholesterol-reducing nanoparticle agent could inhibit SARS-CoV-2 entry.

Coronaviruses are enveloped viruses with positive stranded RNA genomes. Enveloped viruses typically infect their host cells in a two-step process whereby viral surface proteins first bind to receptors on the cell surface to initiate viral attachment, followed by a fusion event which leads to internalization of the virion by the host cell. Each virus in the coronavirus family expresses three structural proteins that are incorporated into the viral capsid, the membrane (M), envelope (E), and spike (S) proteins. The S protein is most important for viral attachment to host cells. For SARS-CoV-1 and 2, viral entry is facilitated by binding of the S protein to its receptor on the surface of certain host cells, ACE2. Furthermore, the high-affinity receptor for native cholesterol-rich high-density lipoproteins (HDL), called scavenger receptor type B-1 (SR-B1), has recently been implicated as a co-receptor to facilitate the entry of SARS-CoV-2, potentially in lock-step with HDL, into cells of the host airway.[223] SR-B1 is expressed by hepatocytes,[139, 224] immune cells[139, 201, 225] and type II pneumocytes,[226] the latter representing a major cell type targeted by SARS-CoV-2. SR-B1 has previously been appreciated as a co-receptor for other viruses and pathogens, including hepatitis C virus[227] and Plasmodium species.[228]

Despite this basic knowledge regarding the mechanism by which SARS-CoV-2 infects host cells, knowledge regarding therapeutic targets that could be exploited to inhibit SARS-CoV-2 infectivity remains limited. Most work has been focused on antibodies or ACE2 receptor decoys that target viral antigens, like the S protein, to reduce the productive interactions between the virus and host cells.[229-232] However, strategies that target host cells to prevent SARS-CoV-2 entry are less well studied. It is known that SARS-CoV-1 and SARS-CoV-2 utilize cholesterol and monosialotetrahexosylganglioside 1 (GM1)-rich lipid microdomains, or lipid rafts, for viral entry in cultured mammalian cells. Specifically, treating cells with the non-specific cholesterol sequestrant, methyl-β-cyclodextrin (MβCD), prior to introducing SARS-CoV-1 or SARS-CoV-2, leads to significantly reduced infection. Furthermore, recent data demonstrate that modulating cell cholesterol biosynthesis may be a critical pathway that controls SARS-CoV-2 entry into host cells.[233] Taken together, a significant amount of data suggest that the entry of SARS-CoV-2 into host cells is cholesterol-dependent and that targeting cell entry with an agent that modulates cell membrane and cellular cholesterol metabolism may provide a unique therapy to prevent SARS-CoV-2 entry into host cells.

HDLs are multi-functional particles that greatly impact inflammation and are taking on increasing importance as guardians of the integrity of endothelial and epithelial barrier function throughout the body. At the most basic level, HDLs are dynamic nanoscale particles (7-13 nm in diameter) that circulate in the bloodstream of mammals and transport cholesterol. HDLs are specifically notable for their functions in so-called reverse cholesterol transport, whereby they remove cholesterol from peripheral cells such as macrophages and deliver cholesterol back to hepatocytes for excretion in the bile. As a result, HDLs can potently modulate cell cholesterol metabolism. Our group and others have developed and tested synthetic HDLs for a variety of therapeutic[14, 34, 159, 202, 234] and imaging[27, 153] purposes. In one iteration, an inorganic core nanoparticle is used as a template to assemble the protein (apolipoprotein A-I) and lipids naturally associated with the surface of native cholesterol-rich HDLs. By virtue of their surface mimicry, HDL NPs tightly bind SR-B1. However, because synthetic HDLs lack a core of esterified cholesterol, and other lipids, they have been shown to differentially modulate cell membrane cholesterol and, by way of reducing cell cholesterol, stimulate a compensatory increase in cellular cholesterol biosynthesis. From a therapeutic perspective, HDL NPs modulate cell membrane cholesterol and lipid rafts, which has been shown to potently inhibit the uptake of extracellular lipid vesicles, often referred to as exosomes, which share many properties with viruses.[235-236] In addition, HDL NP modulation of cell cholesterol has been leveraged to develop potent anticancer therapies for tumor types that heavily depend upon cholesterol uptake through SR-B1.[14] And, finally, tuning the lipids bound to the outer surface of HDL NP enables profound targeting of Gram-negative bacterial lipopolysaccharide (LPS) to attenuate the activation of NF-κB and attendant cytokine expression.[50] Because of these properties, and a growing body of evidence demonstrating the dependence of SARS-CoV-2 infection upon cell cholesterol, we employed synthetic HDLs to determine whether targeted reduction of cellular cholesterol would inhibit viral entry of a SARS-CoV-2 spike protein pseudovirus.

5.3 Results and Discussion

Synthetic HDL NPs target the high-affinity receptor for native cholesterol-rich HDLs, SR-B1. As such, we assayed for the presence of SR-B1 in model cell lines of SARS-CoV-2 infection. The HepG2 and HEK293 (ACE2 over-expressing) cell lines both expressed SR-B1 as determined by Western blot (Figure 5.1 a,b). Moreover, treating HEK293 (ACE2) and HepG2 cells with siRNA against SR-B1 was shown to knock down SR-B1 protein expression (Figure 5.1 a,b) in each of these cell lines. The latter result is important for downstream SR-B1-dependence studies. Next, we treated HEK293 (ACE2) and HepG2 cells with PBS control or HDL NPs to determine any alterations in SR-B1 expression. We found that HDL NPs did not alter SR-B1 expression in these cell lines (Figure 5.1 c) at the concentration and treatment duration used for viral entry experiments later in the study (50 nM HDL NP for 48 h).

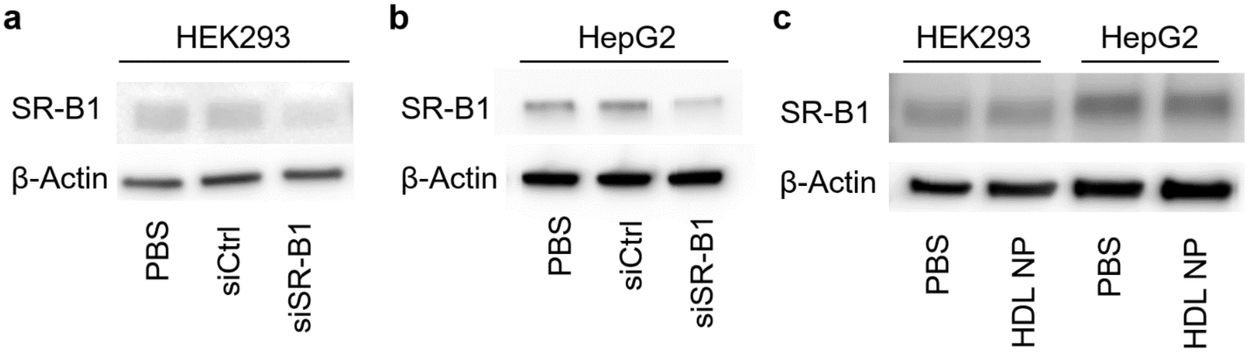

Figure 5.1: HEK293 (ACE2) and HepG2 cells express the native HDL receptor SR-B1

Western blot results for SR-B1 expression in a) HEK293 (ACE2 over-expressing) cells with either PBS, scramble RNA (siCntrl) or siRNA against SR-B1 (siSR-B1), b) HepG2 cells with either PBS, scramble RNA (siCntrl) or siRNA against SR-B1 (siSR-B1), c) HEK293 and HepG2 cells under conditions where cells were treated with HDL NPs (50 nM) or PBS control. In all cases, blots for β-actin were used as a control.

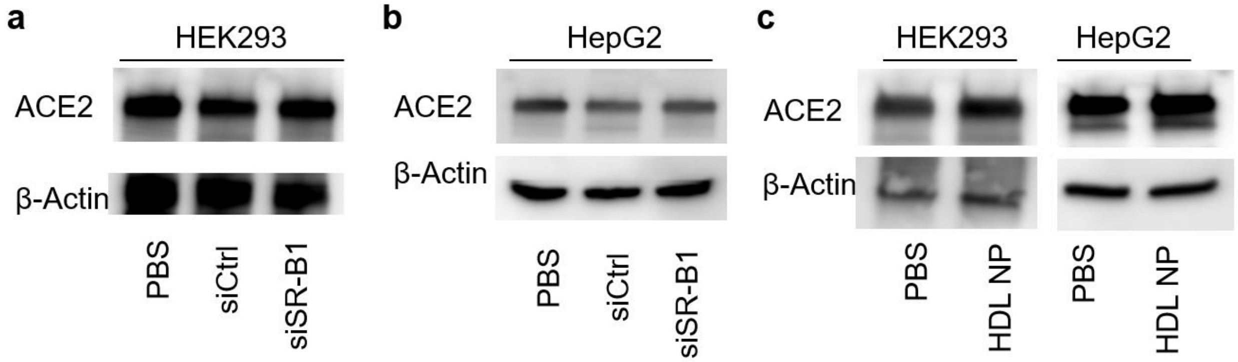

Figure 5.2: Neither SR-B1 knockdown nor HDL NP treatment alter ACE2 expression

Western blot results for ACE2 expression in a) HEK293 (ACE2 over-expressing) cells with either PBS, scramble RNA (siCntrl) or siRNA against SR-B1 (siSR-B1), b) HepG2 cells with either PBS, scramble RNA (siCntrl) or siRNA against SR-B1 (siSR-B1), c) HEK293 and HepG2 cells under conditions where cells were treated with HDL NPs (50 nM) or PBS control. In all cases, blots for β-actin were used as a control.

We then investigated whether HDL NP treatment or SR-B1 knockdown altered ACE2 expression. Because one of the overarching objectives of this study is to determine if HDL NPs effectively inhibit SARS-CoV-2 infection, we sought to determine first whether ACE2 expression was stable upon HDL NP treatment, to rule out the possibility that HDL NP treatment may indirectly alter SARS-CoV-2 infection by regulating ACE2 expression. We found that HDL NP treatment of HEK293 (ACE2) and HepG2 cells did not appreciably alter ACE2 expression (Figure 5.2c). Because we used siRNA against SR-B1 for mechanistic experiments later in the study, we also wanted to confirm that knocking down SR-B1 would not significantly alter ACE2 expression compared to treatment with a scramble RNA control. We found that ACE2 expression in HEK293 (ACE2) and HepG2 cells subjected to SR-B1 knockdown did not differ from cells treated with a scramble RNA control (Figure 5.2a, b).

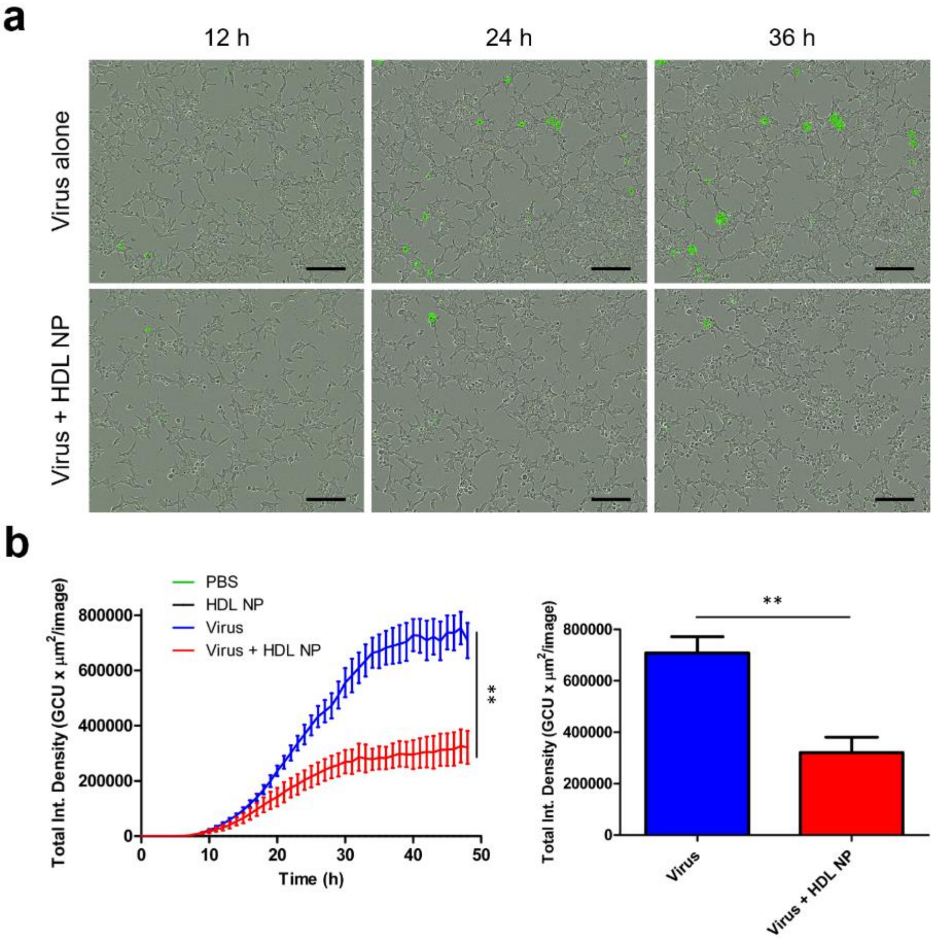

Figure 5.3: HDL NP treatment inhibits infection of SARS-CoV-2 pseudovirus in HEK293 (ACE2) cells

a) Live cell imaging snapshots of HEK293 (ACE2) cells treated with GFP-expressing SARS-CoV-2 pseudovirus with or without HDL NP (50 nM) co-treatment. b) Quantification of GFP$^+$ HEK293 (ACE2) cells (total integrated green fluorescence density) after 48 h of infection with or without HDL NP co-treatment. Scale bars = 200 µm.

Having established that HEK293 (ACE2) and HepG2 cells express SR-B1 and would therefore potentially be susceptible to HDL NP targeting, we next performed experiments to determine whether HDL NP treatment had any impact on the infectivity of a GFP-expressing SARS-CoV-2 spike protein pseudovirus (SARS-CoV-2 pseudovirus). Cells were treated with HDL NPs (50 nM) at the same time as SARS-CoV-2 pseudovirus was introduced, and cells were monitored with live cell fluorescence imaging for 48 h for GFP expression. Live cell imaging snapshots (Figure 5.3a, 5.4a) and quantifications (Figure 5.3b, 5.4b) showed that HDL NP treatment significantly inhibited SARS-CoV-2 pseudovirus infectivity by approximately 55% in HEK293 (ACE2) cells and 80% in HepG2 cells after 48 h. These results are consistent with the relative SR-B1 expression of the two cell lines, with HepG2 cells expressing more SR-B1 than HEK293 (ACE2) cells (Figure 5.1).

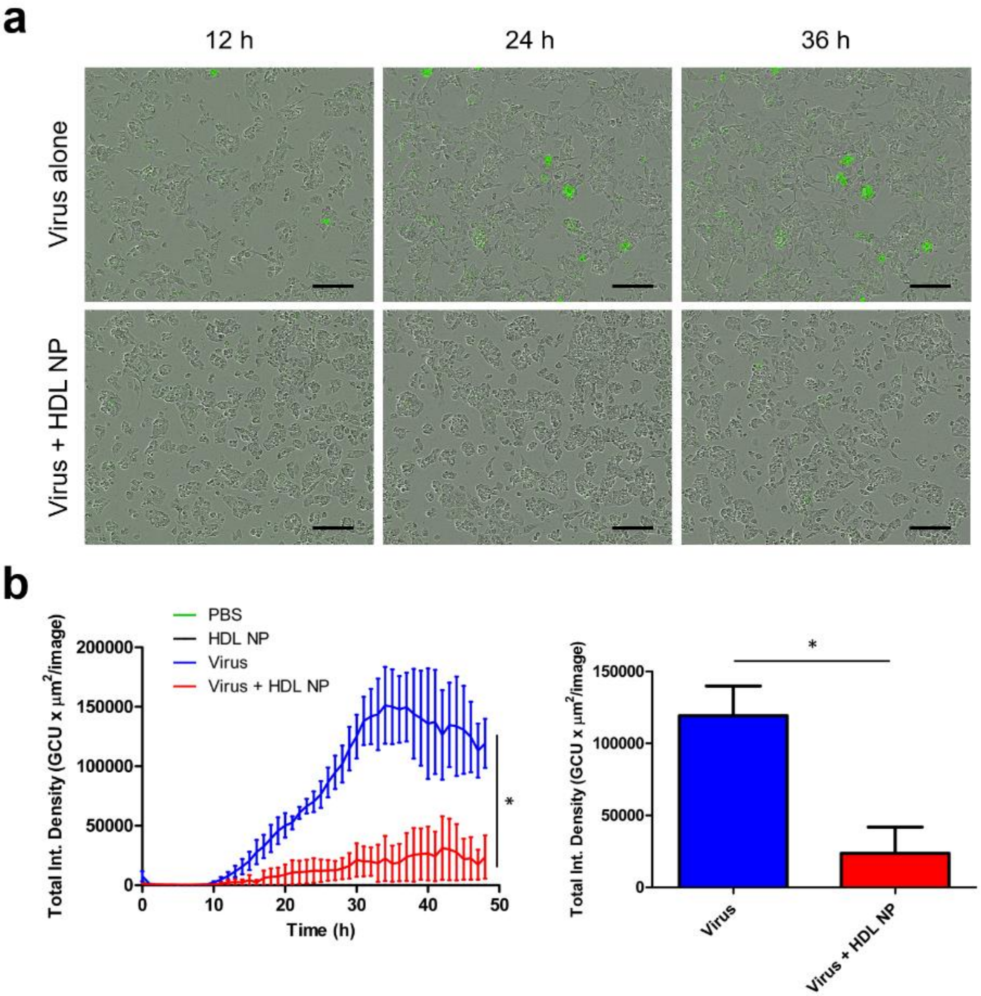

Figure 5.4: HDL NPs inhibit infection of SARS-CoV-2 pseudovirus in HepG2 cells

a) Live cell imaging snapshots of HepG2 cells treated with GFP-expressing SARS-CoV-2 pseudovirus with or without HDL NP (50 nM) co-treatment. b) Quantification of GFP$^+$ HepG2 cells (total integrated green fluorescence density) after 48 h of infection with or without HDL NP co-treatment. Scale bars = 200 µm.

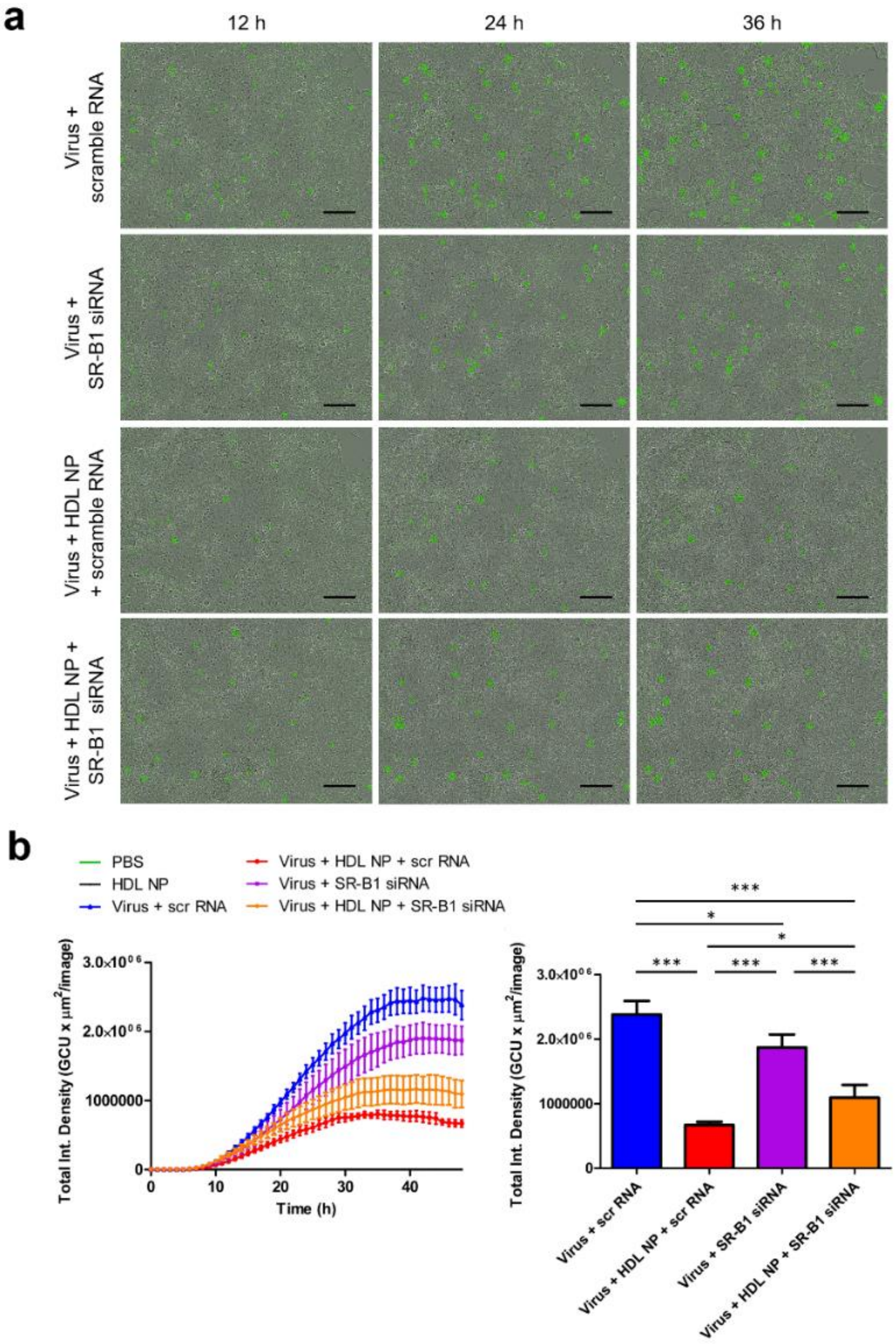

Figure 5.5: Impact of SR-B1 knockdown on SARS-CoV-2 infection and HDL NP inhibition

a) Live cell imaging of HEK293 (ACE2) cells infected with SARS-CoV-2 pseudovirus subjected to treatment regimens of HDL NPs, anti-SR-B1 siRNA, and/or scramble RNA. b) Quantification of GFP$^+$ cells (total integrated green fluorescence density) in groups infected with SARS-CoV-2 pseudovirus with or without treatment with HDL NPs, SR-B1 siRNA, or scramble RNA control. Scale bars = 200 µm.

With the knowledge the SR-B1 has been identified as a possible co-receptor for SARS-CoV-2, we then investigated whether knocking down SR-B1 had any effect on SARS-CoV-2 infectivity. To do this, we transfected HEK293 (ACE2) cells for 48 h with anti-SR-B1 siRNA or a scrambled RNA control using Lipofectamine RNAiMAX, and then introduced the SARS-CoV-2 pseudovirus and allowed infection to proceed for 48 h. We found that knocking down SR-B1 led to reduced viral entry (Figure 5.5a, top two rows; Figure 5.5b), consistent with the hypothesis that SR-B1 is a co-receptor for SARS-CoV-2.

Finally, we sought to interrogate the complex relationship between viral entry, HDL NP inhibition, and SR-B1 by knocking down SR-B1 prior to infection, in conjunction with HDL NP treatment. Viral entry experiments were performed using SARS-CoV-2 pseudovirus in HEK293 (ACE2) cells treated with anti-SR-B1 siRNA for 48 h to reduce the expression of SR-B1. Subsequently, cells were treated with SARS-CoV-2 pseudovirus with or without HDL NP (50 nM) for an additional 48 h. Live cell imaging revealed that cells treated with HDL NPs in addition to SR-B1 knockdown exhibited lower rates of viral entry than merely reducing SR-B1 alone (Figure 5.5); however, the rate of viral entry was not as low as virus + HDL NP without siRNA (Figure 5.5).

Taken together, these results demonstrate that SARS-CoV-2 viral entry is reduced upon SR-B1 knockdown, suggesting that SR-B1 is a co-receptor for SARS-CoV-2; moreover, data support that HDL NPs target SR-B1 to inhibit SARS-CoV-2 entry.

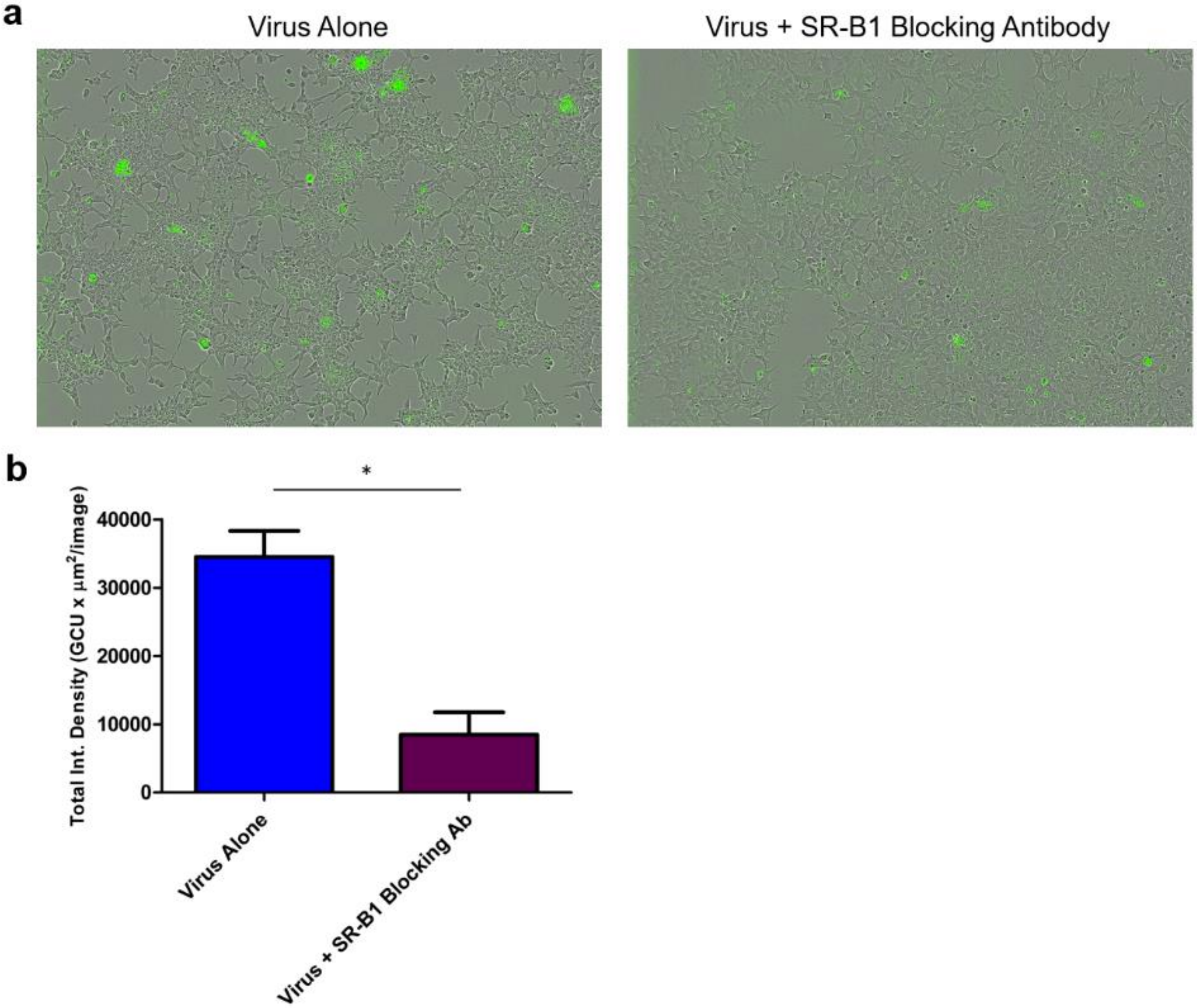

Figure 5.6: An SR-B1 blocking antibody inhibits SARS-CoV-2 infection

a) Live cell imaging of HEK293 (ACE2) cells infected with SARS-CoV-2 pseudovirus with or without an SR-B1 blocking antibody. b) Quantification of GFP$^+$ cells (total integrated green fluorescence density) in groups infected with SARS-CoV-2 pseudovirus with or without an SR-B1 blocking antibody. Scale bars = 200 µm.

5.4 Conclusions

The novel SARS-CoV-2 virus has caused a global pandemic. Recent data clearly demonstrate that cellular infection by SARS-CoV-2 is impacted by cell membrane and cellular cholesterol levels, as well as requiring the presence of the putative co-receptor SR-B1. As such, we employed our synthetic HDL NP to target SR-B1 on the surface of cultured cells known to be targets of SARS-CoV-2. Our data clearly demonstrate potent reduction of productive infection of target cells at low nM therapeutic doses of the HDL NP. Furthermore, inhibition of SARS-CoV-2 is long lasting, up to 48 hours after the initiation of culture. No untoward side effects of HDL NP therapy were observed. Furthermore, using siRNA to reduce the expression of SR-B1 in the host cell types, data show that the HDL NPs are actively targeting this receptor; and data support that SR-B1 is a co-receptor for SARS-CoV-2 entry as reduced infection is observed after SR-B1 knockdown in the absence of HDL NP treatment. Overall, HDL NPs are a promising therapeutic candidate to inhibit SARS-CoV-2 infection and are also a candidate therapy for the general reduction of viral entry to target host cells that express SR-B1 and depend upon cell membrane cholesterol and lipid raft integrity for cell entry.

5.5 Materials and Methods

Materials and Methods:

Cell culture: HEK293 cells expressing the human ACE2 receptor and HepG2 cells were cultured in DMEM containing 10% fetal bovine serum (FBS) and 1% penicillin/streptomycin (PenStrep). All cell cultures were maintained at 37°C and 5% CO_2. Frozen aliquots of 10^6 cells were used and cells were passaged fewer than 10 times for all experiments.

High-density lipoprotein nanoparticle (HDL NP) synthesis: HDL NPs were synthesized according to previously published protocols. Briefly, particle synthesis was initiated by adding apoA-1 (MyBioSource) at a 5:1 mole ratio to a colloidal suspension of 5 nm diameter citrate-stabilized gold nanoparticles (AuNP) (Ted Pella). The suspension was vortexed briefly and then incubated at RT for 1 h on a flat-bottom shaker. Next, a phospholipid--1,2-dipalmitoyl-*sn*-

glycero-3-phosphoethanolamine-*N*-[3-(2-pyridyldithio)propionate] (PDP PE) (Avanti Polar Lipids)—was added to the suspension at a 250-fold molar excess to [AuNP], followed by two additional phospholipids, 1,2-dilinoleoyl-*sn*-glycero-3-phospho-(1'-rac-glycerol) (18:2 PG) and cardiolipin (Avanti Polar Lipids), each at 125-fold molar excess to the AuNP. The lipids were incubated with the suspension in a mixture of ethanol and water (1:4) for 4 h at RT with gentle mixing on a flat-bottom shaker. The HDL NPs were then purified by tangential flow filtration. The HDL NP concentration was determined by UV-Vis spectroscopy and Beer's law (ε_{AuNP} = 9.696 x 10^6 $M^{-1}cm^{-1}$, λ_{max} = 520 nm). Particle hydrodynamic diameter was determined by dynamic light scattering.

SARS-CoV-2 pseudovirus production: First, 293T cells grown to ~70-80% confluency. Before transfection, the culture media was aspirated and changed to serum-free DMEM. Cells were transfected with a SARS-CoV-2 spike expression plasmid (NR-52310 from BEI Resources) using PEI. After 24 hours, VSV-dG*G-GFP virus was added at an MOI of 3, and incubated for 2 hours, rocking gently every 15 min. Two hours after infection, the media was replaced with DMEM with 2% FBS and then cultured for another 48 hours. Finally, the cell supernatant was removed and filtered through a 0.45 µM filter and then concentrated using an Amicon concentrator (UFC910024 from Sigma Millipore).

Viral entry inhibition experiments: HepG2 and HEK293 (ACE2) cells were seeded in 24-well or 96-well tissue culture plates at 50,000 or 10,000 cells/ well, respectively. After 24 h, cells were washed once in PBS and SARS-CoV-2 pseudovirus was added to the cells in culture medium containing 1% FBS at a concentration of 350 fluorescence-forming units (FFU)/mL. For indicated groups, HDL NPs were then added to the wells at a final concentration of 50 nM.

Plates were then placed in an IncuCyte S3 to enable live cell imaging. Phase and green fluorescence images were acquired every hour for 48 h. IncuCyte S3 analysis software was used to process the data. For experiments using SR-B1 siRNA or scramble control, the same protocol was used as above with the exception that 24 h after cell seeding, cells were treated with SR-B1 siRNA or scramble RNA using Lipofectamine RNAiMAX according to the manufacturer's instructions for 48 h prior to addition of virus with or without HDL NP.

SR-B1 knockdown experiments: HEK293 (ACE2) cells were plated at 400,000 cells per well in 6-well tissue culture plates. When cells had reached approximately 70% confluence, siRNA targeting SR-B1 (Ambion) and negative control scramble RNA (Ambion) were prepared using Lipofectamine RNAiMAX in Opti-MEM according to the manufacturer's instructions. Pre-prepared RNA was added to the cells at 30 nM and SR-B1 knockdown proceeded for 48 h. Cell lysates were harvested using M-PER lysis buffer, samples were centrifuged for 10 min at 14,000 x *g* to pellet cellular debris. The supernatant was then transferred to a new tube and protease and phosphatase inhibitors were added prior to processing for western blot.

Western blot: Sample protein concentration was determined using bicinchoninic acid (BCA) assay. Samples were then normalized to total protein, mixed with 4X Laemmli loading buffer containing β-mercaptoethanol, and boiled for 10 minutes at 100 °C. Proteins were resolved using a 4%- 20% polyacrylamide gel (120 V, 1 h) and transferred to a 0.45 μm PVDF membrane (60 V, 1 h). The membrane was blocked using 5% milk in Tris buffered saline (TBS) and Tween-20 (0.1%) for 1 hour. SR-B1 antibody was applied (1:2000) (Abcam, ab52629) and incubated overnight at 4 °C. Blot was washed 10 minutes (3X) in TBST (0.1% Tween-20) secondary goat anti-rabbit antibody (BioRad, 1721019) was applied (1:1000) for 1 hour at R.T. and blot was washed (3X) same as described above. Protein was detected using enhanced chemiluminescence (ECL) detection (Bio-Rad, 1705060) and an Azure 300 (Azure Biosystems) gel imaging system.

Chapter 6: Discussion and Future Directions

6.1 HDL mimics as therapy for ASCVD

Strategies for the development of HDL mimics have primarily fallen into one of three categories: 1) using a combination of phospholipids and apoA-1 or apoA-1 mimetic peptides to assemble particles that resemble small, discoidal HDLs, 2) using an inorganic nanoparticle as a scaffold to template the assembly of large, spherical HDL mimics upon addition of phospholipids and apoA-1, and 3) using an organic nanoparticle (e.g. polymeric nanoparticle) as a template to assemble HDL mimics upon addition of phospholipids and apoA-1. Representative members of each of these groups are 1) rHDLs, 2) gold nanoparticle templated HDL NPs, and 3) PLGA HDL NPs.

Of the different classes of HDL mimics, rHDLs have been the most extensively investigated *in vitro* and *in vivo*, and are the only class of HDL mimic that has been tested in human trials (along with apoA-1 Milano).[39] Historically, rHDLs have garnered significant interest due to their mimicry of small, discoidal HDL (or pre-β HDL), which has long been thought to be the primary HDL sub-species responsible for RCT and HDL's anti-ASCVD functions. However, multiple clinical trials have thus far failed to demonstrate therapeutic efficacy of rHDLs for reducing ASCVD burden.[39] Thus, the future of HDL-based therapies for ASCVD is currently uncertain.

Despite the ongoing prevailing view that discoidal HDLs are the dominant players in ASCVD, there is growing evidence that large spherical HDLs may play greater roles in reducing ASCVD risk that previously thought.[19-20, 165] Hence, one possible route moving forward would be to invest greater time and energy developing spherical HDL mimics for translation to the clinic. There are several obstacles that have thus far impeded the development of spherical HDL mimics, in addition to the long-held perception that they may be inferior to small, discoidal HDLs as promotors of RCT. These obstacles involve the core composition and the synthetic pathway. The use of inorganic materials as templates, such as gold nanoparticles and quantum dots, is extremely powerful for enabling the fabrication of monodisperse, sub-20 nm nanoparticles that mimic spherical HDLs in their size and surface chemistry.[25, 27] However, one of the major limitations to these approaches is that the resulting particles do not possess a dynamic core capable of loading and unloading large amounts of cholesterol and cholesteryl esters. In brief, the inorganic template consumes too much real estate within the particle and also fails to provide a hydrophobic milieu to support efficient loading of cholesterol cargo. Thus, the translational potential of these materials for ASCVD therapy is limited. Polymeric nanoparticle templates, such as PLGA, perform comparatively better for providing a hydrophobic core to support cholesterol transport; however, synthetic approaches using PLGA as a core material have thus far typically led to a heterogenous population of larger particles that don’t truly resemble HDLs in their size, shape, and composition.[46-47]

Given these limitations of existing synthetic HDL platforms, the field could stand to benefit from a robust, organic core scaffold that enables the synthesis of monodisperse, spherical HDL-like nanoparticles with a hydrophobic core that are squarely in the size regime of native HDLs. In this thesis, we have described the development of precisely such a class of core scaffolds. Our approach was motivated by an objective to fabricate HDL mimics that resembled native HDLs not only with respect to their surface chemistry but also with respect to the properties of their core. Using organic scaffold materials with externally oriented hydrophobic domains represents a robust, tunable method for assembling HDL mimics that have a dynamic core region capable of loading and unloading cholesterol, and supporting LCAT-mediated esterification. We also demonstrated that these materials successfully regress atherosclerotic plaques in LDL-R$^{-/-}$ mice by a striking 65-75% after only three weeks of treatment.

Because the synthetic approach is modular, with the ability to incorporate different linker moieties, a library of core scaffolds could be developed and screened for their ability to support supramolecular assembly of HDL-like particles, as well as their anti-ASCVD activity *in vivo*. For instance, DNA linkers could be exchanged for the incorporation of peptide linkers with hydrophobic amino acid residues which may better support cholesterol loading and esterification. Short polymer linkers such as PEG could also be tested. Other organic scaffolds with appropriate size and composition for the production of HDL mimics could also be investigated, such as dendrimers or dendrimer-nanocomposites. Moreover, while externally oriented phospholipid acyl chains were used as the hydrophobic domain in our work, other hydrophobic domains could be employed, such as cholesteryl ester conjugates, triglycerides, sphingolipids, or a variety of long-chain alkyl groups incorporated into a synthetic scaffold. Finally, the hydrophobic core of these particles may be compatible for loading various anti-ASCVD drugs, which would enable the production of dual-functioning nanoparticles. In sum, there is considerable room for further testing and optimization of the synthetic approach used here to direct the assembly of spherical HDL mimics using organic core scaffolds for their use in ASCVD. These materials may provide a new source of hope for the prospect of using synthetic HDLs for ASCVD therapy in human patients, in a landscape recently marked by significant obstacles and pitfalls.

6.2 Cholesterol dependence of metastatic signaling

An impressive amount of evidence has been reported over the past decade demonstrating that TEx can mediate intercellular communication with cells at distant pre-metastatic sites to promote PMN formation. This exosome-mediated pro-metastatic signaling can lead to radical pro-tumorigenic changes in the pre-metastatic microenvironment, including alterations in extracellular matrix composition, anti-tumor immunity, inflammation, and angiogenesis.

While there have been many contributions to our collective knowledge regarding mechanisms of exosome-mediated PMN formation, there has been considerably less attention paid to the manner in which this pro-metastatic signaling is regulated and the ways in which it might be inhibited. In this thesis we have reported that in the setting of PCa, exosome-mediated pro-metastatic signaling in bone is highly sensitive to cholesterol burden in the recipient bone marrow cells. Specifically, exosome-induced changes in gene expression, intracellular signaling, extracellular matrix composition, and osteoclast differentiation were all dependent upon cholesterol homeostasis in the target bone marrow cells. Targeted reduction of cellular cholesterol using HDL NPs inhibited each of these exosome-mediated pro-metastatic signaling processes. Importantly, exosome-mediated enhancement of metastasis itself was also prevented by HDL NP treatment in a metastatic PCa mouse model.

While our studies were performed specifically in the context of PCa, our findings have strong implications for exosome-mediated PMN formation in other cancers. In particular, exosome-induced mobilization of BMDCs has been shown to be a feature of PMN formation in both the lung and liver for melanoma and pancreatic cancer, respectively.[130, 132] In fact, mobilization of BMDCs from the marrow and subsequent infiltration at pre-metastatic sites seems to be a nearly ubiquitous feature of PMN formation.[115] Thus, our results demonstrating that reducing cellular cholesterol in bone marrow cells inhibits PCa TEx signaling suggest that targeted depletion of cholesterol in BMDCs might be an effective general tactic for inhibiting exosome-mediated PMN formation.

These results also have important implications for metastasis risk in humans. For instance, our data suggest that metabolic factors such as elevated cholesterol may be significant markers of metastasis risk for certain cancers. Follow-up studies examining the relationship between plasma cholesterol levels and bone marrow cholesterol burden would provide valuable insight for determining whether elevated plasma cholesterol could be a relevant marker to indicate heightened risk of metastasis. Alternatively, assays that directly quantify the cholesterol content of circulating BMDCs could also be useful for prognostic testing. Moreover, if cholesterol burden in bone marrow cells is positively correlated with pro-metastatic signal transduction and metastasis risk, the use of statins and other cholesterol lowering agents for metastasis prevention may be warranted in some cases. In sum, we have established a strong mechanistic link between bone marrow cholesterol burden and metastasis which could be exploited for various diagnostic and therapeutic interventions.

References

1. Casares, D.; Escriba, P. V.; Rossello, C. A., Membrane Lipid Composition: Effect on Membrane and Organelle Structure, Function and Compartmentalization and Therapeutic Avenues. *Int J Mol Sci* **2019,** *20* (9).
2. Berg, J. M., Biochemistry, revised edition. *Chem Eng News* **2001,** *79* (13), 130-130.
3. Nicolson, G. L., The Fluid-Mosaic Model of Membrane Structure: Still relevant to understanding the structure, function and dynamics of biological membranes after more than 40 years. *Bba-Biomembranes* **2014,** *1838* (6), 1451-1466.
4. Axmann, M.; Strobl, W. M.; Plochberger, B.; Stangl, H., Cholesterol transfer at the plasma membrane. *Atherosclerosis* **2019,** *290*, 111-117.
5. Feingold, K. R., Introduction to Lipids and Lipoproteins. In *Endotext*, Feingold, K. R.; Anawalt, B.; Boyce, A.; Chrousos, G.; de Herder, W. W.; Dhatariya, K.; Dungan, K.; Grossman, A.; Hershman, J. M.; Hofland, J.; Kalra, S.; Kaltsas, G.; Koch, C.; Kopp, P.; Korbonits, M.; Kovacs, C. S.; Kuohung, W.; Laferrere, B.; McGee, E. A.; McLachlan, R.; Morley, J. E.; New, M.; Purnell, J.; Sahay, R.; Singer, F.; Stratakis, C. A.; Trence, D. L.; Wilson, D. P., Eds. South Dartmouth (MA), 2000.
6. Brouillette, C. G.; Anantharamaiah, G. M.; Engler, J. A.; Borhani, D. W., Structural models of human apolipoprotein A-I: a critical analysis and review. *Biochimica et biophysica acta* **2001,** *1531* (1-2), 4-46.
7. Silva, R. A.; Huang, R.; Morris, J.; Fang, J.; Gracheva, E. O.; Ren, G.; Kontush, A.; Jerome, W. G.; Rye, K. A.; Davidson, W. S., Structure of apolipoprotein A-I in spherical high density lipoproteins of different sizes. *Proc Natl Acad Sci U S A* **2008,** *105* (34), 12176-81.
8. Rothblat, G. H.; Phillips, M. C., High-density lipoprotein heterogeneity and function in reverse cholesterol transport. *Curr Opin Lipidol* **2010,** *21* (3), 229-38.
9. Heinecke, J. W., The HDL proteome: a marker-and perhaps mediator-of coronary artery disease. *Journal of lipid research* **2009,** *50*, S167-S171.
10. Eroglu, M.; Yilmaz, N.; Yalcinkaya, S.; Ay, N.; Aydin, O.; Sezer, C., Enhanced HDL-cholesterol-associated anti-oxidant PON-1 activity in prostate cancer patients. *Kaohsiung J Med Sci* **2013,** *29* (7), 368-73.
11. Rosenblat, M.; Vaya, J.; Shih, D.; Aviram, M., Paraoxonase 1 (PON1) enhances HDL-mediated macrophage cholesterol efflux via the ABCA1 transporter in association with increased HDL binding to the cells: a possible role for lysophosphatidylcholine. *Atherosclerosis* **2005,** *179* (1), 69-77.
12. Kurano, M.; Yatomi, Y., Sphingosine 1-Phosphate and Atherosclerosis. *J Atheroscler Thromb* **2018,** *25* (1), 16-26.
13. Vickers, K. C.; Palmisano, B. T.; Shoucri, B. M.; Shamburek, R. D.; Remaley, A. T., MicroRNAs are transported in plasma and delivered to recipient cells by high-density lipoproteins. *Nature Cell Biology* **2011,** *13*, 423-433.
14. Henrich, S. E.; Thaxton, C. S., An update on synthetic high-density lipoprotein-like nanoparticles for cancer therapy. *Expert Rev Anticancer Ther* **2019,** *19* (6), 515-528.
15. Lund-Katz, S.; Phillips, M. C., High density lipoprotein structure-function and role in reverse cholesterol transport. *Subcell Biochem* **2010,** *51*, 183-227.
16. Kuai, R.; Li, D.; Chen, Y. E.; Moon, J. J.; Schwendeman, A., High-Density Lipoproteins: Nature's Multifunctional Nanoparticles. *Acs Nano* **2016,** *10* (3), 3015-3041.

17. Zhou, L.; Li, C.; Gao, L.; Wang, A., High-density lipoprotein synthesis and metabolism (Review). *Mol Med Rep* **2015,** *12* (3), 4015-4021.

18. Khera, A. V.; Rader, D. J., Future therapeutic directions in reverse cholesterol transport. *Curr Atheroscler Rep* **2010,** *12* (1), 73-81.

19. Sacks, F. M.; Jensen, M. K., From High-Density Lipoprotein Cholesterol to Measurements of Function: Prospects for the Development of Tests for High-Density Lipoprotein Functionality in Cardiovascular Disease. *Arteriosclerosis, thrombosis, and vascular biology* **2018,** *38* (3), 487-499.

20. Mendivil, C. O.; Furtado, J.; Morton, A. M.; Wang, L.; Sacks, F. M., Novel Pathways of Apolipoprotein A-I Metabolism in High-Density Lipoprotein of Different Sizes in Humans. *Arteriosclerosis, thrombosis, and vascular biology* **2016,** *36* (1), 156-65.

21. Scanu, A., Binding of human serum high density lipoprotein apoprotein with aqueous dispersions of phospholipids. *The Journal of biological chemistry* **1967,** *242* (4), 711-9.

22. Denisov, I. G.; Grinkova, Y. V.; Lazarides, A. A.; Sligar, S. G., Directed self-assembly of monodisperse phospholipid bilayer Nanodiscs with controlled size. *Journal of the American Chemical Society* **2004,** *126* (11), 3477-87.

23. Zhao, Y.; Imura, T.; Leman, L. J.; Curtiss, L. K.; Maryanoff, B. E.; Ghadiri, M. R., Mimicry of high-density lipoprotein: functional peptide-lipid nanoparticles based on multivalent peptide constructs. *Journal of the American Chemical Society* **2013,** *135* (36), 13414-24.

24. Mooberry, L. K.; Nair, M.; Paranjape, S.; McConathy, W. J.; Lacko, A. G., Receptor mediated uptake of paclitaxel from a synthetic high density lipoprotein nanocarrier. *J Drug Target* **2010,** *18* (1), 53-8.

25. Thaxton, C. S.; Daniel, W. L.; Giljohann, D. A.; Thomas, A. D.; Mirkin, C. A., Templated Spherical High Density Lipoprotein Nanoparticles. **2009**.

26. Luthi, A. J.; Lyssenko, N. N.; Quach, D.; McMahon, K. M.; Millar, J. S.; Vickers, K. C.; Rader, D. J.; Phillips, M. C.; Mirkin, C. A.; Thaxton, C. S., Robust passive and active efflux of cellular cholesterol to a designer functional mimic of high density lipoprotein. *Journal of lipid research* **2015,** *56* (5), 972-85.

27. Cormode, D. P.; Skajaa, T.; van Schooneveld, M. M.; Koole, R.; Jarzyna, P.; Lobatto, M. E.; Calcagno, C.; Barazza, A.; Gordon, R. E.; Zanzonico, P.; Fisher, E. A.; Fayad, Z. A.; Mulder, W. J., Nanocrystal core high-density lipoproteins: a multimodality contrast agent platform. *Nano Lett* **2008,** *8* (11), 3715-23.

28. Yetukuri, L.; Söderlund, S.; Koivuniemi, A.; Seppänen-Laakso, T.; Niemelä, P. S.; Hyvönen, M.; Taskinen, M.-R.; Vattulainen, I.; Jauhiainen, M.; Orešič, M., Composition and lipid spatial distribution of HDL particles in subjects with low and high HDL-cholesterol. **2010**.

29. Redmond, K. A.; Nguyen, T. S.; Ryan, R. O., All-trans-retinoic acid nanodisks. *International Journal of Pharmaceutics* **2007,** *339* (1-2), 246-250.

30. Singh, A. T. K.; Ghosh, M.; Forte, T. M.; Ryan, R. O.; Gordon, L. I., Curcumin nanodisk-induced apoptosis in mantle cell lymphoma. *Leukemia Lymphoma* **2011,** *52* (8), 1537-1543.

31. Burgess, B. L.; He, Y. M.; Baker, M. M.; Luo, B.; Carroll, S. F.; Forte, T. M.; Oda, M. N., NanoDisk containing super aggregated amphotericin B: a high therapeutic index antifungal formulation with enhanced potency. *International journal of nanomedicine* **2013,** *8*, 4733-4742.

32. McMahon, K. M.; Mutharasan, R. K.; Tripathy, S.; Veliceasa, D.; Bobeica, M.; Shumaker, D. K.; Luthi, A. J.; Helfand, B. T.; Ardehali, H.; Mirkin, C. A.; Volpert, O.; Thaxton, C. S., Biomimetic High Density Lipoprotein Nanoparticles For Nucleic Acid Delivery. **2011**.

33. Yang, M.; Jin, H. L.; Chen, J. A.; Ding, L. L.; Ng, K. K.; Lin, Q. Y.; Lovell, J. F.; Zhang, Z. H.; Zheng, G., Efficient Cytosolic Delivery of siRNA Using HDL-Mimicking Nanoparticles. *Small* **2011,** *7* (5), 568-573.

34. McMahon, K. M.; Plebanek, M. P.; Thaxton, C. S., Properties of Native High-Density Lipoproteins Inspire Synthesis of Actively Targeted In Vivo siRNA Delivery Vehicles. *Adv Funct Mater* **2016,** *26* (43), 7824-7835.

35. Ghosh, M.; Ren, G.; Simonsen, J. B.; Ryan, R. O., Cationic lipid nanodisks as an siRNA delivery vehicle. *Biochem Cell Biol* **2014,** *92* (3), 200-205.

36. Simonsen, J. B., Evaluation of reconstituted high-density lipoprotein (rHDL) as a drug delivery platform - a detailed survey of rHDL particles ranging from biophysical properties to clinical implications. *Nanomedicine* **2016,** *12* (7), 2161-2179.

37. Low, H.; Hoang, A.; Sviridov, D., Cholesterol efflux assay. *J Vis Exp* **2012,** (61), e3810.

38. Chen, J.; Zhang, X.; Millican, R.; Creutzmann, J. E.; Martin, S.; Jun, H. W., High density lipoprotein mimicking nanoparticles for atherosclerosis. *Nano Converg* **2020,** *7* (1), 6.

39. Karalis, I.; Jukema, J. W., HDL Mimetics Infusion and Regression of Atherosclerosis: Is It Still Considered a Valid Therapeutic Option? *Curr Cardiol Rep* **2018,** *20* (8), 66.

40. Nissen, S. E.; Tsunoda, T.; Tuzcu, E. M.; Schoenhagen, P.; Cooper, C. J.; Yasin, M.; Eaton, G. M.; Lauer, M. A.; Sheldon, W. S.; Grines, C. L.; Halpern, S.; Crowe, T.; Blankenship, J. C.; Kerensky, R., Effect of recombinant ApoA-I Milano on coronary atherosclerosis in patients with acute coronary syndromes: a randomized controlled trial. *JAMA* **2003,** *290* (17), 2292-300.

41. Tardif, J. C.; Ballantyne, C. M.; Barter, P.; Dasseux, J. L.; Fayad, Z. A.; Guertin, M. C.; Kastelein, J. J.; Keyserling, C.; Klepp, H.; Koenig, W.; L'Allier, P. L.; Lesperance, J.; Luscher, T. F.; Paolini, J. F.; Tawakol, A.; Waters, D. D.; Can, H. D. L. I. S. Q. A. R. I., Effects of the high-density lipoprotein mimetic agent CER-001 on coronary atherosclerosis in patients with acute coronary syndromes: a randomized trial. *Eur Heart J* **2014,** *35* (46), 3277-86.

42. Tardy, C.; Goffinet, M.; Boubekeur, N.; Cholez, G.; Ackermann, R.; Sy, G.; Keyserling, C.; Lalwani, N.; Paolini, J. F.; Dasseux, J. L.; Barbaras, R.; Baron, R., HDL and CER-001 Inverse-Dose Dependent Inhibition of Atherosclerotic Plaque Formation in apoE-/- Mice: Evidence of ABCA1 Down-Regulation. *PLoS One* **2015,** *10* (9), e0137584.

43. Gibson, C. M.; Kastelein, J. J. P.; Phillips, A. T.; Aylward, P. E.; Yee, M. K.; Tendera, M.; Nicholls, S. J.; Pocock, S.; Goodman, S. G.; Alexander, J. H.; Lincoff, A. M.; Bode, C.; Duffy, D.; Heise, M.; Berman, G.; Mears, S. J.; Tricoci, P.; Deckelbaum, L. I.; Steg, P. G.; Ridker, P.; Mehran, R., Rationale and design of ApoA-I Event Reducing in Ischemic Syndromes II (AEGIS-II): A phase 3, multicenter, double-blind, randomized, placebo-controlled, parallel-group study to investigate the efficacy and safety of CSL112 in subjects after acute myocardial infarction. *Am Heart J* **2021,** *231*, 121-127.

44. Duivenvoorden, R.; Tang, J.; Cormode, D. P.; Mieszawska, A. J.; Izquierdo-Garcia, D.; Ozcan, C.; Otten, M. J.; Zaidi, N.; Lobatto, M. E.; Rijs, S. M. v.; Priem, B.; Kuan, E. L.; Martel, C.; Hewing, B.; Sager, H.; Nahrendorf, M.; Randolph, G. J.; Stroes, E. S. G.; Fuster, V.; Fisher, E. A.; Fayad, Z. A.; Mulder, W. J. M., A statin-loaded reconstituted high-density lipoprotein nanoparticle inhibits atherosclerotic plaque inflammation. *Nature Communications* **2014,** *5*, 3065.

45. Liu, L.; He, H.; Zhang, M.; Zhang, S.; Zhang, W.; Liu, J., Hyaluronic acid-decorated reconstituted high density lipoprotein targeting atherosclerotic lesions. *Biomaterials* **2014,** *35* (27), 8002-14.

46. Sanchez-Gaytan, B. L.; Fay, F.; Lobatto, M. E.; Tang, J.; Ouimet, M.; Kim, Y.; Staay, S. E. M. v. d.; Rijs, S. M. v.; Priem, B.; Zhang, L.; Fisher, E. A.; Moore, K. J.; Langer, R.; Fayad, Z. A.; Mulder, W. J. M., HDL-Mimetic PLGA Nanoparticle To Target Atherosclerosis Plaque Macrophages. **2015**.

47. Zhang, M.; He, J.; Jiang, C.; Zhang, W.; Yang, Y.; Wang, Z.; Liu, J., Plaque-hyaluronidase-responsive high-density-lipoprotein-mimetic nanoparticles for multistage intimal-macrophage-targeted drug delivery and enhanced anti-atherosclerotic therapy. *International journal of nanomedicine* **2017,** *12*, 533-558.

48. Rink, J. S.; Sun, W.; Misener, S.; Wang, J.-J.; Zhang, Z. J.; Kibbe, M. R.; Dravid, V. P.; Venkatraman, S.; Thaxton, C. S., Nitric Oxide-Delivering High-Density Lipoprotein-like Nanoparticles as a Biomimetic Nanotherapy for Vascular Diseases. **2018**.

49. Lavker, R. M.; Kaplan, N.; McMahon, K. M.; Calvert, A. E.; Henrich, S. E.; Onay, U. V.; Lu, K. Q.; Peng, H.; Thaxton, C. S., Synthetic high-density lipoprotein nanoparticles: Good things in small packages. *Ocul Surf* **2021,** *21*, 19-26.

50. Foit, L.; Thaxton, C. S., Synthetic high-density lipoprotein-like nanoparticles potently inhibit cell signaling and production of inflammatory mediators induced by lipopolysaccharide binding Toll-like receptor 4. *Biomaterials* **2016,** *100*, 67-75.

51. Pirro, M.; Ricciuti, B.; Rader, D. J.; Catapano, A. L.; Sahebkar, A.; Banach, M., High density lipoprotein cholesterol and cancer: Marker or causative? *Prog Lipid Res* **2018,** *71*, 54-69.

52. Jafri, H.; Alsheikh-Ali, A. A.; Karas, R. H., Baseline and on-treatment high-density lipoprotein cholesterol and the risk of cancer in randomized controlled trials of lipid-altering therapy. *J Am Coll Cardiol* **2010,** *55* (25), 2846-54.

53. Yang, C.; Tian, G.; Mi, J.; Wei, X.; Li, X.; Li, X.; Wang, W.; Wang, B., Causal relevance of circulating high-density lipoprotein cholesterol with cancer: a Mendelian randomization meta-analysis. *Scientific reports* **2015,** *5*, 9495.

54. Scribano, D.; Baroni, S.; Pagano, L.; Zuppi, C.; Leone, G.; Giardino, B., Return to normal values of lipid pattern after effective chemotherapy in acute lymphoblastic leukemia. *Haematologica* **1996,** *81* (4), 343-345.

55. Lv, Y.; Miao, L. Y.; Chen, Q. F.; Li, Y.; Shi, Z. X.; Ding, X. S., Monitoring of high-density lipoprotein cholesterol level is predictive of EGFR mutation and efficacy of EGFR-TKI in patients with advanced lung adenocarcinoma. *Oncotargets Ther* **2016,** *9*, 461-468.

56. Zhang, Z.; Cao, W.; Jin, H.; Lovell, J. F.; Yang, M.; Ding, L.; Chen, J.; Corbin, I.; Luo, Q.; Zheng, G., Biomimetic nanocarrier for direct cytosolic drug delivery. *Angew Chem Int Ed Engl* **2009,** *48* (48), 9171-5.

57. Lim, U.; Gayles, T.; Katki, H. A.; Stolzenberg-Solomon, R.; Weinstein, S. J.; Pietinen, P.; Taylor, P. R.; Virtamo, J.; Albanes, D., Serum high-density lipoprotein cholesterol and risk of non-hodgkin lymphoma. *Cancer Res* **2007,** *67* (11), 5569-74.

58. Kucharska-Newton, A. M.; Rosamond, W. D.; Mink, P. J.; Alberg, A. J.; Shahar, E.; Folsom, A. R., HDL-cholesterol and incidence of breast cancer in the ARIC cohort study. *Ann Epidemiol* **2008,** *18* (9), 671-7.

59. Furberg, A. S.; Veierod, M. B.; Wilsgaard, T.; Bernstein, L.; Thune, I., Serum high-density lipoprotein cholesterol, metabolic profile, and breast cancer risk. *J Natl Cancer Inst* **2004,** *96* (15), 1152-60.

60. Penson, P.; Long, D. L.; Howard, G.; Howard, V. J.; Jones, S. R.; Martin, S. S.; Mikhailidis, D. P.; Muntner, P.; Rizzo, M.; Rader, D. J.; Safford, M. M.; Sahebkar, A.; Toth, P. P.; Banach, M., Associations between cardiovascular disease, cancer, and very low high-density lipoprotein cholesterol in the REasons for Geographical and Racial Differences in Stroke (REGARDS) study. *Cardiovasc Res* **2019,** *115* (1), 204-212.

61. Cooper, R. A., Influence of Increased Membrane Cholesterol on Membrane Fluidity and Cell-Function in Human Red Blood-Cells. *J Supramol Str Cell* **1978,** *8* (4), 413-430.

62. Simons, K.; Ehehalt, R., Cholesterol, lipid rafts, and disease. *J Clin Invest* **2002,** *110* (5), 597-603.

63. Porter, F. D.; Herman, G. E., Malformation syndromes caused by disorders of cholesterol synthesis. *Journal of lipid research* **2011,** *52* (1), 6-34.

64. Rudney, H.; Sexton, R. C., Regulation of Cholesterol-Biosynthesis. *Annu Rev Nutr* **1986,** *6*, 245-272.

65. Gutierrez-Pajares, J. L.; Ben Hassen, C.; Chevalier, S.; Frank, P. G., SR-BI: Linking Cholesterol and Lipoprotein Metabolism with Breast and Prostate Cancer. *Front Pharmacol* **2016,** *7*, 338.

66. Rink, J. S.; Yang, S.; Cen, O.; Taxter, T.; McMahon, K. M.; Misener, S.; Behdad, A.; Longnecker, R.; Gordon, L. I.; Thaxton, C. S., Rational Targeting of Cellular Cholesterol in Diffuse Large B-Cell Lymphoma (DLBCL) Enabled by Functional Lipoprotein Nanoparticles: A Therapeutic Strategy Dependent on Cell of Origin. *Mol Pharm* **2017,** *14* (11), 4042-4051.

67. Monroe, J. G., ITAM-mediated tonic signalling through pre-BCR and BCR complexes. *Nat Rev Immunol* **2006,** *6* (4), 283-94.

68. Juszczynski, P.; Chen, L.; O'Donnell, E.; Polo, J. M.; Ranuncolo, S. M.; Dalla-Favera, R.; Melnick, A.; Shipp, M. A., BCL6 modulates tonic BCR signaling in diffuse large B-cell lymphomas by repressing the SYK phosphatase, PTPROt. *Blood* **2009,** *114* (26), 5315-21.

69. Spady, D. K., Lipoproteins in biological fluids and compartments: synthesis, interconversions, and catabolism. *Targeted Diagn Ther* **1991,** *5*, 1-44.

70. Goldstein, J. L.; Brown, M. S., The LDL receptor. *Arteriosclerosis, thrombosis, and vascular biology* **2009,** *29* (4), 431-8.

71. Pirillo, A.; Catapano, A. L.; Norata, G. D., Biological consequences of dysfunctional HDL. *Curr Med Chem* **2018**.

72. Trigatti, B. L., SR-B1 and PDZK1: partners in HDL regulation. *Curr Opin Lipidol* **2017,** *28* (2), 201-208.

73. Mooberry, L. K.; Sabnis, N. A.; Panchoo, M.; Nagarajan, B.; Lacko, A. G., Targeting the SR-B1 Receptor as a Gateway for Cancer Therapy and Imaging. *Frontiers in Pharmacology* **2016,** *7*.

74. Li, J.; Wang, J.; Li, M.; Yin, L.; Li, X.-A.; Zhang, T.-G., Up-regulated expression of scavenger receptor class B type 1 (SR-B1) is associated with malignant behaviors and poor prognosis of breast cancer. *Pathology - Research and Practice* **2016,** *212* (6), 555-559.

75. Ganjali, S.; Ricciuti, B.; Pirro, M.; Butler, A. E.; Atkin, S. L.; Banach, M.; Sahebkar, A., High-Density Lipoprotein Components and Functionality in Cancer: State-of-the-Art. *Trends Endocrinol Metab* **2019,** *30* (1), 12-24.

76. Plebanek, M. P.; Bhaumik, D.; Thaxton, C. S., HDL and the golden key to cancer immunity? *Oncoscience* **2018,** *5* (5-6), 164-166.

77. Vanpouille-Box, C.; Diamond, J. M.; Pilones, K. A.; Zavadil, J.; Babb, J. S.; Formenti, S. C.; Barcellos-Hoff, M. H.; Demaria, S., TGF beta Is a Master Regulator of Radiation Therapy-Induced Antitumor Immunity. *Cancer Research* **2015,** *75* (11), 2232-2242.

78. Kumar, V.; Patel, S.; Tcyganov, E.; Gabrilovich, D. I., The Nature of Myeloid-Derived Suppressor Cells in the Tumor Microenvironment. *Trends Immunol* **2016,** *37* (3), 208-220.

79. Plebanek, M. P.; Bhaumik, D.; Bryce, P. J.; Thaxton, C. S., Scavenger Receptor Type B1 and Lipoprotein Nanoparticle Inhibit Myeloid Derived Suppressor Cells. **2017**.

80. Yvan-Charvet, L.; Pagler, T.; Gautier, E. L.; Avagyan, S.; Siry, R. L.; Han, S.; Welch, C. L.; Wang, N.; Randolph, G. J.; Snoeck, H. W.; Tall, A. R., ATP-binding cassette transporters and HDL suppress hematopoietic stem cell proliferation. *Science* **2010,** *328* (5986), 1689-93.

81. Yvan-Charvet, L.; Wang, N.; Tall, A. R., Role of HDL, ABCA1, and ABCG1 transporters in cholesterol efflux and immune responses. *Arteriosclerosis, thrombosis, and vascular biology* **2010,** *30* (2), 139-43.

82. Hoofnagle, A. N.; Heinecke, J. W., Lipoproteomics: using mass spectrometry-based proteomics to explore the assembly, structure, and function of lipoproteins. *Journal of lipid research* **2009,** *50* (10), 1967-1975.

83. Mazidi, M.; Mikhailidis, D. P.; Banach, M., Associations between risk of overall mortality, cause-specific mortality and level of inflammatory factors with extremely low and high high-density lipoprotein cholesterol levels among American adults. *Int J Cardiol* **2019,** *276*, 242-247.

84. Nordestgaard, B. G.; Madsen, C. M.; Varbo, A., Extreme High High-Density Lipoprotein Cholesterol Is Paradoxically Associated with High Mortality in Men and Women: Two Prospective Cohort Studies. *Atherosclerosis* **2017,** *263*, E89-E89.

85. Song, G.; Petschauer, J. S.; Madden, A. J.; Zamboni, W. C., Nanoparticles and the mononuclear phagocyte system: pharmacokinetics and applications for inflammatory diseases. *Curr Rheumatol Rev* **2014,** *10* (1), 22-34.

86. Lundqvist, M.; Stigler, J.; Elia, G.; Lynch, I.; Cedervall, T.; Dawson, K. A., Nanoparticle size and surface properties determine the protein corona with possible implications for biological impacts. *Proc Natl Acad Sci U S A* **2008,** *105* (38), 14265-70.

87. Choi, H. S.; Liu, W.; Misra, P.; Tanaka, E.; Zimmer, J. P.; Ipe, B. I.; Bawendi, M. G.; Frangioni, J. V., Renal clearance of quantum dots. *Nature Biotechnology* **2007,** *25* (10), 1165-1170.

88. Yang, H.; Fogo, A. B.; Kon, V., Kidneys: key modulators of high-density lipoprotein levels and function. *Curr Opin Nephrol Hypertens* **2016,** *25* (3), 174-9.

89. Keyserling, C. H.; Barbaras, R.; Benghozi, R.; Dasseux, J. L., Development of CER-001: Preclinical Dose Selection Through to Phase I Clinical Findings. *Clin Drug Investig* **2017,** *37* (5), 483-491.

90. Andrews, J.; Janssan, A.; Nguyen, T.; Pisaniello, A. D.; Scherer, D. J.; Kastelein, J. J.; Merkely, B.; Nissen, S. E.; Ray, K.; Schwartz, G. G.; Worthley, S. G.; Keyserling, C.; Dasseux, J. L.; Butters, J.; Girardi, J.; Miller, R.; Nicholls, S. J., Effect of serial infusions of reconstituted high-density lipoprotein (CER-001) on coronary atherosclerosis: rationale and design of the CARAT study. *Cardiovasc Diagn Ther* **2017,** *7* (1), 45-51.

91. Easton, R.; Gille, A.; D'Andrea, D.; Davis, R.; Wright, S. D.; Shear, C., A Multiple Ascending Dose Study of CSL112, an Infused Formulation of ApoA-I. *J Clin Pharmacol* **2014,** *54* (3), 301-310.

92. Li, D.; Fawaz, M. V.; Morin, E. E.; Ming, R.; Sviridov, D.; Tang, J.; Ackermann, R.; Olsen, K.; Remaley, A. T.; Schwendeman, A., Effect of Synthetic High Density Lipoproteins Modification with Polyethylene Glycol on Pharmacokinetics and Pharmacodynamics. *Mol Pharm* **2018,** *15* (1), 83-96.

93. Murphy, A. J.; Funt, S.; Gorman, D.; Tall, A. R.; Wang, N., Pegylation of high-density lipoprotein decreases plasma clearance and enhances antiatherogenic activity. *Circ Res* **2013,** *113* (1), e1-e9.

94. Tang, J.; Kuai, R.; Yuan, W.; Drake, L.; Moon, J. J.; Schwendeman, A., Effect of size and pegylation of liposomes and peptide-based synthetic lipoproteins on tumor targeting. *Nanomedicine* **2017,** *13* (6), 1869-1878.

95. Verhoef, J. J.; Carpenter, J. F.; Anchordoquy, T. J.; Schellekens, H., Potential induction of anti-PEG antibodies and complement activation toward PEGylated therapeutics. *Drug Discov Today* **2014,** *19* (12), 1945-52.

96. Verhoef, J. J. F.; Anchordoquy, T. J., Questioning the use of PEGylation for drug delivery. *Drug Deliv Transl Re* **2013,** *3* (6), 499-503.

97. Yuan, B.; Wu, C.; Wang, X.; Wang, D.; Liu, H.; Guo, L.; Li, X. A.; Han, J.; Feng, H., High scavenger receptor class B type I expression is related to tumor aggressiveness and poor prognosis in breast cancer. *Tumour Biol* **2016,** *37* (3), 3581-8.

98. Johnson, R.; Sabnis, N.; Sun, X.; Ahluwalia, R.; Lacko, A. G., SR-B1-targeted nanodelivery of anti-cancer agents: a promising new approach to treat triple-negative breast cancer. *Breast Cancer (Dove Med Press)* **2017,** *9*, 383-392.

99. Wang, W.; Chen, K.; Su, Y.; Zhang, J.; Li, M.; Zhou, J., Lysosome-Independent Intracellular Drug/Gene Codelivery by Lipoprotein-Derived Nanovector for Synergistic Apoptosis-Inducing Cancer-Targeted Therapy. **2018**.

100. Kuai, R.; Subramanian, C.; White, P. T.; Timmermann, B. N.; Moon, J. J.; Cohen, M. S.; Schwendeman, A., Synthetic high-density lipoprotein nanodisks for targeted withalongolide delivery to adrenocortical carcinoma. *International journal of nanomedicine* **2017,** *12*, 6581-6594.

101. Wang, Y.; Wang, C.; Ding, Y.; Li, J.; Li, M.; Liang, X.; Zhou, J.; Wang, W., Biomimetic HDL nanoparticle mediated tumor targeted delivery of indocyanine green for enhanced photodynamic therapy. *Colloids Surf B Biointerfaces* **2016,** *148*, 533-540.

102. Plebanek, M. P.; Mutharasan, R. K.; Volpert, O.; Matov, A.; Gatlin, J. C.; Thaxton, C. S., Nanoparticle Targeting and Cholesterol Flux Through Scavenger Receptor Type B-1 Inhibits Cellular Exosome Uptake. *Scientific reports* **2015,** *5*, 15724.

103. Thery, C.; Witwer, K. W.; Aikawa, E.; Alcaraz, M. J.; Anderson, J. D.; Andriantsitohaina, R.; Antoniou, A.; Arab, T.; Archer, F.; Atkin-Smith, G. K.; Ayre, D. C.; Bach, J. M.; Bachurski, D.; Baharvand, H.; Balaj, L.; Baldacchino, S.; Bauer, N. N.; Baxter, A. A.; Bebawy, M.; Beckham, C.; Bedina Zavec, A.; Benmoussa, A.; Berardi, A. C.; Bergese, P.; Bielska, E.; Blenkiron, C.; Bobis-Wozowicz, S.; Boilard, E.; Boireau, W.; Bongiovanni, A.; Borras, F. E.; Bosch, S.; Boulanger, C. M.; Breakefield, X.; Breglio, A. M.; Brennan, M. A.; Brigstock, D. R.; Brisson, A.; Broekman, M. L.; Bromberg, J. F.; Bryl-Gorecka, P.; Buch, S.; Buck, A. H.; Burger, D.; Busatto, S.; Buschmann, D.; Bussolati, B.; Buzas, E. I.; Byrd, J. B.;

Camussi, G.; Carter, D. R.; Caruso, S.; Chamley, L. W.; Chang, Y. T.; Chen, C.; Chen, S.; Cheng, L.; Chin, A. R.; Clayton, A.; Clerici, S. P.; Cocks, A.; Cocucci, E.; Coffey, R. J.; Cordeiro-da-Silva, A.; Couch, Y.; Coumans, F. A.; Coyle, B.; Crescitelli, R.; Criado, M. F.; D'Souza-Schorey, C.; Das, S.; Datta Chaudhuri, A.; de Candia, P.; De Santana, E. F.; De Wever, O.; Del Portillo, H. A.; Demaret, T.; Deville, S.; Devitt, A.; Dhondt, B.; Di Vizio, D.; Dieterich, L. C.; Dolo, V.; Dominguez Rubio, A. P.; Dominici, M.; Dourado, M. R.; Driedonks, T. A.; Duarte, F. V.; Duncan, H. M.; Eichenberger, R. M.; Ekstrom, K.; El Andaloussi, S.; Elie-Caille, C.; Erdbrugger, U.; Falcon-Perez, J. M.; Fatima, F.; Fish, J. E.; Flores-Bellver, M.; Forsonits, A.; Frelet-Barrand, A.; Fricke, F.; Fuhrmann, G.; Gabrielsson, S.; Gamez-Valero, A.; Gardiner, C.; Gartner, K.; Gaudin, R.; Gho, Y. S.; Giebel, B.; Gilbert, C.; Gimona, M.; Giusti, I.; Goberdhan, D. C.; Gorgens, A.; Gorski, S. M.; Greening, D. W.; Gross, J. C.; Gualerzi, A.; Gupta, G. N.; Gustafson, D.; Handberg, A.; Haraszti, R. A.; Harrison, P.; Hegyesi, H.; Hendrix, A.; Hill, A. F.; Hochberg, F. H.; Hoffmann, K. F.; Holder, B.; Holthofer, H.; Hosseinkhani, B.; Hu, G.; Huang, Y.; Huber, V.; Hunt, S.; Ibrahim, A. G.; Ikezu, T.; Inal, J. M.; Isin, M.; Ivanova, A.; Jackson, H. K.; Jacobsen, S.; Jay, S. M.; Jayachandran, M.; Jenster, G.; Jiang, L.; Johnson, S. M.; Jones, J. C.; Jong, A.; Jovanovic-Talisman, T.; Jung, S.; Kalluri, R.; Kano, S. I.; Kaur, S.; Kawamura, Y.; Keller, E. T.; Khamari, D.; Khomyakova, E.; Khvorova, A.; Kierulf, P.; Kim, K. P.; Kislinger, T.; Klingeborn, M.; Klinke, D. J., 2nd; Kornek, M.; Kosanovic, M. M.; Kovacs, A. F.; Kramer-Albers, E. M.; Krasemann, S.; Krause, M.; Kurochkin, I. V.; Kusuma, G. D.; Kuypers, S.; Laitinen, S.; Langevin, S. M.; Languino, L. R.; Lannigan, J.; Lasser, C.; Laurent, L. C.; Lavieu, G.; Lazaro-Ibanez, E.; Le Lay, S.; Lee, M. S.; Lee, Y. X. F.; Lemos, D. S.; Lenassi, M.; Leszczynska, A.; Li, I. T.; Liao, K.; Libregts, S. F.; Ligeti, E.; Lim, R.; Lim, S. K.; Line, A.; Linnemannstons, K.; Llorente, A.; Lombard, C. A.; Lorenowicz, M. J.; Lorincz, A. M.; Lotvall, J.; Lovett, J.; Lowry, M. C.; Loyer, X.; Lu, Q.; Lukomska, B.; Lunavat, T. R.; Maas, S. L.; Malhi, H.; Marcilla, A.; Mariani, J.; Mariscal, J.; Martens-Uzunova, E. S.; Martin-Jaular, L.; Martinez, M. C.; Martins, V. R.; Mathieu, M.; Mathivanan, S.; Maugeri, M.; McGinnis, L. K.; McVey, M. J.; Meckes, D. G., Jr.; Meehan, K. L.; Mertens, I.; Minciacchi, V. R.; Moller, A.; Moller Jorgensen, M.; Morales-Kastresana, A.; Morhayim, J.; Mullier, F.; Muraca, M.; Musante, L.; Mussack, V.; Muth, D. C.; Myburgh, K. H.; Najrana, T.; Nawaz, M.; Nazarenko, I.; Nejsum, P.; Neri, C.; Neri, T.; Nieuwland, R.; Nimrichter, L.; Nolan, J. P.; Nolte-'t Hoen, E. N.; Noren Hooten, N.; O'Driscoll, L.; O'Grady, T.; O'Loghlen, A.; Ochiya, T.; Olivier, M.; Ortiz, A.; Ortiz, L. A.; Osteikoetxea, X.; Ostergaard, O.; Ostrowski, M.; Park, J.; Pegtel, D. M.; Peinado, H.; Perut, F.; Pfaffl, M. W.; Phinney, D. G.; Pieters, B. C.; Pink, R. C.; Pisetsky, D. S.; Pogge von Strandmann, E.; Polakovicova, I.; Poon, I. K.; Powell, B. H.; Prada, I.; Pulliam, L.; Quesenberry, P.; Radeghieri, A.; Raffai, R. L.; Raimondo, S.; Rak, J.; Ramirez, M. I.; Raposo, G.; Rayyan, M. S.; Regev-Rudzki, N.; Ricklefs, F. L.; Robbins, P. D.; Roberts, D. D.; Rodrigues, S. C.; Rohde, E.; Rome, S.; Rouschop, K. M.; Rughetti, A.; Russell, A. E.; Saa, P.; Sahoo, S.; Salas-Huenuleo, E.; Sanchez, C.; Saugstad, J. A.; Saul, M. J.; Schiffelers, R. M.; Schneider, R.; Schoyen, T. H.; Scott, A.; Shahaj, E.; Sharma, S.; Shatnyeva, O.; Shekari, F.; Shelke, G. V.; Shetty, A. K.; Shiba, K.; Siljander, P. R.; Silva, A. M.; Skowronek, A.; Snyder, O. L., 2nd; Soares, R. P.; Sodar, B. W.; Soekmadji, C.; Sotillo, J.; Stahl, P. D.; Stoorvogel, W.; Stott, S. L.; Strasser, E. F.; Swift, S.; Tahara, H.; Tewari, M.; Timms, K.; Tiwari, S.; Tixeira, R.; Tkach, M.; Toh, W. S.; Tomasini, R.; Torrecilhas, A. C.; Tosar, J. P.; Toxavidis, V.; Urbanelli, L.; Vader, P.; van Balkom, B. W.; van der Grein, S. G.; Van Deun, J.; van Herwijnen, M. J.; Van Keuren-Jensen, K.; van Niel, G.; van Royen, M. E.; van Wijnen, A. J.; Vasconcelos, M. H.; Vechetti, I. J., Jr.; Veit, T. D.; Vella, L. J.;

Velot, E.; Verweij, F. J.; Vestad, B.; Vinas, J. L.; Visnovitz, T.; Vukman, K. V.; Wahlgren, J.; Watson, D. C.; Wauben, M. H.; Weaver, A.; Webber, J. P.; Weber, V.; Wehman, A. M.; Weiss, D. J.; Welsh, J. A.; Wendt, S.; Wheelock, A. M.; Wiener, Z.; Witte, L.; Wolfram, J.; Xagorari, A.; Xander, P.; Xu, J.; Yan, X.; Yanez-Mo, M.; Yin, H.; Yuana, Y.; Zappulli, V.; Zarubova, J.; Zekas, V.; Zhang, J. Y.; Zhao, Z.; Zheng, L.; Zheutlin, A. R.; Zickler, A. M.; Zimmermann, P.; Zivkovic, A. M.; Zocco, D.; Zuba-Surma, E. K., Minimal information for studies of extracellular vesicles 2018 (MISEV2018): a position statement of the International Society for Extracellular Vesicles and update of the MISEV2014 guidelines. *J Extracell Vesicles* **2018,** *7* (1), 1535750.

104. Kalra, H.; Drummen, G. P.; Mathivanan, S., Focus on Extracellular Vesicles: Introducing the Next Small Big Thing. *Int J Mol Sci* **2016,** *17* (2), 170.

105. Kalluri, R.; LeBleu, V. S., The biology, function, and biomedical applications of exosomes. *Science* **2020,** *367* (6478).

106. Zhang, Y.; Liu, Y.; Liu, H.; Tang, W. H., Exosomes: biogenesis, biologic function and clinical potential. *Cell Biosci* **2019,** *9*, 19.

107. Emanueli, C.; Shearn, A. I.; Angelini, G. D.; Sahoo, S., Exosomes and exosomal miRNAs in cardiovascular protection and repair. *Vascul Pharmacol* **2015,** *71*, 24-30.

108. Jadli, A. S.; Ballasy, N.; Edalat, P.; Patel, V. B., Inside(sight) of tiny communicator: exosome biogenesis, secretion, and uptake. *Mol Cell Biochem* **2020,** *467* (1-2), 77-94.

109. Larios, J.; Mercier, V.; Roux, A.; Gruenberg, J., ALIX- and ESCRT-III-dependent sorting of tetraspanins to exosomes. *J Cell Biol* **2020,** *219* (3).

110. Johnstone, R. M.; Mathew, A.; Mason, A. B.; Teng, K., Exosome formation during maturation of mammalian and avian reticulocytes: evidence that exosome release is a major route for externalization of obsolete membrane proteins. *Journal of cellular physiology* **1991,** *147* (1), 27-36.

111. Brinton, L. T.; Sloane, H. S.; Kester, M.; Kelly, K. A., Formation and role of exosomes in cancer. *Cell Mol Life Sci* **2015,** *72* (4), 659-71.

112. Lobb, R. J.; Lima, L. G.; Moller, A., Exosomes: Key mediators of metastasis and pre-metastatic niche formation. *Semin Cell Dev Biol* **2017,** *67*, 3-10.

113. Meldolesi, J., Exosomes and Ectosomes in Intercellular Communication. *Curr Biol* **2018,** *28* (8), R435-R444.

114. Henrich, S. E.; McMahon, K. M.; Plebanek, M. P.; Calvert, A. E.; Feliciano, T. J.; Parrish, S.; Tavora, F.; Mega, A.; De Souza, A.; Carneiro, B. A.; Thaxton, C. S., Prostate cancer extracellular vesicles mediate intercellular communication with bone marrow cells and promote metastasis in a cholesterol-dependent manner. *J Extracell Vesicles* **2020,** *10* (2), e12042.

115. Peinado, H.; Zhang, H. Y.; Matei, I. R.; Costa-Silva, B.; Hoshino, A.; Rodrigues, G.; Psaila, B.; Kaplan, R. N.; Bromberg, J. F.; Kang, Y. B.; Bissell, M. J.; Cox, T. R.; Giaccia, A. J.; Erler, J. T.; Hiratsuka, S.; Ghajar, C. M.; Lyden, D., Pre-metastatic niches: organ-specific homes for metastases. *Nature Reviews Cancer* **2017,** *17* (5), 302-317.

116. Tian, T.; Zhu, Y. L.; Zhou, Y. Y.; Liang, G. F.; Wang, Y. Y.; Hu, F. H.; Xiao, Z. D., Exosome uptake through clathrin-mediated endocytosis and macropinocytosis and mediating miR-21 delivery. *The Journal of biological chemistry* **2014,** *289* (32), 22258-67.

117. Gupta, S. K.; Bang, C.; Thum, T., Circulating microRNAs as biomarkers and potential paracrine mediators of cardiovascular disease. *Circ Cardiovasc Genet* **2010,** *3* (5), 484-8.

118. Zhang, H.; Freitas, D.; Kim, H. S.; Fabijanic, K.; Li, Z.; Chen, H.; Mark, M. T.; Molina, H.; Martin, A. B.; Bojmar, L.; Fang, J.; Rampersaud, S.; Hoshino, A.; Matei, I.; Kenific, C. M.;

Nakajima, M.; Mutvei, A. P.; Sansone, P.; Buehring, W.; Wang, H.; Jimenez, J. P.; Cohen-Gould, L.; Paknejad, N.; Brendel, M.; Manova-Todorova, K.; Magalhaes, A.; Ferreira, J. A.; Osorio, H.; Silva, A. M.; Massey, A.; Cubillos-Ruiz, J. R.; Galletti, G.; Giannakakou, P.; Cuervo, A. M.; Blenis, J.; Schwartz, R.; Brady, M. S.; Peinado, H.; Bromberg, J.; Matsui, H.; Reis, C. A.; Lyden, D., Identification of distinct nanoparticles and subsets of extracellular vesicles by asymmetric flow field-flow fractionation. *Nat Cell Biol* **2018,** *20* (3), 332-343.

119. Kowal, J.; Arras, G.; Colombo, M.; Jouve, M.; Morath, J. P.; Primdal-Bengtson, B.; Dingli, F.; Loew, D.; Tkach, M.; Thery, C., Proteomic comparison defines novel markers to characterize heterogeneous populations of extracellular vesicle subtypes. *Proc Natl Acad Sci U S A* **2016,** *113* (8), E968-77.

120. Mizutani, K.; Terazawa, R.; Kameyama, K.; Kato, T.; Horie, K.; Tsuchiya, T.; Seike, K.; Ehara, H.; Fujita, Y.; Kawakami, K.; Ito, M.; Deguchi, T., Isolation of prostate cancer-related exosomes. *Anticancer research* **2014,** *34* (7), 3419-23.

121. Azmi, A. S.; Bao, B.; Sarkar, F. H., Exosomes in Cancer Development, Metastasis and Drug Resistance: A Comprehensive Review. *Cancer metastasis reviews* **2013,** *32* (0).

122. Kwon, Y.; Kim, M.; Kim, Y.; Jung, H. S.; Jeoung, D., Exosomal MicroRNAs as Mediators of Cellular Interactions Between Cancer Cells and Macrophages. *Front Immunol* **2020,** *11*.

123. Zhang, X.; Yuan, X.; Shi, H.; Wu, L.; Qian, H.; Xu, W., Exosomes in cancer: small particle, big player. In *J Hematol Oncol*, 2015; Vol. 8.

124. Zhang, L.; Department of Urology, T. F. A. H. o. C. M. U., Chongqing 400016, P.R. China; Wu, X.; Department of Urology, T. F. A. H. o. C. M. U., Chongqing 400016, P.R. China; Luo, C.; College of Laboratory Medicine, K. L. o. M. D. i. t. M. o. E., Chongqing Medical University, Chongqing 400016, P.R. China; Chen, X.; Department of Urology, T. F. A. H. o. C. M. U., Chongqing 400016, P.R. China; Yang, L.; Department of Urology, T. F. A. H. o. C. M. U., Chongqing 400016, P.R. China; Tao, J.; College of Laboratory Medicine, K. L. o. M. D. i. t. M. o. E., Chongqing Medical University, Chongqing 400016, P.R. China; Shi, J.; Department of Urology, T. F. A. H. o. C. M. U., Chongqing 400016, P.R. China, The 786-0 renal cancer cell-derived exosomes promote angiogenesis by downregulating the expression of hepatocyte cell adhesion molecule. *Molecular Medicine Reports* **2016,** *8* (1), 272-276.

125. Umezu, T.; Tadokoro, H.; Azuma, K.; Yoshizawa, S.; Ohyashiki, K.; Ohyashiki, J. H., Exosomal miR-135b shed from hypoxic multiple myeloma cells enhances angiogenesis by targeting factor-inhibiting HIF-1. **2014**.

126. Takano, Y.; Masuda, T.; Iinuma, H.; Yamaguchi, R.; Sato, K.; Tobo, T.; Hirata, H.; Kuroda, Y.; Nambara, S.; Hayashi, N.; Iguchi, T.; Ito, S.; Eguchi, H.; Ochiya, T.; Yanaga, K.; Miyano, S.; Mimori, K., Circulating exosomal microRNA-203 is associated with metastasis possibly via inducing tumor-associated macrophages in colorectal cancer. *Oncotarget* **2017,** *8* (45), 78598-78613.

127. Han, Q.; Yin, C.; Zhao, H.; Zhang, J., SALL4-mediated upregulation of exosomal miR-146a-5p drives T-cell exhaustion by M2 tumor-associated macrophages in HCC. *Eur J Immunol* **2019,** *49*, 1273-1273.

128. Yang, J.; Zhang, Z.; Chen, C.; Liu, Y.; Si, Q.; Chuang, T. H.; Li, N.; Gomez-Cabrero, A.; Reisfeld, R. A.; Xiang, R.; Luo, Y., MicroRNA-19a-3p inhibits breast cancer progression and metastasis by inducing macrophage polarization through downregulated expression of Fra-1 proto-oncogene. *Oncogene* **2014,** *33* (23), 3014-3023.

129. Richards, K. E.; Zeleniak, A. E.; Fishel, M. L.; Wu, J.; Littlepage, L. E.; Hill, R., Cancer-associated fibroblast exosomes regulate survival and proliferation of pancreatic cancer cells. *Oncogene* **2017,** *36* (13), 1770-1778.

130. Peinado, H.; Alečković, M.; Lavotshkin, S.; Matei, I.; Costa-Silva, B.; Moreno-Bueno, G.; Hergueta-Redondo, M.; Williams, C.; García-Santos, G.; Nitadori-Hoshino, A.; Hoffman, C.; Badal, K.; Garcia, B. A.; Callahan, M. K.; Yuan, J.; Martins, V. R.; Skog, J.; Kaplan, R. N.; Brady, M. S.; Wolchok, J. D.; Chapman, P. B.; Kang, Y.; Bromberg, J.; Lyden, D., Melanoma exosomes educate bone marrow progenitor cells toward a pro-metastatic phenotype through MET. *Nature medicine* **2012,** *18* (6), 883-91.

131. Liu, Y.; Cao, X., Characteristics and Significance of the Pre-metastatic Niche. *Cancer cell* **2016,** *30* (5), 668-681.

132. Costa-Silva, B.; Aiello, N. M.; Ocean, A. J.; Singh, S.; Zhang, H.; Thakur, B. K.; Becker, A.; Hoshino, A.; Mark, M. T.; Molina, H.; Xiang, J.; Zhang, T.; Theilen, T. M.; Garcia-Santos, G.; Williams, C.; Ararso, Y.; Huang, Y.; Rodrigues, G.; Shen, T. L.; Labori, K. J.; Lothe, I. M.; Kure, E. H.; Hernandez, J.; Doussot, A.; Ebbesen, S. H.; Grandgenett, P. M.; Hollingsworth, M. A.; Jain, M.; Mallya, K.; Batra, S. K.; Jarnagin, W. R.; Schwartz, R. E.; Matei, I.; Peinado, H.; Stanger, B. Z.; Bromberg, J.; Lyden, D., Pancreatic cancer exosomes initiate pre-metastatic niche formation in the liver. *Nat Cell Biol* **2015,** *17* (6), 816-26.

133. Dai, J.; Escara-Wilke, J.; Keller, J. M.; Jung, Y.; Taichman, R. S.; Pienta, K. J.; Keller, E. T., Primary prostate cancer educates bone stroma through exosomal pyruvate kinase M2 to promote bone metastasis. *J Exp Med* **2019,** *216* (12), 2883-2899.

134. Orgaz, J. L.; Ladhani, O.; Hoek, K. S.; Fernandez-Barral, A.; Mihic, D.; Aguilera, O.; Seftor, E. A.; Bernad, A.; Rodriguez-Peralto, J. L.; Hendrix, M. J.; Volpert, O. V.; Jimenez, B., 'Loss of pigment epithelium-derived factor enables migration, invasion and metastatic spread of human melanoma'. *Oncogene* **2009,** *28* (47), 4147-61.

135. Plebanek, M. P.; Angeloni, N. L.; Vinokour, E.; Li, J.; Henkin, A.; Martinez-Marin, D.; Filleur, S.; Bhowmick, R.; Henkin, J.; Miller, S. D.; Ifergan, I.; Lee, Y.; Osman, I.; Thaxton, C. S.; Volpert, O. V., Pre-metastatic cancer exosomes induce immune surveillance by patrolling monocytes at the metastatic niche. *Nature Communications* **2017,** *8*.

136. Lajoie, P.; Nabi, I. R., Lipid rafts, caveolae, and their endocytosis. *International review of cell and molecular biology* **2010,** *282*, 135-63.

137. Sviridov, D.; Mukhamedova, N.; Miller, Y. I., Lipid rafts as a therapeutic target. *Journal of lipid research* **2020,** *61* (5), 687-695.

138. Svensson, K. J.; Christianson, H. C.; Wittrup, A.; Bourseau-Guilmain, E.; Lindqvist, E.; Svensson, L. M.; Morgelin, M.; Belting, M., Exosome uptake depends on ERK1/2-heat shock protein 27 signaling and lipid Raft-mediated endocytosis negatively regulated by caveolin-1. *The Journal of biological chemistry* **2013,** *288* (24), 17713-24.

139. Shen, W. J.; Asthana, S.; Kraemer, F. B.; Azhar, S., Scavenger receptor B type 1: expression, molecular regulation, and cholesterol transport function. *Journal of lipid research* **2018,** *59* (7), 1114-1131.

140. Roth, G. A.; Huffman, M. D.; Moran, A. E.; Feigin, V.; Mensah, G. A.; Naghavi, M.; Murray, C. J., Global and regional patterns in cardiovascular mortality from 1990 to 2013. *Circulation* **2015,** *132* (17), 1667-78.

141. Shepard, D.; VanderZanden, A.; Moran, A.; Naghavi, M.; Murray, C.; Roth, G., Ischemic Heart Disease Worldwide, 1990 to 2013: Estimates From the Global Burden of Disease Study 2013. *Circ Cardiovasc Qual Outcomes* **2015,** *8* (4), 455-6.

142. Feig, J. E.; Rong, J. X.; Shamir, R.; Sanson, M.; Vengrenyuk, Y.; Liu, J.; Rayner, K.; Moore, K.; Garabedian, M.; Fisher, E. A., HDL promotes rapid atherosclerosis regression in mice and alters inflammatory properties of plaque monocyte-derived cells. *Proc Natl Acad Sci U S A* **2011,** *108* (17), 7166-71.

143. Lacko, A. G.; Sabnis, N. A.; Nagarajan, B.; McConathy, W. J., HDL as a drug and nucleic acid delivery vehicle. *Front Pharmacol* **2015,** *6*, 247.

144. Rosenson, R. S.; Brewer, H. B., Jr.; Chapman, M. J.; Fazio, S.; Hussain, M. M.; Kontush, A.; Krauss, R. M.; Otvos, J. D.; Remaley, A. T.; Schaefer, E. J., HDL measures, particle heterogeneity, proposed nomenclature, and relation to atherosclerotic cardiovascular events. *Clin Chem* **2011,** *57* (3), 392-410.

145. Kontush, A.; Chapman, M. J., Functionally defective high-density lipoprotein: a new therapeutic target at the crossroads of dyslipidemia, inflammation, and atherosclerosis. *Pharmacol Rev* **2006,** *58* (3), 342-74.

146. Cao, Y. N.; Xu, L.; Han, Y. C.; Wang, Y. N.; Liu, G.; Qi, R., Recombinant high-density lipoproteins and their use in cardiovascular diseases. *Drug Discov Today* **2017,** *22* (1), 180-185.

147. Kataoka, Y.; Andrews, J.; Duong, M.; Nguyen, T.; Schwarz, N.; Fendler, J.; Puri, R.; Butters, J.; Keyserling, C.; Paolini, J. F.; Dasseux, J. L.; Nicholls, S. J., Regression of coronary atherosclerosis with infusions of the high-density lipoprotein mimetic CER-001 in patients with more extensive plaque burden. *Cardiovasc Diagn Ther* **2017,** *7* (3), 252-263.

148. Murakami, T., Phospholipid nanodisc engineering for drug delivery systems. *Biotechnol J* **2012,** *7* (6), 762-767.

149. Ng, K. K.; Lovell, J. F.; Vedadi, A.; Hajian, T.; Zheng, G., Self-Assembled Porphyrin Nanodiscs with Structure-Dependent Activation for Phototherapy and Photodiagnostic Applications. *Acs Nano* **2013,** *7* (4), 3484-3490.

150. Sabnis, N.; Nair, M.; Israel, M.; McConathy, W. J.; Lacko, A. G., Enhanced solubility and functionality of valrubicin (AD-32) against cancer cells upon encapsulation into biocompatible nanoparticles. *International journal of nanomedicine* **2012,** *7*, 975-83.

151. Skajaa, T.; Cormode, D. P.; Falk, E.; Mulder, W. J.; Fisher, E. A.; Fayad, Z. A., High-density lipoprotein-based contrast agents for multimodal imaging of atherosclerosis. *Arteriosclerosis, thrombosis, and vascular biology* **2010,** *30* (2), 169-76.

152. Forte, T. M.; Nordhausen, R. W., Electron microscopy of negatively stained lipoproteins. *Methods Enzymol* **1986,** *128*, 442-57.

153. Cormode, D. P.; Roessl, E.; Thran, A.; Skajaa, T.; Gordon, R. E.; Schlomka, J. P.; Fuster, V.; Fisher, E. A.; Mulder, W. J.; Proksa, R.; Fayad, Z. A., Atherosclerotic plaque composition: analysis with multicolor CT and targeted gold nanoparticles. *Radiology* **2010,** *256* (3), 774-82.

154. Brouillette, C. G.; Jones, J. L.; Ng, T. C.; Kercret, H.; Chung, B. H.; Segrest, J. P., Structural studies of apolipoprotein A-I/phosphatidylcholine recombinants by high-field proton NMR, nondenaturing gradient gel electrophoresis, and electron microscopy. *Biochemistry* **1984,** *23* (2), 359-67.

155. Mitra, K.; Ubarretxena-Belandia, I.; Taguchi, T.; Warren, G.; Engelman, D. M., Modulation of the bilayer thickness of exocytic pathway membranes by membrane proteins rather than cholesterol. *Proc Natl Acad Sci U S A* **2004,** *101* (12), 4083-8.

156. Melcrova, A.; Pokorna, S.; Pullanchery, S.; Kohagen, M.; Jurkiewicz, P.; Hof, M.; Jungwirth, P.; Cremer, P. S.; Cwiklik, L., The complex nature of calcium cation interactions with phospholipid bilayers. *Scientific reports* **2016,** *6*.

157. Yetukuri, L.; Soderlund, S.; Koivuniemi, A.; Seppanen-Laakso, T.; Niemela, P. S.; Hyvonen, M.; Taskinen, M. R.; Vattulainen, I.; Jauhiainen, M.; Oresic, M., Composition and lipid spatial distribution of HDL particles in subjects with low and high HDL-cholesterol. *Journal of lipid research* **2010,** *51* (8), 2341-51.

158. Huang, R.; Silva, R. A. G. D.; Jerome, W. G.; Kontush, A.; Chapman, M. J.; Curtiss, L. K.; Hodges, T. J.; Davidson, W. S., Apolipoprotein A-I structural organization in high-density lipoproteins isolated from human plasma. *Nature Structural & Molecular Biology* **2011,** *18* (4), 416-U44.

159. Henrich, S. E.; Hong, B. J.; Rink, J. S.; Nguyen, S. T.; Thaxton, C. S., Supramolecular Assembly of High-Density Lipoprotein Mimetic Nanoparticles Using Lipid-Conjugated Core Scaffolds. *Journal of the American Chemical Society* **2019,** *141* (25), 9753-9757.

160. Pandey, P.; Farha, O. K.; Spokoyny, A. M.; Mirkin, C. A.; Kanatzidis, M. G.; Hupp, J. T.; Nguyen, S. T., A "click-based" porous organic polymer from tetrahedral building blocks. *J Mater Chem* **2011,** *21* (6), 1700-1703.

161. Chan, Y. H.; van Lengerich, B.; Boxer, S. G., Lipid-anchored DNA mediates vesicle fusion as observed by lipid and content mixing. *Biointerphases* **2008,** *3* (2), FA17.

162. Hong, B. J.; Eryazici, I.; Bleher, R.; Thaner, R. V.; Mirkin, C. A.; Nguyen, S. T., Directed Assembly of Nucleic Acid-Based Polymeric Nanoparticles from Molecular Tetravalent Cores. *Journal of the American Chemical Society* **2015,** *137* (25), 8184-8191.

163. Stock, R. S.; Ray, W. H., Interpretation of photon correlation spectroscopy data: A comparison of analysis methods. *J. Polym. Sci., Polym. Phys. Ed.* **1985,** *23* (7), 1393-1447.

164. Fielding, C. J.; Fielding, P. E., Molecular Physiology of Reverse Cholesterol Transport. *Journal of lipid research* **1995,** *36* (2), 211-228.

165. Li, J. J.; Zhang, Y.; Li, S.; Cui, C. J.; Zhu, C. G.; Guo, Y. L.; Wu, N. Q.; Xu, R. X.; Liu, G.; Dong, Q.; Sun, J., Large HDL Subfraction But Not HDL-C Is Closely Linked With Risk Factors, Coronary Severity and Outcomes in a Cohort of Nontreated Patients With Stable Coronary Artery Disease A Prospective Observational Study. *Medicine* **2016,** *95* (4).

166. Morgan, J.; Carey, C.; Lincoff, A.; Capuzzi, D., High-density lipoprotein subfractions and risk of coronary artery disease. *Curr Atheroscler Rep* **2004,** *6* (5), 359-65.

167. Hoshino, A.; Costa-Silva, B.; Shen, T.-L.; Rodrigues, G.; Hashimoto, A.; Mark, M. T.; Molina, H.; Kohsaka, S.; Giannatale, A. D.; Ceder, S.; Singh, S.; Williams, C.; Soplop, N.; Uryu, K.; Pharmer, L.; King, T.; Bojmar, L.; Davies, A. E.; Ararso, Y.; Zhang, T.; Zhang, H.; Hernandez, J.; Weiss, J. M.; Dumont-Cole, V. D.; Kramer, K.; Wexler, L. H.; Narendran, A.; Schwartz, G. K.; Healey, J. H.; Sandstrom, P.; Labori, K. J.; Kure, E. H.; Grandgenett, P. M.; Hollingsworth, M. A.; Sousa, M. d.; Kaur, S.; Jain, M.; Mallya, K.; Batra, S. K.; Jarnagin, W. R.; Brady, M. S.; Fodstad, O.; Muller, V.; Pantel, K.; Minn, A. J.; Bissell, M. J.; Garcia, B. A.; Kang, Y.; Rajasekhar, V. K.; Ghajar, C. M.; Matei, I.; Peinado, H.; Bromberg, J.; Lyden, D., Tumour exosome integrins determine organotropic metastasis. *Nature* **2015,** *527* (7578), 329.

168. Karnezis, T.; Shayan, R.; Caesar, C.; Roufail, S.; Harris, N. C.; Ardipradja, K.; Zhang, Y. F.; Williams, S. P.; Farnsworth, R. H.; Chai, M. G.; Rupasinghe, T. W.; Tull, D. L.; Baldwin, M. E.; Sloan, E. K.; Fox, S. B.; Achen, M. G.; Stacker, S. A., VEGF-D promotes tumor metastasis

by regulating prostaglandins produced by the collecting lymphatic endothelium. *Cancer cell* **2012,** *21* (2), 181-95.

169. Fessler, M. B.; Parks, J. S., Intracellular Lipid Flux and Membrane Microdomains as Organizing Principles in Inflammatory Cell Signaling. *J Immunol* **2011,** *187* (4), 1529-1535.

170. Bethani, I.; Skanland, S. S.; Dikic, I.; Acker-Palmer, A., Spatial organization of transmembrane receptor signalling. *Embo J* **2010,** *29* (16), 2677-2688.

171. Steck, T. L.; Lange, Y., Transverse distribution of plasma membrane bilayer cholesterol: Picking sides. *Traffic* **2018,** *19* (10), 750-760.

172. Sheng, R.; Chen, Y.; Gee, H. Y.; Stec, E.; Melowic, H. R.; Blatner, N. R.; Tun, M. P.; Kim, Y.; Kallberg, M.; Fujiwara, T. K.; Hong, J. H.; Kim, K. P.; Lu, H.; Kusumi, A.; Lee, M. G.; Cho, W., Cholesterol modulates cell signaling and protein networking by specifically interacting with PDZ domain-containing scaffold proteins. *Nature Communications* **2012,** *3*.

173. Epand, R. M.; Sayer, B. G.; Epand, R. F., Caveolin scaffolding region and cholesterol-rich domains in membranes. *J Mol Biol* **2005,** *345* (2), 339-350.

174. Paila, Y. D.; Chattopadhyay, A., Membrane cholesterol in the function and organization of G-protein coupled receptors. *Subcell Biochem* **2010,** *51*, 439-66.

175. Martinez-Seara, H.; Rog, T.; Karttunen, M.; Vattulainen, I.; Reigada, R., Cholesterol Induces Specific Spatial and Orientational Order in Cholesterol/Phospholipid Membranes. *Plos One* **2010,** *5* (6).

176. Hoop, C. L.; Sivanandam, V. N.; Kodali, R.; Srnec, M. N.; van der Wel, P. C. A., Structural Characterization of the Caveolin Scaffolding Domain in Association with Cholesterol-Rich Membranes. *Biochemistry* **2012,** *51* (1), 90-99.

177. Rosen, C. J.; Ackert-Bicknell, C.; Rodriguez, J. P.; Pino, A. M., Marrow Fat and the Bone Microenvironment: Developmental, Functional, and Pathological Implications. *Crit Rev Eukar Gene* **2009,** *19* (2), 109-124.

178. Wang, H. F.; Leng, Y. M.; Gong, Y. P., Bone Marrow Fat and Hematopoiesis. *Front Endocrinol* **2018,** *9*.

179. Yu, S. H.; Liu, C. R.; Su, K. H.; Wang, J. H.; Liu, Y. L.; Zhang, L. M.; Li, C. Y.; Cong, Y. Z.; Kimberly, R.; Grizzle, W. E.; Falkson, C.; Zhang, H. G., Tumor exosomes inhibit differentiation of bone marrow dendritic cells. *J Immunol* **2007,** *178* (11), 6867-6875.

180. Chow, A.; Zhou, W. Y.; Liu, L.; Fong, M. Y.; Champer, J.; Van Haute, D.; Chin, A. R.; Ren, X. B.; Gugiu, B. G.; Meng, Z. P.; Huang, W. D.; Ngo, V.; Kortylewski, M.; Wang, S. E., Macrophage immunomodulation by breast cancer-derived exosomes requires Toll-like receptor 2-mediated activation of NF-kappa B. *Scientific reports* **2014,** *4*.

181. Maas, S. L. N.; Breakefield, X. O.; Weaver, A. M., Extracellular Vesicles: Unique Intercellular Delivery Vehicles. *Trends Cell Biol* **2017,** *27* (3), 172-188.

182. Bubendorf, L.; Schopfer, A.; Wagner, U.; Sauter, G.; Moch, H.; Willi, N.; Gasser, T. C.; Mihatsch, M. J., Metastatic patterns of prostate cancer: an autopsy study of 1,589 patients. *Human pathology* **2000,** *31* (5), 578-83.

183. Thysell, E.; Surowiec, I.; Hornberg, E.; Crnalic, S.; Widmark, A.; Johansson, A. I.; Stattin, P.; Bergh, A.; Moritz, T.; Antti, H.; Wikstrom, P., Metabolomic characterization of human prostate cancer bone metastases reveals increased levels of cholesterol. *PLoS One* **2010,** *5* (12), e14175.

184. Kregel, S.; Chen, J. L.; Tom, W.; Krishnan, V.; Kach, J.; Brechka, H.; Fessenden, T. B.; Isikbay, M.; Paner, G. P.; Szmulewitz, R. Z.; Griend, D. J. V., Acquired resistance to the second-

generation androgen receptor antagonist enzalutamide in castration-resistant prostate cancer. *7* **2016**.

185. Alix-Panabieres, C.; Riethdorf, S.; Pantel, K., Circulating tumor cells and bone marrow micrometastasis. *Clin Cancer Res* **2008,** *14* (16), 5013-5021.

186. Bidard, F. C.; Vincent-Salomon, A.; Sastre, X.; Sigal-Zafrani, A.; Nos, C.; Mignot, L.; Dieras, V.; Asselah, J.; Thiery, J. P.; Pierga, J. Y., Bone marrow micrometastasis and circulating tumor cells are respectively strong prognostic factors in early and metastatic breast cancer, a comparative study on 759 patients. *Breast Cancer Res Tr* **2007,** *106*, S26-S26.

187. Pantel, K., Bone Marrow Micrometastasis and Circulating Tumor Cells in Cancer Patients. *Tumor Biol* **2010,** *31*, S2-S2.

188. Jacome-Galarza, C. E.; Lee, S. K.; Lorenzo, J. A.; Aguila, H. L., Identification, characterization, and isolation of a common progenitor for osteoclasts, macrophages, and dendritic cells from murine bone marrow and periphery. *Journal of bone and mineral research : the official journal of the American Society for Bone and Mineral Research* **2013,** *28* (5), 1203-13.

189. Takegahara, N.; Kim, H.; Mizuno, H.; Sakaue-Sawano, A.; Miyawaki, A.; Tomura, M.; Kanagawa, O.; Ishii, M.; Choi, Y., Involvement of Receptor Activator of Nuclear Factor-kappaB Ligand (RANKL)-induced Incomplete Cytokinesis in the Polyploidization of Osteoclasts. *The Journal of biological chemistry* **2016,** *291* (7), 3439-54.

190. Catena, R.; Bhattacharya, N.; El Rayes, T.; Wang, S. M.; Choi, H.; Gao, D. C.; Ryu, S.; Joshi, N.; Bielenberg, D.; Lee, S. B.; Haukaas, S. A.; Gravdal, K.; Halvorsen, O. J.; Akslen, L. A.; Watnick, R. S.; Mittal, V., Bone Marrow-Derived Gr1(+) Cells Can Generate a Metastasis-Resistant Microenvironment Via Induced Secretion of Thrombospondin-1. *Cancer Discov* **2013,** *3* (5), 578-589.

191. Gao, D. C.; Joshi, N.; Choi, H. J.; Ryu, S. H.; Hahn, M.; Catena, R.; Sadik, H.; Argani, P.; Wagner, P.; Vahdat, L. T.; Port, J. L.; Stiles, B.; Sukumar, S.; Altorki, N. K.; Rafii, S.; Mittal, V., Myeloid Progenitor Cells in the Premetastatic Lung Promote Metastases by Inducing Mesenchymal to Epithelial Transition. *Cancer Research* **2012,** *72* (6), 1384-1394.

192. Shiozawa, Y.; Eber, M. R.; Berry, J. E.; Taichman, R. S., Bone marrow as a metastatic niche for disseminated tumor cells from solid tumors. *BoneKEy Reports* **2015,** *4*.

193. Weidle, U. H.; Birzele, F.; Kollmorgen, G.; Ruger, R., Molecular Mechanisms of Bone Metastasis. *Cancer Genomics Proteomics* **2016,** *13* (1), 1-12.

194. Zheng, H.; Li, W.; Kang, Y., Tumor-Stroma Interactions in Bone Metastasis: Molecular Mechanisms and Therapeutic Implications. *Cold Spring Harb Symp Quant Biol* **2016,** *81*, 151-161.

195. Sottnik, J. L.; Keller, E. T., Understanding and targeting osteoclastic activity in prostate cancer bone metastases. *Curr Mol Med* **2013,** *13* (4), 626-39.

196. Keller, E. T.; Brown, J., Prostate cancer bone metastases promote both osteolytic and osteoblastic activity. *J Cell Biochem* **2004,** *91* (4), 718-29.

197. Roato, I.; D'Amelio, P.; Gorassini, E.; Grimaldi, A.; Bonello, L.; Fiori, C.; Delsedime, L.; Tizzani, A.; De Libero, A.; Isaia, G.; Ferracini, R., Osteoclasts are active in bone forming metastases of prostate cancer patients. *PLoS One* **2008,** *3* (11), e3627.

198. Specific bone region localization of osteolytic versus osteoblastic lesions in a patient-derived xenograft model of bone metastatic prostate cancer. **2016,** *3* (4), 229–239.

199. Smith, M. R.; Saad, F.; Coleman, R.; Shore, N.; Fizazi, K.; Tombal, B.; Miller, K.; Sieber, P.; Karsh, L.; Damiao, R.; Tammela, T. L.; Egerdie, B.; Van Poppel, H.; Chin, J.; Morote, J.; Gomez-Veiga, F.; Borkowski, T.; Ye, Z.; Kupic, A.; Dansey, R.; Goessl, C., Denosumab and bone-metastasis-free survival in men with castration-resistant prostate cancer: results of a phase 3, randomised, placebo-controlled trial. *Lancet (London, England)* **2012,** *379* (9810), 39-46.

200. Collin-Osdoby, P.; Osdoby, P., RANKL-mediated osteoclast formation from murine RAW 264.7 cells. *Methods in molecular biology (Clifton, N.J.)* **2012,** *816*, 187-202.

201. Plebanek, M. P.; Bhaumik, D.; Bryce, P. J.; Thaxton, C. S., Scavenger Receptor Type B1 and Lipoprotein Nanoparticle Inhibit Myeloid-Derived Suppressor Cells. **2018**.

202. Yang, S.; Damiano, M. G.; Zhang, H.; Tripathy, S.; Luthi, A. J.; Rink, J. S.; Ugolkov, A. V.; Singh, A. T. K.; Dave, S. S.; Gordon, L. I.; Thaxton, C. S., Biomimetic, synthetic HDL nanostructures for lymphoma. **2013**.

203. Shen, W. J.; Azhar, S.; Kraemer, F. B., SR-B1: A Unique Multifunctional Receptor for Cholesterol Influx and Efflux. *Annu Rev Physiol* **2018,** *80*, 95-116.

204. Murphy-Ullrich, J. E.; Hook, M., Thrombospondin modulates focal adhesions in endothelial cells. *J Cell Biol* **1989,** *109* (3), 1309-19.

205. Murphy-Ullrich, J. E.; Lightner, V. A.; Aukhil, I.; Yan, Y. Z.; Erickson, H. P.; Hook, M., Focal adhesion integrity is downregulated by the alternatively spliced domain of human tenascin. *J Cell Biol* **1991,** *115* (4), 1127-36.

206. Mondul, A. M.; Clipp, S. L.; Helzlsouer, K. J.; Platz, E. A., Association between plasma total cholesterol concentration and incident prostate cancer in the CLUE II cohort. *Cancer Cause Control* **2010,** *21* (1), 61-68.

207. Platz, E. A.; Clinton, S. K.; Giovannucci, E., Association between plasma cholesterol and prostate cancer in the PSA era. *International Journal of Cancer* **2008,** *123* (7), 1693-1698.

208. Platz, E. A.; Till, C.; Goodman, P. J.; Parnes, H. L.; Figg, W. D.; Albanes, D.; Neuhouser, M. L.; Klein, E. A.; Thompson, I. M.; Kristal, A. R., Men with Low Serum Cholesterol Have a Lower Risk of High-Grade Prostate Cancer in the Placebo Arm of the Prostate Cancer Prevention Trial. *Cancer Epidem Biomar* **2009,** *18* (11), 2807-2813.

209. Van Hemelrijck, M.; Walldius, G.; Jungner, I.; Hammar, N.; Garmo, H.; Binda, E.; Hayday, A.; Lambe, M.; Holmberg, L., Low levels of apolipoprotein A-I and HDL are associated with risk of prostate cancer in the Swedish AMORIS study. *Cancer Cause Control* **2011,** *22* (7), 1011-1019.

210. Jacobs, E. J.; Rodriguez, C.; Bain, E. B.; Wang, Y.; Thun, M. J.; Calle, E. E., Cholesterol-lowering drugs and advanced prostate cancer incidence in a large U.S. cohort. *Cancer Epidemiol Biomarkers Prev* **2007,** *16* (11), 2213-7.

211. Jiang, S.; Wang, X.; Song, D.; Liu, X.; Gu, Y.; Xu, Z.; Wang, X.; Zhang, X.; Ye, Q.; Tong, Z.; Yan, B.; Yu, J.; Chen, Y.; Sun, M.; Wang, Y.; Gao, S., Cholesterol Induces Epithelial-to-Mesenchymal Transition of Prostate Cancer Cells by Suppressing Degradation of EGFR through APMAP. *Cancer Res* **2019,** *79* (12), 3063-3075.

212. Alfaqih, M. A.; Nelson, E. R.; Liu, W.; Safi, R.; Jasper, J. S.; Macias, E.; Geradts, J.; Thompson, J. W.; Dubois, L. G.; Freeman, M. R.; Chang, C. Y.; Chi, J. T.; McDonnell, D. P.; Freedland, S. J., CYP27A1 Loss Dysregulates Cholesterol Homeostasis in Prostate Cancer. *Cancer Res* **2017,** *77* (7), 1662-1673.

213. Gallagher, E. J.; Zelenko, Z.; Neel, B. A.; Antoniou, I. M.; Rajan, L.; Kase, N.; LeRoith, D., Elevated tumor LDLR expression accelerates LDL cholesterol-mediated breast cancer growth in mouse models of hyperlipidemia. *Oncogene* **2017,** *36* (46), 6462-6471.

214. Wortham, J. M.; Lee, J. T.; Althomsons, S.; Latash, J.; Davidson, A.; Guerra, K.; Murray, K.; McGibbon, E.; Pichardo, C.; Toro, B.; Li, L.; Paladini, M.; Eddy, M. L.; Reilly, K. H.; McHugh, L.; Thomas, D.; Tsai, S.; Ojo, M.; Rolland, S.; Bhat, M.; Hutchinson, K.; Sabel, J.; Eckel, S.; Collins, J.; Donovan, C.; Cope, A.; Kawasaki, B.; McLafferty, S.; Alden, N.; Herlihy, R.; Barbeau, B.; Dunn, A. C.; Clark, C.; Pontones, P.; McLafferty, M. L.; Sidelinger, D. E.; Krueger, A.; Kollmann, L.; Larson, L.; Holzbauer, S.; Lynfield, R.; Westergaard, R.; Crawford, R.; Zhao, L.; Bressler, J. M.; Read, J. S.; Dunn, J.; Lewis, A.; Richardson, G.; Hand, J.; Sokol, T.; Adkins, S. H.; Leitgeb, B.; Pindyck, T.; Eure, T.; Wong, K.; Datta, D.; Appiah, G. D.; Brown, J.; Traxler, R.; Koumans, E. H.; Reagan-Steiner, S., Characteristics of Persons Who Died with COVID-19 - United States, February 12-May 18, 2020. *MMWR Morb Mortal Wkly Rep* **2020,** *69* (28), 923-929.

215. Bansal, M., Cardiovascular disease and COVID-19. *Diabetes Metab Syndr* **2020,** *14* (3), 247-250.

216. Guijarro, C., COVID-19 and cardiovascular disease. *Clin Investig Arterioscler* **2020,** *32* (6), 263-266.

217. Schiffrin, E. L.; Flack, J. M.; Ito, S.; Muntner, P.; Webb, R. C., Hypertension and COVID-19. *Am J Hypertens* **2020,** *33* (5), 373-374.

218. Barrera, F. J.; Shekhar, S.; Wurth, R.; Moreno-Pena, P. J.; Ponce, O. J.; Hajdenberg, M.; Alvarez-Villalobos, N. A.; Hall, J. E.; Schiffrin, E. L.; Eisenhofer, G.; Porter, F.; Brito, J. P.; Bornstein, S. R.; Stratakis, C. A.; Gonzalez-Gonzalez, J. G.; Rodiguez-Gutierrez, R.; Hannah-Shmouni, F., Prevalence of Diabetes and Hypertension and Their Associated Risks for Poor Outcomes in Covid-19 Patients. *J Endocr Soc* **2020,** *4* (9), bvaa102.

219. Wang, H. L.; Yang, P.; Liu, K. T.; Guo, F.; Zhang, Y. L.; Zhang, G. Y.; Jiang, C. Y., SARS coronavirus entry into host cells through a novel clathrin- and caveolae-independent endocytic pathway. *Cell Res* **2008,** *18* (2), 290-301.

220. Wang, H.; Yuan, Z.; Pavel, M. A.; Hansen, S. B., The role of high cholesterol in age-related COVID19 lethality. *bioRxiv* **2020**.

221. Wang, S.; Li, W.; Hui, H.; Tiwari, S. K.; Zhang, Q.; Croker, B. A.; Rawlings, S.; Smith, D.; Carlin, A. F.; Rana, T. M., Cholesterol 25-Hydroxylase inhibits SARS-CoV-2 and other coronaviruses by depleting membrane cholesterol. *Embo J* **2020,** *39* (21), e106057.

222. Baglivo, M.; Baronio, M.; Natalini, G.; Beccari, T.; Chiurazzi, P.; Fulcheri, E.; Petralia, P. P.; Michelini, S.; Fiorentini, G.; Miggiano, G. A.; Morresi, A.; Tonini, G.; Bertelli, M., Natural small molecules as inhibitors of coronavirus lipid-dependent attachment to host cells: a possible strategy for reducing SARS-COV-2 infectivity? *Acta Biomed* **2020,** *91* (1), 161-164.

223. Wei, C.; Wan, L.; Yan, Q.; Wang, X.; Zhang, J.; Zhang, Y.; Sun, J.; Yang, X.; Gong, J.; Fan, C.; Yang, X.; Wang, Y.; Wang, X.; Li, J.; Yang, H.; Li, H.; Zhang, Z.; Wang, R.; Du, P.; Zong, Y.; Yin, F.; Zhang, W.; Peng, Y.; Lin, H.; Zhang, R.; Chen, W.; Gao, Q.; Cao, Y.; Zhong, H., SARS-CoV-2 manipulates the SR-B1-mediated HDL uptake pathway for its entry. *bioRxiv* **2020**.

224. Clayton, R. F.; Rinaldi, A.; Kandyba, E. E.; Edward, M.; Willberg, C.; Klenerman, P.; Patel, A. H., Liver cell lines for the study of hepatocyte functions and immunological response. *Liver Int* **2005,** *25* (2), 389-402.

225. Song, G. J.; Kim, S. M.; Park, K. H.; Kim, J.; Choi, I.; Cho, K. H., SR-BI mediates high density lipoprotein (HDL)-induced anti-inflammatory effect in macrophages. *Biochemical and biophysical research communications* **2015,** *457* (1), 112-8.

226. Rhainds, D.; Brissette, L., The role of scavenger receptor class B type I (SR-BI) in lipid trafficking. defining the rules for lipid traders. *Int J Biochem Cell Biol* **2004,** *36* (1), 39-77.

227. Bartosch, B.; Vitelli, A.; Granier, C.; Goujon, C.; Dubuisson, J.; Pascale, S.; Scarselli, E.; Cortese, R.; Nicosia, A.; Cosset, F. L., Cell entry of hepatitis C virus requires a set of co-receptors that include the CD81 tetraspanin and the SR-B1 scavenger receptor. *The Journal of biological chemistry* **2003,** *278* (43), 41624-30.

228. Areschoug, T.; Gordon, S., Scavenger receptors: role in innate immunity and microbial pathogenesis. *Cell Microbiol* **2009,** *11* (8), 1160-9.

229. Glasgow, A.; Glasgow, J.; Limonta, D.; Solomon, P.; Lui, I.; Zhang, Y.; Nix, M. A.; Rettko, N. J.; Zha, S.; Yamin, R.; Kao, K.; Rosenberg, O. S.; Ravetch, J. V.; Wiita, A. P.; Leung, K. K.; Lim, S. A.; Zhou, X. X.; Hobman, T. C.; Kortemme, T.; Wells, J. A., Engineered ACE2 receptor traps potently neutralize SARS-CoV-2. *Proc Natl Acad Sci U S A* **2020,** *117* (45), 28046-28055.

230. Wu, Y.; Wang, F.; Shen, C.; Peng, W.; Li, D.; Zhao, C.; Li, Z.; Li, S.; Bi, Y.; Yang, Y.; Gong, Y.; Xiao, H.; Fan, Z.; Tan, S.; Wu, G.; Tan, W.; Lu, X.; Fan, C.; Wang, Q.; Liu, Y.; Zhang, C.; Qi, J.; Gao, G. F.; Gao, F.; Liu, L., A noncompeting pair of human neutralizing antibodies block COVID-19 virus binding to its receptor ACE2. *Science* **2020,** *368* (6496), 1274-1278.

231. Shi, R.; Shan, C.; Duan, X.; Chen, Z.; Liu, P.; Song, J.; Song, T.; Bi, X.; Han, C.; Wu, L.; Gao, G.; Hu, X.; Zhang, Y.; Tong, Z.; Huang, W.; Liu, W. J.; Wu, G.; Zhang, B.; Wang, L.; Qi, J.; Feng, H.; Wang, F. S.; Wang, Q.; Gao, G. F.; Yuan, Z.; Yan, J., A human neutralizing antibody targets the receptor-binding site of SARS-CoV-2. *Nature* **2020,** *584* (7819), 120-124.

232. Case, J. B.; Rothlauf, P. W.; Chen, R. E.; Liu, Z.; Zhao, H.; Kim, A. S.; Bloyet, L. M.; Zeng, Q.; Tahan, S.; Droit, L.; Ilagan, M. X. G.; Tartell, M. A.; Amarasinghe, G.; Henderson, J. P.; Miersch, S.; Ustav, M.; Sidhu, S.; Virgin, H. W.; Wang, D.; Ding, S.; Corti, D.; Theel, E. S.; Fremont, D. H.; Diamond, M. S.; Whelan, S. P. J., Neutralizing Antibody and Soluble ACE2 Inhibition of a Replication-Competent VSV-SARS-CoV-2 and a Clinical Isolate of SARS-CoV-2. *Cell Host Microbe* **2020,** *28* (3), 475-485 e5.

233. Wang, R.; Simoneau, C. R.; Kulsuptrakul, J.; Bouhaddou, M.; Travisano, K.; Hayashi, J. M.; Carlson-Stevermer, J.; Oki, J.; Holden, K.; Krogan, N. J.; Ott, M.; Puschnik, A. S., Functional genomic screens identify human host factors for SARS-CoV-2 and common cold coronaviruses. *bioRxiv* **2020**.

234. Duivenvoorden, R.; Tang, J.; Cormode, D. P.; Mieszawska, A. J.; Izquierdo-Garcia, D.; Ozcan, C.; Otten, M. J.; Zaidi, N.; Lobatto, M. E.; van Rijs, S. M.; Priem, B.; Kuan, E. L.; Martel, C.; Hewing, B.; Sager, H.; Nahrendorf, M.; Randolph, G. J.; Stroes, E. S.; Fuster, V.; Fisher, E. A.; Fayad, Z. A.; Mulder, W. J., A statin-loaded reconstituted high-density lipoprotein nanoparticle inhibits atherosclerotic plaque inflammation. *Nat Commun* **2014,** *5*, 3065.

235. Pelchen-Matthews, A.; Raposo, G.; Marsh, M., Endosomes, exosomes and Trojan viruses. *Trends Microbiol* **2004,** *12* (7), 310-6.

236. Meckes, D. G., Exosomal Communication Goes Viral. *J Virol* **2015,** *89* (10), 5200-5203.